UNIVERSITY OF CALIFORNIA SAN DIEGO

SAN DIEGO STATE UNIVERSITY

Advances in the level set method for multiphase fluid-structure interaction with ocean engineering applications

A dissertation submitted in partial satisfaction of the
requirements for the degree Doctor of Philosophy

in

Engineering Sciences (Mechanical and Aerospace Engineering)

by

Kaustubh Manik Khedkar

Committee in charge:

University of California San Diego:

Professor Abhishek Saha, Co-Chair
Professor Robert Bitmead
Professor Qiang Zhu

San Diego State University:

Professor Amneet Pal Singh Bhalla, Co-Chair
Professor Zahra Nili Ahmadabadi

2024

The dissertation of Kaustubh Manik Khedkar is approved, and it is acceptable in quality and form for publication on microfilm and electronically.

_____

_____

_____

_____

Co-Chair

_____

Co-Chair

University of California San Diego

San Diego State University

2024

DEDICATION

I dedicate this dissertation to my loving parents, Rajashree Khedkar and Manik Khedkar, whose unwavering support and boundless love have been my guiding light throughout this journey.

EPIGRAPH

You have a right to perform your prescribed duty, but are not entitled to the fruits of action.
Never consider yourself the cause of the results of your activities,
and never be attached to not doing your duty.

The Bhagavad Gita, Chapter 2, Verse 47

TABLE OF CONTENTS

LIST OF FIGURES

LIST OF TABLES

LIST OF ALGORITHMS

ACKNOWLEDGEMENTS

Pursuing my Ph.D. has been a journey filled with hard work, challenges, and profound personal growth. I am highly grateful to all those who stood by me, offering unwavering support and guidance, helping me navigate the twists and turns of this academic endeavor. and would like to appreciate all those who supported me to achieve this milestone.

Foremost, my heartfelt appreciation goes to my Ph.D. advisor, Professor Amneet Pal Singh Bhalla, for giving me the invaluable opportunity to work with him on multitude of projects. His sage guidance, relentless encouragement and insightful feedback have not only shaped my research trajectory but also molded me into the scholar I am today. Professor Bhalla's unwavering passion for research serves as a beacon of inspiration. I highly admire his patience with me while teaching me how to write efficient codes, GitHub workflows, and working out complex math to get insightful meaning into problems. His strong handle on the fundamentals helped us both quickly delve into unfamiliar domains like control theory and reinforcement learning which has been a cornerstone of my research. I am deeply grateful for his generosity with his time, always available for code reviews, feedback sessions, analysis with results and illuminating discussions that have enriched my understanding and sharpened my skills. His constructive criticism and mentorship with my writing and presentation skills have honed my communication abilities, making me a more effective conveyer of ideas. Professor Bhalla's mentorship has been transformative, and I am indebted to him for his invaluable teachings and profound influence on my academic journey.

I extend my sincere gratitude to the members of my committee, Dr. Abhishek Saha, Dr. Robert Bitmead, Dr. Zahra Nili Ahmadabadi, and Dr. Qiang Zhu, for their invaluable suggestions and constructive feedback, which have enriched the quality of my thesis and bolstered the rigor of my research. Special thanks to Dr. David Kamensky for his guidance and insights during the formative years of my Ph.D.

The IBAMR developers group deserves heartfelt appreciation for their unwavering commitment to excellence in software design and their invaluable feedback during rigorous code

reviews. I am grateful for the enriching learning experiences and the opportunity to contribute meaningfully to IBAMR under their guidance.

Special thanks to Dr. Pieter Ghysels for graciously hosting me during my internships at the Lawrence Berkeley National Laboratory (LBNL), providing invaluable insights and fostering a conducive research environment.

I am also deeply indebted to Prof. Ganesh Natarajan and Dr. Amaresh Dalal for providing me the opportunity to develop CFD solvers at the AnuPravaha Lab, IIT Guwahati. Their encouragement played a pivotal role in shaping my decision to pursue a Ph.D.

Thanks to the San Diego State University (SDSU) startup fund and the National Science Foundation (NSF) awards OAC 1931368 and CBET CAREER 2234387 awarded to Professor Amneet Bhalla. Compute time on SDSU's high performance computing cluster Fermi is greatly acknowledged.

A very special thanks goes to my dear friend and colleague, Ramakrishnan Thirumalaisamy, whose steadfast companionship over the past seven years has made my academic journey truly enjoyable. His unwavering support, both professionally and personally, has been a source of strength and comfort. I am immensely fortunate to have shared this voyage with him. My heartfelt gratitude also goes to the San Diego Warriors Cricket team, whose camaraderie provided a sense of belonging and familial support throughout my Ph.D. journey, both on and off the Cricket field.

Lastly, I express my deepest gratitude to my family for their boundless love and unwavering support. Their faith in my abilities has been a constant source of motivation, propelling me to strive for excellence. Their enduring encouragement and resilience have instilled in me the fortitude to persevere in the face of challenges, and for that, I am eternally grateful.

Chapter 2 in full, is a reprint of the material as it appears in Preventing mass loss in the standard level set method: New insights from variational analyses, Kaustubh Khedkar; Amirreza Charchi Mamaghani, Pieter Ghysels, Neelesh A. Patankar, Amneet Pal Singh Bhalla, arXiv:2404.03132, 2024. The dissertation author was the primary investigator and author of this

paper.

Chapter 3, in part is a reprint of the material as it appears in An effective preconditioning strategy for volume penalized incompressible/low Mach multiphase flow solvers, Kaustubh Khedkar; Ramakrishnan Thirumalaisamy, Pieter Ghysels, Amneet Pal Singh Bhalla, Journal of Computational Physics, Volume 490, 2023, and Preventing mass loss in the standard level set method: New insights from variational analyses, Kaustubh Khedkar; Amirreza Charchi Mamaghani, Pieter Ghysels, Neelesh A. Patankar, Amneet Pal Singh Bhalla, arXiv:2404.03132, 2024. The dissertation author was the primary investigator and author of these papers.

Chapter 4 in full, is a reprint of the material as it appears in The inertial sea wave energy converter (ISWEC) technology: Device-physics, multiphase modeling and simulations, Kaustubh Khedkar; Nishant Nangia, Ramakrishnan Thirumalaisamy, Amneet Pal Singh Bhalla, Ocean Engineering, Volume 229, 2021. The dissertation author was the primary investigator and author of this paper.

Chapter 5 in full, is a reprint of the material as it appears in A model predictive control (MPC)-integrated multiphase immersed boundary (IB) framework for simulating wave energy converters (WECs), Kaustubh Khedkar; Amneet Pal Singh Bhalla, Ocean Engineering, Volume 260, 2022. The dissertation author was the primary investigator and author of this paper.

Chapter 6 in full, is not published. Investigators of the study were Kaustubh Khedkar, and Amneet Pal Singh Bhalla. The dissertation author was the primary investigator and author of this work.

VITA

2015	Bachelor of Engineering, Mechanical Engineering, Savitribai Phule Pune University, India.
2018	Master of Technology, Mechanical Engineering, Specialization in Fluids and Thermal Engineering, Indian Institute of Technology Guwahati, India.
2018–2019	Senior Research Fellow, AnuPravaha Laboratory, Department of Mechanical Engineering, Indian Institute of Technology Guwahati, India.
2022	Summer internship at Lawrence Berkeley National Laboratory, Berkeley.
2023	Summer internship at Lawrence Berkeley National Laboratory, Berkeley.
2024	Doctor of Philosophy in Engineering Sciences (Mechanical and Aerospace Engineering), San Diego State University and University of California, San Diego.

PUBLICATIONS

1. **Kaustubh Khedkar**, Amirreza Charchi Mamaghani, Pieter Ghysels, Neelesh A. Patankar, Amneet Pal Singh Bhalla, Preventing mass loss in the standard level set method: New insights from variational analyses, arXiv:2404.03132, 2024.

2. Ramakrishnan Thirumalaisamy, **Kaustubh Khedkar**, Pieter Ghysels, Amneet Pal Singh Bhalla, An effective preconditioning strategy for volume penalized incompressible/low Mach multiphase flow solvers, Journal of Computational Physics, Volume 490, 2023.

3. **Kaustubh Khedkar**, Amneet Pal Singh Bhalla, A model predictive control (MPC)-integrated multiphase immersed boundary (IB) framework for simulating wave energy converters (WECs), Ocean Engineering, Volume 260, 2022.

4. **Kaustubh Khedkar**, Nishant Nangia, Ramakrishnan Thirumalaisamy, Amneet Pal Singh Bhalla, The inertial sea wave energy converter (ISWEC) technology: Device-physics, multiphase modeling and simulations, Ocean Engineering, Volume 229, 2021.

ABSTRACT OF THE DISSERTATION

Advances in the level set method for multiphase fluid-structure interaction with ocean engineering applications

by

Kaustubh Manik Khedkar

Doctor of Philosophy in Engineering Sciences (Mechanical and Aerospace Engineering)

University of California San Diego, 2024
San Diego State University, 2024

Professor Amneet Pal Singh Bhalla, Co-Chair
Professor Abhishek Saha, Co-Chair

The computational multiphase flow community has grappled with mass loss in the level set method for decades. Numerous solutions have been proposed, from fixing the reinitialization step to combining the level set method with other conservative schemes. However, our work reveals a more fundamental culprit: the smooth Heaviside and delta functions inherent to the standard formulation. We propose a novel approach using variational analysis to incorporate a mass conservation constraint. It introduces a Lagrange multiplier that enforces overall mass balance. Notably, as the delta function sharpens, i.e., approaches the Dirac delta limit, the

Lagrange multiplier approaches zero. However, the exact Lagrange multiplier method disrupts the signed distance property of the level set function. This motivates us to develop an approximate version of the Lagrange multiplier that preserves both overall mass and signed distance property of the level set function. Our framework even recovers existing mass-conserving level set methods, revealing some inconsistencies in prior analyses. We extend this approach to three-phase flows for fluid-structure interaction (FSI) simulations. Rigorous test problems confirm that the FSI dynamics produced by our simple, easy-to-implement immersed formulation with the approximate Lagrange multiplier method are accurate and match state-of-the-art solvers.

Next, we develop a simulation infrastructure to perform fully resolved simulations of wave energy converter (WEC) devices. We use the fictitious domain Brinkman penalization (FD/BP) technique, which is computationally more efficient than the body-conforming grid techniques. Simulating WEC devices involves complex fluid-structure interactions and, if done accurately, can be used to test different types of controllers in a more realistic setting. We simulate the dynamics of an inertial sea wave energy converter (ISWEC) device and a heaving vertical cylinder point absorber device in a numerical wave tank (NWT) for regular and irregular waves. We test various control strategies: proportional-derivative (PD) control, model predictive control (MPC), and model-free reinforcement learning (RL) techniques to optimize the performance of such devices. Results show that the fully resolved multiphase simulations are closer to reality than the predominantly used boundary element method (BEM) based on linear potential flow theory models that overpredict the WEC dynamics.

Chapter 1

Introduction

Multiphase flows are ubiquitous in nature and industrial processes. Some examples are gas bubbles rising in a liquid column, droplets falling on a liquid pool, flow of water and/or oil with gas in a pipeline, and floating naval vessels at sea. Tracking the moving interface between different phases is crucial when simulating multiphase flow problems. Many interface tracking methods are developed like the volume of fluid method (VOF) [1, 2], level set method (LSM) [3, 4], diffuse interface methods [5, 6, 7, 8], front tracking methods [9, 10], and Lagrangian-Eulerian methods [11, 12]. Among all these methods, the level set method is the most popular interface capturing method due to its ease of implementation, especially for continuously changing interfaces that can break up and coalesce [4, 13, 14]. Also, it can perform fast numerical computations of geometric properties like normal vector and surface curvature [3]. In the standard level set method, a scalar field ϕ is initialized to a signed distance function. At the interface, the value of ϕ is zero and has positive values in one of the fluids and negative values in the other. To evolve the interface, the level set field is advected using the flow field, which is easy to solve numerically.

With all its attractive features, the level set method has a drawback: it cannot conserve the mass of the fluid exactly [4]. There has been extensive research on the mass loss issue associated with the level set method. The main culprit has been identified as the level set reinitialization equation, which restores the signed distance function (SDF) property. The SDF

property is disrupted by the advection of the level set function. Many fixes have been proposed in the literature to limit the motion of the interface (represented as the zero contour of the level set) during reinitialization. Solomenko et al. [15] compares many of these fixes proposed in the literature for the reinitialization equation on benchmarking problems. While some fixes perform better than others, the level set method still loses a substantial amount of mass over time, particularly as complex motions occur at the interface.

Some variations of the level set method have been developed to overcome the mass loss issue. One such method is the coupled level set/volume of fluid method (CLSVOF) [16]. The CLSVOF method combines the advantages of both methods, i.e., ease of computation of geometric properties using the level set and inherent mass conservation property of the VOF method. Another method called the hybrid particle level set method [17] is used to simulate problems where the fluid interface breaks into tiny fluid particles that escape off the surface of the larger. If LSM alone is used in such problems, the escaped particles remain under-resolved, and a very fine mesh needs to be used to resolve the tiny particles, which can get computationally expensive. In the hybrid particle LSM, Lagrangian marker particles are used to rebuild the under-resolved level set field. The hybrid moment of fluid–level set (HyMOFLS) method [18] combines the moment of fluid (MOF) [19, 20, 21] and CLSVOF method to simulate primary atomization of liquid fuel accurately. The idea behind the HyMOFLS method is to use the MOF method in the computational domain only when necessary and use the CLSVOF method almost all the time for interface reconstruction. All the hybrid methods complicate the implementation and the solution procedure and increase the computational costs.

We revisit the root cause of mass loss in the level set method. While reinitialization can contribute, our findings show that the primary culprit lies in the use of smooth Heaviside and delta functions within the standard formulation. Even if reinitialization is done exactly, i.e., the zero contour interface remains stationary, the standard level set method violates the mass conservation principle. Based on this insight, we propose a novel approach – incorporating a mass conservation constraint into the level set equation using variational analysis. This

approach introduces a Lagrange multiplier to enforce mass/volume conservation within the two-phase level set framework. As the smooth delta function becomes sharper, the Lagrange multiplier approaches zero. However, the exact Lagrange multiplier method disrupts the signed distance property to conserve mass. This motivates us to develop an approximate Lagrange multiplier method that preserves both properties. Although they are derived differently, exact and approximate Lagrange multipliers are related. Furthermore, our framework can be used to derive existing mass-conserving two-phase level set methods [22, 23], revealing some inconsistencies in the previous analyses [22].

We extend our variational analysis to three-phase flows, enabling fluid-structure interaction (FSI) simulations in two-fluid systems using the fictitious domain Brinkman penalization (FD/BP) technique. We present variational equations for three-phase flows in both non-immersed and immersed forms. As the diffuse body delta function in the immersed formulation sharpens, it converges to the non-immersed form. In this case, both formulations lead to identical exact and approximate Lagrange multipliers. To assess the immersed formulation's practical performance compared to the non-immersed one, we design rigorous test problems for three-phase flows. The immersed formulation is tested using the FD/BP method, while the non-immersed approach utilizes inherently mass-conserving techniques such as the geometric VOF technique with moving unstructured grids and cut-cell methods, and particle-based hydrodynamics methods. We demonstrate that our (simple to implement) immersed formulation in conjunction with the (approximate) Lagrange multiplier method produces FSI dynamics that match very well with the other state-of-the-art solvers. Further we demonstrate, if the computational domain size is large compared to the rigid body dimensions, our mass preserving level set method redundant. Taking this into account, we simulate applications related to ocean engineering–wave energy converter (WEC) devices which is the focus of this work.

The thesis is structured as follows. Chapter 2 describes the continuous equations of motion for incompressible fluid flows. It delves into the level set method and identifies the exact reasons behind the mass loss issue with the standard level set method. Next, it presents our

variational/constraint formulation for conserving mass for two and three phase flows. Chapter 3 discusses the discretization of the continuous equations on staggered Cartesian grids and describes a solution procedure for the developed projection preconditioner for the fully coupled Brinkman penalized Stokes system. We validate the efficacy of the preconditioner and the mass preserving level set method by simulating stringent numerical test cases. Chapter 4 highlights the need to transition to renewable wave energy technology. In this chapter we develop a robust and computationally efficient wave energy converter (WEC) device simulation infrastructure. We simulate the inertial sea wave energy converter (ISWEC) device with reactive control strategy and conduct parametric analysis on it. We describe the numerical wave tank (NWT) setup to simulate the WEC dynamics in a realistic setting. In Chapter 5, we implement an optimal control strategy called the model predictive control (MPC) for a point absorber WEC device. We justify the necessity of conducting CFD simulations for such devices by comparing our results with the predominantly used linear potential theory (LPT) based solvers. Finally, Chapter 6 presents model-free reinforcement learning (RL) based control strategies for WECs. It gives a background on RL and its implementation to optimize the performance of WEC devices in regular and irregular sea states using the LPT based models. At the end of this chapter we emphasize the need to conduct CFD simulations of WEC devices.

Chapter 2

Continuous Equations of Motion for Multiphase Fluid Flows

In this chapter, we begin by stating the continuous equations of motion for the multiphase flow system. This includes a continuous description of the level-set interface tracking method and its reasons for mass loss in the context of two phase flows. Next, a new variational analysis is presented, which introduces a Lagrange multiplier to impose mass/volume conservation constraints with the level set method. Additionally, we extend the two phase variational analysis to three phase flows, which allows us to simulate fluid structure interaction (FSI) in the presence of two fluids using fictitious domain Brinkman penalization (FD/BP) technique. Variational equations for three-phase flows are presented in non-immersed and immersed forms.

2.1 Continuous equations of motion

We use the single fluid formulation [24] for multiphase flows, which considers a single viscous incompressible fluid with spatially and temporally varying density $\rho(\mathbf{x},t)$ and viscosity $\mu(\mathbf{x},t)$ in a fixed region of space $\Omega \subset \mathbb{R}^d$, where $d = 3$ represents a three-dimensional region in space. The equations of motion for an incompressible fluid are given by the Navier-Stokes

equations, which in conservative form read as

$$\frac{\partial \rho \mathbf{u}(\mathbf{x},t)}{\partial t} + \nabla \cdot (\rho\, \mathbf{u}(\mathbf{x},t) \otimes \mathbf{u}(\mathbf{x},t)) \\ = -\nabla p(\mathbf{x},t) + \nabla \cdot \left[\mu \left(\nabla \mathbf{u}(\mathbf{x},t) + \nabla \mathbf{u}(\mathbf{x},t)^{\intercal}\right)\right] + \mathrm{f_{st}} + \mathrm{f_c} + \rho \mathbf{g}, \tag{2.1}$$

$$\nabla \cdot \mathbf{u}(\mathbf{x},t) = 0. \tag{2.2}$$

Eq. (2.1) describes the momentum of the system and Eq. (2.2) expresses the incompressibility of various phases present in the system. In the above equations, $\mathbf{u}(\mathbf{x},t)$ and $p(\mathbf{x},t)$ denote the Eulerian velocity and pressure fields, respectively, $\mathbf{x} = (x,y,z) \in \mathbb{R}^3$, $\mathrm{f_{st}}$ denotes the continuous surface tension force along the gas-liquid interface, and $\mathrm{f_c}$ is the Brinkman penalty term that imposes a rigid body velocity in the solid domain [25, 26]. The FD/BP method is also used for simulating elastic and deforming bodies in [27]. For two phase problems the $\mathrm{f_c}$ term is absent from Eq. (2.1). The specific forms of $\mathrm{f_{st}}$ and $\mathrm{f_c}$ will be provided later in Sec. 3.5.2 and Sec. 2.5, respectively. The acceleration due to gravity is directed towards the negative z-direction, $\mathbf{g} = (0,0,-g)$.

2.2 The standard level set interface tracking method

We use the level set method for capturing the interface between two fluids. The interface $\partial\Omega^{\mathrm{F}}(t)$ between two fluids is captured implicitly by the zero-contour of the level set function $\phi(\mathbf{x},t)$, which denotes the distance of a fixed location $\mathbf{x} \in \Omega$ from the time-evolving interface with a sign. At time t, fluid-1 and fluid-2 occupy non-overlapping regions $\Omega_1(t)$ and $\Omega_2(t)$, respectively, such that $\Omega_1(t) \cup \Omega_2(t) = \Omega$; see Fig. 2.1. In our sign convection, $\phi > 0$ in $\Omega_1(t)$ and $\phi < 0$ in $\Omega_2(t)$. In the absence of mass transfer across the interface, the interface moves with the local fluid velocity $\mathbf{u}(\mathbf{x},t)$, which can be described by an advection equation of the form

$$\frac{\partial \phi}{\partial t} + \mathbf{u} \cdot \nabla \phi = 0. \tag{2.3}$$

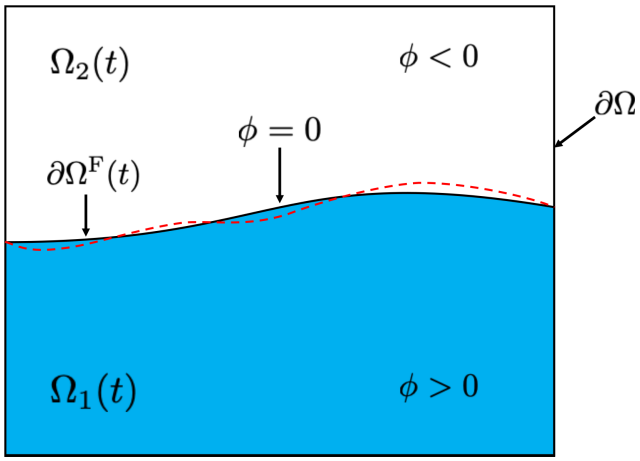

Figure 2.1. Schematic of the computational domain Ω for two phase flows depicting the time evolving interface $\partial\Omega^{\mathrm{F}}(t)$. The variation of the two-fluid interface $\partial\Omega^{\mathrm{F}}$ is illustrated by the red dashed line. For two phase flows $\Omega_1(t) \cup \Omega_2(t) = \Omega$.

The density and viscosity in the computational domain is set using the signed distance function $\phi(\mathbf{x},t)$

$$\rho(\phi) = \rho_1 H(\phi) + \rho_2 (1 - H(\phi)), \tag{2.4}$$

$$\mu(\phi) = \mu_1 H(\phi) + \mu_2 (1 - H(\phi)), \tag{2.5}$$

in which, ρ_1 and ρ_2, and μ_1 and μ_2, are the density and viscosity of fluid-1 and fluid-2, respectively. $H(\phi)$ is a smoothed Heaviside function, which allows material properties to vary smoothly over n_{cells} grid cells for numerical stability, see Eqs. (3.3) and (3.4). The derivative of the smoothed Heaviside function produces a smoothed delta function $\delta(\phi)$.

It is well known that the level set field does not maintain the signed distance property after advection [4, 28]. Retaining the signed distance property is essential as the advected ϕ is used to prescribe various material properties for the one-fluid model and calculate geometric quantities like the interface curvature and surface normals. To regain the signed distance property of ϕ, a reinitialization step is typically performed after the advection step. The reinitialization

step involves time-advancing the Hamilton-Jacobi equation to steady state

$$\frac{\partial \phi}{\partial \tau} + \mathrm{sgn}(\tilde{\phi})\,(|\nabla \phi| - 1) = 0. \tag{2.6}$$

Here, $\tilde{\phi}$ denotes the level set field before reinitialization and τ is the pseudo time used for time-marching Eq. (2.6). It is widely believed that the reinitialization step leads to mass loss because it artificially shifts the zero-contour or the two phase interface $\partial\Omega^{\mathrm{F}}$. In the next section, we show that is not entirely correct: the level set method would still lead to mass loss even if the interface remains static during the reinitialization step.

2.3 Precise reason for mass loss with the standard level set method

It is helpful to note down the Leibniz integral rule and Reynolds transport theorem (RTT) for performing differentiation under the integral sign for a general integrand f before working out the details of mass loss. We use both these rules several times in this and other sections. The Leibniz integral rule reads as

Leibniz rule for a moving domain:

$$\frac{\mathrm{d}}{\mathrm{d}t}\int_{\mathscr{V}(t)} f \,\mathrm{d}\mathscr{V} = \int_{\mathscr{V}(t)} \frac{\partial f}{\partial t}\,\mathrm{d}\mathscr{V} + \int_{\mathscr{A}(t)} f\,(\mathbf{u}_{\mathrm{s}}\cdot\mathbf{n})\,\mathrm{d}\mathscr{A}, \tag{2.7a}$$

Leibniz rule for a static domain:

$$\frac{\mathrm{d}}{\mathrm{d}t}\int_{\mathscr{V}} f \,\mathrm{d}\mathscr{V} = \int_{\mathscr{V}} \frac{\partial f}{\partial t}\,\mathrm{d}\mathscr{V}, \tag{2.7b}$$

in which, $\mathbf{n}$ and $\mathbf{u}_{\mathrm{s}}$ are the outward unit normal vector and velocity of the surface $\mathscr{A}(t)$ enclosing the time-varying domain $\mathscr{V}(t)$, respectively. When the domain is stationary $\mathscr{V}(t) \equiv \mathscr{V}$, Eq. (2.7a) becomes Eq. (2.7b). Note that the region $\mathscr{V}(t)$ is a geometric region that moves with a kinematic velocity $\mathbf{u}_{\mathrm{s}}$, which in general is different from the fluid/material velocity $\mathbf{u}$. The Leibniz integral

rule should not be confused with the Reynolds transport theorem. The two are related, but different because the latter uses a material control volume instead of a geometric one. A material control volume is defined as the one whose surface moves with the fluid/material velocity $\mathbf{u}$. Thus, a material control volume is a special case of a geometric volume. It is more restrictive because the amount of matter contained inside it cannot change over time as long as the fluid at every point within the volume moves with material velocity $\mathbf{u}$ governed by the conservation laws (mass and momentum). In general, a geometric control volume does not conserve the amount of matter within itself. The two theorems/rules are related to each other as

$$\text{RTT for a material volume:} \qquad \frac{\mathrm{d}}{\mathrm{d}t}\int_{\mathscr{V}(t)} f \,\mathrm{d}\mathscr{V} = \int_{\mathscr{V}(t)} \frac{\partial f}{\partial t}\,\mathrm{d}\mathscr{V} + \int_{\mathscr{A}(\mathrm{t})} f\,(\mathbf{u}\cdot\mathbf{n})\,\mathrm{d}\mathscr{A}. \tag{2.8}$$

Comparing Eq. (2.8) to (2.7a) it can be seen that the RTT is a Leibniz integral rule applied to a material control volume (whose surface moves with the material velocity) to express the rate of change of a conserved quantity. In this work, we leverage both the RTT and the Leibniz integral rule to express the rate of change of conserved and non-conserved quantities, respectively. This distinction clarifies the context and avoids potential confusion, as the terms RTT and Leibniz integral rule are sometimes used interchangeably in the literature.

To see why the standard level set method leads to mass loss, consider the rate of change of mass (which is a conserved quantity) contained within a closed domain Ω

$$\frac{\mathrm{d}}{\mathrm{d}t}\int_\Omega \rho \,\mathrm{dV} = \frac{\mathrm{d}}{\mathrm{d}t}\int_\Omega \left\{\rho_1 H(\phi) + \rho_2(1-H(\phi))\right\}\,\mathrm{dV}, \tag{2.9a}$$

$$= (\rho_1-\rho_2)\int_\Omega \delta(\phi)\frac{\partial \phi}{\partial t}\,\mathrm{dV}, \tag{2.9b}$$

$$= (\rho_1-\rho_2)\int_\Omega \delta(\phi)(-\breve{\mathbf{u}}\cdot\nabla\phi)\,\mathrm{dV}, \tag{2.9c}$$

in which we used the mixture model of density (Eq. (2.4)), RTT (Eq. (2.8)) with zero material velocity at the domain boundary, and the level set advection equation (Eq. (2.3)) in arriving at Eq. (2.9c). During the reinitialization process, the contours of the level set function surrounding

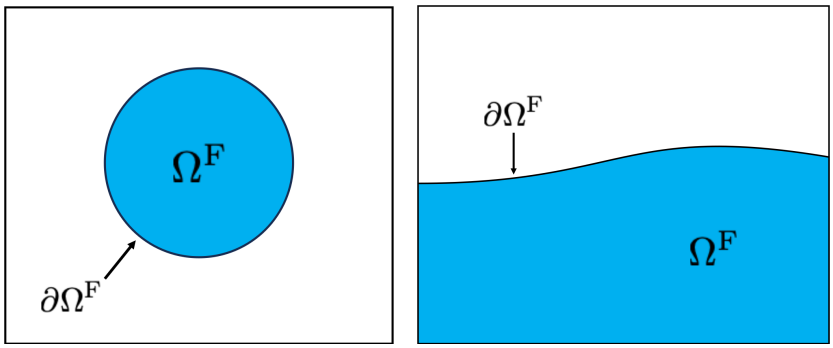

(a) A closed interface (b) An open interface

Figure 2.2. Two possible configurations of a two-phase interface $\partial\Omega^F$ in a closed domain Ω.

the interface $\partial\Omega^F$ move with velocity $\mathbf{u}^{\text{reinit}} = \text{sgn}(\tilde{\phi})\frac{\nabla\phi}{|\nabla\phi|}$ and adjust themselves to satisfy the Eikonal property $|\nabla\phi| = 1$. Overall ϕ gets advected with a combination of $\mathbf{u}$ and $\mathbf{u}^{\text{reinit}}$, which is denoted by $\breve{\mathbf{u}}$ in Eq. (2.9c).

To ensure mass conservation, the term on the right hand side (RHS) of Eq. (2.9c) must equal zero. This is possible if and only if (i) $\delta(\phi)$ is the Dirac/sharp delta function and (ii) $\mathbf{u}^{\text{reinit}} \equiv 0$ for $\partial\Omega^F$. In this case $\int_\Omega \delta(\phi)(\breve{\mathbf{u}}\cdot\nabla\phi)\,\text{dV} = \int_{\partial\Omega^F} \mathbf{u}\cdot|\nabla\phi|\mathbf{n}\,\text{dS} = \int_{\partial\Omega^F} \mathbf{u}\cdot\mathbf{n}\,\text{dS}$ represents the net normal (advective) velocity of the interface. For a closed domain, this surface integral is zero. We prove this identity at the end of this section. However, if δ is smooth, which is almost always the case in numerical simulations, the RHS of Eq. (2.9c) is non-zero, even when $\partial\Omega^F$ stays stationary during the reinitialization process. Thus, the smooth Heaviside and delta functions are the "main culprits" that lead to spurious mass loss/gain in the level set method from continuous equations point of view. This also explains why previous methods that have solely aimed to "fix" the reinitialization equation have not yielded satisfactory results for curbing the mass loss with the level set method.

Eq. (2.9c) helps explain why level set method continues to lose/gain mass over time. To see this integrate Eq. (2.9c) over a time period $\Delta t = t_f - t_i$. A straightforward integration shows that the spurious mass ΔM gained/lost over a period Δt is proportional to the interfacial region

displacement:

$$\begin{aligned}\Delta M &= (\rho_1-\rho_2)\int_{\Delta t}\int_{\Omega}\delta(\phi)(-\breve{\mathbf{u}}\cdot\nabla\phi)\ \mathrm{dV\ dt},\\ &= (\rho_1-\rho_2)\int_{\Delta t}\int_{\Omega}\delta(\phi)(-\breve{\mathbf{u}}\cdot|\nabla\phi|\mathbf{n})\ \mathrm{dV\ dt},\\ &= -(\rho_1-\rho_2)\int_{\Delta t}\int_{\Omega}\delta(\phi)\,\breve{u}_{\mathrm{n}}\ \mathrm{dV\ dt}. \end{aligned} \tag{2.10}$$

In numerical experiments, it is commonly observed that problems with large interface motion perform poorly in terms of mass conservation. The culprit is the smeared delta function that picks up the "residual" displacement around $\partial\Omega^{\mathrm{F}}$. In Sec. 3.5.2 we devise a special test problem that verifies Eq. (2.10).

To prove that $\int_{\partial\Omega^{\mathrm{F}}}\mathbf{u}\cdot\mathbf{n}\ \mathrm{dS}=0$ holds for a two-phase interface, consider Fig. 2.2, which depicts two possible configurations of the interface $\partial\Omega^{\mathrm{F}}$ in a closed domain Ω. An application of the Gauss-divergence theorem to a closed interface (shown in Fig. 2.2(a)) results in $\int_{\partial\Omega^{\mathrm{F}}}\mathbf{u}\cdot\mathbf{n}\ \mathrm{dS}=\int_{\Omega^{\mathrm{F}}}\nabla\cdot\mathbf{u}\ \mathrm{dV}$. The identity is proved by the fact that velocity $\mathbf{u}$ is divergence-free. An open interface is only possible if its two ends touch the domain boundary; see Fig. 2.2(b). Applying the Gauss-divergence theorem to the integrand $\nabla\cdot\mathbf{u}$ defined over the domain and interface bounded region Ω^{F} proves the identity.

2.4 A variational/constraint formulation for conserving mass for two phase flows with the standard level set method

To conserve mass with the standard level set method we need to explicitly add in a constraint to the level set advection equation. A variational approach is followed that introduces a Lagrange multiplier that enforces mass conservation. The mass of fluid-1 and its rate of change

can be computed from ϕ as

$$M_1(t) = \int_\Omega \rho_1 H(\phi)\ \mathrm{dV}, \tag{2.11a}$$

$$\frac{\mathrm{d}M_1}{\mathrm{d}t} = \frac{\mathrm{d}}{\mathrm{d}t}\int_\Omega \rho_1 H(\phi)\ \mathrm{dV} = \int_\Omega \rho_1 \delta(\phi)\frac{\partial \phi}{\partial t}\ \mathrm{dV}. \tag{2.11b}$$

Here, we made use of the RTT in deriving Eq. (2.11b). If the mass of fluid-1 is conserved then $M_1(t) \equiv M_1^0\ \forall\, t$, in which M_1^0 is the initial mass of fluid-1. For simplicity we have assumed that the domain is closed and there is no inflow and outflow of the phases. Thus, conserving mass of fluid-1 is equivalent to imposing a constraint on ϕ of the form

$$\mathscr{C}(\phi) \triangleq \int_\Omega \left(\rho_1 H(\phi) - \frac{M_1^0}{V}\right)\ \mathrm{dV} = 0, \tag{2.12}$$

in which, $V = \int_\Omega \mathrm{dV}$ is the volume of the computational domain.

The dynamical equation of the level set function ϕ in strong and weak form reads as

Strong form:

$$\mathscr{S}(\phi) \triangleq \frac{\mathrm{D}\phi}{\mathrm{D}t} = \frac{\partial \phi}{\partial t} + \breve{\mathbf{u}}\cdot\nabla\phi = 0, \ \text{ at } \forall\, \mathbf{x} \in \Omega \tag{2.13a}$$

Weak form:

$$\mathscr{W}(\phi, \hat{\delta}\phi) \triangleq \int_\Omega \left[\frac{\partial \phi}{\partial t} + \breve{\mathbf{u}}\cdot\nabla\phi\right]\hat{\delta}\phi\ \mathrm{dV} = 0, \ \ \phi \in H^1(\Omega)^3,\ \forall\ \hat{\delta}\phi \in H^1(\Omega)^3. \tag{2.13b}$$

The strong form of the level set Eq. (2.13a) considers the motion of ϕ due to both advection and reinitialization velocity fields (*cf.* Sec. 2.3). For the purposes of this derivation, it is convenient to consider that $\breve{\mathbf{u}}$ is known *a priori* using which ϕ can be computed (Eq. (2.13a)). This assumption is consistent with how incompressible multiphase flow simulations work in practice—level set (or for that matter VOF) advection and reinitialization are decoupled from momentum and continuity equations through operator splitting. The weak form of the equation is obtained by multiplying

the strong form with variation[1] in ϕ (also referred to as test function) and integrating it over the domain. Neither the strong nor the weak form of the equation guarantees mass conservation. In other words, $\breve{\mathbf{u}}$ is such that mass conservation is not guaranteed by the resulting ϕ field, which in turn is used to determine the density field. However, overall mass conservation constraint can be included through the use of a Lagrange multiplier λ_1. Adding this constraint does not change $\breve{\mathbf{u}}$ but it should modify the equation for ϕ. To derive the modified equation for ϕ, we define the Lagrangian $\mathscr{L}$ of the constraint $\mathscr{C}(\phi)$ and take its variation denoted by $\hat{\delta}\mathscr{L}$

$$\mathscr{L}(\Lambda_1,\phi) \triangleq \lambda_1 \int_\Omega \left(\rho_1 H(\phi) - \frac{M_1^0}{V}\right) \mathrm{dV}, \;\; \lambda_1 \in L^2(\Omega)^3 \tag{2.14a}$$

$$\hat{\delta}\mathscr{L}(\Lambda_1,\phi) \triangleq \hat{\delta}\lambda_1 \int_\Omega \left(\rho_1 H(\phi) - \frac{M_1^0}{V}\right) \mathrm{dV} + \lambda_1 \int_\Omega \rho_1 \delta(\phi)\hat{\delta}\phi \; \mathrm{dV}, \;\; \hat{\delta}\lambda_1 \in L^2(\Omega)^3. \tag{2.14b}$$

Adding the variation of the Lagrangian of the constraint to the weak form of the level set Eq. (2.13b) yields the overall weak form of the constrained level set function ϕ

$$\begin{aligned}\mathscr{T}(\hat{\delta}\phi,\hat{\delta}\lambda_1) \triangleq & \int_\Omega \left[\frac{\partial \phi}{\partial t} + \breve{\mathbf{u}}\cdot\nabla\phi\right]\hat{\delta}\phi \; \mathrm{dV} \\ & + \lambda_1 \int_\Omega \rho_1 \delta(\phi)\hat{\delta}\phi \; \mathrm{dV} + \hat{\delta}\lambda_1 \int_\Omega \left(\rho_1 H(\phi) - \frac{M_1^0}{V}\right) \mathrm{dV} = 0, \\ & \forall \; \hat{\delta}\phi \in H^1(\Omega)^3, \; \hat{\delta}\lambda_1 \in L^2(\Omega)^3. \end{aligned} \tag{2.15}$$

Collecting terms in $\hat{\delta}\lambda_1$ and $\hat{\delta}\phi$, and equating them to zero separately, yields the original constraint (Eq. (2.12)) and a new constrained dynamical equation for ϕ that aims to conserve the mass of fluid-1, respectively. The latter equation reads as

$$\frac{\partial \phi}{\partial t} + \breve{\mathbf{u}}\cdot\nabla\phi = -\lambda_1\rho_1\delta(\phi). \tag{2.16}$$

The value of the Lagrange multiplier λ_1 is obtained by substituting $\frac{\partial\phi}{\partial t} = -\breve{\mathbf{u}}\cdot\nabla\phi - \lambda_1\rho_1\delta(\phi)$

[1] We use the symbol $\hat{\delta}$ to denote variation of a quantity and δ to denote the Dirac/smooth delta function in this work.

into Eq. (2.11b) and setting $\frac{\mathrm{d}M_1}{\mathrm{d}t} = 0$. This yields

$$\begin{aligned} \frac{\mathrm{d}M_1}{\mathrm{d}t} &= \int_\Omega \rho_1 \delta(\phi)\left(-\breve{\mathbf{u}}\cdot\nabla\phi - \lambda_1\rho_1\delta(\phi)\right)\,\mathrm{dV} = 0, \\ \hookrightarrow \lambda_1 &= \frac{-\int_\Omega \delta(\phi)(\breve{\mathbf{u}}\cdot\nabla\phi)\mathrm{dV}}{\int_\Omega \rho_1\delta^2(\phi)\mathrm{dV}}. \end{aligned} \tag{2.17}$$

Note that Eq. (2.17) is not an explicitly solvable equation for λ_1. This is because the ϕ field used on the right hand side of the equation depends on the value of λ_1 itself as seen in Eq. (2.16). Thus, a fully implicit numerical implementation would require iterations. Due to the decoupling of level set advection from the incompressible Navier-Stokes equation, $\breve{\mathbf{u}}$ should remain fixed while iterating for λ_1. This means momentum, advection, and reinitialization equations are not solved during iterations.

Proceeding analogously, one can conserve the mass of fluid-2 $M_2 = \int_\Omega \rho_2(1-H(\phi))\,\mathrm{dV}$ by imposing a constraint of the form $\mathscr{C}(\phi) \stackrel{\triangle}{=} \int_\Omega \rho_2(1-H(\phi)) - M_2^0/V\,\mathrm{dV} = 0$ with the help of Lagrange multiplier $\lambda_2 \in L^2(\Omega)^3$. In this case the dynamical equation for the level set reads as

$$\frac{\partial\phi}{\partial t} + \breve{\mathbf{u}}\cdot\nabla\phi = \lambda_2\rho_2\delta(\phi). \tag{2.18}$$

The Lagrange multiplier λ_2 is obtained analogously as

$$\lambda_2 = \frac{\int_\Omega \delta(\phi)(\breve{\mathbf{u}}\cdot\nabla\phi)\,\mathrm{dV}}{\int_\Omega \rho_2\delta^2(\phi)\,\mathrm{dV}}. \tag{2.19}$$

From Eqs. (2.16)-(2.19), it is easy to verify that $-\lambda_1\rho_1 = \lambda_2\rho_2$. In light of this, we can see that Eqs. (2.16) and (2.18) are essentially the same, which in expanded form reads as

$$\frac{\partial\phi}{\partial t} + \breve{\mathbf{u}}\cdot\nabla\phi = \beta\delta(\phi) = \frac{\int_\Omega \delta(\phi)(\breve{\mathbf{u}}\cdot\nabla\phi)\,\mathrm{dV}}{\int_\Omega \delta^2(\phi)\,\mathrm{dV}}\delta(\phi). \tag{2.20}$$

Physically speaking, for two phase flows, conserving the mass of phase-1 leads to mass conservation for the other phase automatically. Thus, imposing a single constraint suffices.

It is instructive to analyze Eq. (2.20) in, both, the continuous differential equation form (with a sharp delta) and the discrete form. In the RHS of Eq. (2.20) β is a constant. When δ is the Dirac/sharp delta function then $\beta \to 0$. This is because β's numerator tends to zero, while its denominator $\int_\Omega \delta^2 \, \mathrm{dV} \to \infty$. As analyzed in Sec. 2.3, the integral term in the numerator of β, $\int_\Omega \delta(\phi)(\breve{\mathbf{u}} \cdot \nabla\phi) \, \mathrm{dV} = \int_{\partial\Omega^\mathrm{F}} \mathbf{u} \cdot |\nabla\phi| \mathbf{n} \, \mathrm{dS} = \int_{\partial\Omega^\mathrm{F}} \mathbf{u} \cdot \mathbf{n} \, \mathrm{dS}$ represents the net normal (advective) velocity of the interface. For a closed domain, this is zero. Thus, from a continuous point of view (when δ is sharp) β, λ_1, and λ_2 are zero. However, the RHS of Eq. (2.20) is $\beta\delta(\phi)$, which has a zero times infinity form. It is seen from Eq. (2.20) that $\beta\delta(\phi) \sim \frac{0}{\delta(0)}\delta(0)$, implying that $\beta\delta(\phi) = 0$. At the discrete level β is non-zero because neither its denominator nor its numerator evaluate to zero due to the finite width of the smooth delta function.

It is also informative to see how the non-linear Eq. (2.20) would be implemented in practice. The most natural way to implement a constrained equation is to employ some sort of operator-splitting technique. For example, in the first step, the level set field is advected. In the second step ϕ is reinitialized to restore its signed distance property, and in the final third step, ϕ is corrected (for mass loss errors) by evaluating the RHS of Eq. (2.20). It is easy to see that the third step essentially disrupts the signed distance property of ϕ near the interface because the corrective term has a non-constant gradient magnitude, i.e., $|\nabla(\beta\delta(\phi))|$ varies spatially. The exact Lagrange multiplier destroys the signed distance property of ϕ at the cost of conserving mass. This motivates the development of an approximate Lagrange multiplier that leads to both mass-conservation and signed distance retention for ϕ. We discuss the approximate Lagrange multiplier technique in Sec. 2.4.3.

2.4.1 Overall versus pointwise mass conservation

The Lagrange multiplier approach of Eq. (2.20) conserves mass in the domain discretely (i.e., when delta function is smooth and $\mathbf{u}^{\mathrm{reinit}} \neq 0$) in an integral sense. This can be proved as

follows

$$\begin{aligned}
\frac{\mathrm{d}}{\mathrm{d}t}\int_\Omega \rho \ \mathrm{dV} &= \frac{\mathrm{d}}{\mathrm{d}t}\int_\Omega \left\{\rho_1 H(\phi) + \rho_2(1-H(\phi))\right\} \mathrm{dV} \\
&= (\rho_1-\rho_2)\int_\Omega \delta(\phi)\frac{\partial \phi}{\partial t}\ \mathrm{dV} \\
&= (\rho_1-\rho_2)\int_\Omega \delta(\phi)\left\{-\breve{\mathbf{u}}\cdot\nabla\phi + \delta(\phi)\frac{\int_\Omega \delta(\phi)(\breve{\mathbf{u}}\cdot\nabla\phi)\ \mathrm{dV}}{\int_\Omega \delta^2(\phi)\ \mathrm{dV}}\right\}\mathrm{dV} \\
&= (\rho_1-\rho_2)\left(\int_\Omega -\delta(\phi)\breve{\mathbf{u}}\cdot\nabla\phi\ \mathrm{dV} + \int_\Omega \delta(\phi)\breve{\mathbf{u}}\cdot\nabla\phi\ \mathrm{dV}\right) \\
&= 0. \qquad (2.21)
\end{aligned}$$

In proving Eq. (2.21) mass of both phases is used. This is different from the derivation of λ_1 or λ_2 in the previous section which involved only one phase. Although Eq. (2.20) conserves mass in an integral sense, it does not guarantee pointwise mass conservation. To demonstrate this consider the pointwise conservation of mass equation

$$\begin{aligned}
\frac{\partial \rho}{\partial t} + \nabla\cdot(\mathbf{u}\rho) &= \frac{\partial \rho}{\partial t} + \mathbf{u}\cdot\nabla\rho \\
&= (\rho_1-\rho_2)\delta(\phi)\left(\frac{\partial \phi}{\partial t} + \mathbf{u}\cdot\nabla\phi\right) \\
&= (\rho_1-\rho_2)\delta(\phi)\left(-\breve{\mathbf{u}}\cdot\nabla\phi + \beta\delta(\phi) + \mathbf{u}\cdot\nabla\phi\right) \\
&= (\rho_1-\rho_2)\delta(\phi)\left([\mathbf{u}-\breve{\mathbf{u}}]\cdot\nabla\phi + \beta\delta(\phi)\right). \qquad (2.22)
\end{aligned}$$

Eq. (2.22) can be analyzed for two cases – the continuous form (with sharp δ and an exact reinitialization step for ϕ) and the discrete form (with a smooth delta). In either case the RHS of Eq. (2.22) is zero wherever δ is zero. Thus, only at the interfacial region (sharp or smooth) needs to be checked.

If the reinitialization step is exact then the $\phi = 0$ interface will not move in this step, implying $\mathbf{u} = \breve{\mathbf{u}}$ on the interface. Additionally, if δ is sharp then $\beta\delta(\phi) = 0$, as discussed above. Furthermore to understand pointwise mass conservation at the interface in this case, integrate

Eq. (2.22) over a pillbox at point on the $\phi = 0$ contour. The integral of the RHS of Eq. (2.22) over the pillbox will be zero because both $\mathbf{u} - \breve{\mathbf{u}}$ and $\beta\delta(\phi)$ are zero in this case. This implies that the jump of $\rho\mathbf{u}\cdot\mathbf{n}$ across the interface is zero which confirms pointwise mass conservation on the interface (note that integral of the time derivative term is zero since the volume of the pillbox is zero).

In the smeared/smoothed interfacial region case Eq. (2.22) suggests that mass is generated/lost in the interfacial region due to: (i) the motion of level set contours at a velocity different than the material velocity, i.e., $\breve{\mathbf{u}} \neq \mathbf{u}$; and (ii) the Lagrange multiplier. The latter term counteracts the effects of reinitialization and the smooth delta function to conserve mass in an average/integral sense, as shown in Eq. (2.21). Thus, Eq. (2.22) highlights the limitation of the level set method to achieve pointwise or local mass conservation with a smooth δ function. This is because there will always be errors associated with $\breve{\mathbf{u}} \neq \mathbf{u}$ in the smeared interface. In other words, a signed distance function based on level set reinitialization is fundamentally incompatible with pointwise mass conservation in the discrete case. However, for many practical applications, including those considered in this work, integral/global mass conservation is sufficient. For problems requiring local mass conservation, a different interface tracking method (e.g., geometric VOF) would be necessary. Another implication of the lack of pointwise mass conservation in the level set method is that a fully coupled (fully implicit) system that arises from the discretization of incompressible Navier-Stokes and level set equations will require future investigation to check for solvability and consistency. The operator-splitting approach is more "forgiving."

2.4.2 Conserving mass is the same as conserving volume for incompressible flows

Though it appears obvious that conserving mass and volume are equivalent for an incompressible fluid, a recent paper by Wen et al. [22] on a mass-preserving level set method has claimed otherwise. Later in Sec. 2.4.4 we show where specifically the authors went wrong. We demonstrate in this section that we will obtain the same dynamical equation for the level set

method as we did in the previous section if we impose constraints on conserving the volume of the two phases instead of mass.

Specially, consider V_1 as the volume of fluid-1 ($\phi > 0$ region) in the domain Ω that needs to be conserved. V_1 and its rate of change can be obtained from ϕ as

$$V_1(t) = \int_\Omega H(\phi)\ \mathrm{dV}, \tag{2.23a}$$

$$\frac{\mathrm{dV_1}}{\mathrm{dt}} = \frac{\mathrm{d}}{\mathrm{d}t}\int_\Omega H(\phi)\ \mathrm{dV} = \int_\Omega \delta(\phi)\frac{\partial \phi}{\partial t}\ \mathrm{dV}. \tag{2.23b}$$

We follow the same procedure outlined in Sec. 2.4 to derive the equations for conserving the volume of fluid-1 by imposing a constraint of the form $\mathscr{C}(\phi) \stackrel{\triangle}{=} \int_\Omega H(\phi)\ \mathrm{dV} - V_1^0 = 0$. Here, V_1^0 is the initial volume of fluid-1 in the domain. The dynamical equation for ϕ in this case reads as

$$\frac{\partial \phi}{\partial t} + \breve{\mathbf{u}} \cdot \nabla \phi = -\lambda_3 \delta(\phi), \tag{2.24a}$$

$$\lambda_3 = \frac{-\int_\Omega \delta(\phi)(\breve{\mathbf{u}} \cdot \nabla \phi)\ \mathrm{dV}}{\int_\Omega \delta^2(\phi)\ \mathrm{dV}}. \tag{2.24b}$$

We could also impose a constraint of the form $\mathscr{C}(\phi) \stackrel{\triangle}{=} \int_\Omega (1 - H(\phi))\ \mathrm{dV} - V_2^0 = 0$ to conserve the volume of fluid-2 ($\phi < 0$ region). In this case the dynamical equation for ϕ reads as

$$\frac{\partial \phi}{\partial t} + \breve{\mathbf{u}} \cdot \nabla \phi = \lambda_4 \delta(\phi), \tag{2.25a}$$

$$\lambda_4 = \frac{\int_\Omega \delta(\phi)(\breve{\mathbf{u}} \cdot \nabla \phi)\ \mathrm{dV}}{\int_\Omega \delta^2(\phi)\ \mathrm{dV}}. \tag{2.25b}$$

Comparing Eqs. (2.24a)-(2.25b), we can observe the relation $-\lambda_3 = \lambda_4$. This implies that Eqs. (2.24a) and (2.25a) are the same. For two-phase flows, if we satisfy volume conservation for one fluid, the other fluid's volume is automatically conserved. Moreover, substituting λ_3 in Eq. (2.24a) or λ_4 in Eq. (2.25a), we obtain the same dynamical equation for ϕ as written in Eq. (2.20).

2.4.3 Towards an approximate Lagrange multiplier method to prevent mass loss with the standard level set method

With the exact Lagrange multipliers λ_1-λ_4, mass can be conserved discretely, but there are two "issues":

1. Near the interface, the level set function does not remain a signed distance function. As discussed near the end of Sec. 2.4, this is due to the RHS of Eq. (2.20), which is of the form $\beta\delta(\phi)$. As a corrective term, this disrupts the signed distance property of ϕ derived from the reinitialization equation. As a result, the Lagrange multiplier "undoes" the reinitialization equation.

2. Computing β, specifically its numerator $\int_\Omega -\delta(\phi)\breve{\mathbf{u}}\cdot\nabla\phi$ dV is not straightforward or convenient.

Despite these challenges, implementing the exact Lagrange multiplier approach is still feasible. With respect to the first issue, although the "quality" of the mixture model given by Eqs. (2.4) and (2.5) gets deteriorated, it is unlikely that the effect will be significant because the Lagrange multiplier magnitude will not be very large (mass loss per time step will be small especially for resolved simulations). In other words, ϕ is unlikely to deviate too much from a signed distance function. Nonetheless, when computing geometric quantities such as the normal to the interface, care must be exercised: $\nabla\phi$ must be explicitly normalized by its magnitude to obtain the unit normal $\mathbf{n}$ to the interface. The second issue can be addressed by an indirect estimation of β. This approach is suggested in Wen et al. [22], where a similar integral term also appears. The dimension of this integral is rate of volume change—in Wen et al. the dimension is rate of mass change. The authors in [22] approximated the integral as $(M_1(t) - M_1^0)/\Delta t$, in which $M_1(t)$ represents the mass of fluid-1, which is estimated from the reinitialized level set function at time t and Δt is the current time step size. In Sec. 2.4.4 we critically analyze Wen et al's mass-conserving technique using our variational framework. Next, we present an alternative method that circumvents both issues while conserving mass with the standard level set method.

Consider the reinitialized level set function $\hat{\phi}$ that is obtained by solving the reinitialization Eq. (2.6) at time t. At this stage $\hat{\phi}$ is a signed distance function that does not satisfy the mass constraint $\mathscr{C}(\hat{\phi})$ of Eq. (2.12). We seek a spatially uniform correction ε for the reinitialized level set $\hat{\phi}$ such that

$$\mathscr{C}(\hat{\phi}+\varepsilon) = f(\varepsilon) = \int_{\Omega} \rho_1 H(\hat{\phi}+\varepsilon)\, \mathrm{dV} - M_1^0 = 0. \tag{2.26}$$

The spatially uniform correction ε guarantees that the corrected level set $\phi = \hat{\phi} + \varepsilon$ is a mass-conserving signed distance function. It will be seen below that the correction ε is proportional to an approximate Lagrange multiplier that enforces mass conservation with the level set method through a predictor-corrector type of a scheme

$$\frac{\hat{\phi} - \phi^n}{\Delta t} + \breve{\mathbf{u}} \cdot \nabla \hat{\phi} = 0, \qquad \text{[predictor step]} \tag{2.27a}$$

$$\frac{\phi - \hat{\phi}}{\Delta t} = \frac{\varepsilon - 0}{\Delta t} = \frac{\Delta \varepsilon}{\Delta t}. \qquad \text{[corrector step]} \tag{2.27b}$$

The equation set (2.27) can be thought of as a representation of a "continuous" equation of the form

$$\frac{\partial \phi}{\partial t} + \breve{\mathbf{u}} \cdot \nabla \phi = \frac{\mathrm{d}\varepsilon}{\mathrm{dt}}. \tag{2.28}$$

To relate the informal Eq. (2.28) and the formal Eq. (2.20), we first consider an intuitive argument and then present a mathematical derivation. Note that the "forcing" that induces a shift in the contour levels of ϕ is the RHS of Eq. (2.28). This term is taken to be uniform in the entire domain leading to the same correction to every contour level. The corresponding RHS of the formal Eq. (2.20) is $\beta\delta(\phi)$, where β is uniform everywhere. However, the $\delta(\phi)$ term makes the "forcing" in the formal equation non-uniform in the domain. If one picks a contour level, say $\phi = 0$, then the "forcing" does have the same value on that entire contour and this will lead to the same correction to ϕ on that contour. Similarly, each contour level has its own constant value of

correction to ϕ. This correction is maximum on $\phi = 0$ contour and decreases away from it until it is zero outside the smeared interfacial region where $\delta(\phi) = 0$. Since, in the formal method of Eq. (2.20) each contour level is corrected by a different amount, the distance function property is lost. The only way to preserve the distance function property of ϕ is to correct all contour levels by the same amount. This is the assumption made in the informal approach of Eq. (2.28). Thus, Eq. (2.28) would arise from Eq. (2.20) under the assumption that $\frac{\mathrm{d}\varepsilon}{\mathrm{dt}} = \beta\,\delta(\phi_m)$, which means that the correction of an appropriately chosen ϕ_m contour in the formal approach is uniformly applied in the entire domain to obtain the informal approach.

We now proceed with the mathematical derivation by obtaining an expression for the rate of change of correction $\frac{\mathrm{d}\varepsilon}{\mathrm{dt}}$. This can be obtained by differentiating Eq. (2.26) with respect to time

$$\frac{\mathrm{d}f(\varepsilon)}{\mathrm{d}t} = \int_\Omega \rho_1 \delta(\hat{\phi}+\varepsilon)\left(\frac{\partial\hat{\phi}}{\partial t} + \frac{\mathrm{d}\varepsilon}{\mathrm{d}t}\right)\,\mathrm{dV} = 0, \tag{2.29a}$$

$$\hookrightarrow \int_\Omega \rho_1 \delta(\hat{\phi}+\varepsilon)\frac{\partial\hat{\phi}}{\partial t}\,\mathrm{dV} = -\int_\Omega \rho_1 \delta(\hat{\phi}+\varepsilon)\frac{\mathrm{d}\varepsilon}{\mathrm{d}t}\,\mathrm{dV}, \tag{2.29b}$$

$$\hookrightarrow \frac{\mathrm{d}\varepsilon}{\mathrm{d}t} = \frac{\int_\Omega \delta(\hat{\phi}+\varepsilon)(\breve{\mathbf{u}}\cdot\nabla\hat{\phi})\,\mathrm{dV}}{\int_\Omega \delta(\hat{\phi}+\varepsilon)\,\mathrm{dV}} = \frac{\int_\Omega \delta(\hat{\phi}+\varepsilon)(\breve{\mathbf{u}}\cdot\nabla(\hat{\phi}+\varepsilon))\,\mathrm{dV}}{\int_\Omega \delta(\hat{\phi}+\varepsilon)\,\mathrm{dV}} = \frac{\int_\Omega \delta(\phi)(\breve{\mathbf{u}}\cdot\nabla\phi)\,\mathrm{dV}}{\int_\Omega \delta(\phi)\,\mathrm{dV}}. \tag{2.29c}$$

In Eq. (2.29a) we used the Leibniz rule to carry out the differentiation of the non-conserved quantity $f(\varepsilon)$ defined over the static region Ω. Eq. (2.29c) is arrived at by using the relations $\nabla\hat{\phi} = \nabla(\hat{\phi}+\varepsilon)$ and $\phi = \hat{\phi}+\varepsilon$. Comparing the right hand sides of Eqs. (2.20) and (2.28), we see that

$$\frac{\mathrm{d}\varepsilon}{\mathrm{d}t} = \frac{\int_\Omega \delta(\phi)(\breve{\mathbf{u}}\cdot\nabla\phi)\,\mathrm{dV}}{\int_\Omega \delta(\phi)\,\mathrm{dV}} = \delta(\phi_m)\,\frac{\int_\Omega \delta(\phi)(\breve{\mathbf{u}}\cdot\nabla\phi)\,\mathrm{dV}}{\delta(\phi_m)\int_\Omega \delta(\phi)\,\mathrm{dV}} = \delta(\phi_m)\widetilde{\beta}. \tag{2.30}$$

Eqs. (2.20) and (2.28) are therefore similar with a slight difference in β and $\widetilde{\beta}$: the latter is an approximation to β in which one of the smooth delta function terms (in the denominator) is

evaluated at the m^{th} contour. A uniform value is used with the approximate method to correct all ϕ contours. This correction corresponds to the shift/correction in the m^{th} contour of ϕ in the exact case. We demonstrate this by taking a commonly used smooth delta function in the level set literature

$$\delta(\phi) = \frac{1}{2\Delta} + \frac{1}{2\Delta}\cos\left(\frac{\pi\phi}{\Delta}\right) \quad \hookrightarrow \int_{-\Delta}^{\Delta} \delta(x)\,\mathrm{dx} = 1 \text{ and } \int_{-\Delta}^{\Delta} \delta^2(\mathrm{x})\,\mathrm{dx} = \frac{3}{4\Delta}, \tag{2.31}$$

in which Δ denotes the half-width of the interfacial region. The m^{th} contour of ϕ can be identified as follows:

$$\beta\,\delta(\phi_m) = \frac{\mathrm{d}\varepsilon}{\mathrm{d}t} = \widetilde{\beta}\,\delta(\phi_m) \implies \beta = \widetilde{\beta} \tag{2.32a}$$

$$\hookrightarrow \frac{\int_\Omega \delta(\phi)(\breve{\mathbf{u}}\cdot\nabla\phi)\,\mathrm{dV}}{\int_\Omega \delta^2(\phi)\,\mathrm{dV}} = \frac{\int_\Omega \delta(\phi)(\breve{\mathbf{u}}\cdot\nabla\phi)\,\mathrm{dV}}{\delta(\phi_m)\int_\Omega \delta(\phi)\,\mathrm{dV}} \tag{2.32b}$$

$$\hookrightarrow \delta(\phi_m) = \frac{\int_\Omega \delta^2(\phi)\,\mathrm{dV}}{\int_\Omega \delta(\phi)\,\mathrm{dV}} \tag{2.32c}$$

$$\hookrightarrow \frac{1}{2\Delta} + \frac{1}{2\Delta}\cos\left(\frac{\pi\phi_m}{\Delta}\right) = \frac{3}{4\Delta} \tag{2.32d}$$

$$\hookrightarrow \phi_m = \pm\frac{\Delta}{3}. \tag{2.32e}$$

The uniform correction applied by the approximate Lagrange multiplier corresponds to the exact correction at the contour $\Delta/3$ distance away from the interface.

Computing ε that preserves mass for the level set method is a simple root-finding problem, $f(\varepsilon) = 0$, for which we can use Newton's method:

$$f(\varepsilon_{k+1}) = f(\varepsilon_k) + \left.\frac{\mathrm{d}f}{\mathrm{d}\varepsilon}\right|_{\varepsilon_k} (\varepsilon_{k+1} - \varepsilon_k). \tag{2.33}$$

Setting $f(\varepsilon_{k+1}) = 0$ in the equation above yields

$$\varepsilon_{k+1} = \varepsilon_k - \frac{f(\varepsilon_k)}{\frac{\mathrm{d}f}{\mathrm{d}\varepsilon}\Big|_{\varepsilon_k}}, \tag{2.34a}$$

$$\begin{aligned} \hookrightarrow \Delta\varepsilon_{k+1} &= -\frac{\int_\Omega \rho_1 H(\hat{\phi}+\varepsilon_k)\,\mathrm{dV} - M_1^0}{\int_\Omega \rho_1 \delta(\hat{\phi}+\varepsilon_k)\,\mathrm{dV}} \\ &= -\frac{\int_\Omega H(\hat{\phi}+\varepsilon_k)\,\mathrm{dV} - M_1^0/\rho_1}{\int_\Omega \delta(\hat{\phi}+\varepsilon_k)\,\mathrm{dV}} \\ &= -\frac{\int_\Omega H(\hat{\phi}+\varepsilon_k)\,\mathrm{dV} - V_1^0}{\int_\Omega \delta(\hat{\phi}+\varepsilon_k)\,\mathrm{dV}}. \end{aligned} \tag{2.34b}$$

Here, k represents the (Newton) iteration counter. With $k = 0$, we start with a zero correction, i.e., $\varepsilon_0 = 0$ and iterate until mass is conserved to machine accuracy. The correction value ε will remain the same even when we impose a volume conservation constraint. This can be seen in the steps leading up to Eq. (2.34b).

Summary of exact vs. approximate Lagrange multiplier approaches: The inexact approach overcomes the two problems of the exact Lagrange multiplier equation, but its main drawback is that it is post-hoc in nature; Eq. (2.28) is formally not a continuous equation. The inexact technique, however, closely mimics the exact Lagrange multiplier approach (implemented via operator splitting). Another key difference between exact and approximate methods lies in how they adjust the level set contours to achieve mass balance. The exact approach prioritizes the zero-contour (interface), moving it the most. This movement gradually diminishes for contours farther away from the interface, with those outside the interfacial region remaining entirely static. In contrast, the approximate Lagrange multiplier approach applies a uniform adjustment across all contours throughout the domain. This acts as a long-range correction mechanism.

2.4.4 Comparison with other level set methods that conserve mass

Although there are many techniques available in the literature for conserving mass using the level set method, we highlight two studies that have applied continuous formulations in

place of pure numerical ones (i.e., combining level set with volume of fluid/moment of fluid methods, particle level set methods, etc.) to address mass loss problems. The conservative level set (CLS) method [29] is a continuous formulation, but we exclude it from this discussion since, despite its name, it also leads to mass loss—for example, see the dam break problem simulated in Parameswaran and Mandal [30] with CLS wherein mass losses up to 50% are reported (refer Fig. 22 of their work).

Mass preserving formulation of Wen et al.

A recent work by Wen et al. [22] describes a method of conserving mass with the standard level set method by including an additional source term in the equation. The source term form is selected ad-hoc with a free parameter η, whose value is determined through fluid-1's mass balance. In addition, the authors used a non-standard definition of mass in their derivation, which results in several inconsistencies. In this section, we present Wen et al.'s mass-preserving level set method based on the variational framework of Sec. 2.4. In our derivation, we will continue to use their mass definition to obtain a similar level set equation as in [22]. Their equation reads as

$$\frac{\partial \phi}{\partial t} + \breve{\mathbf{u}} \cdot \nabla \phi = \eta \, \delta(\phi) |\nabla \phi|, \tag{2.35a}$$

$$\eta = \frac{\int_\Omega L(\phi) \mu_\phi \, \mathrm{dV}}{\int_\Omega L(\phi) \delta(\phi) |\nabla \phi| \, \mathrm{dV}} \, . \tag{2.35b}$$

Here, $L(\phi) = \delta(\phi)\,[2(\rho_1 - \rho_2)H(\phi) + \rho_2]$ (see Eq. (26) in [22]) and μ_ϕ represents the "discretization error" in approximating $-\breve{\mathbf{u}} \cdot \nabla \phi$. Though the authors did not justify the form of the RHS of Eq. (2.35a), it resembles the RHS of our Eq. (2.20). Note that for level set methods, $|\nabla \phi| = 1$ thanks to the reinitialization process. Therefore, the use of $|\nabla \phi|$ in Eqs. (2.35) is redundant.

In [22], η is arrived at by defining mass of fluid-1 as

$$M_1(\phi) = \int_\Omega \rho(\phi) H(\phi) \, \mathrm{dV}, \tag{2.36}$$

which is different from the standard definition of mass used in Eq. (2.12). The implications of defining M_1 through Eq. (2.36) will be discussed later. For now we will continue using Eq. (2.36) to derive Wen et al.'s Eq. (2.35a) utilizing our variational framework. The rate of change of mass for fluid-1 can be computed using RTT as

$$\begin{aligned}\frac{\mathrm{d}M_1}{\mathrm{d}t} &= \frac{\mathrm{d}}{\mathrm{d}t}\int_\Omega \rho(\phi)H(\phi)\ \mathrm{dV},\\ &= \int_\Omega \left[H(\phi)\frac{\partial \rho(\phi)}{\partial t} + \rho(\phi)\frac{\partial H(\phi)}{\partial t}\right]\ \mathrm{dV},\\ &= \int_\Omega \left[2(\rho_1-\rho_2)H(\phi)+\rho_2\right]\delta(\phi)\frac{\partial \phi}{\partial t}\ \mathrm{dV},\\ &= \int_\Omega L(\phi)\frac{\partial \phi}{\partial t}\ \mathrm{dV}. \end{aligned} \tag{2.37}$$

The strong and weak form of the level set equation remains the same as the equation set (2.13). Based on the definition of mass of fluid-1, a constraint of the form

$$\mathscr{C}(\phi) = \int_\Omega \left(\rho(\phi)H(\phi) - \frac{M_1^0}{V}\right)\ \mathrm{dV} = 0, \tag{2.38}$$

is imposed with the help of the Lagrange multiplier $\Gamma \in L^2(\Omega)^3$. Following the derivation steps of Sec. 2.4 we obtain an equation for the mass-conserving level set field

$$\frac{\partial \phi}{\partial t} + \breve{\mathbf{u}}\cdot\nabla\phi = -\Gamma L(\phi), \tag{2.39a}$$

$$\Gamma = \frac{-\int_\Omega L(\phi)(\breve{\mathbf{u}}\cdot\nabla\phi)\ \mathrm{dV}}{\int_\Omega L^2(\phi)\ \mathrm{dV}}. \tag{2.39b}$$

The Lagrange multiplier Γ is obtained by substituting $\partial\phi/\partial t = -\Gamma L(\phi) - \breve{\mathbf{u}}\cdot\nabla\phi$ from Eq. (2.39a) into Eq. (2.37) and setting $\frac{\mathrm{d}M_1}{\mathrm{d}t} = 0$. Overall, Eq. (2.39a) reads as

$$\frac{\partial \phi}{\partial t} + \breve{\mathbf{u}}\cdot\nabla\phi = L(\phi)\frac{\int_\Omega L(\phi)(\breve{\mathbf{u}}\cdot\nabla\phi)\ \mathrm{dV}}{\int_\Omega L^2(\phi)\ \mathrm{dV}}. \tag{2.40}$$

Aside from the (redundant) $|\nabla\phi|$ terms, Eq. (2.40) is similar, but not the same as Eq. (2.35a).

Accordingly, Wen et al.'s Eq. (2.35a) does not follow the constraint formulation. Additionally, the discretization error μ_ϕ has not been quantified in [22]. If $\mu_\phi = 0$ for some advective scheme, then $\eta = 0$. In this case Eq. (2.35a) reverts back to the standard level set equation, which does not conserve mass. The interpretation of μ_ϕ as a discretization error is therefore not correct. Furthermore, the use of a non-standard definition of mass also leads to several inconsistencies. The inconsistencies can best be described by determining the constrained level equation that aims to conserve the mass of fluid-2 $M_2(\phi) = \int_\Omega \rho(\phi)[1 - H(\phi)]$ dV. Following the same procedure as above, we can derive fluid-2's mass-conserving equation, which reads as

$$\frac{\partial \phi}{\partial t} + \breve{\mathbf{u}} \cdot \nabla \phi = L_*(\phi) \frac{\int_\Omega L_*(\phi)(\breve{\mathbf{u}} \cdot \nabla \phi)\ \mathrm{dV}}{\int_\Omega L_*^2(\phi)\ \mathrm{dV}}. \tag{2.41}$$

Here, $L_*(\phi) = [(\rho_1 - 2\rho_2) + 2(\rho_2 - \rho_1)H(\phi)]\delta(\phi)$. Note that Eq. (2.41) differs from Eq. (2.40). Each fluid has its own governing equation. As part of their numerical experiments, Wen et al. (arbitrarily) chose the level set equation to preserve fluid-1's mass. The only way to conserve both fluids' masses simultaneously with this approach is to have $L(\phi) = L_*(\phi)$. This condition simplifies to yield $4(\rho_1 - \rho_2)H(\phi) = \rho_1 - 3\rho_2$. Considering that the RHS is constant, and the LHS varies spatially, this is a contradiction. There is also an unphysical condition $\rho_1 = -\rho_2$ at the interface where $\phi = 0$ and $H(\phi = 0) = 1/2$.

While Wen et al's method is inconsistent, their numerical results for two-phase flows match well with existing literature. We attribute this fortunate match to the fact that for well-resolved simulations, η (or the Lagrange multipliers) do not cause a substantial change in ϕ.

Mass preserving formulation of Kees et al.

Next, we describe the mass-conserving level set approach of Kees et al. [23] that can be considered an extension of the approximate Lagrange multiplier approach of Sec. 2.4.3. Their approach uses an advected volume fraction field $\widehat{H}$ as a target field to modify the reinitialized

level set function $\widehat{\phi}$ directly to correct for spurious mass loss/gain. Their mass-preserving level set approach can be described by the following equations:

$$\text{volume fraction advection:} \quad \frac{\partial \widehat{H}}{\partial t} + \nabla \cdot (\mathbf{u}\widehat{H}) = 0, \tag{2.42a}$$

$$\text{level set advection:} \quad \frac{\partial \tilde{\phi}}{\partial t} + \mathbf{u} \cdot \nabla \tilde{\phi} = 0, \tag{2.42b}$$

$$\text{level set reinitialization:} \quad \frac{\partial \widehat{\phi}}{\partial \tau} + \operatorname{sgn}(\tilde{\phi}) \left(|\nabla \widehat{\phi}| - 1 \right) = 0, \tag{2.42c}$$

$$\text{level set mass correction:} \quad \gamma \nabla^2 \varepsilon(\mathbf{x}) = H(\widehat{\phi} + \varepsilon(\mathbf{x})) - \widehat{H} \;\text{ with } \nabla \varepsilon(\mathbf{x}) \cdot \mathbf{n} = 0 \text{ on } \partial\Omega. \tag{2.42d}$$

Assuming no numerical diffusion errors, advecting fluid-1's volume fraction $\widehat{H}$ in a closed domain yields $\int_\Omega \widehat{H}(t)\ \mathrm{dV} = V_1^0$. The main idea behind the mass conserving approach of Kees et al. [23] is to solve (the nonlinear reaction-diffusion) Eq. (2.42d) with homogenous Neumann boundary conditions for a spatially varying level set correction field $\varepsilon(\mathbf{x})$. Integrating Eq. (2.42d) over the computational domain Ω reveals the constraint that Eq. (2.42d) imposes

$$\begin{aligned} &\int_\Omega H(\hat{\phi} + \varepsilon(\mathbf{x}))\ \mathrm{dV} - \int_\Omega \widehat{H}\ \mathrm{dV} = \gamma \int_\Omega \nabla^2 \varepsilon(\mathbf{x})\ \mathrm{dV}, \\ \hookrightarrow &\int_\Omega H(\hat{\phi} + \varepsilon(\mathbf{x}))\ \mathrm{dV} - \int_\Omega \widehat{H}\ \mathrm{dV} = \gamma \int_{\partial\Omega} \nabla \varepsilon(\mathbf{x}) \cdot \mathbf{n}\ \mathrm{dS} = 0, \\ \hookrightarrow &\int_\Omega H(\hat{\phi} + \varepsilon(\mathbf{x}))\ \mathrm{dV} = \int_\Omega \widehat{H}\ \mathrm{dV} = V_1^0. \end{aligned} \tag{2.43}$$

Eq. (2.43) defines essentially the same constraint as Eq. (2.26) with the difference that the corrective field ε is allowed to vary spatially. In their work, Kees et al. mention "γ *is a parameter that penalizes the deviation of* $\varepsilon(\mathbf{x})$ *from a global constant.* " In their numerical experiments, the authors take a large value of the penalty parameter γ. According to their results (see Figs. 5 and 6, and Table 1), ε remains essentially constant throughout the domain. In practice, Kees et al.'s approach is the same as the approximate Lagrange multiplier approach introduced in Sec. 2.4.3. The approximate Lagrange multiplier method is computationally more efficient than Kees et

al.'s approach because it does not require maintaining an additional advective field $\widehat{H}$. It also avoids inverting a large system of equations. The need for the latter arises due to the presence of a Laplacian operator in Eq. (2.42d).

2.5 Extension to three phase flows - FD/BP method

In this section, we extend mass conserving level set techniques for two-phase flows, i.e., exact and approximate Lagrange multiplier methods, to three-phase flows, by including a (moving) solid phase in the domain; see Fig. 2.3(a). Fluid-structure interactions are modeled using the fictitious domain Brinkman Penalization (FD/BP) method, which is an immersed boundary method. The FD/BP method solves a single momentum equation in the entire computational domain Ω, including the immersed solid region $\Omega_3(t) \subset \Omega$. The momentum of the solid body is accounted for by the penalty term $\mathrm{f_c}(\mathbf{x},t)$ in the momentum Eq. (2.1), whose form reads as

$$\mathrm{f_c}(\mathbf{x},t) = \frac{\chi(\mathbf{x},t)}{\kappa}\left(\mathbf{u_b}(\mathbf{x},t) - \mathbf{u}(\mathbf{x},t)\right). \tag{2.44}$$

The penalty term $\mathrm{f_c}$ ensures that the velocity inside the structure region $\Omega_3(t)$ is a rigid body velocity $\mathbf{u_b}(\mathbf{x},t)$. $\mathbf{u_b}$ is determined by hydrodynamic and gravity forces acting on the body [31]. An indicator function $\chi(\mathbf{x},t)$ tracks the location of a solid body within Ω. χ is non-zero only within $\Omega_3(t)$. The Brinkman penalization method treats the solid body as a porous region with vanishing permeability $\kappa \ll 1$. At the fluid-solid interface, the penalty force $\mathrm{f_c}$ can also be treated differently in the normal and tangential directions. This possibility is explored in Sec. 3.5.4.

The interface $\partial\Omega^{\mathrm{S}}(t)$ between fluid and solid domains is tracked by a level set function $\zeta(\mathbf{x},t)$: $\zeta > 0$ in $\Omega^{\mathrm{F}}(t)$, $\zeta < 0$ in $\Omega_3(t)$, and $\zeta = 0$ on $\partial\Omega^{\mathrm{S}}(t)$. The solid level set is advected using

$$\frac{\partial \zeta}{\partial t} + \mathbf{u}\cdot\nabla\zeta = 0. \tag{2.45}$$

In what follows next, we assume that the solid domain does not loose mass/volume due

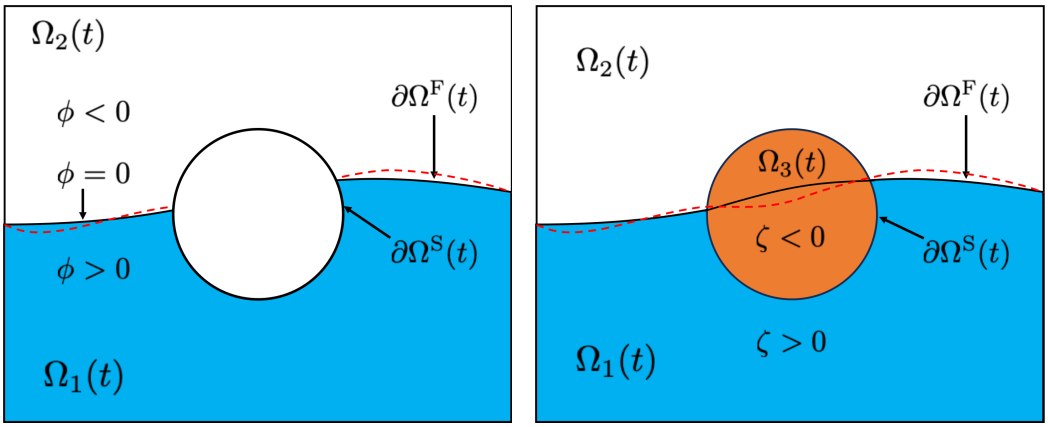

(a) Non-immersed formulation (b) Immersed formulation

Figure 2.3. Schematic of the computational domain Ω for three phase flows considered in (a) non-immersed and (b) immersed formulations. The variation of the two-fluid interface $\partial\Omega^{\mathrm{F}}$ is illustrated by the red dashed line.

to the motion/advection of $\zeta(\mathbf{x},t)$ within Ω, and all mass/volume issues stem from the level set function $\phi(\mathbf{x},t)$ which defines the interface $\partial\Omega^{\mathrm{F}}(t)$ between the two fluid phases.

2.5.1 Conservation of mass/volume for non-immersed bodies

Exact Lagrange multiplier approach: We first present the non-immersed formulation, in which the level set function $\phi(\mathbf{x},t)$ does not exist within the structure region. $\phi(\mathbf{x},t)$ is assumed to satisfy appropriate boundary conditions on $\partial\Omega$ and $\partial\Omega^{\mathrm{S}}(t)$. The non-immersed scenario is akin to a deforming/moving mesh that has a hole (to represents the body) inside it. We aim to conserve volume V_1 of fluid-1, which can be expressed in terms of ϕ as

$$V_1 = \int_{\Omega^{\mathrm{F}}(t)} H(\phi)\,\mathrm{dV}. \tag{2.46}$$

The rate change of volume V_1 (a conserved quantity) can be expressed using the RTT Eq. (2.8) as

$$\frac{\mathrm{d}V_1}{\mathrm{d}t} = \int_{\Omega^{\mathrm{F}}(t)} \delta(\phi)\frac{\partial\phi}{\partial t}\,\mathrm{dV} + \int_{\partial\Omega^{\mathrm{S}}(t)} H(\phi)(\mathbf{u}_{\mathrm{s}}\cdot\mathbf{n})\,\mathrm{dS}, \tag{2.47}$$

In Eq. (2.47) $\mathbf{n}$ represents a unit normal vector to the fluid-solid interface that points away from the fluid and into the solid. The no-slip condition on fluid-structure interface implies $\mathbf{u} = \mathbf{u}_{\mathrm{s}} = \mathbf{u}_{\mathrm{b}}(\partial\Omega^{\mathrm{S}}(t), t)$.

The strong and weak form of the dynamical equation for $\phi(\mathbf{x},t)$, $\mathscr{S}(\phi)$ and $\mathscr{W}(\phi)$, respectively, the volume constraint $\mathscr{C}(\phi)$, the Lagrangian of the constraint and its variation, $\mathscr{L}(\Lambda_1,\phi)$ and $\hat{\delta}\mathscr{L}(\Lambda_1,\phi)$. respectively, in the time-varying fluid domain $\Omega^{\mathrm{F}}(t)$ read as

$$\mathscr{S}(\phi) \triangleq \frac{\partial\phi}{\partial t} + \breve{\mathbf{u}}\cdot\nabla\phi = 0, \ \text{ at } \forall\, \mathbf{x} \in \Omega^{\mathrm{F}}(t), \tag{2.48a}$$

$$\mathscr{W}(\phi,\hat{\delta}\phi) \triangleq \int_{\Omega^{\mathrm{F}}(t)} \left[\frac{\partial\phi}{\partial t} + \breve{\mathbf{u}}\cdot\nabla\phi\right]\hat{\delta}\phi \ \mathrm{dV}, \ \ \phi \in H^1(\Omega^{\mathrm{F}}(t))^3, \ \forall\ \hat{\delta}\phi \in H^1(\Omega^{\mathrm{F}}(t))^3, \tag{2.48b}$$

$$\mathscr{C}(\phi) \triangleq \int_{\Omega^{\mathrm{F}}(t)} \left(H(\phi) - \frac{V_1^0}{V}\right) \mathrm{dV} = 0, \tag{2.48c}$$

$$\mathscr{L}(\Lambda_1,\phi) \triangleq \Lambda_1 \int_{\Omega^{\mathrm{F}}(t)} \left(H(\phi) - \frac{V_1^0}{V}\right) \mathrm{dV}, \ \ \Lambda_1 \in L^2(\Omega^{\mathrm{F}}(t))^3, \tag{2.48d}$$

$$\begin{aligned}\hat{\delta}\mathscr{L}(\Lambda_1,\phi) \triangleq\ & \hat{\delta}\Lambda_1 \int_{\Omega^{\mathrm{F}}(t)} \left(H(\phi) - \frac{V_1^0}{V}\right) \mathrm{dV} \\ & + \Lambda_1 \int_{\Omega^{\mathrm{F}}(t)} \delta(\phi)\hat{\delta}\phi \ \mathrm{dV}, \ \ \hat{\delta}\Lambda_1 \in L^2(\Omega^{\mathrm{F}}(t))^3.\end{aligned} \tag{2.48e}$$

Note that in Eq. (2.48e) the variation in the movement of the fluid domain $\Omega^{\mathrm{F}}(t)$ is not included. This is because the solid interface moves with the material velocity field. As noted earlier we are assuming that the velocity field is known (operator splitting with an explicit level set approach). The effect of domain variation would have to be probed if the velocity field was also an unknown. In that case, probing the effect of variation in the velocity field would cause variation in the movement of the fluid domain which in turn would lead to an extra term in the variation of the Lagrangian of the volume conservation constraint. The total variation, including the effect of variation in the domain movement on the Lagrangian of the constraint, would be:

$$\hat{\delta}^{\mathrm{total}}\mathscr{L}(\Lambda_1,\phi) = \hat{\delta}\mathscr{L}(\Lambda_1,\phi) + \Lambda_1 \int_{\partial\Omega^{\mathrm{S}}(t)} \left(H(\phi) - \frac{V_1^0}{V}\right) (\mathbf{v}_{\mathrm{s}}\mathrm{dt}\cdot\mathbf{n}) \ \mathrm{dS},$$

in which $\mathbf{v}_\mathrm{s}$ is the variation in velocity. The last term in the equation above arises due to variation in velocity (and the corresponding variation in domain movement) and is similar to that in the Leibniz theorem. If it is assumed that the velocity field is known *a priori* when solving for ϕ, then the last term is dropped because $\mathbf{v}_\mathrm{s}$ is zero.

Adding variation of the Lagrangian $\hat{\delta}\mathscr{L}(\Lambda_1,\phi)$ to the weak form $\mathscr{W}(\phi,\hat{\delta}\phi)$, collecting terms in $\hat{\delta}\Lambda_1$ and $\hat{\delta}\phi$, and equating them to zero separately, yields the original constraint (Eq. (2.48c)) and a new dynamical equation for ϕ that reads as

$$\frac{\partial\phi}{\partial t}+\breve{\mathbf{u}}\cdot\nabla\phi=-\Lambda_1\delta(\phi), \tag{2.49a}$$

$$\Lambda_1=\frac{-\int_{\Omega^\mathrm{F}(t)}\delta(\phi)(\breve{\mathbf{u}}\cdot\nabla\phi)\,\mathrm{dV}+\int_{\partial\Omega^\mathrm{S}(t)}H(\phi)(\mathbf{u}_\mathrm{s}\cdot\mathbf{n})\,\mathrm{dS}}{\int_{\Omega^\mathrm{F}(t)}\delta^2(\phi)\,\mathrm{dV}}. \tag{2.49b}$$

The value of the Lagrange multiplier Λ_1 is obtained by substituting $\frac{\partial\phi}{\partial t}=-\breve{\mathbf{u}}\cdot\nabla\phi-\Lambda_1\delta(\phi)$ into Eq. (2.47) and setting $\frac{\mathrm{d}V_1}{\mathrm{d}t}=0$.

Proceeding analogously, we can conserve the volume of fluid-2 $V_2=\int_{\Omega^\mathrm{F}(t)}(1-H(\phi))\,\mathrm{dV}$ by imposing a constraint of the form $\mathscr{C}(\phi)\overset{\triangle}{=}\int_{\Omega^\mathrm{F}(t)}(1-H(\phi))-V_2^0/V\,\mathrm{dV}=0$ with the help of Lagrange multiplier $\Lambda_2\in L^2(\Omega)^3$. In this case the dynamical equation for the level set reads as

$$\frac{\partial\phi}{\partial t}+\breve{\mathbf{u}}\cdot\nabla\phi=\Lambda_2\delta(\phi), \tag{2.50a}$$

$$\Lambda_2=\frac{\int_{\Omega^\mathrm{F}(t)}\delta(\phi)(\breve{\mathbf{u}}\cdot\nabla\phi)\,\mathrm{dV}-\int_{\partial\Omega^\mathrm{S}(t)}H(\phi)(\mathbf{u}_\mathrm{s}\cdot\mathbf{n})\,\mathrm{dS}}{\int_{\Omega^\mathrm{F}(t)}\delta^2(\phi)\,\mathrm{dV}}. \tag{2.50b}$$

In arriving at the RHS of Eq. (2.50b), we used $\frac{\mathrm{d}V_2}{\mathrm{d}t}=0$ and the relation $\int_{\partial\Omega^\mathrm{S}(t)}(\mathbf{u}_\mathrm{s}\cdot\mathbf{n})\,\mathrm{dS}=\int_{\Omega_3}\nabla\cdot\mathbf{u}_\mathrm{b}\,\mathrm{dV}=0$. The latter holds because $\mathbf{u}_\mathrm{b}$ is a volume-preserving rigid body velocity field.

Comparing the two level set equation sets (2.49) and (2.50), we observe the relation $-\Lambda_1=\Lambda_2$. Therefore, Eqs. (2.49a) and (2.50a) are the same, given by

$$\frac{\partial\phi}{\partial t}+\breve{\mathbf{u}}\cdot\nabla\phi=\alpha\delta(\phi)=\frac{\int_{\Omega^\mathrm{F}(t)}\delta(\phi)(\breve{\mathbf{u}}\cdot\nabla\phi)\,\mathrm{dV}-\int_{\partial\Omega^\mathrm{S}(t)}H(\phi)(\mathbf{u}_\mathrm{s}\cdot\mathbf{n})\,\mathrm{dS}}{\int_{\Omega^\mathrm{F}(t)}\delta^2(\phi)\,\mathrm{dV}}\,\delta(\phi). \tag{2.51}$$

Thus, conserving volume of fluid-1 automatically conserves the volume of fluid-2, even in the moving domain $\Omega^{\mathrm{F}}(t)$. Furthermore, it is straightforward to show that the equation for ϕ remains the same (as Eq. (2.51)), if we impose mass conservation constraints instead of volume ones. We omit the derivation steps for brevity.

Approximate Lagrange multiplier approach: Here we follow the derivation procedure of Sec. 2.4.3 to derive an approximate Lagrange multiplier to conserve mass/volume of the two fluid phases in the moving domain $\partial\Omega^{\mathrm{F}}(t)$. Consider the reinitialized level set function $\widehat{\phi}$ at time t that is a signed distance function, but it does not satisfy the constraint Eq. (2.48c) yet. We seek a spatially uniform correction ε that corrects $\widehat{\phi}$ to $\phi = \widehat{\phi} + \varepsilon$ while maintaining its signed distance property $|\nabla\phi| = |\nabla(\widehat{\phi} + \varepsilon)| = 1$. This is achieved by finding the root of the nonlinear equation

$$\mathscr{C}(\widehat{\phi} + \varepsilon) = f(\varepsilon) = \int_{\Omega^{\mathrm{F}}(t)} H(\widehat{\phi} + \varepsilon)\ \mathrm{dV} - V_1^0 = 0, \tag{2.52}$$

using Newton's method. The correction at the k^{th} Newton iteration becomes

$$\varepsilon_{k+1} = \varepsilon_k - \frac{f(\varepsilon_k)}{\left.\frac{\mathrm{d}f}{\mathrm{d}\varepsilon}\right|_{\varepsilon_k}}, \tag{2.53a}$$

$$\hookrightarrow \Delta\varepsilon_{k+1} = -\frac{\int_{\Omega^{\mathrm{F}}(t)} H(\widehat{\phi} + \varepsilon_k)\ \mathrm{dV} - V_1^0}{\int_{\Omega^{\mathrm{F}}(t)} \delta(\widehat{\phi} + \varepsilon_k)\ \mathrm{dV}}, \tag{2.53b}$$

which is iterated till the relative error ($\Delta = f(\varepsilon_k)/V_1^0$) drops to machine accuracy. To show the similarity between the exact and approximate Lagrange multiplier approaches for three phase flows, we need an expression for level set correction per unit time $\frac{\mathrm{d}\varepsilon}{\mathrm{dt}}$ instead of the total one: ε. This can obtained by differentiating $f(\varepsilon)$, which is a non conserved quantity defined over a

moving domain, with respect to time using the Leibniz integral rule

$$\frac{\mathrm{d}f(\varepsilon)}{\mathrm{d}t} = \int_{\Omega^{\mathrm{F}}(t)} \delta(\widehat{\phi}+\varepsilon)\left(\frac{\partial\widehat{\phi}}{\partial t}+\frac{\mathrm{d}\varepsilon}{\mathrm{d}t}\right)\,\mathrm{dV} + \int_{\partial\Omega^{\mathrm{S}}(t)} H(\widehat{\phi}+\varepsilon)(\mathbf{u}_{\mathrm{s}}\cdot\mathbf{n})\,\mathrm{dS} = 0, \tag{2.54a}$$

$$\hookrightarrow \frac{\mathrm{d}\varepsilon}{\mathrm{d}t} = \frac{\int_{\Omega^{\mathrm{F}}(t)} \delta(\widehat{\phi}+\varepsilon)(\breve{\mathbf{u}}\cdot\nabla(\widehat{\phi}+\varepsilon))\,\mathrm{dV} - \int_{\partial\Omega^{\mathrm{S}}(t)} H(\widehat{\phi}+\varepsilon)(\mathbf{u}_{\mathrm{s}}\cdot\mathbf{n})\,\mathrm{dS}}{\int_{\Omega^{\mathrm{F}}(t)} \delta(\widehat{\phi}+\varepsilon)\,\mathrm{dV}}, \tag{2.54b}$$

$$\hookrightarrow \frac{\mathrm{d}\varepsilon}{\mathrm{d}t} = \frac{\int_{\Omega^{\mathrm{F}}(t)} \delta(\phi)(\breve{\mathbf{u}}\cdot\nabla\phi)\,\mathrm{dV} - \int_{\partial\Omega^{\mathrm{S}}(t)} H(\phi)(\mathbf{u}_{\mathrm{s}}\cdot\mathbf{n})\mathrm{dS}}{\delta(\phi_m)\int_{\Omega^{\mathrm{F}}(t)} \delta(\phi)\,\mathrm{dV}}\,\delta(\phi_m) = \widetilde{\alpha}\,\delta(\phi_m). \tag{2.54c}$$

Here, again it can be seen that the RHS of Eq. (2.51) is similar to $\frac{\mathrm{d}\varepsilon}{\mathrm{d}t}$ with a slight difference in α and $\widetilde{\alpha}$: the latter is an approximation to α in which one of the smooth delta function terms (in the denominator) is evaluated at the m^{th} contour. Overall, there is no spatial variation in the correction and ϕ retains its signed distance property. Moreover, the root finding technique avoids calculating the numerator of α or $\widetilde{\alpha}$.

2.5.2 Conservation of mass/volume for immersed bodies

For non-immersed formulations with Cartesian grids, significant bookkeeping and stencil modifications are required to avoid solving the level set equation inside the (moving) structure domain Ω_3. With unstructured grids, when a solid body moves, the mesh can deform significantly, causing several problems. An alternate approach is to use an immersed formulation and allow the two-fluid interface to pass through the solid body as shown in Fig 2.3(b). The implementation of the level set method is greatly simplified as a result. Because the two phases existing inside the solid body are fictitious, care must be taken when imposing constraints. To calculate the actual volume (or mass) of the three phases, we introduce a second level set function ζ (outlined in

Sec. 2.5), which can be expressed as follows:

$$V_1 = \int_\Omega H(\phi)H(\zeta)\ \mathrm{dV}, \tag{2.55a}$$

$$V_2 = \int_\Omega (1-H(\phi))H(\zeta)\ \mathrm{dV}, \tag{2.55b}$$

$$V_3 = \int_\Omega (1-H(\zeta))\ \mathrm{dV}. \tag{2.55c}$$

In Eqs. (2.55a) and (2.55b) the inclusion of $H(\zeta)$ term ensures that the fluid volume is considered only outside the body. We will assume that the solid volume V_3 remains conserved, and the issue of mass/volume loss pertains to only fluids 1 and 2.

Using the RTT (Eq. (2.8)), the time derivatives of V_1 and V_2 (conserved quantities) in the closed and stationary computational domain Ω are obtained as:

$$\frac{\mathrm{d}V_1}{\mathrm{d}t} = \int_\Omega \left[\delta(\phi)H(\zeta)\frac{\partial\phi}{\partial t} + H(\phi)\delta(\zeta)\frac{\partial\zeta}{\partial t}\right]\ \mathrm{dV}, \tag{2.56a}$$

$$\frac{\mathrm{d}V_2}{\mathrm{d}t} = \int_\Omega \left[-\delta(\phi)H(\zeta)\frac{\partial\phi}{\partial t} + (1-H(\phi))\delta(\zeta)\frac{\partial\zeta}{\partial t}\right]\ \mathrm{dV}. \tag{2.56b}$$

The strong and weak form of the level set equation remains the same as Eq. (2.48a) and Eq. (2.48b), respectively, with the difference that they are now defined over the entire (static) domain Ω. That is $\phi \in H^1(\Omega)^3$ and $\hat{\delta}\phi \in H^1(\Omega)^3$. Working with the constraint of conserving fluid-1 volume, the Lagrangian of the constraint and its variation reads as

$$\mathscr{L}(\Lambda_3,\phi) \triangleq \Lambda_3 \int_\Omega \left(H(\phi)H(\zeta) - \frac{V_1^0}{V}\right)\ \mathrm{dV},\ \ \Lambda_3 \in L^2(\Omega)^3, \tag{2.57a}$$

$$\begin{aligned}\hat{\delta}\mathscr{L}(\Lambda_3,\phi) \triangleq\ & \hat{\delta}\Lambda_3 \int_\Omega \left(H(\phi)H(\zeta) - \frac{V_1^0}{V}\right)\ \mathrm{dV} \\ & + \Lambda_3 \int_\Omega \delta(\phi)H(\zeta)\hat{\delta}\phi\ \mathrm{dV},\ \ \hat{\delta}\Lambda_3 \in L^2(\Omega)^3.\end{aligned} \tag{2.57b}$$

Adding variation of the Lagrangian to the weak form, collecting terms in $\hat{\delta}\Lambda_3$ and $\hat{\delta}\phi$, and equating them to zero separately, yield the original constraint and a new dynamical equation for

ϕ that reads as

$$\frac{\partial \phi}{\partial t} + \breve{\mathbf{u}} \cdot \nabla \phi = -\Lambda_3 \delta(\phi) H(\zeta), \tag{2.58a}$$

$$\Lambda_3 = \frac{-\int_\Omega \delta(\phi) H(\zeta) (\breve{\mathbf{u}} \cdot \nabla \phi) \, \mathrm{dV} - \int_\Omega H(\phi) \delta(\zeta) (\mathbf{u} \cdot \nabla \zeta) \, \mathrm{dV}}{\int_\Omega \delta^2(\phi) H^2(\zeta) \, \mathrm{dV}}, \tag{2.58b}$$

$$\hookrightarrow \Lambda_3 = \frac{-\int_\Omega \delta(\phi) H(\zeta) (\breve{\mathbf{u}} \cdot \nabla \phi) \, \mathrm{dV} + \int_{\partial \Omega^{\mathrm{S}}(t)} H(\phi) (\mathbf{u}_{\mathrm{s}} \cdot \mathbf{n}) \, \mathrm{dS}}{\int_\Omega \delta^2(\phi) H^2(\zeta) \, \mathrm{dV}}. \tag{2.58c}$$

The value of the Lagrange multiplier Λ_3 in Eq. (2.58b) is obtained by substituting $\frac{\partial \phi}{\partial t} = -\breve{\mathbf{u}} \cdot \nabla \phi - \Lambda_3 \delta(\phi) H(\zeta)$ from Eq. (2.58a) and $\partial \zeta / \partial t = -\mathbf{u} \cdot \nabla \zeta$ from Eq. (2.45) into Eq. (2.56a) and setting $\frac{\mathrm{dV_I}}{\mathrm{dt}} = 0$. If the body delta function $\delta(\zeta)$ is sharp, then the expression for Λ_3 in Eq. (2.58b) can be further simplified to Eq. (2.58c) by using the relation $\int_\Omega H(\phi) \delta(\zeta) (\mathbf{u} \cdot \nabla \zeta) = \int_{\partial \Omega^{\mathrm{S}}(t)} H(\phi) (\mathbf{u}_{\mathrm{s}} \cdot \nabla \zeta) \, \mathrm{dS} = \int_{\partial \Omega^{\mathrm{S}}(t)} H(\phi) (\mathbf{u}_{\mathrm{s}} \cdot \mathbf{n}_{\mathrm{s}}) \, \mathrm{dS} = -\int_{\partial \Omega^{\mathrm{S}}(t)} H(\phi) (\mathbf{u}_{\mathrm{s}} \cdot \mathbf{n}) \, \mathrm{dS}$. Here, $\mathbf{n}_{\mathrm{s}} = -\mathbf{n}$ is the outward unit normal to the solid surface, which can be obtained from the signed distance function ζ as $\mathbf{n}_{\mathrm{s}} = \nabla \zeta / |\nabla \zeta| = \nabla \zeta$.

Proceeding analogously, we can conserve the volume of fluid-2 with the help of the Lagrange multiplier $\Lambda_4 \in L^2(\Omega)^3$. In this case the level set equation and the value of the Lagrange multiplier reads as

$$\frac{\partial \phi}{\partial t} + \breve{\mathbf{u}} \cdot \nabla \phi = \Lambda_4 \delta(\phi) H(\zeta), \tag{2.59a}$$

$$\Lambda_4 = \frac{\int_\Omega \delta(\phi) H(\zeta) (\breve{\mathbf{u}} \cdot \nabla \phi) \, \mathrm{dV} - \int_\Omega (1 - H(\phi)) \delta(\zeta) (\mathbf{u} \cdot \nabla \zeta) \, \mathrm{dV}}{\int_\Omega \delta^2(\phi) H^2(\zeta) \, \mathrm{dV}}, \tag{2.59b}$$

$$\hookrightarrow \Lambda_4 = \frac{\int_\Omega \delta(\phi) H(\zeta) (\breve{\mathbf{u}} \cdot \nabla \phi) \, \mathrm{dV} - \int_{\partial \Omega^{\mathrm{S}}(t)} H(\phi) (\mathbf{u}_{\mathrm{s}} \cdot \mathbf{n}) \, \mathrm{dS}}{\int_\Omega \delta^2(\phi) H^2(\zeta) \, \mathrm{dV}}. \tag{2.59c}$$

Comparing equations sets (2.58) and (2.59), we observe the relation $-\Lambda_4 = \Lambda_3$. Therefore, the level set equations (2.58a) and (2.59a) are the same. More importantly, the immersed formulation of the mass/volume conserving level set equation converges to the non-immersed one as the smeared body delta function $\delta(\zeta)$ becomes sharp. This can be observed by comparing equation sets (2.49) and (2.50), and equation sets (2.58) and (2.59). Outside the solid region where

$H(\zeta) = 1$, these equations are exactly the same. The equations remain the same if we impose mass conservation constraints instead of volume ones. The derivation steps are omitted for brevity.

Approximate Lagrange multiplier approach: Here we derive an approximate Lagrange multiplier to conserve mass/volume of the two fluid phases in an immersed sense. The nonlinear equation to solve for the spatially uniform correction ε in this case is

$$\mathscr{C}(\widehat{\phi}+\varepsilon) = f(\varepsilon) = \int_{\Omega} H(\widehat{\phi}+\varepsilon)H(\zeta)\ \mathrm{dV} - V_1^0 = 0 \tag{2.60}$$

Eq. (2.60) can be solved to machine accuracy using Newton's method. As done before, the connection between the approximate and exact Lagrange multipliers emerges through $\frac{\mathrm{d}\varepsilon}{\mathrm{d}t}$. Differentiating the non-conserved quantity $f(\varepsilon)$ defined over a static domain Ω with respect to time (using the Leibniz integral rule) yields

$$\frac{\mathrm{d}\varepsilon}{\mathrm{d}t} = \frac{\int_{\Omega} \delta(\widehat{\phi}+\varepsilon)H(\zeta)(\breve{\mathbf{u}}\cdot\nabla(\widehat{\phi}+\varepsilon))\ \mathrm{dV} + \int_{\Omega} H(\widehat{\phi}+\varepsilon)\delta(\zeta)(\mathbf{u}_{\mathrm{s}}\cdot\nabla\zeta)\mathrm{dV}}{\int_{\Omega} \delta(\widehat{\phi}+\varepsilon)H(\zeta)\ \mathrm{dV}}, \tag{2.61a}$$

$$\hookrightarrow \frac{\mathrm{d}\varepsilon}{\mathrm{d}t} = \widetilde{\Lambda}\delta(\phi_m)H(\zeta_n) = \frac{\left[\int_{\Omega} \delta(\phi)H(\zeta)(\breve{\mathbf{u}}\cdot\nabla\phi)\ \mathrm{dV} - \int_{\partial\Omega^{\mathrm{S}}(t)} H(\phi)(\mathbf{u}_{\mathrm{s}}\cdot\mathbf{n})\ \mathrm{dS}\right]}{\delta(\phi_m)H(\zeta_n)\int_{\Omega}\delta(\phi)H(\zeta)\ \mathrm{dV}}\ \delta(\phi_m)H(\zeta_n). \tag{2.61b}$$

Comparing Eqs. (2.59c) and (2.61b), it can be seen that $\widetilde{\Lambda}$ is approximately equal to the exact Lagrange multiplier Λ_4: the former is obtained by evaluating one of the smooth delta function terms and one of the smooth Heaviside function terms (in the denominator) at the m^{th} and n^{th} contour, respectively. Overall, there is no spatial variation in the correction and ϕ retains its signed distance property.

Enforcing the constraint defined by Eq. (2.60) using Newton's method ensures that the volume of phase-1 (defined by Eq. (2.55a)) is preserved to machine accuracy. Since the sum of the volumes for all three phases (Eqs. (2.55a) - (2.55c)) equals the total volume of the

domain, this constraint guarantees a key property for closed domains: if the volume of phase-1 is conserved to machine precision, the combined volumes of phase-2 and phase-3 will also be conserved to machine precision irrespective of the smeared body Heaviside function. The numerical simulations of Sec. 5.11 confirm this property.

Contact angle conditions

Material triple points are the points (or lines in 3D) where the two-fluid interface $\partial\Omega^{\mathrm{F}}$ intersects the solid surface $\partial\Omega^{\mathrm{S}}$. Under equilibrium/static conditions, $\partial\Omega^{\mathrm{F}}$ pins at $\partial\Omega^{\mathrm{S}}$ at an angle θ_{s} according to the Young-Laplace equation. A dynamic contact angle θ_{d} condition is better suited for transient conditions. For problems at the capillary length scale, the contact angle condition is relevant. The capillary length scale[2] in an air-water system is about 2.7 mm. The contact angle condition is not necessary for many fluid-structure problems in ocean engineering, since the relevant length scales are much larger than capillary ones.

If a specific contact angle θ needs to be imposed at the triple points, an equation similar to the reinitialization equation Eq. (2.6) can be used. This idea is proposed by Jettestuen et al. [32] who suggest using an equation of the form

$$\frac{\partial \phi}{\partial \tau} + \mathrm{sgn}(\zeta)\left(\nabla\zeta \cdot \nabla\phi - \cos(\theta)|\nabla\phi||\nabla\zeta|\right) = 0. \tag{2.62}$$

As with the reinitialization equation, the contact angle Eq. (2.62) is also solved till steady state to obtain the desired geometric relation between the fluid and solid level sets at the triple points

$$\frac{\nabla\zeta}{|\nabla\zeta|} \cdot \frac{\nabla\phi}{|\nabla\phi|} = \cos(\theta). \tag{2.63}$$

[2]The capillary length scale can be estimated as $l_{\mathrm{c}} \propto \sqrt{\frac{\sigma}{(\rho_{\mathrm{l}}-\rho_{\mathrm{g}})g}}$.

Eq. (2.62) implies that the level set function ϕ moves with a velocity

$$\mathbf{u}^{\text{cont}} = \text{sgn}(\zeta)\left(\nabla\zeta - \cos(\theta)\frac{\nabla\phi}{|\nabla\phi|}\right)^{3}. \tag{2.64}$$

Overall ϕ moves with a combination of fluid velocity $\mathbf{u}$, reinitialization velocity $\mathbf{u}^{\text{reinit}}$ and contact angle imposing velocity $\mathbf{u}^{\text{cont}}$. If we denote the overall velocity by $\breve{\breve{\mathbf{u}}}$, then the analysis presented in Sec. 2.5.1 still applies. The terms involving $\breve{\mathbf{u}}$ are replaced by $\breve{\breve{\mathbf{u}}}$. Additionally, it can be seen that Λ_3 and Λ_4 will disrupt the signed distance property of ϕ, as well as change the contact angle at the triple points. In contrast, the approximate Lagrange multiplier approach will respect the contact angle condition since the shifted contours of ϕ retain their original geometric shape.

Due to the length scales of FSI problems consider in this work, we do not consider the contact angle condition.

2.6 Conclusions

In this chapter, we presented the continuous equations of motion for two phase fluid flows. The critically analyzed the reasons for mass loss with the standard level set method. It is primarily due to the use of smooth Heaviside and delta functions. However, level set reinitialization errors can still contribute to mass loss, and existing methods available in literature address these issues but cannot completely eliminate them. To prevent mass loss with the standard level set method, we propose a novel variational approach that introduces a Lagrange multiplier within the standard level set method. This variational analysis is applied to two-phase and three-phase (non-immersed body and immersed body) flows. The exact Lagrange multiplier ensures mass conservation but disrupts the signed distance property of the level set function. Hence, we developed an approximate Lagrange multiplier method that achieves mass conservation as well as signed distance property. We also show that mass conservation of an incompressible fluid in the domain is same as volume conservation.

[3]This additional motion also relaxes the no-slip condition on the fluid-solid interface.

Acknowledgement

This chapter, in full, is a reprint of the material as it appears in “Preventing mass loss in the standard level set method: New insights from variational analyses”, Kaustubh Khedkar, Amirreza Charchi Mamaghani, Pieter Ghysels, Neelesh A. Patankar, Amneet Pal Singh Bhalla, arXiv:2404.03132, 2024. The dissertation author was the primary investigator and author of this paper.

Chapter 3

Discretization and Solution Methodology

This chapter details the discretization of the conservative form of the governing equations presented in Chapter 2. Next, the solution methodology to solve the coupled velocity-pressure system is introduced with developed projection preconditioner which includes the Brinkman penalty term in the pressure Poisson equation (PPE). This crucial detail leads to robust convergence of the velocity-pressure solver which is demonstrated solving a method of manufactured solutions. Further, two phase and stringent three phase FSI problems are simulated to demonstrate the effectiveness of the developed mass conserving level set method. Mass conservation up to machine accuracy is achieved. Finally, differential treatment of the Brinkman penalization factor with different amounts of slip in the normal and tangential directions leads to incorrect FSI dynamics is presented.

3.1 Spatial discretization

The continuous equations of motion governing an incompressible fluid given by Eqs. (2.1) and (2.2) are discretized on a locally refined staggered Cartesian grid. The coarsest grid level covers the domain Ω with $N_x \times N_y \times N_z$ rectangular cells of grid spacing in three spatial directions are Δx, Δy, and Δz, respectively. Unless stated, a uniform grid spacing $\Delta x = \Delta y = \Delta z = h$ is used for all simulations in this work. Without any loss of generality, the lower left corner of the domain is taken as the origin $(0,0,0)$. The cell center of the grid has a

position $\mathbf{x}_{i,j,k} = \left((i+\frac{1}{2})\Delta x, (j+\frac{1}{2})\Delta y, (k+\frac{1}{2})\Delta z\right)$ for $i = 0,\ldots,N_x-1$, $j = 0,\ldots,N_y-1$, and $k = 0,\ldots,N_z-1$. The cell face location that is half a grid cell away from $\mathbf{x}_{i,j,k}$ in the x-direction is at $\mathbf{x}_{i-\frac{1}{2},j,k} = \left(i\Delta x, (j+\frac{1}{2})\Delta y, (k+\frac{1}{2})\Delta z\right)$. Similarly, for the location of a cell face that is half a grid cell away from $\mathbf{x}_{i,j,k}$ in the y-directions is $\mathbf{x}_{i,j-\frac{1}{2},k} = \left((i+\frac{1}{2})\Delta x, j\Delta y, (k+\frac{1}{2})\Delta z\right)$ and in the z-direction it is $\mathbf{x}_{i,j,k-\frac{1}{2}} = \left((i+\frac{1}{2})\Delta x, (j+\frac{1}{2})\Delta y, k\Delta z\right)$. See Fig. 3.1(a). The simulation time at time step n is denoted by t^n. The scalar quantities: level set functions, pressure, and the material properties (density and viscosity) are all approximated at cell centers and are denoted $\phi^n_{i,j,k} \approx \phi\left(\mathbf{x}_{i,j,k}, t^n\right)$, $\zeta^n_{i,j,k} \approx \zeta\left(\mathbf{x}_{i,j,k}, t^n\right)$, $p^n_{i,j,k} \approx p\left(\mathbf{x}_{i,j,k}, t^n\right)$, $\rho^n_{i,j,k} \approx \rho\left(\mathbf{x}_{i,j,k}, t^n\right)$ and $\mu^n_{i,j,k} \approx \mu\left(\mathbf{x}_{i,j,k}, t^n\right)$, respectively. See Fig. 3.1(b). Scalar quantities are interpolated onto the required degrees of freedom as and when required, see Nangia et al. [33] for further details. The vector velocity is approximated on the cell face as $u^n_{i-\frac{1}{2},j,k} \approx u\left(\mathbf{x}_{i-\frac{1}{2},j,k}, t^n\right)$, $v^n_{i,j-\frac{1}{2},k} \approx v\left(\mathbf{x}_{i,j-\frac{1}{2},k}, t^n\right)$, $w^n_{i,j,k-\frac{1}{2}} \approx w\left(\mathbf{x}_{i,j,k-\frac{1}{2}}, t^n\right)$. The body force terms in the momentum equation are also approximated at the cell faces. Second-order finite differences are used for all spatial derivatives. All simulations performed in this paper use uniform grid spacing $\Delta x = \Delta y = \Delta z = h$ unless stated otherwise. For the ease of readability, the discretized version of the differential operators are denoted with a h subscript, e.g., $\nabla \approx \nabla_h$. For further details on the spatial discretization and boundary conditions for uniform grids on a hierarchy of adaptively refined meshes, refer [33, 34, 35, 36].

3.1.1 Density and viscosity specification

We use a smooth Heaviside function varying over n_{cells} grid cells on either side of the air-water interface $\Gamma(t)$ and the fluid-solid interface $\partial\Omega^{\text{F}}(t)$ to smoothly vary the material properties in the transition region. For a given material property $\mathfrak{I}$, say density or viscosity, is set in the computational domain by first calculating the *flowing* phase (i.e., air and water) property as

$$\mathfrak{I}^{\text{flow}}_{i,j,k} = \mathfrak{I}_l + (\mathfrak{I}_g - \mathfrak{I}_l)\widetilde{H}^{\text{flow}}_{i,j,k}, \tag{3.1}$$

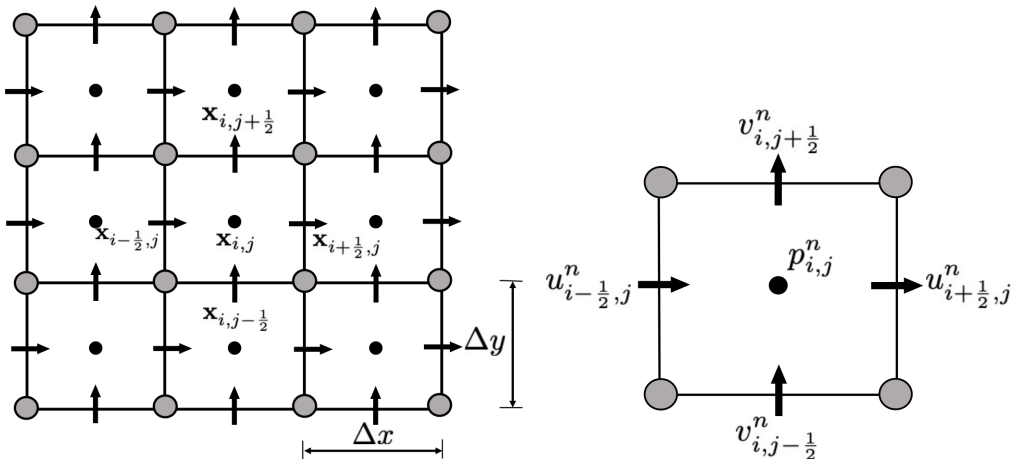

(a) Staggered Cartesian grid (b) Single grid cell

Figure 3.1. Schematic representation of a 2D staggered Cartesian grid. (a) Shows the coordinate system for the staggered grid. (b) shows a single grid cell with velocity components u and v approximated at the cell faces ($\rightarrow$) and scalar level set variable ϕ approximated at the cell center ($\bullet$) at n^{th} time step.

and later correcting $\Im^{\text{flow}}$ to account for the solid body by

$$\Im^{\text{full}}_{i,j,k} = \Im_s + (\Im^{\text{flow}}_{i,j,k} - \Im_s)\widetilde{H}^{\text{body}}_{i,j,k}. \tag{3.2}$$

where, $\Im^{\text{full}}$ is the final scalar material property (density or viscosity) field throughout Ω. The transitions specified by Eqs. (3.1) and (3.2), the standard numerical Heaviside functions are used:

$$\widetilde{H}^{\text{flow}}_{i,j,k} = \begin{cases} 0, & \phi_{i,j,k} < -n_{\text{cells}}\, h, \\ \frac{1}{2}\left(1 + \frac{1}{n_{\text{cells}}\, h}\phi_{i,j,k} + \frac{1}{\pi}\sin\left(\frac{\pi}{n_{\text{cells}}\, h}\phi_{i,j,k}\right)\right), & |\phi_{i,j,k}| \leq n_{\text{cells}}\, h, \\ 1, & \text{otherwise.} \end{cases} \tag{3.3}$$

$$\widetilde{H}^{\text{body}}_{i,j,k} = \begin{cases} 0, & \zeta_{i,j,k} < -n_{\text{cells}}\, h, \\ \frac{1}{2}\left(1 + \frac{1}{n_{\text{cells}}\, h}\zeta_{i,j,k} + \frac{1}{\pi}\sin\left(\frac{\pi}{n_{\text{cells}}\, h}\zeta_{i,j,k}\right)\right), & |\zeta_{i,j,k}| \leq n_{\text{cells}}\, h, \\ 1, & \text{otherwise.} \end{cases} \tag{3.4}$$

In all simulations performed in this work, the number of transition cells $n_{\text{cells}} = 1$ for two

phase cases and $n_{\text{cells}} = 2$ for FSI cases, for both air-water and fluid-solid interfaces are used.

3.2 Temporal discretization

We employ a fixed-point iteration time stepping with n_{cycles} cycles per time step to evolve quantities from time level t^n to time level $t^{n+1} = t^n + \Delta t$. The superscript k is used to denote the cycle number for the fixed-point iteration. At the beginning of every time step, the solutions from the previous time step are used to initialize cycle $k = 0$: $\mathbf{u}^{n+1,0} = \mathbf{u}^n$, $p^{n+\frac{1}{2},0} = p^{n-\frac{1}{2}}$, $\phi^{n+1,0} = \phi^n$, and $\zeta^{n+1,0} = \zeta^n$. Initial conditions are prescribed for the physical quantities at the initial time $n = 0$. A larger number of cycles in the simulation allows a larger, more stable time step size. In this work, we limit $n_{\text{cycles}} = 2$ for 2D cases and $n_{\text{cycles}} = 1$ for 3D cases to reduce computationally expensive linear solves per time step. For more details on the time-stepping algorithm, refer [33].

3.2.1 Level set advection

We evolve the two level set/signed distance functions ϕ and ζ using a standard explicit advection scheme as follows

$$\frac{\phi^{n+1,k+1} - \phi^n}{\Delta t} + Q\left(\mathbf{u}^{n+\frac{1}{2},k}, \phi^{n+\frac{1}{2},k}\right) = 0, \tag{3.5}$$

$$\frac{\zeta^{n+1,k+1} - \zeta^n}{\Delta t} + Q\left(\mathbf{u}^{n+\frac{1}{2},k}, \zeta^{n+\frac{1}{2},k}\right) = 0, \tag{3.6}$$

in which $Q(\cdot,\cdot)$ represents an cubic upwind interpolation (CUI) approximation to the linear advection terms on cell centers. Let ϕ denote the level set function after an advection procedure which is not guaranteed to retain sign distance property after time stepping through the interval $[t^n, t^{n+1}]$. We reinitialize the level set field solving the Hamilton-Jacobi Eq. (2.6) to steady state which reconstructs the signed distance property. The Hamilton-Jacobi equation is discretized using high-order essentially non-oscillatory (ENO) or weighted ENO (WENO) schemes [37].

3.2.2 Multiphase incompressible Navier-Stokes

The multiphase incompressible Navier-Stokes Eqs. (2.1) and (2.2) in conservative form with the Brinkman penalization term $\mathrm{f_c}$ included in the momentum equation are discretized as,

$$\frac{\breve{\rho}^{n+1,k+1}\mathbf{u}^{n+1,k+1}-\rho^{n}\mathbf{u}^{n}}{\Delta t}+\mathrm{C}^{n+1,k}=-\nabla_h\, p^{n+\frac{1}{2},k+1}+\left(\mathrm{L}_\mu\mathbf{u}\right)^{n+\frac{1}{2},k+1}+\wp^{n+1,k+1}\mathbf{g}+\mathrm{f}_c^{n+1,k+1}, \tag{3.7}$$

$$\nabla_h\cdot\mathbf{u}^{n+1,k+1}=0, \tag{3.8}$$

where, $\mathrm{C}^{n+1,k}$ is the discretized version of the convective term $\nabla\cdot(\rho\,\mathbf{u}\otimes\mathbf{u})$ and a consistent mass/momentum transport scheme is used to compute the density approximation $\breve{\rho}^{n+1,k+1}$ which ensures numerical stability of cases that involve high density contrast between various phases. See Nangia et al. [33] and Bhalla et al. [38] for details of the consistent mass/momentum transport scheme employed in this work. The viscous strain rate in Eq. (3.7) is calculated using the Crank-Nicolson approximation: $\left(\mathrm{L}_\mu\mathbf{u}\right)^{n+\frac{1}{2},k+1}=\frac{1}{2}\left[\left(\mathrm{L}_\mu\mathbf{u}\right)^{n+1,k+1}+\left(\mathrm{L}_\mu\mathbf{u}\right)^{n}\right]$, in which $\left(\mathrm{L}_\mu\right)^{n+1}=\nabla_h\cdot\left[\mu^{n+1}\left(\nabla\mathbf{u}+\nabla\mathbf{u}^T\right)^{n+1}\right]$. The newest approximation to the viscosity $\mu^{n+1,k+1}$ is obtained using the two-stage process described by Eqs. (3.1) and (3.2). To avoid the spurious currents generated due to large density variations near the fluid-solid interface [39], the gravitational body force term $\wp\mathbf{g}=\rho^{\mathrm{flow}}\mathbf{g}$ is calculated using the flow density field.

3.2.3 Fluid-structure coupling

The Brinkman penalization term f_c given by Eq. (2.44) is treated implicitly in the discretized version of the momentum Eq. (3.7) and calculated as,

$$\mathrm{f}_c^{n+1,k+1}=\frac{\widetilde{\chi}}{\kappa}\left(\mathbf{u}_b^{n+1,k+1}-\mathbf{u}^{n+1,k+1}\right), \tag{3.9}$$

where, the discretized indicator function $\widetilde{\chi}$ is defined using the body Heaviside function given in Eq. (3.4) as $\widetilde{\chi}=1-\widetilde{H}^{\mathrm{body}}$ with $\widetilde{\chi}=1$ inside the solid body region. The rigid body velocity $\mathbf{u}_b$

is expressed as the sum of translational $\mathbf{U}_r$ and rotational $\mathbf{W}_r$ velocities:

$$\mathbf{u}_b = \mathbf{U}_r + \mathbf{W}_r \times (\mathbf{x} - \mathbf{X}_{\text{com}}), \tag{3.10}$$

in which $\mathbf{X}_{\text{com}}$ is the position of the center of mass of the body. The rigid body velocity can be obtained by integrating Newton's second law of motion.

$$\mathrm{M_b}\frac{\mathbf{U}_{\text{r}}^{n+1,k+1} - \mathbf{U}_{\text{r}}^{n}}{\Delta t} = \mathscr{F}^{n+1,k} + \mathrm{M_b}\mathbf{g}, \tag{3.11}$$

$$\mathrm{I_b}\frac{\mathbf{W}_{\text{r}}^{n+1,k+1} - \mathbf{W}_{\text{r}}^{n}}{\Delta t} = \mathscr{M}^{n+1,k} \tag{3.12}$$

in which $\mathrm{M_b}$ is the mass, $\mathrm{I_b}$ is the moment of inertia, $\mathscr{F}$ is the net hydrodynamic force, $\mathscr{M}$ is the net hydrodynamic torque and $\mathrm{M_b}\mathbf{g}$ is the net gravitational force acting on the body. Eqs. (3.11) and (3.12) are integrated using a forward-Euler scheme to compute $\mathbf{U}_{\text{r}}^{n+1,k+1}$, $\mathbf{W}_{\text{r}}^{n+1,k+1}$ and $\mathbf{X}_{\text{com}}^{n+1,k+1}$.

3.3 Solution methodology: Projection preconditioner for fully coupled Brinkman penalized Stokes system

To solve for $\mathbf{u}^{n+1,k+1}$ and $p^{n+\frac{1}{2},k+1}$ in Eqs. (3.7) and (3.8), the solution to the following block linear system is required.

$$\mathbf{M}\,\mathbf{x} = \mathbf{b},$$
$$\begin{bmatrix} \mathbf{A} & \mathbf{G} \\ -\mathbf{D}\cdot & \mathbf{0} \end{bmatrix} \begin{bmatrix} \mathbf{x_u} \\ \mathbf{x_p} \end{bmatrix} = \begin{bmatrix} \mathbf{b}_u \\ \mathbf{b}_p \end{bmatrix}, \tag{3.13}$$

in which $\mathbf{M}$ denotes the Stokes-BP operator, $\mathbf{A} = \frac{1}{\Delta t}\breve{\rho}^{n+1,k+1} + \frac{1}{\kappa}\widetilde{\chi}^{n+1,k+1} - \frac{1}{2}\mathrm{L}_{\mu}{}^{n+1,k+1}$ denotes the discretization of the temporal, Brinkman penalty and viscous operator, $\mathbf{x_u}$ and $\mathbf{x_p}$ denote the

velocity $\mathbf{u}^{n+1,k+1}$ and pressure $p^{n+1,k+1}$ degrees of freedom, $\mathbf{b}_p = 0$, and $\mathbf{b}_u$ is,

$$\mathbf{b}_u = \left(\frac{1}{\Delta t}\rho^n + \frac{1}{2}\mathrm{L}_\mu{}^n\right)\mathbf{u}^n + \left(\frac{\widetilde{\chi}}{\kappa}\right)^{n+1,k+1}\mathbf{u}_b^{n+1,k+1} - \mathrm{C}^{n+1,k} + \mathrm{f}_c^{n+\frac{1}{2}}. \tag{3.14}$$

For matrix $\mathbf{A}$ in Eq. (3.13), $\breve{\rho}^{n+1,k+1}$ and $\widetilde{\chi}^{n+1,k+1} = 1 - \widetilde{\mathrm{H}}^{\mathrm{body}}$ are diagonal matrices of face-centered densities and body characteristic function corresponding to each velocity degree of freedom, respectively. The operator on the left-hand side of Eq. (3.13) is the time-dependent, incompressible staggered Stokes operator with an additional Brinkman penalty term in the (1,1) block. It is called the Brinkman penalized Stokes operator or *Stokes-BP* operator for short [40].

We use the projection method as a preconditioner to solve the coupled velocity-pressure system given in Eq. (3.13). Several advantages to using the projection method as a preconditioner rather than as a solver are listed in [40, 34, 35]. We also include the Brinkman penalty term $\widetilde{\chi}/\kappa$ in the pressure Poisson equation (PPE) of the projection algorithm. Including the penalty term in the projection algorithm ensures robust convergence of the monolithic fluid solver, particularly when κ values are small. Formally, the projection method can be derived by approximating the inverse of the Schur complement of the saddle-point system Eq. (3.13) [40].

Algorithmically, in the first step of the projection method, an intermediate approximation to $\mathbf{u}$ is computed by solving

$$\mathbf{A}\widehat{\mathbf{x}}_{\mathbf{u}} = \mathbf{b}_u. \tag{3.15}$$

Note that this approximation does not in general satisfy the discrete continuity equation i.e., $-\mathbf{D}\cdot\widehat{\mathbf{x}}_{\mathbf{u}} \neq \mathbf{b}_p$. This condition can be satisfied by introducing an auxiliary scalar field Φ and writing out a fractional timestep

$$\left(\frac{\breve{\rho}}{\Delta t} + \frac{\widetilde{\chi}}{\kappa}\right)(\mathbf{x}_{\mathbf{u}} - \widehat{\mathbf{x}}_{\mathbf{u}}) = -\mathbf{G}\Phi, \tag{3.16}$$

$$-\mathbf{D}\cdot\mathbf{x}_{\mathbf{u}} = \mathbf{b}_p. \tag{3.17}$$

Multiplying Eq. (3.16) by

$$\rho_{\chi}^{-1} = \left(\breve{\rho} + \frac{\widetilde{\chi} \Delta t}{\kappa} \right)^{-1}, \tag{3.18}$$

taking the discrete divergence $\mathbf{D}\cdot$, and substituting in Eq. (3.16) yields the *density and Brinkman penalty*-weighted Poisson problem

$$-(\mathbf{D} \cdot \rho_{\chi}^{-1} \mathbf{G}) \Phi = -\mathrm{L}_{\rho_{\chi}} \Phi = -\frac{1}{\Delta t} \left(\mathbf{b}_p + \mathbf{D} \cdot \widehat{\mathbf{x}}_{\mathbf{u}} \right). \tag{3.19}$$

The updated velocity solution can be computed as

$$\mathbf{x}_{\mathbf{u}} = \widehat{\mathbf{x}}_{\mathbf{u}} - \Delta t \rho_{\chi}^{-1} \mathbf{G} \Phi, \tag{3.20}$$

and that of pressure can be computed as

$$\mathbf{x}_{\mathbf{p}} = \Phi. \tag{3.21}$$

The main difference between our projection method and that of Bergmann and Iolla [41] and Sharaborin et al. [42] is that we include the stiff Brinkman penalty term $\widetilde{\chi}/\kappa$ in the pressure Poisson Eq. (3.19) and the velocity update Eq. (3.20). This is a small but a crucial detail that leads to robust convergence of the monolithic velocity-pressure solver, particularly when κ is small. In Sec. 3.5.1, we careful study the effect of the Brinkman penalty term on the solver convergence rate. For more details on the implementation see [40].

3.4 Software implementation

The Brinkman penalization multiphase fluid flow solver described in this work is implemented within the open-source C++ software called the IBAMR library [43], enabling simulation of immersed boundary-like methods with adaptive mesh refinement. The code is hosted on GitHub at https://github.com/IBAMR/IBAMR. IBAMR relies on SAMRAI [44, 45] for Cartesian

grid management and the AMR framework. Solver support in IBAMR is provided by the PETSc library [46, 47, 48].

All solvers and preconditioners have been implemented are matrix-free to improve computational efficiency, especially on dynamically adaptive grids. In this work, we use locally refined grids but not adaptive grids.

3.5 Numerical examples

In this section, first we consider a test problems to demonstrate the efficacy of the projection preconditioner to solve the coupled velocity-pressure system written in Eq. (3.13). In this problem, a uniform density and viscosity flow is considered in a complex domain. Using the method of manufactured solutions, we compute the spatial order of accuracy of the solution ($\mathbf{u}$ and p), and monitor the number of iterations the outer FGMRES solver takes to converge with decreasing values of κ.

In the test, the outer FGMRES solver is deemed to be converged if a value of 10^{-9} or below is reached for the norm of the relative residual

$$\mathscr{R} = \frac{||\mathbf{r}||}{||\mathbf{b}||} = \frac{||\mathbf{b} - \mathbf{M}\mathbf{x}||}{||\mathbf{b}||}. \tag{3.22}$$

Next, several two-phase and three-phase flow problems are simulated to demonstrate the effectiveness of the approximate Lagrange multiplier technique. We selected the approximate Lagrange multiplier approach (henceforth called the mass loss fix) because of its simplicity, its ability to retain the signed distance property of the level set function.

For three phase flows, two stringent test problems are devised to demonstrate that (i) imposing the mass conservation constraint is essential for the level set method to obtain correct dynamics; and (ii) the immersed formulation of the level set equation produces dynamics that agree very well with non-immersed and conservative methods such as moving unstructured grid-based methods, cut-cell methods, and particle-based methods. Next, we explore the possibility,

if we impose different amounts of slip in the normal and tangential directions by splitting κ. For example, no slip in the normal direction and some slip in the tangential direction.

3.5.1 Uniform density and viscosity flow in a complex domain

Consider a computational domain $\Omega \in [0, 2\pi]^2$ which embeds a circular cylinder of radius $R = 1.5$ at its center (π, π) as shown in Fig. 3.2. A steady state manufactured solution for velocity $\mathbf{u}$ and pressure p

$$u_{\text{exact}}(\mathbf{x}, t \to \infty) = \sin(x)\cos(y), \tag{3.23}$$

$$v_{\text{exact}}(\mathbf{x}, t \to \infty) = -\cos(x)\sin(y), \tag{3.24}$$

$$p_{\text{exact}}(\mathbf{x}, t \to \infty) = \sin(x)\sin(y), \tag{3.25}$$

is used to drive a constant density $\rho(\mathbf{x},t) \equiv 1$ and viscosity $\mu(\mathbf{x},t) \equiv 1$ flow in the domain. Specifically, Eqs. (3.23)-(3.25) are plugged into the momentum Eq. (2.1) to determine the body force f that drives the flow. The manufactured solution is also used to impose boundary conditions on $\partial\Omega$ and inside the fictitious cylinder Ω_b. On the left and right ends of the domain, we impose velocity boundary conditions $u = u_{\text{exact}}$ and $v = v_{\text{exact}}$. On the top and bottom boundaries a combination of normal traction $\mathbf{n} \cdot \tau \cdot \mathbf{n} = g = -p + 2\mu \frac{\partial v}{\partial y} = \sin(x)\sin(y) - 2\mu\cos(x)\cos(y)$ and tangential velocity $u = u_{\text{exact}}$ condition is imposed. Here, $\tau = -p\mathrm{I} + \mu\left(\nabla\mathbf{u} + \nabla\mathbf{u}^{\intercal}\right)$ denotes the hydrodynamic stress tensor. The velocity inside the cylinder is prescribed to be $\mathbf{u}_b = \mathbf{u}_{\text{exact}}$. The initial conditions for velocity and pressure are taken to be zero.

Five grid sizes $N \times N = \{64^2, 128^2, 256^2, 512^2, 1024^2\}$ are used to run the simulations starting from $t = 0$ till steady state is reached. $n_{\text{cells}} = 1$ is used in Eq. (3.4) to smear the fluid-solid interface. A constant time step size of $\Delta t = 1 \times 10^{-3}$ is used in all simulations, which maintains convective CFL number below 0.35 for all grid sizes N. The permeability coefficient κ should be kept small, but not too small to avoid the plateauing of spatial discretization errors [25, 42]. To study the effect of κ on the spatial order of accuracy of $\mathbf{u}$ and p solutions, as well as on the solver

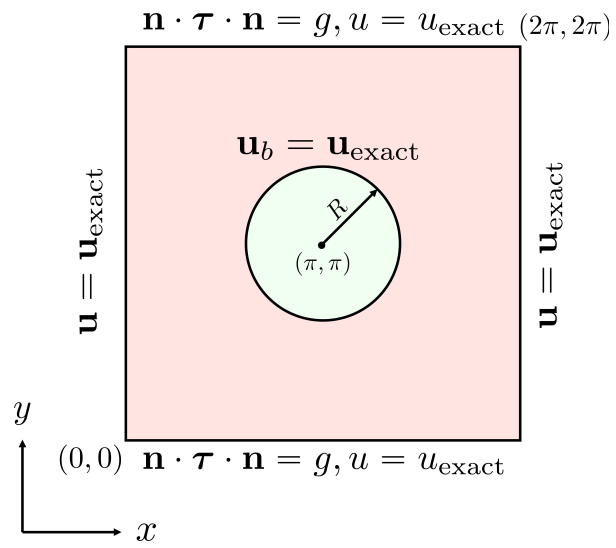

Figure 3.2. Schematic of the computational domain. Normal traction is imposed on yhe top and bottom boundary given by, $g=-p+2\mu\frac{\partial v}{\partial y}=\sin(x)\sin(y)-2\cos(x)\cos(y)$. For the top boundary $\mathbf{n}=(0,1)$ and for the bottom boundary $\mathbf{n}=(0,-1)$.

convergence rate, we consider three different values for $\kappa=\{\Delta t/\rho, \Delta t/100\rho, \Delta t/10000\rho\}$ in the numerical experiments. Note that $\Delta t/\rho$ is the maximum value which κ can or should take as per the inertial scale $\chi/\kappa\sim\rho/\Delta t$. Another possibility is to select κ based on the viscous scale $\chi/\kappa\sim\mu/h^2$, in which h is the uniform cell size. Here, our strategy is to start with the maximum value of κ based on the inertial scale, and then reduce it progressively till no further improvement in the solution is observed.

We first present the spatial order of accuracy of the Brinkman penalized $\mathbf{u}$ and p solutions. The error between steady state numerical and analytical solutions is denoted $\mathscr{E}$. As can be observed in Fig. 3.3, second-order pointwise (L^∞-norm) convergence rate is obtained for both velocity and pressure errors when $\kappa=\Delta t/\rho$, $\Delta t/100\rho$. For a very small value of $\kappa=\Delta t/10000\rho=1\times10^{-7}$, the error in velocity and pressure saturates after a certain grid size ($N=128$ in Fig. 3.3(c)). To understand this trend, we compare the magnitudes of the Brinkman penalty coefficient χ/κ and the discrete inertial and viscous scales, by plotting the latter two as a function of grid size N in Fig. 3.4. The discrete inertial scale $\rho/\Delta t$ remains constant (because of the constant time step size Δt), whereas the discrete viscous scale varies

quadratically (linearly on a log scale) with N. The magnitude of the inertial scale is larger than the viscous scale for the first two grids, and vice versa for the remaining grids. For the largest value of $\kappa = \Delta t/\rho$, although the penalty coefficient $\chi/\kappa = \rho/\Delta t$ is not always larger than the viscous scale, second-order convergence is still observed. When $\kappa = \Delta t/100\rho$, the Brinkman penalty coefficient is significantly larger than the inertial scale and comparable with the viscous scale. Second-order pointwise convergence is obtained for this κ value as well. However, when κ is decreased further to $\Delta t/10000\rho$, the Brinkman penalty becomes four orders larger than the inertial scale and two orders larger than the viscous scale. This large penalty value causes the errors to saturate. Note that in this problem we imposed spatially-varying traction boundary condition on the top and bottom boundaries of $\partial\Omega$, and obtained second-order convergence rates for velocity and pressure solutions. This is not possible to achieve if pressure and velocity are solved in a split manner using projection method as a solver.

Next, we study the impact of κ on the convergence rate of the preconditioned FGMRES solver. For this problem, the first time step poses the most difficultly for the (iterative) Krylov solver as the initial zero guess for velocity and pressure is far-off from the true solution at $t = \Delta t$. Therefore, it suffices to monitor the solver performance at the first time step only to evaluate the efficacy of the preconditioner. We run this test case with and without the Brinkman penalty term $\widetilde{\chi}/\kappa$ in the projection preconditioner. In practice, we re-define ρ_χ^{-1} with the help of a boolean parameter θ

$$\rho_\chi^{-1} = \left(\breve{\rho} + \theta\frac{\widetilde{\chi}\Delta t}{\kappa}\right)^{-1}, \tag{3.26}$$

so that by setting $\theta = 1$ in ρ_χ^{-1} we obtain the new projection method and by setting $\theta = 0$ we revert to the projection methods of Bergmann and Iolla [41] and Sharaborin et al. [42].

Fig. 3.5 compares the convergence rate of the projection method preconditioned FGMRES solver for different κ values. The grid size is taken to be $N = 256$. When the Brinkman penalty is excluded from the projection step (i.e., $\theta = 0$ in Eq. (3.26)), we note from Fig. 3.5(a) that the number of iterations required to convergence to a relative residual of $\mathscr{R} = 10^{-9}$ increases

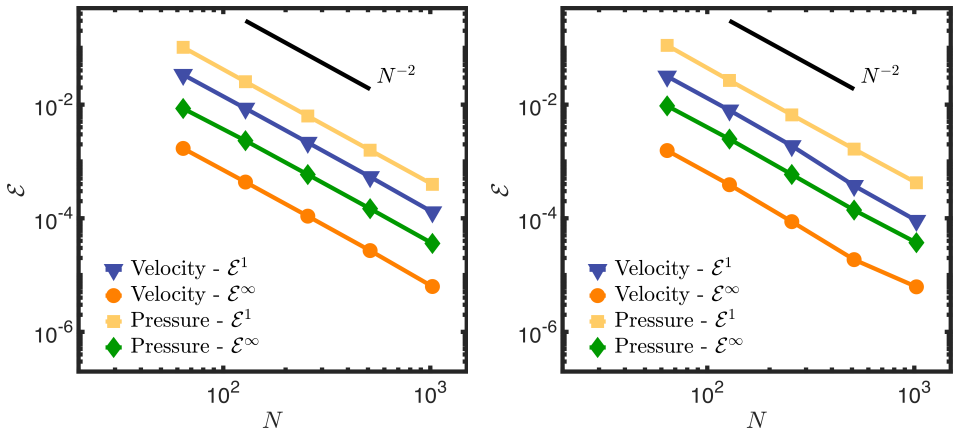

(a) $\kappa = \Delta t/\rho$ (b) $\kappa = \Delta t/100\rho$

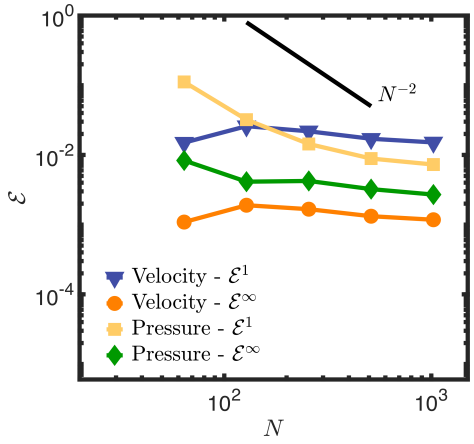

(c) $\kappa = \Delta t/10000\rho$

Figure 3.3. Spatial order of convergence of the volume penalized Navier-Stokes system using manufactured solutions and different values of κ.

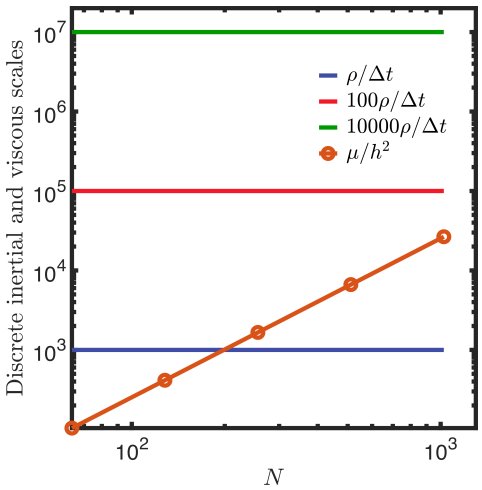

Figure 3.4. Discrete inertial and viscous scales as a function of grid size N.

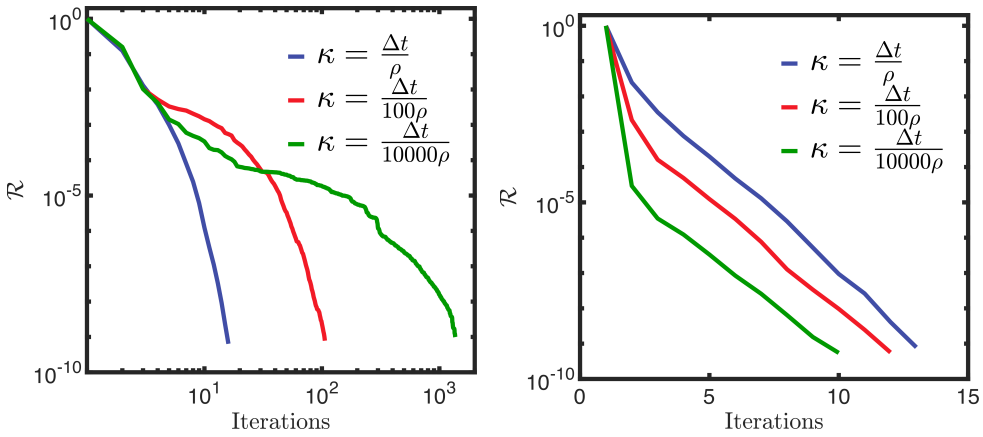

(a) Relative residual when $\theta = 0$ (b) Relative residual when $\theta = 1$

Figure 3.5. Convergence rate of the preconditioned FGMRES solver during the first time step of the simulation (a) without and (b) with the Brinkman penalty term in the projection preconditioner. The grid size is $N = 256$.

approximately by a factor of 10 with decreasing values of κ. However, with the proposed projection method (i.e., $\theta = 1$ in Eq. (3.26)) the convergence of the FGMRES solver remains robust. This can be observed in Fig. 3.5(b) where the solver converges with approximately 10 iterations for all three κ values. This clearly demonstrates the importance of including the Brinkman term in the projection method. In fact, with decreasing κ (or increasing penalty) values, the convergence rate of the solver actually improves. This can be attributed to $\mathbf{A}$ matrix of Eq. (3.15) which becomes diagonally dominant when the penalty coefficient is larger than the viscous scale. This in turn makes the velocity subdomain problem "easier" to solve.

To present a more complete picture of the solver performance as the simulation progresses, Fig. 3.6 presents the number of iterations to converge for the first 200 time steps. The grid size is taken to be $N = 256$ and the same three κ values are considered. It is clearly seen that with decreasing κ values or conversely with increasing penalty values, the average number of iterations to converge decreases.

Thus far in this section, we demonstrated the efficacy of the new projection preconditioner on a single grid $N = 256$. To demonstrate that the proposed preconditioner is scalable, Fig. 3.7 reports the convergence rate of the preconditioned FGMRES solver on three grids:

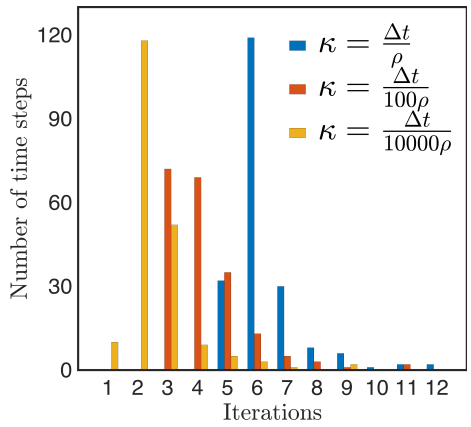

Figure 3.6. Performance of the preconditioned ($\theta = 1$) FGMRES solver during the first 200 time steps of the simulations. The average number of iterations required to converge for $\kappa = \Delta t/\rho$, $\kappa = \Delta t/100\rho$, and $\kappa = \Delta t/10000\rho$ are 6, 4 and 2, respectively. The grid size is $N = 256$.

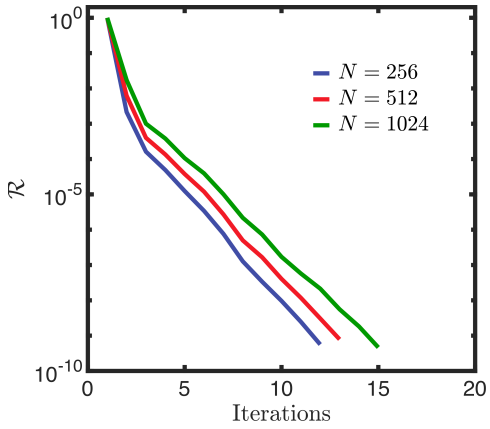

Figure 3.7. Convergence rate of the preconditioned ($\theta = 1$) FGMRES solver during the first time step of the simulation on three grids: $N = 256, 512, 1024$. The permeability parameter is taken to be $\kappa = \Delta t/100\rho$.

$N = 256, 512, 1024$. The permeability parameter is taken to be $\kappa = \Delta t/100\rho$, which is larger than both inertial and viscous scales as discussed earlier. In Fig. 3.7 it can be observed that the solver's convergence rate remains approximately the same, even when the degrees of freedom, $\mathbf{x_u}$ and $\mathbf{x_p}$, increase substantially with increasing grid size.

Based on the results presented in this section we conclude that: (**1**) the proposed projection method is a scalable preconditioner for the volume penalized incompressible Navier-Stokes system; (**2**) it is possible to achieve pointwise second-order accuracy in velocity and pressure solutions with nontrivial traction boundary conditions without sacrificing computational efficiency; and (**3**) a reasonable starting value for the permeability parameter is $\kappa = \Delta t/\rho$.

3.5.2 Two-phase flows

Vortex test

Vortex in a box is a standard two-phase flow problem used in the literature [49] to test interface tracking and capturing methods' ability to resolve thin filaments. In this problem, a circular interface is stretched over time due to an imposed velocity field of the form

$$u = -2\sin^2(\pi x)\sin(\pi y)\cos(\pi y),$$
$$v = 2\sin(\pi x)\cos(\pi x)\sin^2(\pi y).$$

The computational domain consists of a unit square with extents $\Omega \in [0,1]^2$. A circular interface with a radius of 0.15 has its initial centroid at (0.5, 0.75). The origin is taken to be the lower left corner. The circular interface gets stretched into a very long and thin filament due to the imposed velocity field, which over time wraps around itself. Fig. 3.8 compares the interfacial dynamics with and without the mass loss fix at time instances t = 4 , 6 , and 8. The domain is discretized into $N \times N = 128 \times 128$ grid cells and a uniform time-step size of $\Delta t = h/10$ is employed, where $\Delta x = \Delta y = h$. As can be observed in the figure, a significant amount of mass is lost by the standard level set method compared to the mass loss fix method.

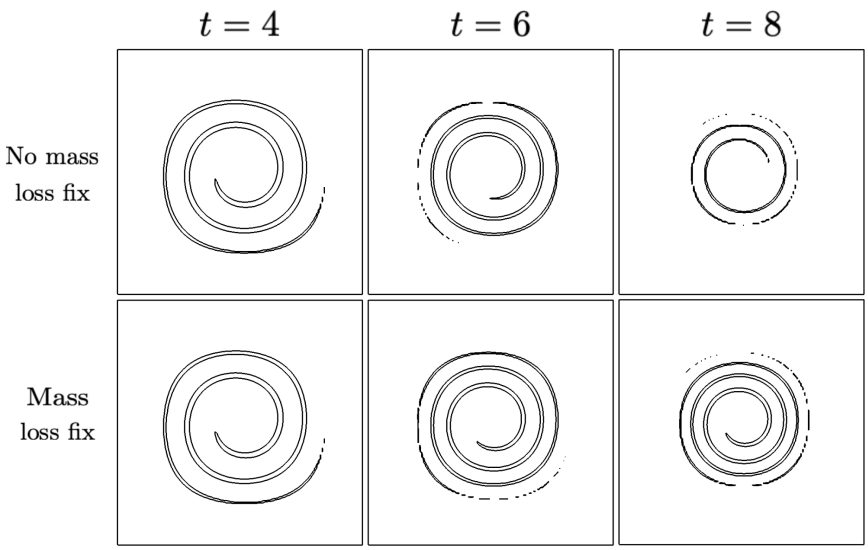

Figure 3.8. Time evolution of the interface for the vortex in a box problem using a 128×128 uniform mesh.

Figs. 3.9(a), 3.9(c) and 3.9(e) show the normalized value of the uniform correction ε/h as a function of time. The normalized correction values are in the order of 10^{-2}, which means that the contours of the level set field $\widehat{\phi}$ are shifted at a sub-grid level. To quantify the amount of fluid lost/gained over time, we plot the relative change in the volume of fluid enclosed by the interface, $\Delta V/V_0 = V(t)/V_0 - 1$. Figs. 3.9(b), 3.9(d) and 3.9(f) show the relative volume change for grid sizes 32×32, 64×64, and 128×128. For all grids, the relative change in volume is close to machine precision. In order to solve $f(\varepsilon) = 0$ to machine precision, it usually takes 2-3 Newton iterations.

Next, we will examine a somewhat different but closely related problem known as the reverse vortex test problem [49, 50]. After rotating counterclockwise for $t = 4$, the initially circular interface stretches into a thin filament before rotating clockwise to return to its original shape at $t = T = 8$. In this case, velocity is a function of time, and is written as

$$u = -2\sin^2(\pi x)\sin(\pi y)\cos(\pi y)\cos\left(\frac{\pi t}{T}\right), \tag{3.27a}$$

$$v = 2\sin(\pi x)\cos(\pi x)\sin^2(\pi y)\cos\left(\frac{\pi t}{T}\right). \tag{3.27b}$$

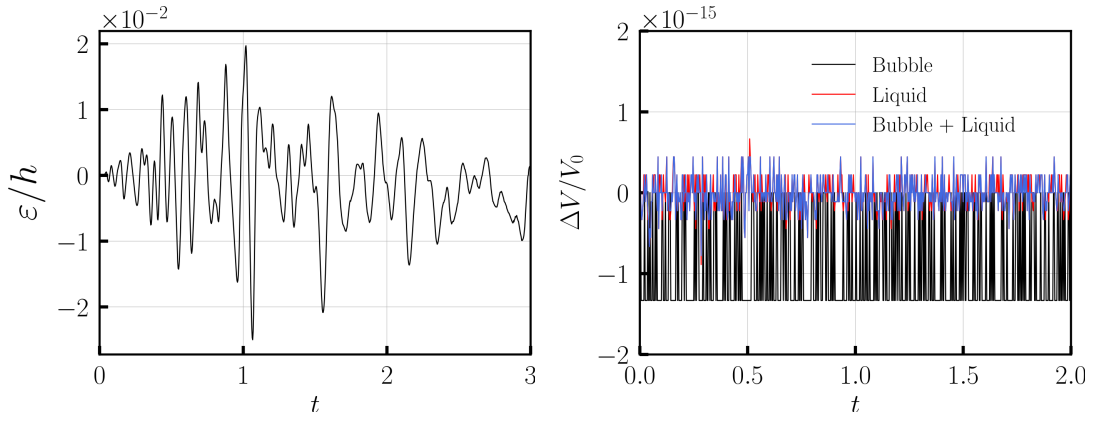

(a) Normalized correction for 32×32 grid (b) Relative error in volume for 32×32 grid

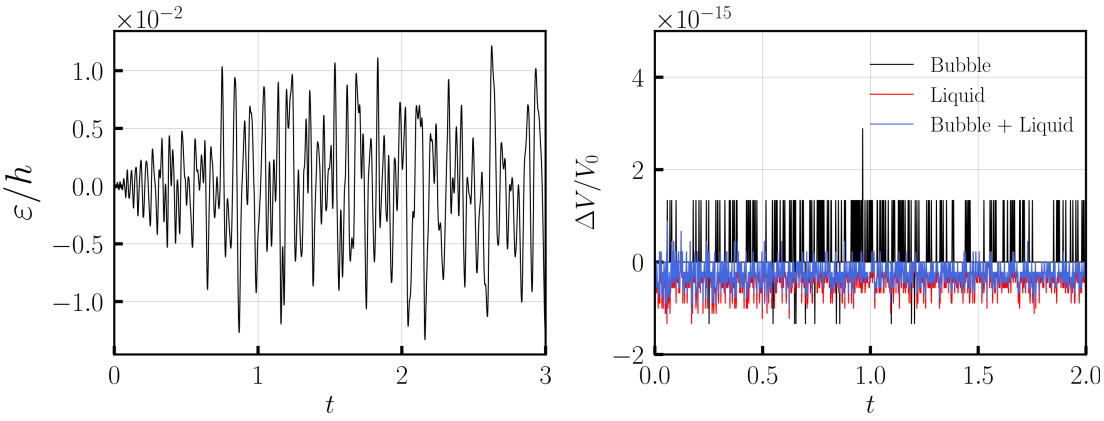

(c) Normalized correction for 64×64 grid (d) Relative error in volume for 64×64 grid

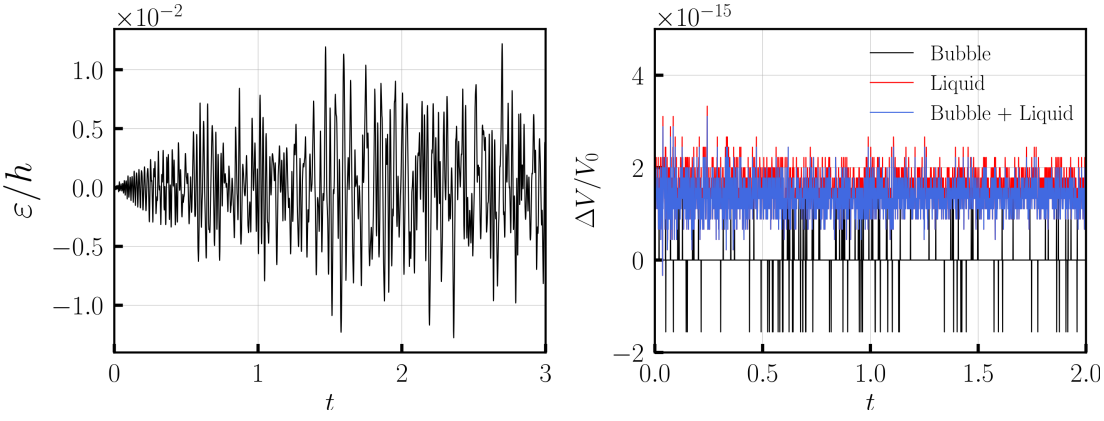

(e) Normalized correction for 128×128 grid (f) Relative error in volume for 128×128 grid

Figure 3.9. Vortex in a box problem simulated using different grid sizes. The normalized correction (ε/h) as a function of time is shown in (a), (c) and (e). The relative error in volume ($\Delta V/V_0$) as a function of time is shown in (b), (d) and (f).

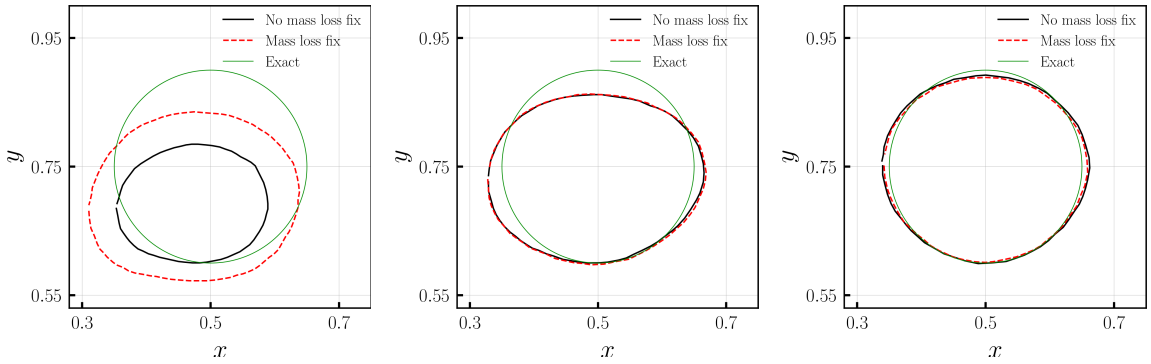

(a) 32×32 (b) 64×64 (c) 128×128

Figure 3.10. Results for the reverse vortex test problem. Comparison of the final interface shape with the exact solution using standard level set method and level set method with mass loss fix. Three grid sizes are considered: (a) 32×32, (b) 64×64, and (c) 128×128.

Fig. 3.10 compares the final shape of the interface at $t = T$ for different grid sizes, with finer grids performing better. For the coarse mesh resolution (32×32) considered here, the mass loss fix method yields a "full" circle than the standard approach, which shrinks the interface. The latter occurs because of the substantial volume loss with the standard level set method. In order to compare the two methods quantitatively, we estimate the geometric and volume errors as E_{g} and E_{v}, respectively, at the end of the process:

$$E_{\mathrm{g}} = \frac{\int_{\Omega} |H(\phi, t = T) - H(\phi, t = 0)| \, \mathrm{dV}}{\int_{\Omega} H(\phi, t = 0) \, \mathrm{dV}}, \tag{3.28}$$

$$E_{\mathrm{v}} = \frac{|\int_{\Omega} H(\phi, t = T) \, \mathrm{dV} - \int_{\Omega} H(\phi, t = 0) \, \mathrm{dV}|}{\int_{\Omega} H(\phi, t = 0) \, \mathrm{dV}}. \tag{3.29}$$

Table 3.1 compares relative geometric and volume errors at different grids with and without mass loss fix. The circular interface recovers well for grids 64×64 and 128×128, and geometric errors are comparable between the two approaches. Significant differences are observed in relative volumes, however. The mass loss fix method conserves the volume enclosed by the interface to machine precision.

Finally, we simulate the reverse vortex case using the standard level set method (without mass loss fix) for a reduced time period of $T = 4$. The grid size is 256×256. The interface

Table 3.1. Comparison of relative geometric E_{g} and volume E_v errors at the final time instant using standard level set method (no mass loss fix) and level set method with mass loss fix for the reverse vortex problem. Three grid sizes are considered.

Errors	Method	32×32	64×64	128×128	256×256
E_{g}	no fix	5.6274×10^{-1}	1.9812×10^{-1}	6.5218×10^{-2}	9.1636×10^{-3}
	fix	4.7861×10^{-1}	2.0243×10^{-1}	6.3858×10^{-2}	9.6954×10^{-3}
E_{v}	no fix	4.8166×10^{-1}	2.3117×10^{-2}	2.9920×10^{-2}	1.0634×10^{-3}
	fix	$< \times 10^{-16}$	2×10^{-16}	$< \times 10^{-16}$	2×10^{-16}

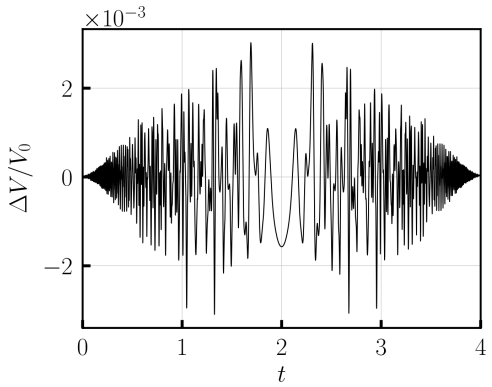

Figure 3.11. Error in relative volume for the reverse vortex test with $T = 4$ s for the no mass loss fix.

rotates counterclockwise until $t = 2$, at which point it reverses motion. By reducing the time period, the interface does not thin out excessively and break. During the second half of the period, the interface follows a "reversible" path. Fig. 3.11 illustrates the relative volume change of the fluid enclosed by the interface over time. As can be seen from the figure, the level set method exhibits a very low volume error at $t = T = 4$ (specifically $\Delta V/V_0 = 2.04 \times 10^{-5}$). Based on this, we can confirm Eq. (2.10). It is generally not possible to find time intervals Δt where mass loss errors are low with the standard level set method. Many practical problems have a two-phase interface that breaks, making it impossible to follow a reversible path to achieve a net normal displacement.

Bubble rise

In this section, we simulate the rise of a two-dimensional bubble in water due to buoyancy, which tests the coupling between the level set method and the flow solver. The density and viscosity of air (bubble) are ρ_a = 1 kg/m^3 and μ_a = 0.1 Pa·s. Water density and viscosity are ρ_w = 1000 kg/m^3 and μ_w = 10 Pa·s, respectively. At t = 0 s, the bubble's center is located at (0.5, 0.5) m and its diameter is D = 0.5 m; see Fig. 3.12. There are two important non-dimensional numbers for this problem, the Reynolds number and the Eötvös number, which are defined as

$$\mathrm{Re} = \frac{\rho_w g^{1/2} D^{3/2}}{\mu_w} \quad \text{and} \quad \mathrm{Eo} = \frac{\rho_w g D^2}{\sigma} \tag{3.30}$$

Here, g is the acceleration due to gravity and σ is the surface tension coefficient. The values for non-dimensional numbers are Re = 35 and Eo = 125. We use the continuum surface tension model of Brackbill et al. [51] also used in [33] to define the volumetric surface tension force in terms of the level set field.

$$\mathbf{f}_s = \sigma \kappa_c \nabla \widetilde{C} \tag{3.31}$$

in which σ is the uniform surface tension coefficient, κ_c is the curvature of the interface computed from the signed distance function as

$$\kappa_c = -\nabla \cdot \mathbf{n} = -\nabla \cdot \frac{\nabla \phi}{||\nabla \phi||} \tag{3.32}$$

$\mathbf{n}$ is the unit normal to the surface, and $\widetilde{C}$ is a mollified version of the Heaviside function $\widetilde{H}$ that ensures the surface tension force is applied only near the zero level set [52]. The computational domain is discretized with uniform grid size of 256×512. A uniform time-step size of $\Delta t = 10^{-3}$ s is used.

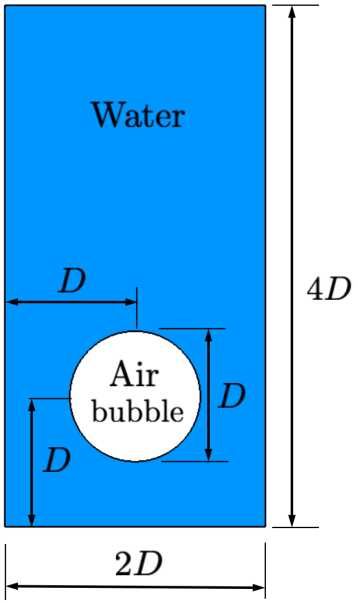

Figure 3.12. Schematic of the bubble rise test case.

Fig. 3.13, compares the evolution of the bubble interface shape at time instances T = 1, 2, 3, 4, and 5 for the without and with mass loss fix method. The time is non-dimensionalized as $T = D/U_g$, where, $U_g = \sqrt{gD}$ is the gravitational velocity. At time T = 1, the bubble starts rising and forms a rounded lower end. This rounded lower end grows as the bubble moves upwards. Further due to large deformation of the bubble, it starts to break off from the lower ends into small bubbles. Clearly, these small bubbles are seen to vanish over time in the no mass loss fix

case, and lose mass significantly. However, with the mass loss fix case, the small bubbles break off from the large bubble and do not vanish as the simulation progresses in time.

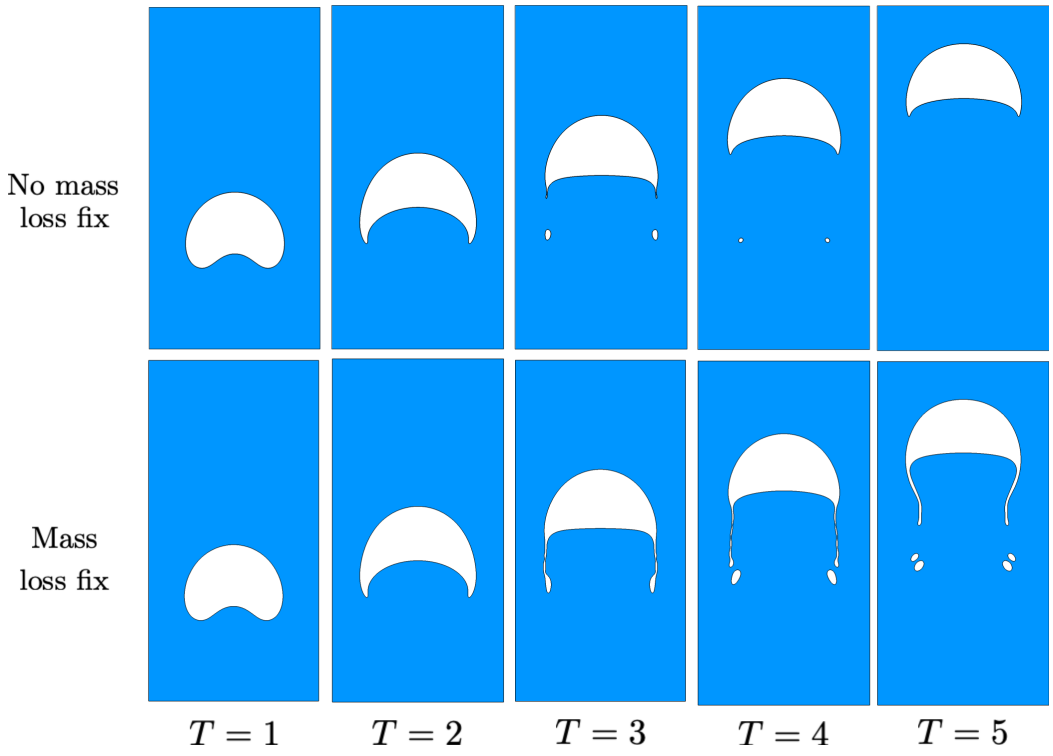

Figure 3.13. Comparison of evolution of bubble interface shape at different time instances for the no mass loss fix and with mass loss fix cases. The time instances are at T = 1, 2, 3, 4, and 5.

Next, in Fig. 3.14, we compare the present mass loss fix method contour of the bubble at $T = 3$ with the benchmark solution of Aland and Voigt [8]. Furthermore, the temporal evolution of the vertical coordinate of the center of mass of the bubble, calculated using Eq. (3.33), is shown in Fig. 3.15. The comparison is done between the no mass loss fix, the mass loss fix and Hysing et al. [53]. The results are in good agreement and prove that the dynamics are not affected with the implementation of our mass preserving method.

$$\mathrm{y_{com}} = \frac{\int_\Omega y H(-\phi)\mathrm{d}\Omega}{\int_\Omega H(-\phi)\mathrm{d}\Omega} \tag{3.33}$$

The Figs. 3.16(a) shows the normalized value of the shift ε in the level set applied after each time-step to adjust for the mass that is lost after the reinitialization step. The normalized

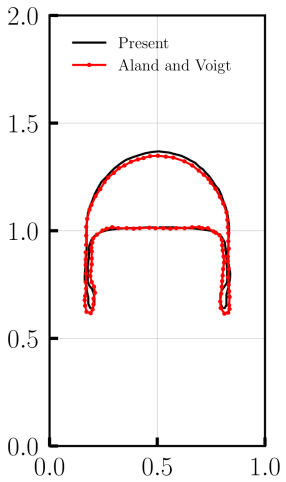

Figure 3.14. Comparison of the bubble shape for present mass loss fix method, and benchmark solution of Aland and Voigt et al. [8] at $T = 3$.

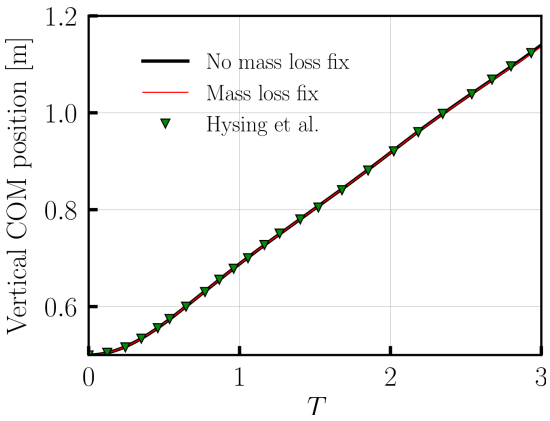

Figure 3.15. Temporal evolution of the Vertical center of mass position of the bubble.

values are of the order of 10^{-3}. Also, Fig. 3.16(b) shows the relative error in the bubble volume over time are seen to be of the order of 10^{-15}. This clearly demonstrates that for a very small shift in the level-set contours, our mass preserving method can conserve mass upto machine precision without losing on momentum conservation.

3.5.3 Three-phase flows: FSI

We test the performance of the approximate Lagrange multiplier method on problems involving rigid bodies interacting with two-fluid interfaces in this section. The FSI problems discussed here are relevant to ocean engineering. To accurately account for buoyancy forces

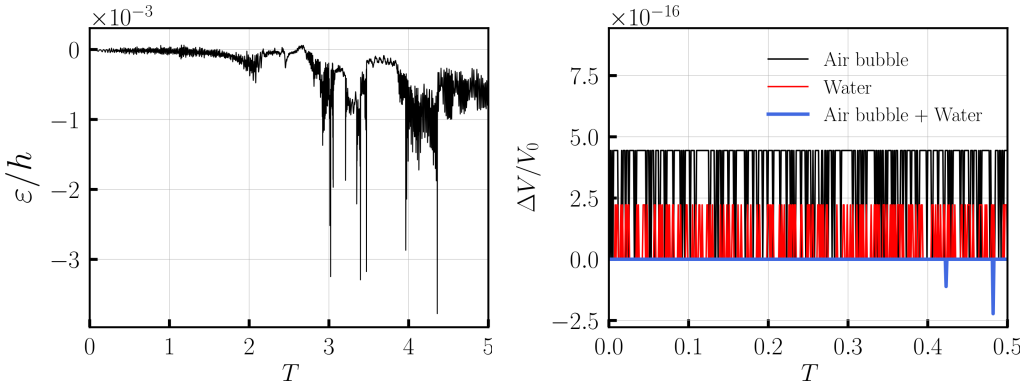

(a) Normalized shift in the level set (b) Relative error in volume

Figure 3.16. (a) Temporal evolution of the normalized shift in the level set contours and (b) relative error in volume of the bubble.

in these FSI problems, we conserve the heavier fluid volume. The volume of the union of complementary phases (light fluid and solid) is also conserved.

Floating rectangular block problem

Ocean engineering problems in the literature typically consider wider domains when studying fluid-structure interactions [31, 39, 54, 55]. There is little change in the mean water level when a solid body interacts with the air-water interface in these large domains. Thus, spurious mass/volume losses do not significantly affect FSI dynamics. To exaggerate the effects of mass loss errors, we consider a relatively large rectangular block interacting with water inside a relatively small tank. The solid's density is half that of water and it is released from a small distance above the air-water interface. Fig. 3.17 shows the problem setup schematic. Since the domain is narrow, the water level rises appreciably at equilibrium. The rectangular block will be half submerged at equilibrium if the domain is very wide. With narrow domains, this is not the case. Using conservation of mass and Archimedes' principles, the exact equilibrium position of the rectangular block and air-water interface can be found analytically. Appendix Sec. A.1 provides the derivation.

Consider a 2D domain as shown in Fig. 3.17 with a rectangular block of height H =

0.075 m and width $W = 2H$. This rectangular block is located with its center at (1.4H, 1.8H) in the 2D domain of size $2.8H \times 2.8H$. The origin O of the domain is at the lower left corner. The initial water level is at $1.2H$ where, $H = 0.075$ m. The density of water is $\rho_w = 1000$ kg/m^3 and viscosity is $\mu_w = 10^{-3}$ Pa·s and for air these values are $\rho_a = 1$ m^3 and viscosity is $\mu_a = 1.8 \times 10^{-5}$ Pa·s. The rectangular block has a density of $\rho_s = 500$ kg/m^3 and fictitious viscosity of μ_s equal to that of water. Only the vertical degree of freedom of the rectangular block is free while others are locked. We simulate this problem on different softwares. We compare the results obtained from our mass preserving level-set method with softwares that use the inherently mass preserving volume of fluid (VOF) and smooth particle hydrodynamics (SPH) method. The problem is simulated on four different codes: 1) our FD/BP solver that uses the level-set method with mass preserving technique [43], 2) CONVERGE CFD software which uses the VOF with the cut-cell method [56], 3) the ANSYS Fluent software which uses the VOF with dynamic meshing [57], and 4) the DualSPHysics software which is a fully Lagrangian mesh-free technique [58]. Our fictitious domain approach differs from the other numerical techniques in that we allow the air-water interface to pass through the immersed solid, whereas the others do not. The FD/BP approach in conjunction with the approximate Lagrange multiplier approach is much easier to implement than the Cartesian cut-cells and/or moving meshes.

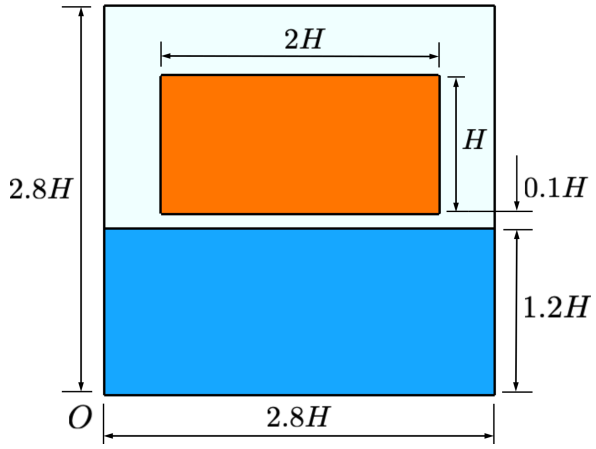

Figure 3.17. Schematic of the floating rectangular block problem.

To obtain respective converged FSI solutions, a grid convergence study is conducted with

Table 3.2. Grid convergence test parameters $\Delta\mathbf{x}$ in m, and Δt in s for the half submerged rectangle case.

Solver	Parameters	Grid		
		Coarse	Medium	Fine
Present	h	7.5×10^{-4}	5×10^{-4}	3.75×10^{-4}
	$\Delta t_{\max}$	7.5×10^{-5}	5×10^{-5}	3.75×10^{-5}
CONVERGE CFD	h	10^{-3}	7.5×10^{-4}	5×10^{-4}
	$\Delta t_{\max}$	10^{-4}	10^{-5}	10^{-4}
ANSYS Fluent	h	10^{-3}	7.5×10^{-4}	5×10^{-4}
	$\Delta t_{\max}$	10^{-3}	10^{-2}	7.5×10^{-3}
DualSPHysics	h	2×10^{-3}	10^{-3}	5×10^{-4}
	$\Delta t_{\max}$	10^{-2}	10^{-2}	10^{-2}

each of the four numerical codes. In all four codes, adaptive time-stepping is used. Table 3.2 lists the grid cell size h and the maximum time step size $\Delta t_{\max}$ which is also the maximum allowable time-step during the simulation. The time-step size of the simulation is adjusted as the rectangular block hits the water surface to keep the simulations stable. Fig. 3.18 shows the block's center of mass position over time as a function of grid size. Fig. 3.19 shows a comparison of the converged results from the four solvers. The FD/BP method produces very similar heaving dynamics as the other three solvers. An overly damped motion is predicted by DualSPHysics at a later time, which is different from the predictions from the other three methods. Table 3.3 compares the equilibrium vertical center of mass position of the block with the analytical solution. As can be observed, all codes predict the block's equilibrium position correctly.

Table 3.3. Vertical center of mass position of the rectangle at equilibrium for various grid sizes for present solver, CONVERGE CFD, ANSYS Fluent, and DualSPHysics software compared with analytically calculated value.

Grid	Present	CONVERGE CFD	ANSYS Fluent	DualSPHysics	Analytical
Coarse	0.1166	0.1168	0.1169	0.1208	0.1167
Medium	0.1167	0.1167	0.1168	0.1199	
Fine	0.1167	0.1168	0.1169	0.1184	

The Fig. 3.20 presents the rectangle block for the present solver which shows the fictituous air-water interface passing through the body, which means fluid is allowed to enter the solid

body region. The air-water interface starts entering the solid body region around $t = 4.5$ s and is seen to completely penetrate at much later time of $t = 25$ s. Fig. 3.20 contrasts sharply with Fig. 3.41, which prevents the interface from entering the body. $\kappa \approx \Delta t/\rho_s$, and $\mathscr{K}_n = \mathscr{K}_t = 1$ are used to obtain physically correct dynamics. These penalty parameters are also proposed in [40, 38, 59, 60].

Fig. 3.21 shows the fluid-structure interaction and the mesh around the bottom right corner of the rectangle block at simulation time $t = 0.06$ s and $t = 0.15$ s for various softwares. All the present solver simulations done in the grid convergence test are performed with the mass loss fix method. In contrast to other predictions, DualSPHysics predicts an "inverted" wave near the block at $t = 0.06$ s. This potentially unphysical behavior might be attributed to artificial gaps arising from SPH kernel interactions between the water and solid material points of the rectangular block and tank walls (as illustrated in Fig. 3.21). The DualSPHysics simulation was configured based on accompanying online examples and guidelines provided in the software's user guide for ocean engineering problems.

Next, we examine the importance of conserving water mass/volume for this problem using the FD/BP method. Fig. 3.22 shows how the block heaves with and without the mass los fix (using medium grid resolution). Without the mass loss fix method, the rectangular block settles in a different location. Fig. 3.23 shows the equilibrium position of the rectangular block achieved after a very long period of time. Under static equilibrium conditions, the submerged portion of the rectangular block without the mass loss fix method measures $Y = 0.03757$ m, while with the mass loss fix method, it is $Y = 0.03753$ m. These values closely align with the analytically calculated value of 0.03749 m (see Section A.1). The original level set method without the mass loss fix must conserve (under grid refinement) the sum total of water volume outside and inside the solid body. In this case, see Fig. 3.23(a) there is significant amount of mass of water that is lost which can be seen by the decrease in water level. This loss occurs due to insufficient grid refinement to accurately capture splashed water.

Without a volume conservation constraint, there is no distinction between real and ficti-

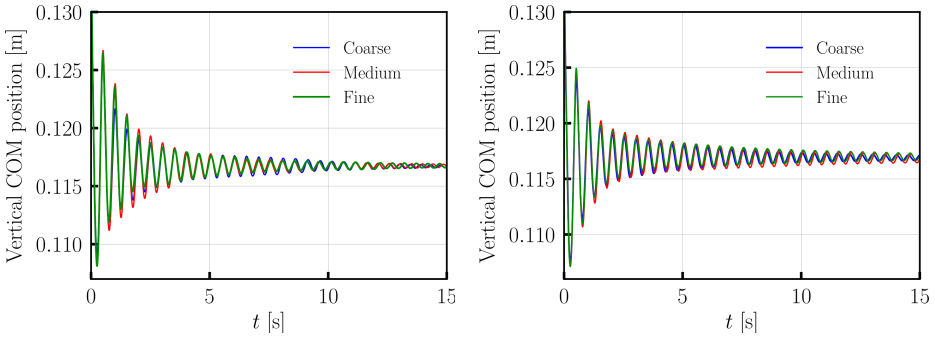

(a) Grid convergence test for present solver (b) Grid convergence test for CONVERGE CFD software

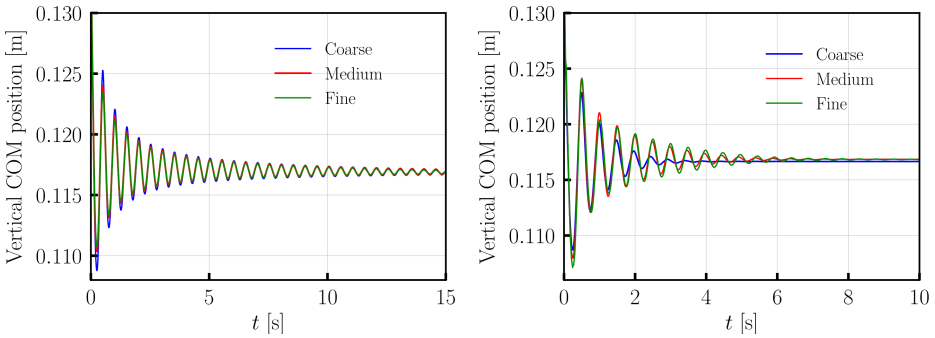

(c) Grid convergence test for ANSYS Fluent software (d) Grid convergence test for DualSPHysics software

Figure 3.18. Vertical center of mass position of the rectangle vs time for various grid sizes for (a) present solver, (b) CONVERGE CFD, (c) ANSYS Fluent, and (d) DualSPHysics software.

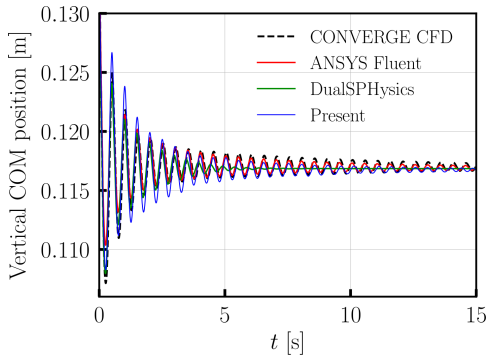

Figure 3.19. Comparison of dynamics of the rectangle block obtained from various softwares.

tious fluids. By imposing a volume conservation constraint on the actual fluid, the approximate Lagrange multiplier method corrects the level set field at each time step. This can be observed from Fig. 3.24(a), which shows the normalized value of the correction as a function of time. Normalized correction values are in the order of 10^{-3}, which is considerably smaller than the

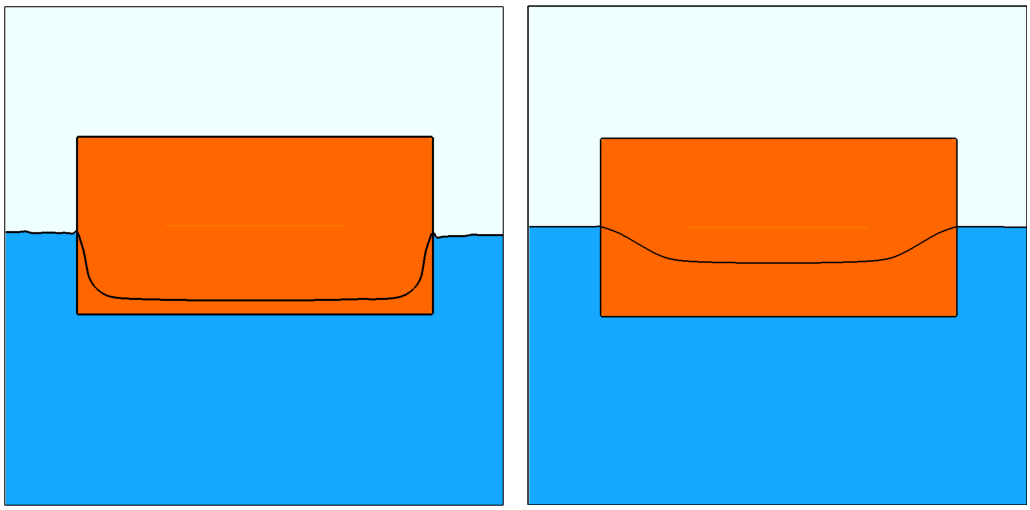

(a) $t = 4.5$ s (b) $t = 25$ s

Figure 3.20. FSI of the rectangle block for the present solver showing air-water interface passing through the solid body at (a) $t = 4.5$ s, and (b) $t = 25$ s.

cell size $h = 0.0005$ m. FSI dynamics are not affected by this subgrid level shift.

Fig. 3.24(b) shows the relative volume change for air, water and solid phases over time when the mass loss fix method is applied. The target fluid volume, in this case water, is conserved to machine precision. In addition, the sum of volumes of the remaining phases, i.e., air and block, is also conserved to machine accuracy. From the results of the floating rectangular block we conclude that our mass preserving level set method conserves mass with correct dynamics even for problems with rigid bodies in the domain.

Half submerged cylinder

In this section, we simulate a similar case as done in Sec. 3.5.3 but the object dropped in water here is a cylinder of radius $R = 0.06$ m. The reason for selection of the cylinder as an object is that it has a non-linear relationship between the submerged volume and the rise in the water level unlike the rectangular block considered in the previous section. The rise in water level for this problem is solved analytically in the appendix Sec. A.2. This example tests the accuracy of the approximate Lagrange multiplier method when dealing with complex geometries.

Fig. 3.25 shows the schematic of the problem setup. The center of the cylinder is located

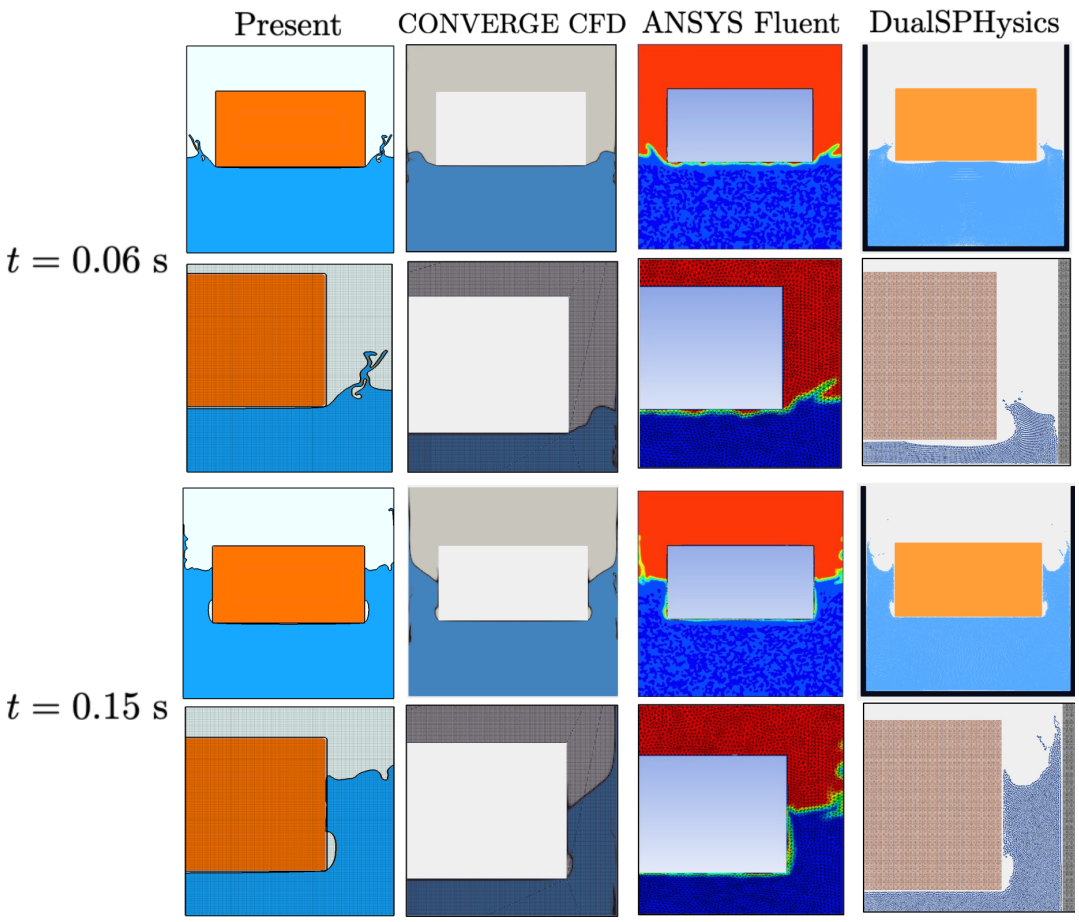

Figure 3.21. Fluid-structure interaction of the rectangle block at time $t = 0.06$ s and $t = 0.15$ s for the present solver which uses the fully Eulerian approach with level set method on uniform Cartesian grid, CONVERGE CFD which uses the VOF with the cut-cell method, ANSYS Fluent uses VOF with dynamic meshing, and DualSPHysics which uses the fully Lagrangian mesh-free technique.

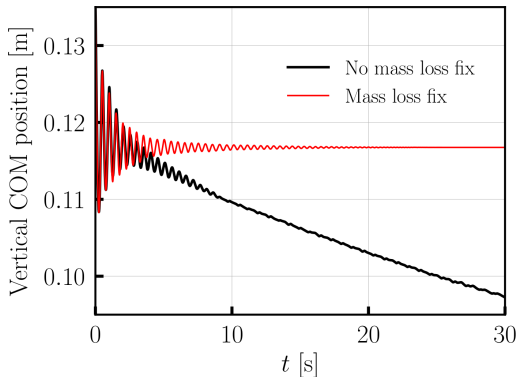

Figure 3.22. Temporal evolution of the vertical center of mass of the rectangle block with and without mass loss fix.

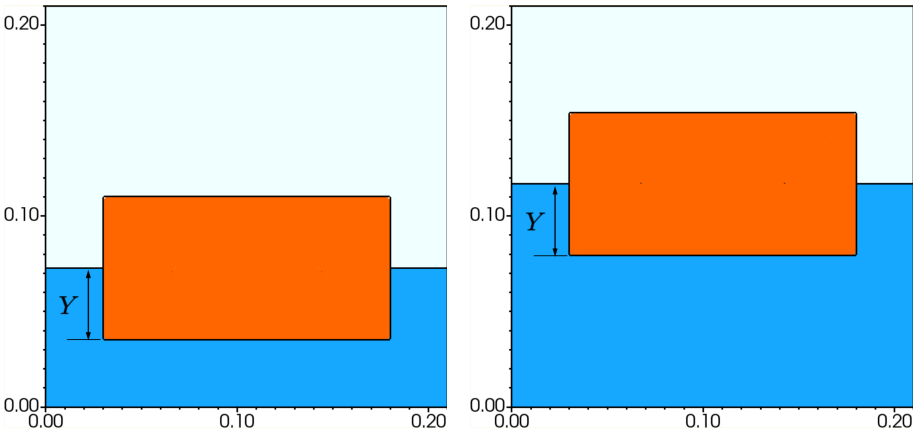

(a) Without mass loss fix method, Y = 0.03757 m (b) Mass loss fix method, Y = 0.03753 m

Figure 3.23. Static equilibrium position of the rectangular block after a very long time for (a) without the mass loss fix method, and (b) the mass loss fix method.

at $(1.75R, 2R)$ in a box of size $(3.5R, 4R)$. The initial level of water is $1.5R$. The cylinder is allowed to move only in the vertical direction while the other degrees of freedom of the cylinder are locked. First we do a grid converge study with three uniform grid sizes of 280×320 (Coarse), 420×480 (Medium), and 560×640 (Fine) which is equal to $\Delta x = 10^{-3}$ m, 7.5×10^{-4} m and 5×10^{-4} m, respectively, and the initial time steps for the present solver are the same as used for floating rectangle case in Table 3.3. All simulations are performed with the mass loss fix method. Fig. 3.26(a) shows the comparison of the temporal evolution of the vertical center of mass position of the cylinder for the three grids. From the result we conclude that the medium grid resolution is good enough for further studies. Next, we validate our dynamics, Fig. 3.26(b) compares the dynamics of the medium grid with the dynamics obtained by CONVERGE CFD software. The CONVERGE CFD simulation is conducted on a grid size of $\Delta x = 0.00075$ m and initial time step of 10^{-5} s. Table 3.4 shows the final equilibrium positions of the cylinder and compares it with the analytically calculated value. Under grid refinement, the present solver's final equilibrium position approaches the analytical value. Also, the cut-cells are complex for complex shaped objects like the cylinder for the CONVERGE CFD solver, hence the reason for equilibrium values being off from the analytical value. The dynamics obtained using the present

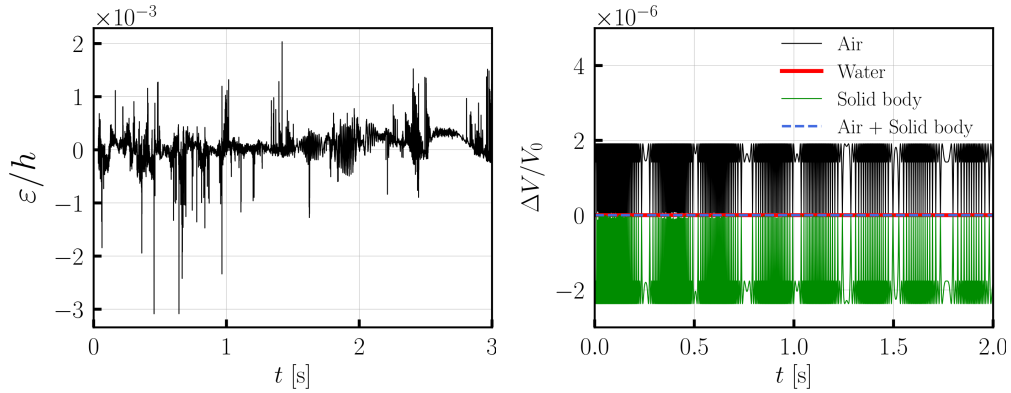

(a) Normalized shift in the level set (b) Relative error in volume

Figure 3.24. (a) Normalized shift in the level set after every time step, and (b) relative error in volume of the various phases involved in the half submerged rectangle block problem.

solver are now validated with that obtained from CONVERGE CFD software. Fig. 3.27 shows the fluid-structure interaction of the cylinder block at simulation time $t = 0.01$ s, $t = 0.32$ s, and $t = 1$ s for the present solver.

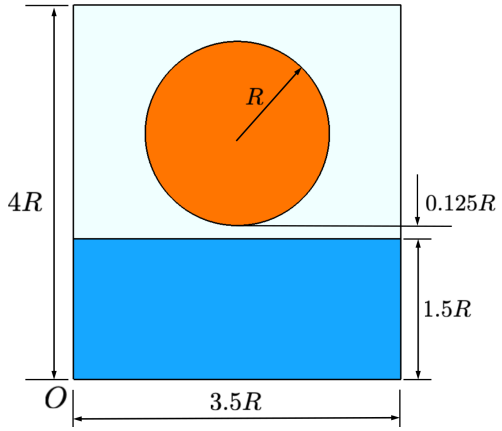

Figure 3.25. Schematic of half submerged cylinder in water test case.

Table 3.4. Vertical center of mass position of the cylinder at equilibrium for various grid sizes for the present solver, and medium grid for CONVERGE CFD compared with analytically calculated value.

Grid	Present	CONVERGE CFD	Analytical
Coarse	0.1179	-	0.1169
Medium	0.1178	0.1162	
Fine	0.1175	-	

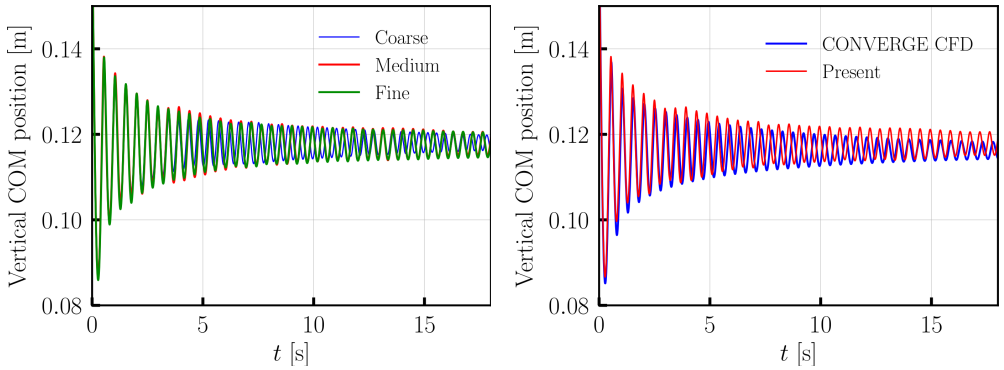

(a) Grid convergence test

(b) Dynamics compared for present solver and CONVERGE CFD software.

Figure 3.26. (a) Temporal evolution of the vertical center of mass position of the cylinder. (b) Comparison of the vertical center of mass position vs time for the present solver and CONVERGE CFD simulations.

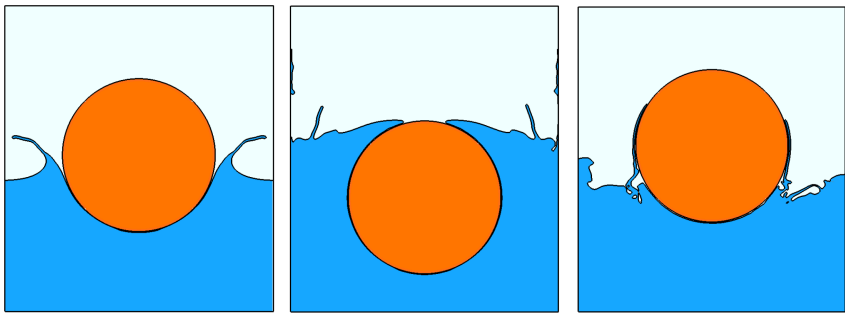

Figure 3.27. Fluid-structure interaction of the cylinder at time $t = 0.1$ s, $t = 0.32$ s, and $t = 1$ s for the present solver.

Next, we compare the dynamics of the cylinder with and without the mass loss fix method in Fig. 3.28. The dynamics without the mass loss fix method are highly irregular and the cylinder settles in the wrong equilibrium position. Next, Fig. 3.29(a) shows the normalized value of the shift applied to the level set field after every time step and is seen to be of the order of 10^{-3} which is at a subgrid level. The Fig. 3.29(b) shows the error in the relative volume of various phases present in the domain vs time. The relative volume error for water is found to be of zero. Also, it is seen if the volume of water is conserved, the volume of the remaining phases present in the domain I.e. (Air + Cylinder) is also conserved. From the results presented above, we conclude that the mass preserving method conserves mass of the target fluid with correct

dynamics for complex shaped geometries in the computational domain.

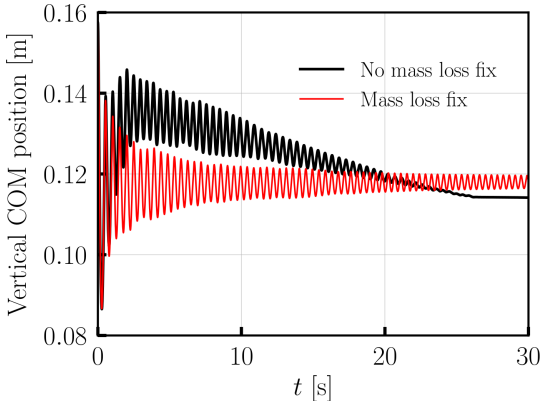

Figure 3.28. Temporal evolution of the vertical center of mass of the cylinder with and without mass loss fix.

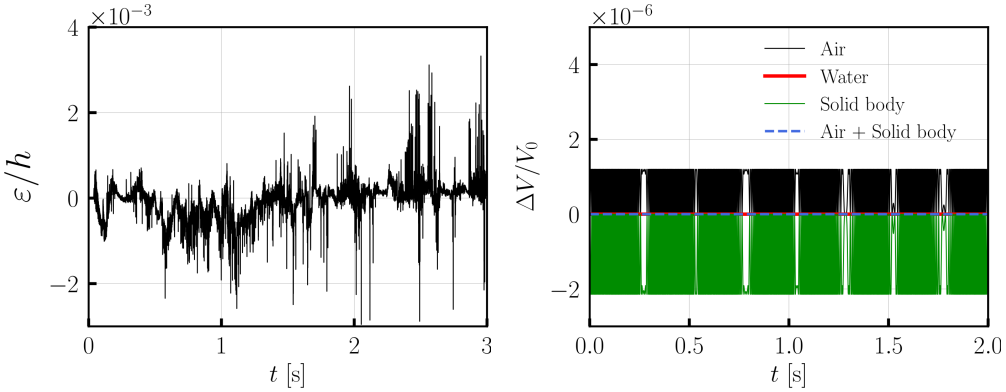

(a) Normalized shift in the level set (b) Relative error in volume

Figure 3.29. (a) Normalized shift in the level set after every time step, and (b) relative error in volume of the various phases involved in the half submerged cylinder problem.

Free fall of a 2D Wedge

We simulate the standard case of free fall of a 2D wedge dropping on air-water interface [61, 62, 39] which is a standard benchmark problem in the ocean engineering literature. The problem schematic is shown in Fig. 3.30. The size of the computational domain is taken to be $\Omega = [0, 10L] \times [0, 2.5L]$, where $L = 1.2$ m is the largest side of the wedge. The wedge angle is $\theta = 25°$. the wedge is oriented in such a way that one of its vertex points downwards, see

Fig. 3.30. The initial water depth is $d = 1$ m. The lower most vertex of the wedge is located at $(L/2, 2.3)$ m. The density of water is ρ_w 1000 kg/m^3 and viscosity is $\mu_w = 10^{-3}$ Pa·s. For air these values are $\rho_a = 1.2$ kg/m^3 and $\mu_a = 1.8 \times 10^{-5}$ Pa·s. For the wedge density is ρ_s = 466.6 kg/m^3 and its fictitious viscosity is set to that of water. The wedge is allowed to move only in the vertical direction while its other degrees of freedom are constrained. This is a challenging test case as large forces are generated when the wedge impacts the water surface which can cause instabilities and incorrect dynamics [39, 54]. We simulate this problem to validate our mass loss fix method for large domains that include rigid bodies.

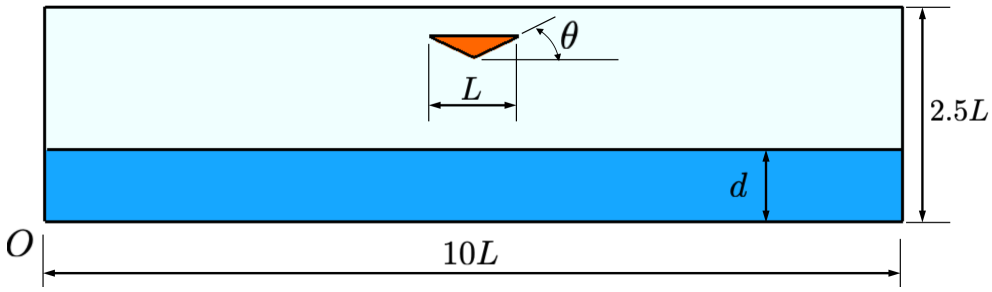

Figure 3.30. Schematic of the 2D wedge problem.

First, we conduct a grid convergence test on the problem. We consider three uniform grid sizes as shown in Table 3.5 with corresponding time-steps used. The Fig. 3.31(a) and 3.31(b) compares the vertical center of mass position and the vertical velocity of the wedge, respectively for the three grids resolutions. As can be seen from the plots, the medium grid size and the corresponding time step size used are adequate to resolve the FSI dynamics of the freely falling 2D wedge. Next, we compare the medium grid resolution results with the 3D volume of fluid simulations of Pathak et al. [61] and experimental results of Yettou et al. [62], in Fig. 3.32. Fig. 3.32(a) compares the vertical center of mass position of the wedge as it falls from a certain height and impacts on the free surface of water. Fig. 3.32(b) compares the vertical velocity of the wedge. The magnitude of the vertical velocity component increases as the wedge falls freely and reduces drastically once it hits the water surface. The dynamics are in good agreement with the inherently mass preserving volume of fluid method simulations of Pathak et al. [61] and also

with the experimental results of Yettou et al. [62]. Additionally, Fig. 3.33 presents the FSI when the wedge impacts the air-water interface and the vorticies generated.

Table 3.5. Grid convergence test parameters for the free fall of 2D wedge on air-water interface.

Grid	Δx (m)	Δt_{max} (s)
Coarse	0.01	6.25×10^{-5}
Medium	0.005	3.125×10^{-5}
Fine	0.0025	1.5652×10^{-5}

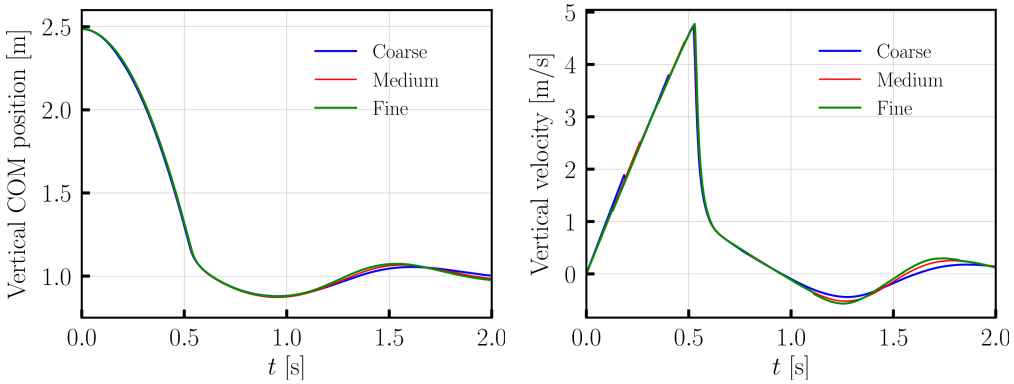

(a) Vertical displacement (b) Vertical velocity

Figure 3.31. Results for the grid convergence test for (a) vertical center of mass position, and (b) vertical velocity of the 2D wedge.

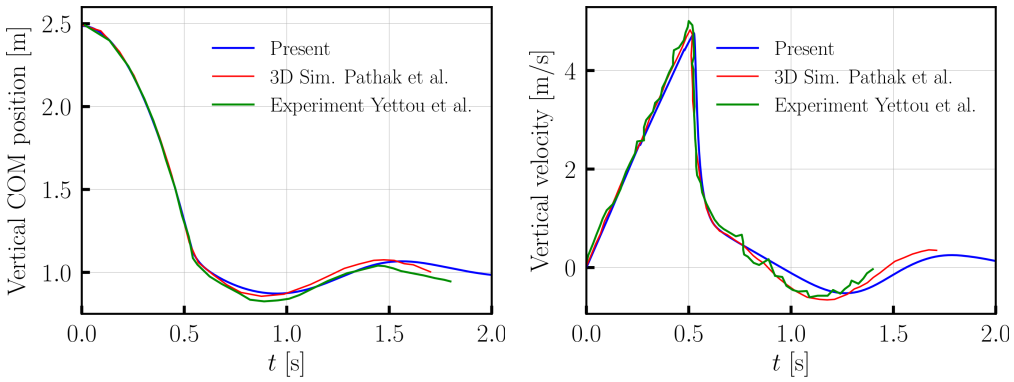

(a) Vertical displacement (b) Vertical velocity

Figure 3.32. Comparison of (a) vertical center of mass position and (b) vertical velocity with 3D volume of fluid simulation of Pathak et al. [61] and Experimental results of Yettou et al. [62].

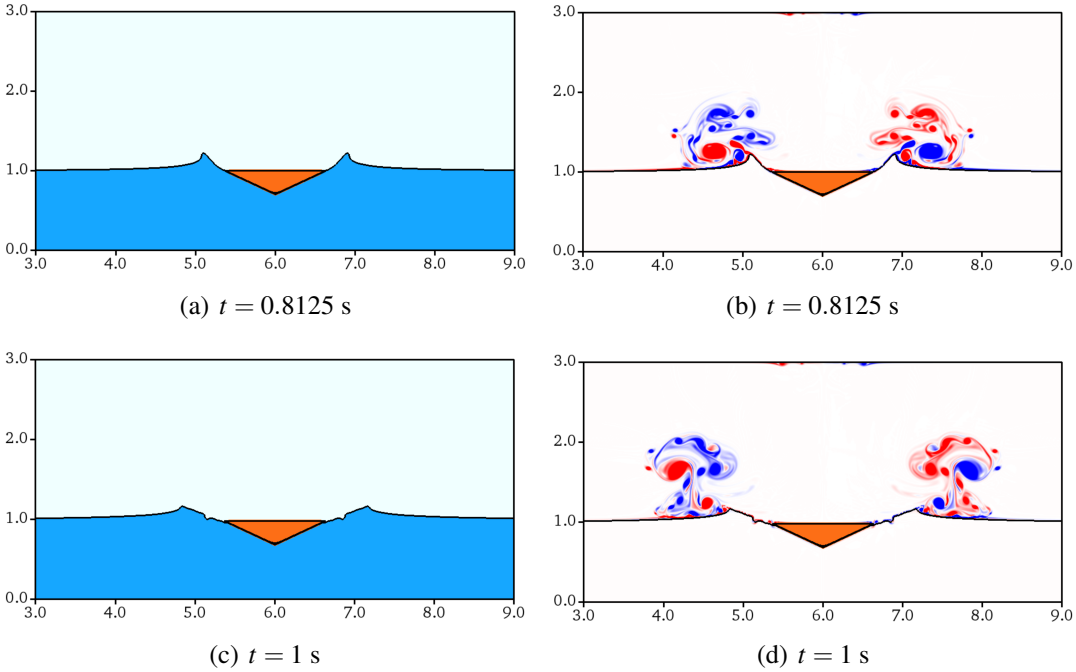

(a) $t = 0.8125$ s (b) $t = 0.8125$ s

(c) $t = 1$ s (d) $t = 1$ s

Figure 3.33. FSI of the free falling 2D wedge impacting the air-water interface: (left) density and (right) vorticity generated in the range -100 to 100 s^{-1}.

Given the large computational domain used for this benchmark problem, we hypothesize that maintaining a constant water volume is not essential for capturing the correct fluid-structure interaction dynamics of the wedge impact. This is because the water level rise is expected to be negligible, even at equilibrium. To verify this, we compare the wedge's heave motion with and without the mass loss fix method. As shown in Fig. 3.34, the dynamics remain identical. Consequently, mass-conservative schemes, such as cut-cell methods or geometric volume of fluid (which are also more challenging to implement), offer less advantage for these types of problems. Their strengths are more evident in problems like those discussed before. Finally, Figs. 3.35(a) and 3.35(b) illustrate the normalized correction and relative volume change for different phases, respectively, when the mass-loss fix is applied. The normalized shifts are of the order of 10^{-5} compared to the grid size and the relative error in volume for water is found to be of the order of 10^{-16} which is machine precision. We also show that if the volume of the water is conserved using our mass loss fix method, the volume of the remaining phase .I.e (Air +

Wedge) is automatically conserved and can be seen in Fig. 3.35(b).

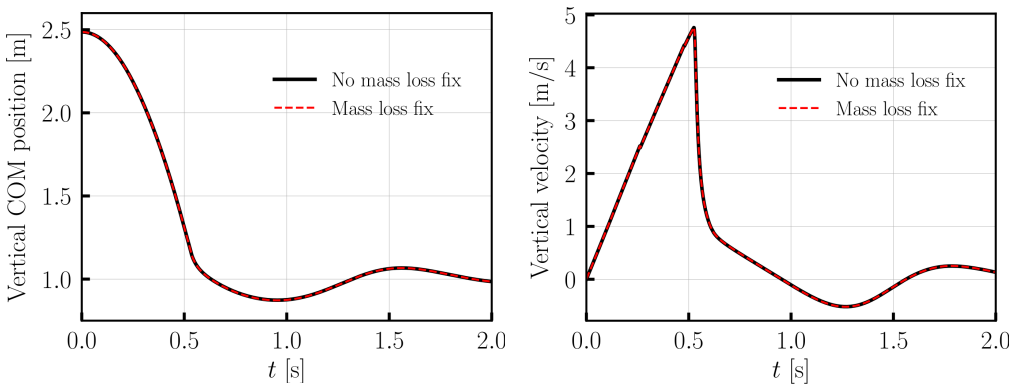

(a) Vertical displacement (b) Vertical velocity

Figure 3.34. Comparison of (a) vertical center of mass position and (b) vertical velocity for simulations results of no mass loss fix and with mass loss fix technique implementation.

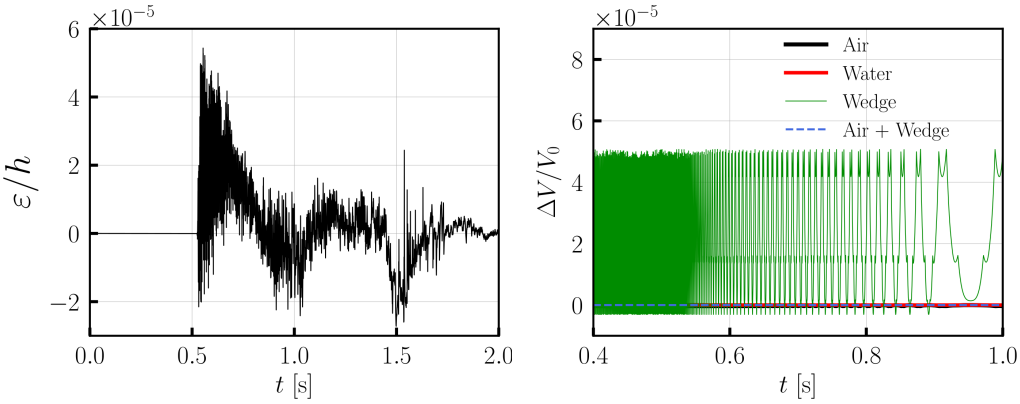

(a) Normalized shift (b)

Figure 3.35. (a) Normalized shift vs time, and (b) relative error in volume of various phases involved in the free fall of 2d wedge problem.

3D Vertical cylinder heaving at air-water interface

In this section, we show the capability of our FSI solver to simulate 3D problems with adaptive mesh refinement and presented mass loss fix method. We simulate the dynamics of a 1:20 scaled down version of a wave energy converter (WEC) device [63] which is a highly potential renewable energy technology under continuous development [64]. We considered a

vertical cylinder type point absorber device heaving on an air-water interface. The device heaves due to interactions with the incoming sea waves simulated in a high-fidelity numerical wave tank (NWT). The device absorbs the wave energy and converts it into electrical energy. For optimization of the WEC device performance different control strategies can be implemented. In our study, we do not consider the control system setup and just simulate the dynamics of the device on regular sea waves which is the main idea of this problem. All boundaries of the tank are modeled as stationary walls, except for the top boundary which is considered to be open (zero pressure boundary condition). The schematic of the wave tank with the device is depicted in Fig. 3.36. We refer this figure later in Chapter 5.

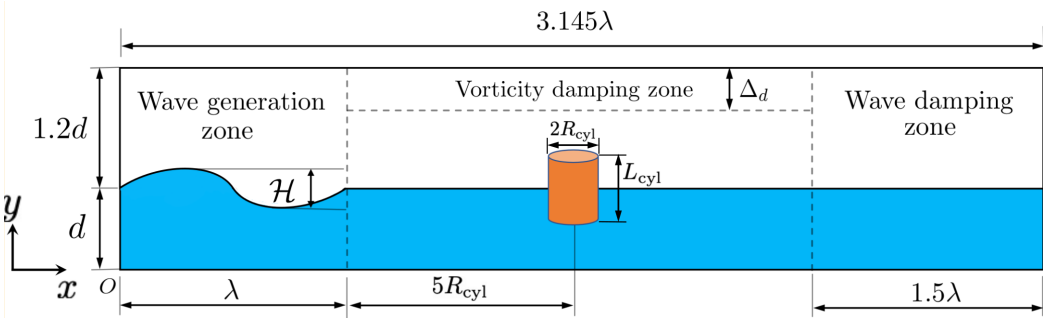

Figure 3.36. Schematic of the 3D vertical cylinder heaving at air-water interface.

The 3D computational domain is of size $\Omega = [0, 3.145\lambda] \times [0, 2.2d] \times [0, 12R_{\text{cyl}}]$ m where, λ is the wavelength of the incoming sea wave, $d = 2$ m is the depth of water when no waves are present and $R_{\text{cyl}} = 0.25$ m is the radius of the cylinder. The cylinder has a length of $L_{\text{cyl}} = 0.8$ m. The cylinder is considered to be half submergible in equilibrium position. The size of the domain is selected based on authors experience on conducting studies on wave energy convertor devices, see [55, 59, 60]. The origin O of the domain is located at the lower left corner. First order Stokes waves [65, 66] also called regular water waves with wave height $\mathscr{H} = 0.1$ m and time period $\mathscr{T}_p = 1.5652$ s are generated in the wave generation zone. These waves have a period (or wavelength) to water depth ratio that classifies them as deep water waves. The Stokes waves

satisfy the dispersion relation, which reads as

$$\omega^2 = g\kappa_w \tanh(\kappa_w d) \tag{3.34}$$

where, $\omega = 2\pi/\mathscr{T}_p$ is the wave frequency in rad/s, $g = 9.81$ m/s the acceleration due to gravity, and $\kappa_w = 2\pi/\lambda$ the wave number in rad/m. The water waves travel in the positive x direction and are smoothly damped out at the right side of the tank in the wave damping zone after interacting with the body, see Fig. 3.36. The wave generation zone is provided so that the waves reflected from the device do not interact with the left boundary and cause instabilities in the simulation. The wave damping zone on the right of the domain is provided to avoid the waves reflected from the right boundary to travel in the negative x direction and affect the dynamics of the device causing unphysical dynamics. The width of the wave generation zone is λ and that of the wave damping zone is 1.5λ. The relaxation method [67] is used to smoothly generate and absorb waves in the wave generation and damping zones. A vorticity damping zone is also provided at the top boundary domain to damp out the vortices generated by the device that interact with the top boundary. To implement the vorticity damping zone a damping force is added to the momentum equation,

$$\mathbf{f}_{\mathrm{d}} = -g(\bar{y})\mathbf{u} \tag{3.35}$$

where, $g(\bar{y}) = \rho_{\mathrm{a}}(\cos(\pi\bar{y})+1)/(4\Delta t)$ is the smoothed damping coefficient, $\rho_{\mathrm{a}} = 1.225$ kg/m^3 is the density of air, Δt is the time step size of the solver, $\bar{y} = (y - y_{\max})/\Delta_d$ is the normalized y coordinate, with $y_{\max} = 2.2d$ and $\Delta_d = 4\Delta x_{\mathrm{coarsest}}$ is the vorticity damping zone width. Initially, the center of mass position of the vertical cylinder is at $(\lambda + 5R_{\mathrm{cyl}}, d, 6R_{\mathrm{cyl}})$. The density of water is $\rho_{\mathrm{w}} = 1025$ kg/m^3, viscosity of water is $\mu_{\mathrm{w}} = 10^{-3}$ Pa·s, and viscosity of air is $\mu_{\mathrm{a}} = 1.8\times10^{-5}$ Pa·s. For more details on the NWT implementation and wave generation, see [59, 60].

First, we perform a grid convergence study to determine the optimal grid spacing to accurately resolve the dynamics of the device. Three grid sizes are considered to perform the

grid convergence test: coarse, medium, fine, as listed in Table 3.6. The computational grid is made up of a heirarchy of ℓ grid levels. The coarsest level has grid size of $N_x \times N_y \times N_z$ cells on the entire computational domain Ω. A sub-region on the coarsest grid level is then locally refined $(\ell - 1)$ times by an integer refinement ratio of n_{ref}. The refining is done in such a way that the regions of interest: the air-water interface and the WEC device are on the finest grid level throughout the simulation. The grid spacing on the finest level is calculated as $\Delta x = \Delta x_0 / n_{\text{ref}}^{\ell-1}$, $\Delta y = \Delta y_0 / n_{\text{ref}}^{\ell-1}$, and $\Delta z = \Delta z_0 / n_{\text{ref}}^{\ell-1}$, where the $\Delta x_0, \Delta y_0$, and Δz_0 are the grid spacing on the coarsest levels. Fig. 3.37(a) shows the locally refined Cartesian grid with two grid levels with the finest grid encompassing the air-water interface region and the 3D vertical cylinder. Fig. 3.37(b) shows the wave structure interaction (WSI) at simulation time $t = 12.9$ s on regular water waves. First order water waves are generated in the wave generation zone on the left side and travel towards the right side. When the waves hit the cylinder it starts heaving. The temporal evolution of the vertical displacement of the cylinder for the three grids is compared in Fig. 3.38(a) and the vertical velocity is compared in Fig. 3.38(b) with the Boundary element method (BEM) results. For more details on the BEM solver, see [60]. A medium grid resolution is seen to be good enough to resolve the WSI accurately. We will use the medium grid resolution for further studies.

Table 3.6. Grid refinement parameters used for the grid convergence test for the vertical heaving cylinder.

Parameters	Coarse	Medium	Fine
n_{ref}	4	4	4
ℓ	2	2	2
N_x	60	120	180
N_y	15	30	45
N_z	22	44	66
$\Delta x_0 = \Delta y_0 = \Delta z_0$ (m)	0.2	0.1	0.0667
$\Delta x = \Delta y = \Delta z$ (m)	0.05	0.025	0.0166
Δt_{max} (s)	5×10^{-3}	2.5×10^{-3}	1.5×10^{-3}

Because the domain is large, we anticipate that the mass loss fix method is not crucial to obtaining the correct WSI dynamics for the WEC device in this problem as well. Figs. 3.39(a)

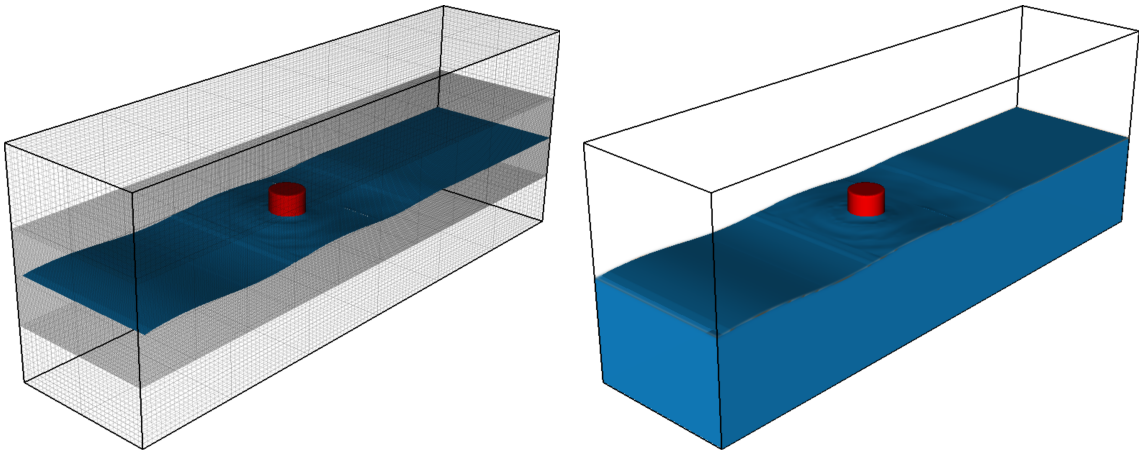

(a) Locally refined Cartesian grid

(b) Vertical cylinder heaving under the action of regular water waves

Figure 3.37. (a) Locally refined grid for two grid levels for the 3D NWT, and (b) WSI of 3D vertical cylinder on regular water waves in NWT at $t = 12.9$ s.

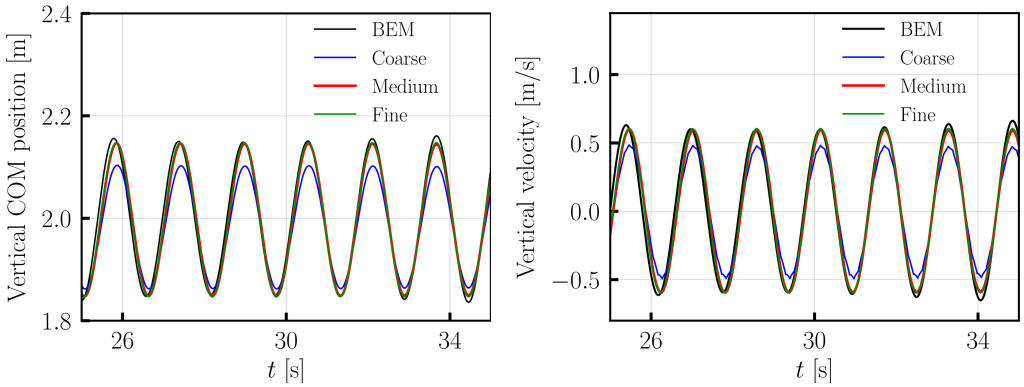

(a) Vertical dispacement vs time

(b) Vertical velocity vs time

Figure 3.38. Temporal evolution of (a) vertical displacement and (b) vertical velocity of the cylinder for three grid sizes: Coarse, Medium, and Fine on first order water waves of $\mathscr{H} = 0.1$ m and $\mathscr{T}_\mathrm{p} = 1.5652$ s compared with the BEM simulation results.

and 3.39(b) compare the vertical center of mass position and velocity of the cylinder over time with and without the mass fix. The results confirm that WEC dynamics remain the same with or without the fix. Also, Fig. 3.40(a) shows the normalized shift in the level set field applied after every time step. The normalization is done with respect to $\Delta x = 0.025$ m, which is the finest grid size for the medium grid resolution. The normalized values are of the order of 10^{-3} which is at a subgrid level. Fig. 3.40(b) shows the relative error in volume for the various phases involved.

The order of relative error in volume for the water phase is of the order 10^{-16}. Also, the error in the remaining phase .I.e (Air + cylinder) is of the order of 10^{-16}. From the results it is concluded that a small shift in the level set field which obeys the signed distance property, the mass of the target fluid is conserved upto machine precision without the loss in accuracy in the dynamics.

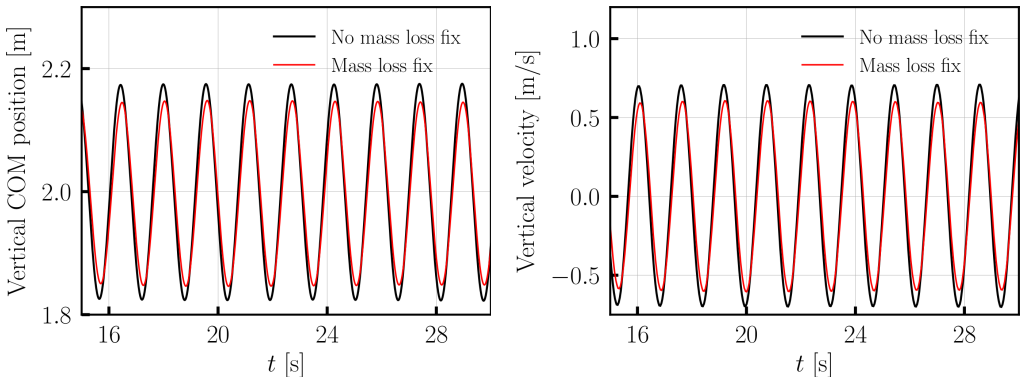

(a) Vertical dispacement vs time (b) Vertical velocity vs time

Figure 3.39. Temporal evolution of (a) vertical displacement and (b) vertical velocity of the cylinder comparison of without mass loss fix and with mass loss fix method implemented.

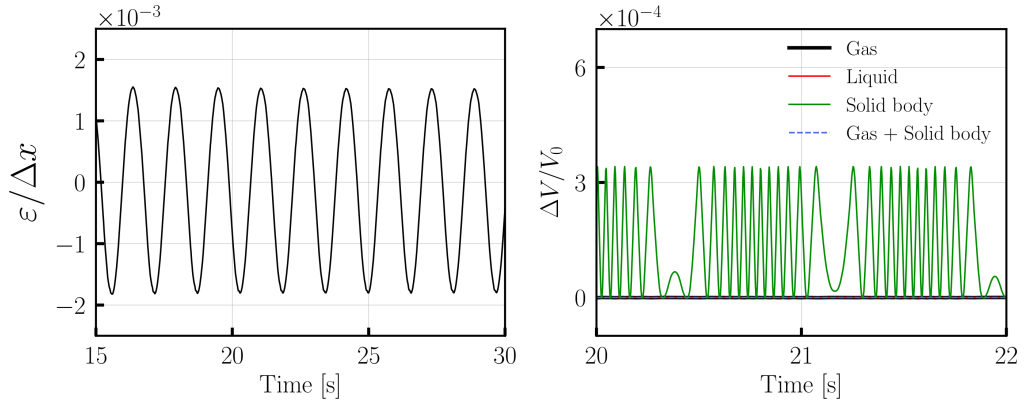

(a) Relative error in volume vs time (b) Normalized shift vs time

Figure 3.40. Temporal evolution of (b) relative error in volume of the various phases involved in the domain and (a) the normalized shift in the level set applied at every time step.

3.5.4 Brinkman penalty factor split into normal and tangential components

In the Brinkman penalty method the permeability of the body needs to be low $\kappa \ll 1$ to represent a non-porous body. In practice, while κ value is small, it does not approach machine zero. This implies that the no-slip condition on the fluid-solid interface is only partially enforced. The approach of κ to machine zero poses two issues:

1. the system of equations become stiff to solve; and

2. a no-slip condition in the tangential direction implies a stress singularity at the material triple points.

Our recent paper describes a preconditioning strategy that overcomes the numerical stiffness issue of the Brinkman penalization method: the fluid solver converges rapidly regardless of κ. Therefore, issue #1 is not a concern with our implementation. The second issue is unavoidable, and one must allow for tangential slip at the triple points. This is necessary for the solid to move across/pierce the two fluid interfaces. The classical no-slip condition at the material triple point breaks down as discussed in Huh and Scriven [68]. A question naturally arises in light of issue #2 for the Brinkman penalization method: is it possible to impose different amounts of slip in the normal and tangential directions? For example, no slip in the normal direction and some slip in the tangential direction. Using numerical experiments, this section explores this possibility.

A three phase FSI problem is simulated in which a rectangular block is released from a small height above the air-water interface. Detailed information on the problem setup is provided in the floating rectangular block case in Sec. 3.5.3, where we focus on the mass loss issues with the level set method. We focus here on the dynamics of the block and the air-water interface as a function of differential slip. This case is studied by splitting the Brinkman penalty force,

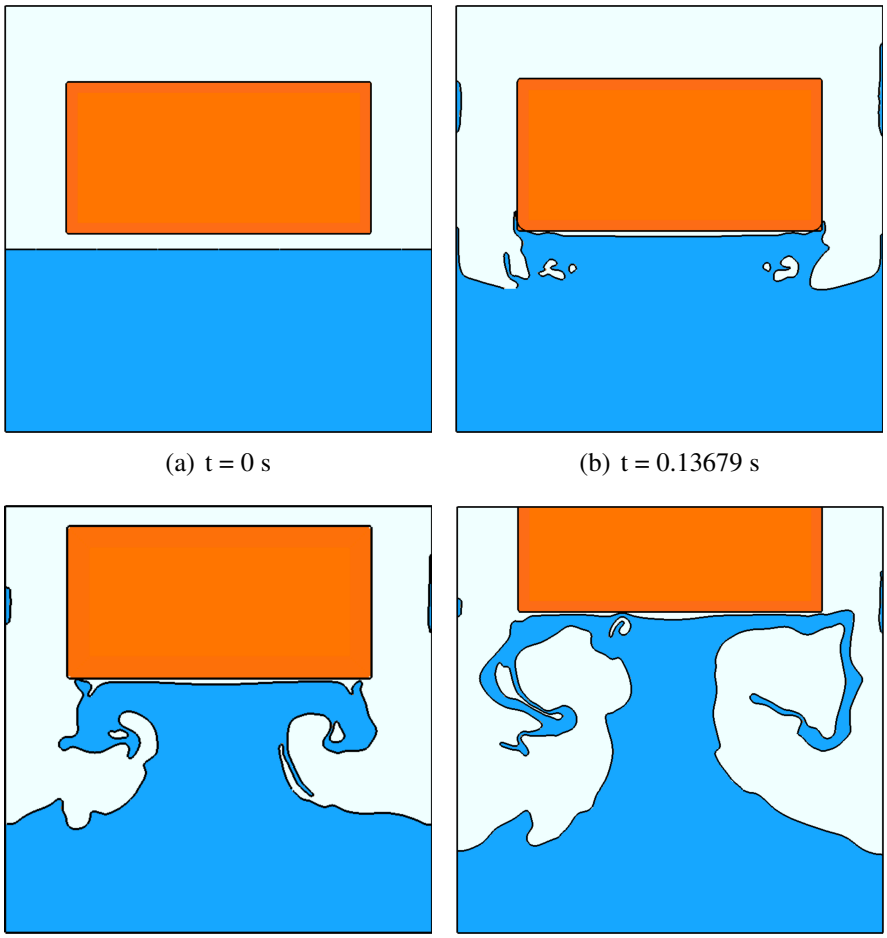

(a) t = 0 s (b) t = 0.13679 s

(c) t = 0.136794 s (d) t = 0.13717 s

Figure 3.41. Three phase fluid-structure interaction of a rectangular block when the air-water interface is not allowed to enter the solid body ($\mathscr{K}_{\mathrm{n}} = 50, \mathscr{K}_{\mathrm{t}} = 1$).

described in Eq. (2.44) into normal and tangential components as

$$\mathrm{f}_c(\mathbf{x},t) = \frac{\chi(\mathbf{x},t)}{\kappa}\left[\mathscr{K}_{\mathrm{n}}(\mathbf{u}_b(\mathbf{x},t)-\mathbf{u}(\mathbf{x},t))\cdot(\mathbf{n}_{\mathrm{s}}\otimes\mathbf{n}_{\mathrm{s}})+\mathscr{K}_{\mathrm{t}}(\mathbf{u}_b(\mathbf{x},t)-\mathbf{u}(\mathbf{x},t))\cdot(\mathrm{I}-(\mathbf{n}_{\mathrm{s}}\otimes\mathbf{n}_{\mathrm{s}}))\right], \tag{3.36}$$

in which, $\mathscr{K}_{\mathrm{n}}$ and $\mathscr{K}_{\mathrm{t}}$ are the normal and tangential penalty factors, respectively, and $\mathbf{n}_{\mathrm{s}}$ is the unit normal to the solid surface. The splitting of the Brinkman force into normal and tangential components is done in the fluid-solid interfacial zone. Inside the body, the penalty force reverts to its original form. When $\mathscr{K}_{\mathrm{n}} = 1$ and $\mathscr{K}_{\mathrm{t}} = 1$, Eq. (3.36) reverts back to Eq. (2.44). We impose a no-normal penetration condition by increasing the normal penalty factor to $\mathscr{K}_{\mathrm{n}} = 50$. The tangential penalty factor is kept at $\mathscr{K}_{\mathrm{t}} = 1$. The large value of the normal penalty factor restricts the air-water interface within the solid body. Fig. 3.41 displays very unphysical FSI dynamics in this case, where the block appears to "ride the waves". After being released, the rectangular block bounces to a higher elevation and continues to rise.

Fig. 3.21 shows physically correct dynamics when both $\mathscr{K}_{\mathrm{n}}$ and $\mathscr{K}_{\mathrm{t}}$ are set to 1. The air-water interface is thus allowed to enter the rectangle block. As long as the mass/volume conservation constraint (of the actual fluid) is maintained, it is not a problem for the fluid to penetrate into the solid region. It corresponds to the immersed formulation of the mass-preserving level set method.

3.6 Conclusions

In this chapter, we presented the spatial and temporal discretization of the continuous equations described in Chapter 2. We presented the fluid-structure coupling that uses the FD/BP method. Next, we present the solution methodology that uses the projection preconditioner for the monolithic solution of the volume penalized incompressible Navier-Stokes equations. The preconditioner uses a projection algorithm that correctly accounts for the Brinkman penalty term in pressure and velocity updates. Using the method of manufactured solutions, it is demonstrated that the proposed preconditioner is scalable, second order spatially accurate, and a reasonable

starting value for the permeability parameter is $\kappa = \Delta t/\rho$ is proposed.

Next, we simulate two-phase and three-phase stringent FSI problems and demonstrate the effectiveness of the approximate Lagrange multiplier technique. We present relative error in the volume of the target fluid for all the numerical test cases and show that mass is conserved to machine precision. Further, we simulate a test case of a floating rectangular block and allow the differential treatment of the Brinkman penalization factor. We demonstrate that this leads to incorrect FSI dynamics, where the solid surface artificially repels the two-fluid interface. Our technique is globally mass-preserving and not point-wise mass preserving. However, for the study of ocean engineering applications, which is the aim of this work, average mass conservation is sufficient for problems that involve small computational domain and no mass conservation is required for problems with large computational domain.

Acknowledgement

This chapter, in part, is a reprint of the material as it appears in ”An effective preconditioning strategy for volume penalized incompressible/low Mach multiphase flow solvers”, Ramakrishnan Thirumalaisamy, Kaustubh Khedkar, Pieter Ghysels, Amneet Pal Singh Bhalla, Journal of Computational Physics, Volume 490, 2023”, and “Preventing mass loss in the standard level set method: New insights from variational analyses”, Kaustubh Khedkar, Amirreza Charchi Mamaghani, Pieter Ghysels, Neelesh A. Patankar, Amneet Pal Singh Bhalla, arXiv:2404.03132, 2024. The dissertation author wasthe primary investigator and author of these papers.

Chapter 4

Reactive Control Strategy for Inertial Sea Wave Energy Converter (ISWEC) Device

In this chapter, we investigate the dynamics of the inertial sea wave energy converter (ISWEC) device using fully-resolved computational fluid dynamics (CFD) simulations. Originally prototyped by the Polytechnic University of Turin, the device consists of a floating, boat-shaped hull that is slack-moored to the sea bed. Internally, a gyroscopic power take-off (PTO) unit converts the wave-induced pitch motion of the hull into electrical energy. The CFD model is based on the incompressible Navier–Stokes equations and utilizes the fictitious domain Brinkman penalization (FD/BP) technique to couple the device physics and water wave dynamics which is presented in Chapter 2 and 3. A numerical wave tank is used to generate both regular waves based on fifth-order Stokes theory and irregular waves based on the JONSWAP spectrum to emulate realistic sea operating conditions. A Froude scaling analysis is performed to enable two- and three-dimensional simulations for a scaled-down (1:20) ISWEC model. It is demonstrated that the scaled-down 2D model is sufficient to accurately simulate the hull's pitching motion and to predict the power generation capability of the converter. A systematic parameter study of the ISWEC is conducted, and its optimal performance in terms of power generation is determined based on the hull and gyroscope control parameters. It is demonstrated that the device achieves peak performance when the gyroscope specifications are chosen based on the reactive control theory. It is shown that a proportional control of the PTO control torque is required to generate

continuous gyroscopic precession effects, without which the device generates no power. In an inertial reference frame, it is demonstrated that the yaw and pitch torques acting on the hull are of the same order of magnitude, informing future design investigations of the ISWEC technology. Further, an energy transfer pathway from the water waves to the hull, the hull to the gyroscope, and the gyroscope to the PTO unit is analytically described and numerically verified. Additional parametric analysis demonstrates that a hull length to wavelength ratio between one-half and one-third yields high conversion efficiency (ratio of power absorbed by the PTO unit to wave power per unit crest width). Finally, device protection during inclement weather conditions is emulated by gradually reducing the gyroscope flywheel speed to zero, and the resulting dynamics are investigated.

4.1 Introduction

Global warming is on the rise and is likely to breach the 1.5°C limit in the coming decades. It is imperative to switch to clean renewable energy, including hydro, solar, and wind, in order to mitigate the effects of climate change and meet the growing energy demands. For perspective, the United States generated 3.7 TWy (terawatt years [1]) worth of energy in 2013, making up about 20% of the world's total energy production. Of this amount, only about 9% or 0.33 TWy was generated from renewable sources. It is estimated that the US will produce approximately 8.65 TWy by 2050 [69]. There is an ever-increasing need to invest in renewable energy harvesting techniques in order to accelerate economic growth while maintaining a safe and healthy planet Earth. This can be achieved, in part, through ocean energy, which remains a largely untapped energy resource.

Ocean waves are a substantial source of renewable energy, with an estimated 2.11 ± 0.05 TW available globally [70]. It is estimated that about 230 TWh/year of wave energy can be extracted from the East Coast and about 590 TWh/year from the West Coast of the United States alone. In spite of this abundantly available energy source, there is currently no commercial-

[1] 1 TWy = 8.76×10^{12} kWh.

scale wave power operation that exists today. There are several unique challenges specific to wave energy extraction processes, including hostile ocean environments, saltwater corrosion, stochasticity of ocean and sea waves, and costly offshore wave farm setup. Nevertheless steady progress is being made both in the design and engineering analyses of wave energy extraction devices, which are known as wave energy converters (WECs). The testing of expensive WEC devices, power take-off units (PTO) and control strategies to optimize their performance in physical wave tanks is another challenge. Consequently, several WEC designs have been proposed over the years after gaining popularity following the 1970s oil crisis. However unlike wind turbines, an ultimate WEC architecture has not yet been identified by researchers.

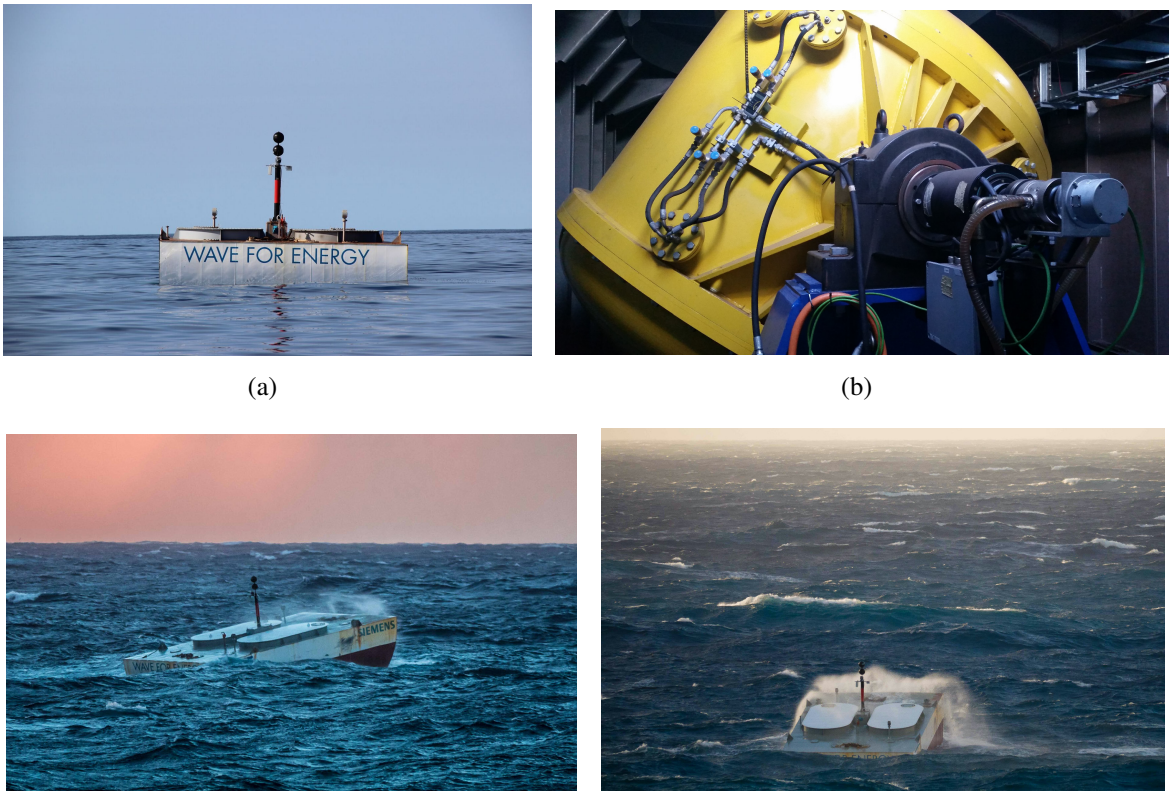

(a) (b)

(c) (d)

Figure 4.1. The inertial sea wave energy converter (ISWEC) device developed by the Mattiazzo Group at Polytechnic University of Turin. (a) ISWEC device freely floating in relatively calm sea conditions. (b) Gyroscope casing mounted on the power take off (PTO) axis. The PTO system is housed inside the hull. (c) Front and (d) side views of the ISWEC exhibiting pitching motion during operation. Image courtesy of the Mattiazzo Group and Wave for Energy S.R.L., Turin.

Numerical modeling of WECs is an efficient way to compare different designs and control strategies. A widely popular modeling approach in WEC research is the boundary element method (BEM) or its time-domain variant, the Cummins equation [71] based on the linear potential theory (LPT) [65, 66] due to its simplicity, low computational cost, and flexibility in simulating the wave structure interaction (WSI) of a variety of WEC devices and control strategies. The linear models, which were created originally to model large sea vessels, ships, and similar seakeeping applications, assume small body motion with respect to the wave amplitudes and lengths. Additionally, inviscid, irrotational, and incompressible flows are assumed. The BEM solvers perform exceptionally well for relatively calm sea states with small wave amplitudes. Nevertheless, the assumptions upon which linear methods are based are severely challenged in conditions of agitated seas or aggressive control. Additionally, BEM solvers use low-dimensional dynamical models that do not provide insights into fluid dynamics resulting from fluid-structure interaction (FSI), such as vortex shedding, wave breaking, and wave overtopping.

In recent years, models based on the non-linear potential flow theory (NLPT) have been proposed [72, 73]. By simulating the actual free water surface and including large body displacements, these models provide more accurate power estimates of the device than LPT-based models. The NLPT-based models are computationally expensive and are not easily applicable to the model-based control of WECs. An acceptable compromise, which is also sufficiently accurate, is the partially non-linear BEM model, which accurately resolves the hydrodynamical interactions between waves and devices [74, 75, 76, 77]. This can be accomplished by modifying the wave excitation force in the linear time-domain Cummins equation. In particular, the wave excitation or Froude-Krylov (FK) force is computed by integrating the incident wave pressure force over an instantaneous wetted surface area instead of assuming it is stationary at its mean equilibrium position. The Cummins equation-based WSI solver employing the non-linear Froude-Krylov (NLFK) method is referred to as the BEM-NLFK solver, and its linear counterpart as the BEM-LFK solver.

Although the NLPT-based models are more accurate than those based on LPT, they still

do not account for the viscous phenomenon or other major hydrodynamical non-linearities, such as wave-breaking and vortex shedding. Computational fluid dynamics (CFD) provides the most accurate description of WSI of WECs [55, 59, 73, 78, 79, 80]. Some groups have recently begun performing control-integrated CFD simulations of WEC devices. These studies, however, are mostly limited to classical control laws, such as reactive control (also called proportional-derivative control) or latching control (also called phase control or bang-bang control); see for example [78, 81, 82, 83]. Agamloh et al. [78] performed CFD simulations of a cylindrical buoy, in which the PTO was modeled as an ideal linear damper to generate a control force proportional to the device velocity, that is, the derivative control law. In [78], the optimal damping coefficient was estimated offline and kept constant throughout the simulation. To accurately capture the motion of the body, their CFD technique remeshed the domain at every time step. Giorgi et al. [82] used the latching control strategy for a 2D heaving cylinder subject to regular waves and compared BEM-LFK and CFD solvers. This is the first paper to implement a latching control for a WEC device within a CFD framework. The authors computed the optimal latching period offline using a combination of analytical techniques and free decay tests of the WEC device in the CFD-based numerical wave tank (NWT). According to Giorgi et al. [82], the BEM-LFK solver overestimates heave amplitude (and therefore power production) compared to the CFD solver. Recently, Windt et al. [83] compared the performance of a heaving WEC using BEM-LFK and CFD solvers. The predictions for three controllers were compared: (1) classical resistive (derivative) control; (2) classical reactive (proportional-derivative) control; and (3) moment-matching optimal control [84]. As for the resistive and reactive controllers, their optimal coefficients/gains were computed offline and kept constant throughout the simulation, while the moment-matching controller used a pre-computed/offline optimal control force sequence. Similarly to Giorgi et al., Windt et al. also found that the BEM-LFK solver over-predicts power absorption of the WEC device (for all three controllers).

This chapter and the next, we primarily focus on the development of WEC simulation infrastructure and test various control strategies. In this work, first we perform a comprehensive

study of the inertial sea wave energy converter (ISWEC) device prototyped by Polytechnic University of Turin [85, 86, 87] using high-fedility simulations using our developed CFD solver based on the multiphase fictitious domain Brinkman penalization (FD/BP) technique as described in Chapter 2. In comparison with body conforming grid techniques that have previously been used to simulate WEC dynamics, the FD/BP method is computationally efficient, since it eliminates the need to remesh the domain to account for body motion. To accurately resolve the wave and WEC dynamics in the specific regions of interest, we also make use of locally refined Cartesian grids. As a result, the computation costs of 3D simulations are low. We consider a more realistic operating conditions for the WEC device by using a numerical wave tank (NWT) to generate both regular and irregular water waves which was not done in previous studies [82, 88].

4.2 Wave dynamics

This section describes the types of waves, both regular and irregular generated in the NWT to simulate the WEC device dynamics.

4.2.1 Regular sea waves

First order waves

First-order Stokes waves, or regular waves, are simple harmonic waves of height $\mathscr{H}$, time period $\mathscr{T}$, and wavelength λ [65, 66]. Assuming that the waves travel in the positive x-direction, the wave elevation $\eta(x,t)$ from the still water surface at a depth of d above the sea floor is

$$\eta(x,t) = \frac{\mathscr{H}}{2}\cos(\kappa_w x - \omega t), \tag{4.1}$$

in which $\kappa_w = 2\pi/\lambda$ is the wavenumber and $\omega = 2\pi/\mathscr{T}$ is the angular wave frequency. The first-order Stokes wave satisfies the dispersion relation given by

$$\omega^2 = g\kappa_w \tanh(\kappa_w d), \tag{4.2}$$

which relates the wave frequency ω to wavenumber κ_w and water depth d. Eq. (4.2) is a transcendental equation that requires an iterative procedure to calculate κ_w for given ω, or vice versa. Instead, we use an explicit relationship between these quantities that is accurate enough for practical purposes at all water depths [89]:

$$\kappa_w d \approx \frac{\Gamma + \beta^2 (\cosh\beta)^{-2}}{\tanh\beta + \beta (\cosh\beta)^{-2}}, \tag{4.3}$$

in which $\beta = \Gamma (\tanh\Gamma)^{-\frac{1}{2}}$ and $\Gamma = \omega^2 d/g$.

As the waves travel along the ocean or sea surface, they carry kinetic and potential energy—this energy is partially absorbed by the WEC device. The time-averaged wave power per unit crest width carried by the regular waves in the direction of propagation is given by [65]

$$\overline{P}_{\text{wave}} = \frac{1}{8}\rho_{\text{w}} g \mathscr{H}^2 c_g, \tag{4.4}$$

in which c_g is the group velocity of the waves, i.e., the velocity with which wave energy is transported and it is given by the relation

$$c_g = \frac{1}{2}\frac{\lambda}{\mathscr{T}}\left(1 + \frac{2\kappa_w d}{\sinh(2\kappa_w d)}\right). \tag{4.5}$$

In the deep water limit, where $d > \lambda/2$ and $\kappa_w d \to \infty$, Eqs. (4.2) and (4.5) become

$$\omega^2 = g\kappa_w \quad \text{or} \quad \lambda = \frac{g\mathscr{T}^2}{2\pi} \qquad \text{and} \qquad c_g = \frac{\lambda}{2\mathscr{T}}. \qquad \text{(deep water limit)} \tag{4.6}$$

Substituting Eq. (4.6) into Eq. (4.4), the wave power per unit crest width in the deep water limit is expressed as

$$\overline{P}_{\text{wave}} = \frac{\rho_{\text{w}} g^2 \mathscr{H}^2 \mathscr{T}}{32\pi} \approx \mathscr{H}^2 \mathscr{T} \text{ kW/m}, \qquad \text{(deep water limit)} \tag{4.7}$$

in which the constant numerical factor $\rho_{\mathrm{w}} g^2/32\pi \approx 10^3$ when all quantities are evaluated in SI units.

Fifth order waves

We use Fenton's fifth-order wave theory [90] to generate regular waves of height $\mathscr{H}$, time period $\mathscr{T}$, and wavelength λ. According to fifth-order Stokes theory and assuming that the waves propagate in the positive x-direction, the wave elevation $\eta(x,t)$ from a still water surface at depth d above the sea floor is

$$\eta(x,t) = s\,\eta_1(x,t) + s^2\,\eta_2(x,t) + s^3\,\eta_3(x,t) + s^4\,\eta_4(x,t) + s^5\,\eta_5(x,t), \tag{4.8}$$

in which, $s = \kappa_w \mathscr{H}/2$ is the wave steepness, $\eta_1 = \kappa_w^{-1}\cos(\omega t - \kappa_w x)$ is the basic harmonic component, $\kappa_w = 2\pi/\lambda$ is the wavenumber, and $\omega = 2\pi/\mathscr{T}$ is the wave frequency. The remaining terms in Eq. (4.8) are higher-order corrections to linear wave theory, whose details are given in [90]. The velocity and pressure solutions to the fifth-order Stokes wave can also be found in Fenton [90].

The (fifth-order) Stokes waves also satisfy the dispersion relationship given by Eq. (4.2). To calculate κ_w given ω, or vice versa, the explicit equation (4.3) can be used with sufficient accuracy in all water depth regimes [89].

4.2.2 Irregular sea waves

A realistic sea state consists of irregular waves. Mathematically, an irregular wave can be described as a linear superposition of a large number of (first-order) regular wave components. Using the superposition principle, the sea surface elevation can be expressed as

$$\eta(x,t) = \sum_{i=1}^{N_w} a_i \cos(\kappa_{wi} x - \omega_i t + \theta_i), \tag{4.9}$$

in which N_w is the number of (regular) wave components. Each wave component has its own amplitude $a_i = \mathscr{H}_i/2$, angular frequency ω_i, wavenumber κ_{wi}, and a random phase θ_i. Each component also satisfies the dispersion relation between κ_{wi} and ω_i given by Eq. (4.2). The random phase θ_i follows the uniform distribution in the interval $[0, 2\pi]$.

The linear superposition of first-order waves implies that the total energy carried by the irregular wave is the sum of wave energy carried by the individual wave components. To describe the energy content of irregular waves, a continuous wave spectral density function $S(\omega)$ is used, wherein the number of wave components N_w tend to infinity and an infinitesimal small frequency bandwidth $\mathrm{d}\omega$ separates the wave components. The area under the $S(\omega)$ versus ω curve gives the total energy of the irregular wave, modulo the factor $\rho_{\mathrm{w}} g$. Discretely, the wave frequencies are chosen at an equal interval of $\Delta\omega$ and the wave spectral density function $S(\omega)$ approaches zero for frequencies outside the narrow bandwidth. In this work, we consider only singly-peaked wave spectra with $S(\omega)$ peaking at a particular frequency ω_p. Each wave component of an irregular wave has a wave amplitude that is related to the spectral density function by

$$a_i = \sqrt{2 \cdot S(\omega_i) \cdot \Delta\omega}\,. \tag{4.10}$$

We consider the Joint North Sea Wave Project (JONSWAP) wave spectrum and two-parameter Bretschneider spectrum [65], which is suited for open seas where our WEC device is considered to be located. The JONSWAP wave spectrum is given by the relation

$$S(\omega) = \frac{320 \cdot \mathscr{H}_{\mathrm{s}}^2}{\mathscr{T}_{\mathrm{p}}^4} \cdot \omega^{-5} \cdot \exp\left(\frac{-1950}{\mathscr{T}_{\mathrm{p}}^4} \cdot \omega^{-4}\right) \cdot \gamma^A, \tag{4.11}$$

in which $\mathscr{H}_{\mathrm{s}}$ is the significant wave height, and $\mathscr{T}_{\mathrm{p}}$ is the peak time period, i.e., the time period

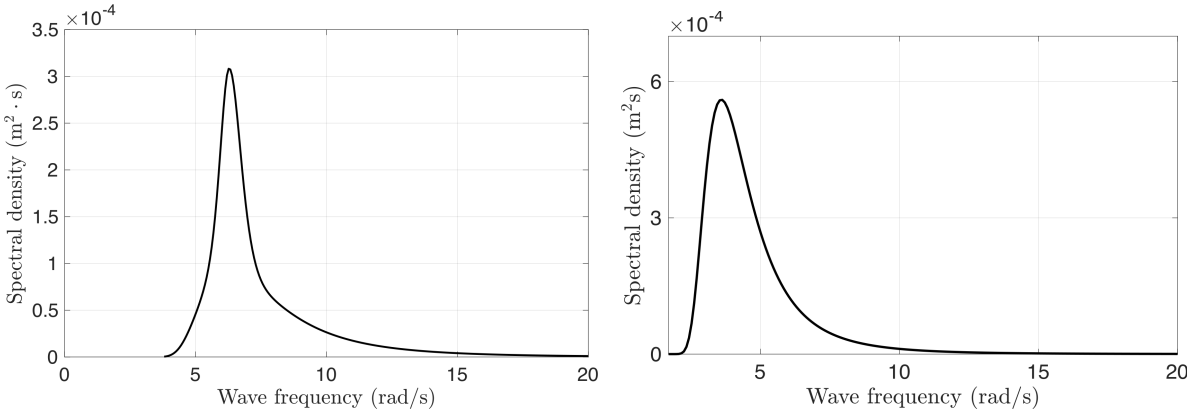

(a) The JONSWAP wave spectrum (b) The Bretschneider wave spectrum

Figure 4.2. Wave spectrum generated for (a) JONSWAP for wave with $\mathscr{H}_{\mathrm{s}} = 0.1$ m, and $\mathscr{T}_{\mathrm{p}} = 1$ s ($\omega_{\mathrm{p}} = 2\pi$ rad/s) and (b) Bretschneider for wave with $\mathscr{H}_s = 0.15$ m and $\mathscr{T}_p = 1.7475$ s ($\omega_p = 2\pi/\mathscr{T}_p = 3.5955$ rad/s.

with the highest spectral peak (see Fig. 4.2(a)). The remaining parameters in Eq. (4.11) are:

$$\gamma = 3.3 \qquad \text{(peakedness factor)} \tag{4.12}$$

$$A = \exp\left[-\left(\frac{\frac{\omega}{\omega_{\mathrm{p}}} - 1}{\sigma\sqrt{2}}\right)^2\right]$$

$$\omega_{\mathrm{p}} = \frac{2\pi}{\mathscr{T}_{\mathrm{p}}} \qquad \text{(angular frequency at spectral peak)} \tag{4.13}$$

$$\sigma = \begin{cases} 0.07 & \text{if} \quad \omega \leq \omega_{\mathrm{p}} \\ 0.09 & \text{if} \quad \omega > \omega_{\mathrm{p}} \end{cases} \tag{4.14}$$

The Bretschneider spectrum $S(\omega)$ is based on the significant wave height $\mathscr{H}_s$ and the peak wave time period $\mathscr{T}_p$ and it reads as

$$S(\omega) = \frac{173 \cdot \mathscr{H}_s^2}{\mathscr{T}_p^4} \cdot \omega^{-5} \cdot \exp\left(\frac{-692}{\mathscr{T}_p^4} \cdot \omega^{-4}\right). \tag{4.15}$$

The peak wave time period $\mathscr{T}_p$ is the time period with the highest spectral density in the spectrum (see Fig. 4.2(b)).

For irregular waves the mean wave power per unit crest width is calculated as

$$\overline{P}_{\text{wave}} = \rho_{\text{w}} g \left(\int_0^\infty S(\omega)\, \mathrm{d}\omega \right) c_g \approx \rho_{\text{w}} g \left(\sum_{i=1}^{N_w} \frac{1}{2} a_i^2 \right) c_g \tag{4.16}$$

in which the group velocity c_g is calculated from Eq. (4.5) using the significant wavelength and peak time period of the spectrum. In the deep water limit, Eq. (4.16) becomes

$$\overline{P}_{\text{wave}} \approx 0.49 \mathscr{H}_{\text{s}}^2 \mathscr{T}_p \text{ kW/m.} \qquad \text{(deep water limit)} \tag{4.17}$$

4.2.3 Wave steepness

The wave steepness (s) defined in Eq. (4.8), which gives a relation between the wave height $\mathscr{H}$ and wavelength λ. Consider the incoming wave as a regular (simple harmonic) wave with elevation $\eta(x,t)$ given by

$$\eta(x,t) = a \cdot \cos(\kappa_w x - \omega t), \tag{4.18}$$

where $a = \mathscr{H}/2$, is the wave amplitude. Differentiating the above equation with respect to x, we obtain

$$\frac{\mathrm{d}\eta(x,t)}{\mathrm{d}x} = a \cdot (-\kappa_w \sin(\kappa_w x - \omega t)). \tag{4.19}$$

The maximum wave steepness (i.e. the slope) is obtained when $\sin(\kappa_w x - \omega t) = -1$,

$$\left(\frac{\mathrm{d}\eta(x,t)}{\mathrm{d}x} \right)_{\max} = \kappa_w \cdot \frac{\mathscr{H}}{2} = s. \tag{4.20}$$

Finally, the maximum wave steepness angle is then given by

$$\delta_{\text{s}} = \tan^{-1} \left(\frac{\kappa_w \mathscr{H}}{2} \right) = \tan^{-1} \left(\frac{\pi \mathscr{H}}{\lambda} \right) \tag{4.21}$$

4.3 Numerical wave tank (NWT)

The wave-structure interaction of the WEC device is simulated in a numerical wave tank (NWT) as shown in Fig. 5.4. Water waves are generated at the left boundary of the domain using Dirichlet boundary conditions for the velocity components. The waves traveling in the positive x-direction are reflected back towards the inlet side from the device surface and also from the right boundary of the domain. This results in wave distortion and wave interference phenomena, which reduces the "quality" of waves reaching the device to study its performance. Several techniques have been proposed in the literature [91, 92, 93] to mitigate these effects, including the relaxation zone method [67], the active wave absorption method [94, 95, 96], the momentum damping method [97, 98], the viscous beach method [99], the porous media method [100, 101], and the mass-balance PDE method [102]. In this work, we use the relaxation zone method at inlet and outlet boundaries. The purpose of the relaxation zone near the channel inlet (the wave generation zone) is to smoothly extend the Dirichlet velocity boundary conditions into the wave tank up to a distance of one wavelength, so that the reflected waves coming from the ISWEC device do not interfere with the left boundary. In contrast, the relaxation zone near the right boundary (the wave damping zone) smoothly damps out the waves reaching the domain outlet near the right end. The wave damping zone is taken to be two wavelengths wide in our simulations. More details on the implementation of the relaxation zone method and level set based NWT can be found in [103].

We impose zero-pressure boundary condition at the channel top boundary, $z_{\max} = 2.75d$. To mitigate the interaction between shed vortices (due to the device motion) and the top boundary of the channel, we use a vorticity damping zone to dissipate the vortex structures reaching the boundary; see Fig. 5.4. The vorticity damping zone is implemented in terms of a damping force $\mathrm{f_d}$ in the momentum equation

$$\mathrm{f_d} = -g(\tilde{y})\mathbf{u}, \tag{4.22}$$

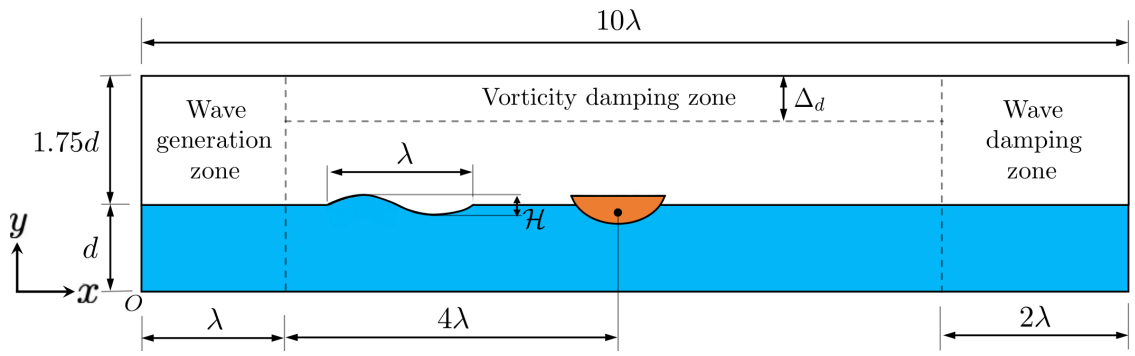

Figure 4.3. Numerical wave tank (NWT) schematic showing wave generation, wave damping, and vorticity damping zones. The ISWEC device is placed in the working zone of length 7λ.

in which, $g(\tilde{y}) = \rho_{\text{air}}\,(\cos(\pi\tilde{y})+1)/(4\Delta t)$ is the smoothed damping coefficient, ρ_{air} is the density of the air phase, Δt is the time step size, $\tilde{y} = (y - y_{\max})/\Delta_{\text{d}}$ is the normalized y coordinate, and Δ_{d} is the vorticity damping zone width, which is taken to be six cells wide in our simulations.

4.4 ISWEC device technology

The ISWEC device consists of a floating, boat-shaped hull that is slack-moored to the seabed, which internally houses a gyroscopic power take off unit (PTO); see Fig. 4.1. The ISWEC can be classified as a pitching point-absorber whose dimensions are shorter than the length of the water waves. The device utilizes precession effects produced from the spinning gyroscope and pitching hull to drive a sealed electric generator/PTO. The rotational velocity of the spinning gyroscope and the PTO control torque act as sea-state tuning parameters that can be optimized/controlled (in real-time or via remote human-machine interfaces) to enhance the conversion efficiency of the device. Since all crucial electro-mechanical parts are sealed within the hull, the ISWEC is a robust and cost-effective wave energy conversion technology. Due to its simple design, devices can be produced by retrofitting abandoned ships, which can potentially reduce manufacturing costs and lead to easy adoption of the technology. Moreover, such devices could be lined up end-to-end just offshore, which would not only ensure maximal wave energy absorption but also protection of the coastline.

Although ISWEC devices have only recently been prototyped since their inception in

2011 by Bracco et al. [85, 104, 105, 106, 107], their design and performance has been of much interest to the greater research community in the past few years. Medeiros and Brizzolara [108] used the boundary element method (BEM) based on linear potential flow equations to simulate the ISWEC and evaluate its power generation capabilities as a function of flywheel speed and derivative control of the PTO torque. They also demonstrated that the spinning gyroscopes can induce yaw torque on the hull. Faedo et al. [84] used an alternative moment-matching-based approach to model the radiation force convolution integral, thereby overcoming the computational and representational drawbacks of simulating ISWEC devices using the BEM-based Cummins equation [84]. Although these lower fidelity methods are able to simulate ISWEC dynamics at low computational costs, they are unable to resolve highly nonlinear phenomena often seen during practical operation such as wave-breaking and wave-overtopping. Unsurprisingly, the Turin group has extensively used carefully calibrated (with respect to wave tank experiments) BEM models to refine and optimize their preliminary designs [109, 110, 111, 112]. In contrast, simulations based on the incompressible Navier-Stokes (INS) equations are able to resolve the wave-structure interaction (WSI) quite accurately and without making small motion approximations employed by low-fidelity BEM models [113, 114]. However, fully-resolved INS simulations are computationally expensive and typically require high performance computing (HPC) frameworks. In a preliminary study, Bergmann et al. enabled fully-resolved simulation of the ISWEC's wave-structure interaction by making use of an INS-based flow solver coupled to an immersed boundary method [88]. The wave propagation in their channel followed the canonical "dam-break" problem setup [103] — a column of water is released from one end of the channel, which is then reflected from the opposite end, and so-forth. Although such simple wave propagation models are not suitable to study the device performance at a real site of operation, Bergmann et al. were nevertheless able to capture key device dynamics in their simulations. In addition to these research efforts, industry has become interested in piloting and manufacturing these devices. Recently, the multinational oil and gas corporation Eni installed an

ISWEC device off the coast of Ravenna [2] near their offshore assets. It is clear that there is a need to further investigate ISWEC dynamics and explore the design space to enable rapid adoption of this technology, possibly through an industry-academic partnership.

In this section, we perform a comprehensive study of the ISWEC device using high fidelity simulations from the developed fictitious domain Brinkman penalization (FD/BP) method based on the incompressible Navier-Stokes equations [38] described in Chpater 2. Although the methodology is similar to the work of Bergmann et al., we consider more realistic operating conditions by using a numerical wave tank (NWT) to generate both regular and irregular water waves. We conduct a systematic variation of control parameters (i.e. PTO control torque, flywheel moment of inertia and speed, hull length) to determine the optimal performance of the device (in term of power generation) and study its dynamics as a function of these parameters. We also provide a theoretical basis to obtain the optimal control parameters for the device's design at a specific installation site. Moreover, we analytically describe an energy transfer pathway from water waves to the hull, the hull to the gyroscope, and the gyroscope to the power take off (PTO) unit, and verify that it is numerically satisfied by our simulations. A Froude scaling analysis is performed to reduce the computational cost of simulating a full-scale ISWEC device, which is used to define the geometry and flow conditions for both two- and three-dimensional simulations of a scaled down 1:20 ISWEC device. Additionally, we verify that the 2D ISWEC model produced similar dynamics to the 3D model, thereby allowing us to obtain accurate results at reduced simulation cycle times. We also simulate a possible device protection strategy during inclement weather conditions and study the resulting dynamics.

4.4.1 ISWEC dynamics

Externally, the ISWEC device appears as a monolithic hull that is slack-moored to the seabed. Internally, the device houses a spinning gyroscopic system that drives a sealed electric generator. The pitching velocity of the hull is mainly responsible for converting the wave motion

[2] https://www.eni.com/en-IT/operations/iswec-eni.html

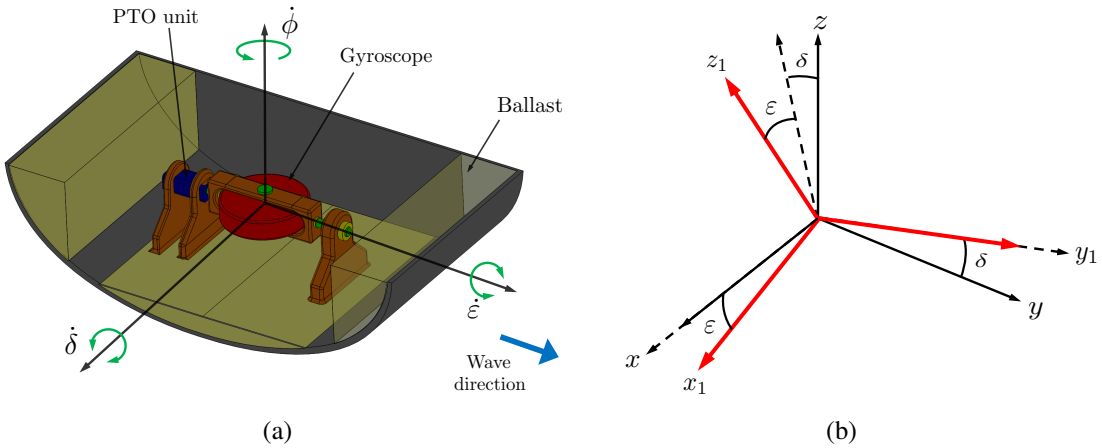

Figure 4.4. (a) ISWEC device schematic and the main rotational velocities of the system: hull's pitch velocity $\dot{\delta}$, gyroscope's angular velocity $\dot{\phi}$, and the induced precession velocity of the PTO shaft $\dot{\varepsilon}$. (b) Hull and gyroscope reference frames.

into electrical output. To simplify the model and discussion, the other remaining degrees of freedom of the hull are not considered in this study. As the device operates, the combination of wave induced pitching velocity $\dot{\delta}$ and spinning gyroscope/flywheel velocity $\dot{\phi}$ induces a precession torque in the ε coordinate direction [3]. The wave energy conversion is made possible by damping the motion along the ε-direction by the electric generator, which is commonly referred to as the power take-off (PTO) unit. Fig. 4.4(a) shows the schematic of the ISWEC device, including the external hull, ballast, gyroscope, and PTO unit.

To derive the three-way coupling between the waves, hull, and gyroscopic system we consider an inertial reference frame xyz attached to the hull and a rotating non-inertial reference frame $x_1y_1z_1$ attached to the gyroscope as shown in Fig. 4.4(b). The gyroscope reference frame is obtained from the hull reference frame by two subsequent finite rotations δ and ε. The origin of both reference frames is taken to be the center of gravity of the device.

In the absence of waves, $\delta = 0$ and $\varepsilon = 0$, and the flywheel rotates with a constant angular velocity $\dot{\phi}$ along the vertical z_1-axis. This configuration is taken to be the initial position of the device, in which the two reference frames also coincide. When the first wave reaches the hull

[3] Here, the definitions of δ, ϕ, and ε are different from that mentioned in Chapters 2 and 3

location, it tilts the device by an angle δ and the hull attains a pitching velocity $\dot{\delta}$ along the x-axis. The gyroscope structure rotates by the same angle δ about the x- (or the x_1-) axis. The rotated configuration of the $x_1y_1z_1$ reference frame is shown by dashed lines in Fig. 4.4(b). As the hull begins to pitch, the gyroscope is subject to two angular velocities: $\dot{\delta}$ along x_1-axis and $\dot{\phi}$ along z_1-axis. This velocity combination produces a precession torque in the third orthogonal direction y_1. This induced torque precesses the gyroscope by an angle ε about the y_1-axis. As a result of the two subsequent rotations, the gyroscope frame attains an orientation shown by bold red lines in Fig. 4.4(b).

The evolution of the gyroscope's dynamics results in a gyroscopic torque $\mathscr{M}_{\mathrm{G}} = (\mathscr{M}_{x_1}, \mathscr{M}_{y_1}, \mathscr{M}_{z_1})$, which can be related to the rotational kinematic variables using conservation of angular momentum. The angular velocity $\mathbf{\Omega}_1$ of the gyroscope reference frame and the angular velocity $\mathbf{\Omega}_{\mathrm{G}}$ of the gyroscope are both written in the $x_1y_1z_1$ coordinate system and their evolution can be expressed in terms of δ, ε, and $\dot{\phi}$ as

$$\Omega_1 = \dot{\delta}\cos\varepsilon\,\hat{i}_1 + \dot{\varepsilon}\,\hat{j}_1 + \dot{\delta}\sin\varepsilon\,\hat{k}_1, \tag{4.23}$$

$$\Omega_{\mathrm{G}} = \dot{\delta}\cos\varepsilon\,\hat{i}_1 + \dot{\varepsilon}\,\hat{j}_1 + (\dot{\delta}\sin\varepsilon + \dot{\phi})\,\hat{k}_1, \tag{4.24}$$

in which $\hat{i}_1$, $\hat{j}_1$, and $\hat{k}_1$ are the unit vectors along x_1-, y_1-, and z_1-directions, respectively. The rate of change of the gyroscope's angular momentum with respect to time is related to the gyroscopic torque $\mathscr{M}_{\mathrm{G}}$ by

$$\mathscr{M}_{\mathrm{G}} = \frac{\mathrm{dH_G}}{\mathrm{d}t}, \tag{4.25}$$

in which $\mathrm{H_G} = \mathbb{I}_{\mathrm{G}}\Omega_{\mathrm{G}}$ is the angular momentum of the gyroscope and $\mathbb{I}_{\mathrm{G}}$ is the inertia matrix of

the gyroscope. In the $x_1y_1z_1$ reference frame, $\mathbb{I}_{\mathrm{G}}$ reads as

$$\mathbb{I}_{\mathrm{G}} = \begin{bmatrix} I_{x_1x_1} & 0 & 0 \\ 0 & I_{y_1y_1} & 0 \\ 0 & 0 & I_{z_1z_1} \end{bmatrix} \approx \begin{bmatrix} I & 0 & 0 \\ 0 & I & 0 \\ 0 & 0 & J \end{bmatrix}. \tag{4.26}$$

The flywheel structure, including its support brackets etc., is typically designed such that $I_{x_1x_1} \approx I_{y_1y_1} = I$ and $I_{z_1z_1} = J \gtrapprox I$. Using Eqs. (4.24) and (4.26), the angular momentum of the flywheel is given by

$$\mathrm{H}_{\mathrm{G}} = I\dot{\delta}\cos\varepsilon\,\hat{i}_1 + I\dot{\varepsilon}\,\hat{j}_1 + J(\dot{\delta}\sin\varepsilon + \dot{\phi})\,\hat{k}_1. \tag{4.27}$$

Differentiating Eq. (4.27) with respect to time in the inertial reference frame involves computing time derivatives of the unit vectors $\hat{i}_1$, $\hat{j}_1$, and $\hat{k}_1$:

$$\frac{\mathrm{d}\hat{i}_1}{\mathrm{d}t} = \Omega_1 \times \hat{i}_1 = -\dot{\varepsilon}\,\hat{k}_1 + \dot{\delta}\sin\varepsilon\,\hat{j}_1, \tag{4.28}$$

$$\frac{\mathrm{d}\hat{j}_1}{\mathrm{d}t} = \Omega_1 \times \hat{j}_1 = \dot{\delta}\cos\varepsilon\,\hat{k}_1 - \dot{\delta}\sin\varepsilon\,\hat{i}_1, \tag{4.29}$$

$$\frac{\mathrm{d}\hat{k}_1}{\mathrm{d}t} = \Omega_1 \times \hat{k}_1 = -\dot{\delta}\cos\varepsilon\,\hat{j}_1 + \dot{\varepsilon}\,\hat{i}_1. \tag{4.30}$$

Finally after some algebraic simplification, a component-wise expression for the gyroscopic torque $\mathscr{M}_{\mathrm{G}}$ is obtained

$$\mathscr{M}_{\mathrm{G}} = \begin{bmatrix} \mathscr{M}_{x_1} \\ \mathscr{M}_{y_1} \\ \mathscr{M}_{z_1} \end{bmatrix} = \begin{bmatrix} I\ddot{\delta}\cos\varepsilon + (J-2I)\,\dot{\delta}\dot{\varepsilon}\sin\varepsilon + J\dot{\phi}\dot{\varepsilon} \\ I\ddot{\varepsilon} + (I-J)\dot{\delta}^2\sin\varepsilon\cos\varepsilon - J\dot{\phi}\dot{\delta}\cos\varepsilon \\ J\ddot{\delta}\sin\varepsilon + J\dot{\delta}\dot{\varepsilon}\cos\varepsilon + J\ddot{\phi} \end{bmatrix}. \tag{4.31}$$

The precession velocity $\dot{\varepsilon}$ of the generator shaft is damped using a proportional derivative (PD) control law implemented in the PTO unit. The PD control torque can be modeled as a

spring-damper system with the following form

$$\mathscr{M}_{\varepsilon} = \mathscr{M}_{\mathrm{G}} \cdot \hat{j}_1 = -k\varepsilon - c\dot{\varepsilon}. \tag{4.32}$$

Here, k is a spring-like stiffness parameter and c is a damper-like dissipation parameter that can be adjusted in real-time (usually through feedback) to enhance the conversion efficiency of the device when the incoming waves change their characteristics. The wave power absorbed by the PTO unit (as a function of time) is

$$P_{\mathrm{PTO}} = c\dot{\varepsilon}^2. \tag{4.33}$$

Therefore, the precession component of the gyroscopic torque is balanced by the PD control torque, $\mathscr{M}_{y_1} = \mathscr{M}_{\varepsilon}$, which is also responsible for extracting the wave energy. The other components $\mathscr{M}_{x_1}$ and $\mathscr{M}_{z_1}$ of the gyroscopic torque are balanced/sustained by the hydrodynamic torques acting on the hull and the subsequent hull-gyroscope interactions. To understand this balance, we consider the hydrodynamic torque and motion of the hull about the pitch (x-direction) as observed from the inertial reference frame xyz

$$\mathscr{M}_{\mathrm{hydro}} = I_{\mathrm{H}} \frac{\mathrm{d}\dot{\delta}}{\mathrm{d}t} + \mathscr{M}_{\delta}, \tag{4.34}$$

in which $\mathscr{M}_{\mathrm{hydro}}$ is the hydrodynamic torque acting on the hull, I_{H} is the moment of inertia of the hull, and $\mathscr{M}_{\delta}$ is the projection of the gyroscopic torque on the x-axis:

$$\begin{aligned}
\mathscr{M}_{\delta} &= \mathscr{M}_{\mathrm{G}} \cdot \hat{i} \\
&= \mathscr{M}_{\mathrm{G}} \cdot (\hat{i}_1 \cos\varepsilon + \hat{k}_1 \sin\varepsilon) \\
&= (J\sin^2\varepsilon + I\cos^2\varepsilon)\ddot{\delta} + J\dot{\phi}\dot{\varepsilon}\cos\varepsilon + 2(J-I)\dot{\delta}\dot{\varepsilon}\sin\varepsilon\cos\varepsilon + J\ddot{\phi}\sin\varepsilon.
\end{aligned} \tag{4.35}$$

From Eq. (4.34) it can be seen that the gyroscopic reaction $\mathscr{M}_{\delta}$ acting on the hull opposes the wave induced pitching motion. Similarly, a second reaction torque $\mathscr{M}_{\phi}$ acts on the hull along the

z-direction and opposes its wave induced yaw motion:

$$\begin{aligned}
\mathscr{M}_{\phi} &= \mathscr{M}_{\mathrm{G}} \cdot \hat{k} \\
&= \mathscr{M}_{\mathrm{G}} \cdot \left[(\hat{k}_1 \cos\varepsilon - \hat{i}_1 \sin\varepsilon)\cos\delta + \hat{j}_1 \sin\delta \right] \\
&= \left[(J-I)\ddot{\delta}\sin\varepsilon\cos\varepsilon + \dot{\delta}\dot{\varepsilon}[J(\cos^2\varepsilon - \sin^2\varepsilon) + 2I\sin^2\varepsilon] - J\dot{\phi}\dot{\varepsilon}\sin\varepsilon + J\ddot{\phi}\cos\varepsilon \right]\cos\delta \\
&+ \left[I\ddot{\varepsilon} + (I-J)\dot{\delta}^2\sin\varepsilon\cos\varepsilon - J\dot{\phi}\dot{\delta}\cos\varepsilon \right]\sin\delta
\end{aligned} \tag{4.36}$$

In Sec. **??**, we show that this yaw torque is the same order of magnitude as the pitch torque $\mathscr{M}_{\delta}$. In practice, however, its contribution is partially cancelled out by the mooring system of the device. Moreover, using an even number of gyroscopic units will cancel the yaw component of the gyroscopic torque acting on the hull if each flywheel pair spins with equal and opposite velocity, as described by Raffero [115]. Therefore, we do not consider the effect of $\mathscr{M}_{\phi}$ on the ISWEC dynamics in our (3D) model.

4.4.2 Power transfer from waves to PTO

To understand the power transfer from waves to the hull and from the hull to the PTO unit, we derive the time-averaged kinetic energy equations of the ISWEC system. These equations highlight the coupled terms that are responsible for wave energy conversion through the ISWEC device.

First, we consider the rotation of the gyroscope around the PTO axis. The equation of motion in the ε coordinate direction, as derived in the previous section is re-written below

$$I\ddot{\varepsilon} + (I-J)\dot{\delta}^2\sin\varepsilon\cos\varepsilon - J\dot{\phi}\dot{\delta}\cos\varepsilon = \mathscr{M}_{\varepsilon} = -k\varepsilon - c\dot{\varepsilon}. \tag{4.37}$$

Rearranging Eq. (4.37) with the approximation $I \approx J$ simplifies the equation to

$$I\ddot{\varepsilon} + c\dot{\varepsilon} + k\varepsilon = J\dot{\phi}\dot{\delta}\cos\varepsilon. \tag{4.38}$$

From the above equation, it can be seen that the product of the hull's pitch velocity $\dot{\delta}$ and the gyroscope's angular velocity $\dot{\phi}$ yields a forcing term that drives the PTO motion. Multiplying Eq. (4.38) by the precession velocity $\dot{\varepsilon}$ and rearranging some terms, we obtain the kinetic energy equation for the PTO dynamics

$$I\frac{\mathrm{d}}{\mathrm{d}t}\left(\frac{\dot{\varepsilon}^2}{2}\right)+c\dot{\varepsilon}^2+k\frac{\mathrm{d}}{\mathrm{d}t}\left(\frac{\varepsilon^2}{2}\right)=J\dot{\phi}\dot{\delta}\dot{\varepsilon}\cos\varepsilon. \tag{4.39}$$

Taking the time-average of Eq. (4.39) over one wave period, the first and third terms on the left hand side of the equation evaluate to zero. The remaining terms describe the transfer of power from the hull to the PTO unit:

$$\langle c\dot{\varepsilon}^2\rangle=\langle J\dot{\phi}\dot{\delta}\dot{\varepsilon}\cos\varepsilon\rangle, \tag{4.40}$$

in which $\langle\cdot\rangle=\frac{1}{\mathscr{T}}\int_t^{t+\mathscr{T}}(.)\,\mathrm{d}t$ represents the time-average of a quantity over one wave period $\mathscr{T}$ [4]. Here, $\langle c\dot{\varepsilon}^2\rangle$ is the average power absorbed by the PTO, denoted $\bar{P}_{\mathrm{PTO}}$, and $\langle J\dot{\phi}\dot{\delta}\dot{\varepsilon}\cos\varepsilon\rangle$ is the average power generated due to the gyroscopic motion through its interaction with the hull, denoted $\bar{P}_{\mathrm{gyro}}$. Similarly, the kinetic energy equation of the hull can be derived by multiplying hull dynamics Eq. (4.34) by the pitch velocity $\dot{\delta}$

$$\mathscr{M}_{\mathrm{hydro}}\dot{\delta}=I_{\mathrm{H}}\ddot{\delta}\dot{\delta}+\mathscr{M}_{\delta}\dot{\delta}. \tag{4.41}$$

Under the assumptions $I\approx J$ and a constant gyroscope spinning speed, $\mathscr{M}_{\delta}$ in Eq. (4.35) simplifies to

$$\mathscr{M}_{\delta}=J\ddot{\delta}+J\dot{\phi}\dot{\varepsilon}\cos\varepsilon. \tag{4.42}$$

Using Eqs. (4.41) and (4.42), and rearranging some terms, we obtain

$$\mathscr{M}_{\mathrm{hydro}}\dot{\delta}=I_{\mathrm{H}}\frac{\mathrm{d}}{\mathrm{d}t}\left(\frac{\dot{\delta}^2}{2}\right)+J\frac{\mathrm{d}}{\mathrm{d}t}\left(\frac{\dot{\delta}^2}{2}\right)+J\dot{\phi}\dot{\delta}\dot{\varepsilon}\cos\varepsilon. \tag{4.43}$$

[4] For irregular waves the time-average could be defined over one significant wave period.

Taking the time-average of Eq. (4.43) over one wave period, the first and second terms on the right hand side evaluate to zero, and the expression reads

$$\langle \mathscr{M}_{\text{hydro}} \dot{\delta} \rangle = \langle J \dot{\phi} \dot{\delta} \dot{\varepsilon} \cos \varepsilon \rangle. \tag{4.44}$$

Here, $\langle \mathscr{M}_{\text{hydro}} \dot{\delta} \rangle$ is power transferred from the waves to the hull, denoted $\bar{P}_{\text{hull}}$, and $\langle J \dot{\phi} \dot{\delta} \dot{\varepsilon} \cos \varepsilon \rangle$ is the same expression on the right side of Eq. (4.40). Hence, combining Eqs. (4.40) and (4.44), we obtain an equation describing the pathway of energy transfer from waves to the PTO:

$$\underbrace{\langle \mathscr{M}_{\text{hydro}} \dot{\delta} \rangle}_{\text{waves}\rightarrow\text{hull}} = \underbrace{\langle J \dot{\phi} \dot{\delta} \dot{\varepsilon} \cos \varepsilon \rangle}_{\text{hull}\rightarrow\text{gyroscope}} = \underbrace{\langle c \dot{\varepsilon}^2 \rangle}_{\text{gyroscope}\rightarrow\text{PTO}}, \tag{4.45}$$

which is written succinctly as $\bar{P}_{\text{hull}} = \bar{P}_{\text{gyro}} = \bar{P}_{\text{PTO}}$. Eq. (4.45) is quantitatively verified for the ISWEC model under both regular and irregular wave environments in Sec. 5.11.

4.4.3 PTO and gyroscope parameters

The energy transfer equation can be used to select the PTO and gyroscope parameters that achieve a rated power of the installed device $\bar{P}_{\text{R}}$. From Eq. (4.45)

$$c = \frac{\bar{P}_{\text{R}}}{\langle \dot{\varepsilon}^2 \rangle} = \frac{2\bar{P}_{\text{R}}}{\dot{\varepsilon}_0^2}, \tag{4.46}$$

in which $\dot{\varepsilon}_0$ is the amplitude of the precession velocity, expressed in terms of the amplitude of the precession angle ε_0 as $\dot{\varepsilon}_0 = \varepsilon_0 \omega$. Here, we assume that all of the ISWEC components are excited at the external wave frequency $\omega = 2\pi/\mathscr{T}$ to achieve optimal performance. Based on experimental data of real ISWEC devices [86, 87], we prescribe ε_0 in the range $40^\circ \leq \varepsilon_0 \leq 80^\circ$ to obtain the damping parameter c from Eq. (4.46). To prescribe the rest of the gyroscope parameters, we make use of Eq. (4.40). Since this expression is nonlinear, we linearize it about $\varepsilon = 0^\circ$ (a reasonable approximation for relatively calm conditions) to estimate the gyroscope

angular momentum as

$$J\dot{\phi} = \frac{c\varepsilon_0}{\delta_0}, \tag{4.47}$$

in which the amplitude of the hull pitch velocity $\dot{\delta}_0 = \delta_0\omega$, expressed in terms of the amplitude of the hull pitch angle δ_0, is used. Again based on the experimental data, we prescribe δ_0 in the range $2^\circ \leq \delta_0 \leq 20^\circ$, and $\dot{\phi}$ in the range $250 \leq \dot{\phi} \leq 1000$ RPM [5] to obtain the J value of the gyroscope from Eq. (4.47). The I value of the gyroscope is set as a scaled value of J, i.e. $I = \gamma J$ where $\gamma \leq 1$. We study the effect of varying γ in Sec. 4.7.2.

The only remaining free parameter is the PTO stiffness k used in the control torque. We make use of reactive control theory [69] and prescribe k as

$$k = \omega^2 I, \tag{4.48}$$

ensuring that the gyroscopic system oscillates at the wave frequency around the PTO axis. Using the linearized version of Eq. (4.38), it can be shown that if the gyroscope oscillates with the external wave forcing frequency, a resonance condition is achieved along the PTO axis and the output power is maximized [69]. In this state, both the hull and gyroscopic systems oscillate at the external wave frequency and their coupling is maximized.

4.4.4 Hull shape

The ISWEC's external hull is a boat-shaped vessel, which we idealize by a half-cylinder of length L, height H, and width W. For the actual device, a part of the outer periphery is flattened out to ease the installation of mechanical and electrical parts near the bottom-center location (see Fig. 4.5(b)). We neglect these geometric details in our model shown in Fig. 4.5(a). The inside of the device is mostly hollow and the buoyancy-countering ballast is placed around the outer periphery.

[5] This range of $\dot{\phi}$ is for the full-scale ISWEC device, which can be scaled by an appropriate factor for the scaled-down model. See Sec. **??** for scaling analyses.

The hull length L is a function of λ, the wavelength of the "design" wave at device installation site. As analyzed by Cagninei et al. [86], the optimal hull length is between $\lambda/3 \leq L \leq \lambda/2$ for an ISWEC device that is mainly excited in the pitch direction. The hull width W is decided based on the rated power of the installed device $\bar{P}_{\mathrm{R}}$, relative capture width (RCW) of the device (or the device conversion efficiency) η, and wave power per unit crest width $\bar{P}_{\mathrm{wave}}$. These quantities are related through the expressions

$$W = \frac{\bar{P}_{\mathrm{R}}}{\eta \cdot \bar{P}_{\mathrm{wave}}} \qquad \text{and} \qquad \eta = \bar{P}_{\mathrm{PTO}}/\bar{P}_{\mathrm{wave}}, \tag{4.49}$$

in which $\bar{P}$ denotes time-averaged power. Sec. **??** provides closed-form expressions of $\bar{P}_{\mathrm{wave}}$ for both regular and irregular waves. For the 2D ISWEC model we use $W = 1$, which corresponds to a unit crest width of the wave.

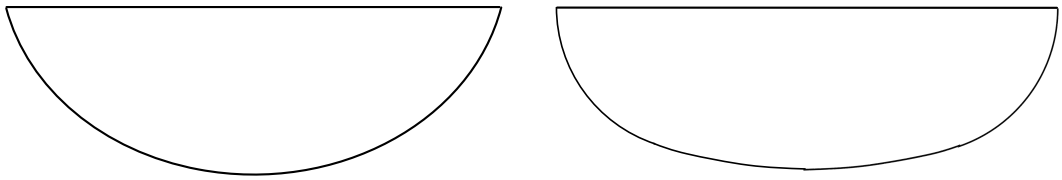

(a) Idealized ISWEC hull geometry (b) Experimental ISWEC hull geometry

Figure 4.5. ISWEC hull shapes.

4.4.5 Scaled ISWEC model and scaled hull parameters

Scaled ISWEC model

In order to reduce the computational cost of simulating a full-scale ISWEC device operating in high Reynolds number (Re) regimes, we use Froude scaling [65] to scale the model problem down by a 1:20 ratio. The Froude number (Fr) measures the resistance of a partially submerged object moving through water and is defined as

$$\mathrm{Fr} = \frac{\text{characteristic velocity}}{\text{gravitational wave velocity}} = \frac{U_{\mathrm{c}}}{\sqrt{gL_{\mathrm{c}}}}, \tag{4.50}$$

in which U_c is the characteristic velocity, L_c is the characteristic length, and g is the gravitational acceleration constant. In offshore marine hydromechanics, Froude scaling allows us to compare the dynamics of two vessels even if their sizes are different (since they produce a similar wake). Two vessels having the same Froude number may not be operating in the same Reynolds number regime. In the present study, the scaled-down model operates in lower Re conditions and it does not capture fine scale details such as extreme wave breaking and spray dynamics that occur at higher Reynolds numbers. These small scale features are mostly dictated by viscous and surface tension effects, and a very fine computational mesh is needed to adequately resolve them. However, the main quantities of interest such as power generated for the full-scale device can be inferred from scaled-down simulations by using appropriate scaling factors, some of which we derive next.

- Length scaling: The geometric parameters such as length, width or height are simply scaled by a factor of α[6]. In the present study, we use $\alpha = 20$. An exception to this length scaling is hull width in 2D, which is taken to be unity in the scaled model. Therefore in 2D, the scaling factor for hull width is W rather than α.

- Acceleration scaling: The full-scale and scaled-down models operate under the same gravitational force field. Therefore, the gravitational constant g (or any other acceleration) remains unchanged.

- Density scaling: Density is an intrinsic material property, and thus it remains the same for both the full-scale and scaled-down models.

- Volume scaling: Since volume is proportional to the length cubed, it is scaled by α^3.

- Mass scaling: Mass can be expressed as a product of density ρ and volume, and its scaling

[6]The definition of α here is different from the one used in Chapter 2

for 2D and 3D ISWEC models are obtained as

$$\frac{M_{\text{model}}}{M_{\text{full-scale}}} = \frac{\rho\left(L\times H\times W\right)\big|_{\text{model}}}{\rho\left(L\times H\times W\right)\big|_{\text{full-scale}}} = \frac{W_{\text{model}}}{\alpha^2\cdot W_{\text{full-scale}}}. \tag{4.51}$$

- Velocity scaling: Velocity scaling is obtained by equating the Froude numbers

$$\left.\frac{U_{\text{c}}}{\sqrt{gL_{\text{c}}}}\right|_{\text{model}} = \left.\frac{U_{\text{c}}}{\sqrt{gL_{\text{c}}}}\right|_{\text{full-scale}} \tag{4.52}$$

$$\Rightarrow \frac{U_{\text{c,model}}}{U_{\text{c,full-scale}}} = \sqrt{\frac{L_{\text{c,model}}}{L_{\text{c,full-scale}}}} = 1/\alpha^{\frac{1}{2}}. \tag{4.53}$$

- Time scaling: Letting t_{c} represent a characteristic time, time scaling can be obtained from the length and velocity scalings as

$$\frac{U_{\text{c,model}}}{U_{\text{c,full-scale}}} = \frac{\left.L_{\text{c}}/t_{\text{c}}\right|_{\text{model}}}{\left.L_{\text{c}}/t_{\text{c}}\right|_{\text{full-scale}}} \tag{4.54}$$

$$\Rightarrow \frac{t_{\text{c,model}}}{t_{\text{c,full-scale}}} = 1/\alpha^{\frac{1}{2}}. \tag{4.55}$$

Similarly, scaling factors of other quantities of interest such as force and power can be obtained in terms of α, and are enumerted in Table 4.1 for both two and three spatial dimensions. Full-scale (scaled-down) quantities should be divided (multiplied) by factors in the third and fourth columns to obtain the scaled-down (full-scale) quantities, in three and two spatial dimensions, respectively.

Scaled hull parameters

We use the Froude scaling to derive the scaled-down hull parameters required for our simulations. The scaled-down parameters of the gyroscope will be presented in Sec. 5.11, where they are systematically varied to study their effect on device performance. The hull properties of the full-scale ISWEC device are taken from an experimental campaign [86, 87] conducted at the

Table 4.1. Froude scaling of various quantities for the 3D and 2D ISWEC models. Dimensional units for the quantities used in this work are shown in column 2.

Quantity	Units	Scaled 3D model	Scaled 2D model
Length	m	α	α
Area	m^2	α^2	α^2
Volume	m^3	α^3	–
Time	s	$\alpha^{\frac{1}{2}}$	$\alpha^{\frac{1}{2}}$
Velocity	m/s	$\alpha^{\frac{1}{2}}$	$\alpha^{\frac{1}{2}}$
Acceleration	m/s^2	1	1
Frequency	s^{-1}	$\alpha^{-\frac{1}{2}}$	$\alpha^{-\frac{1}{2}}$
Angular velocity	s^{-1}	$\alpha^{-\frac{1}{2}}$	$\alpha^{-\frac{1}{2}}$
Mass	kg	α^3	$\alpha^2 \cdot W$
Density	kg/m^3	1	1
Force	$kg \cdot m/s^2$	α^3	$\alpha^2 \cdot W$
Moment of inertia	$kg \cdot m^2$	α^5	$\alpha^4 \cdot W$
Torque	$kg \cdot m^2/s^2$	α^4	$\alpha^3 \cdot W$
Power	$kg \cdot m^2/s^3$	$\alpha^{\frac{7}{2}}$	$\alpha^{\frac{5}{2}} \cdot W$

Pantelleria test site in the Mediterranean Sea.

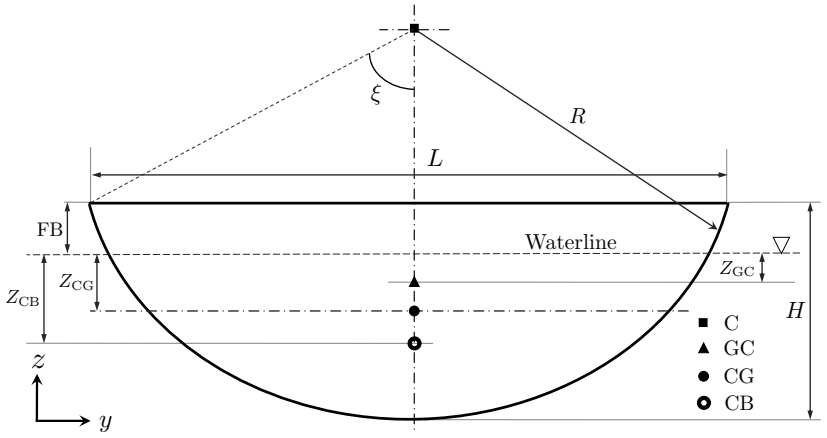

Figure 4.6. Hull geometry with properties: $L = 0.7665$ m, $H = 0.225$ m, $R = 0.4389$ m and $\xi = 60.83°$.

The scaled-down (1:20) values of the hull properties are tabulated in Table 4.2. To verify that the scaled-down values correlate well to the model geometry, we perform geometric estimation of the hull properties by assuming the hull to be a filled sector of a circle in two spatial dimensions. The geometric center (GC) and the center of buoyancy (CB) of the submerged sector

Table 4.2. ISWEC hull full-scale and scaled-down parameters. Freeboard (FB) is the distance between the hull top surface and the still waterline, which is found experimentally.

Hull property	Notation	Units	Full-scale	Scaled-down	
				3D model	2D model
Length	L	m	15.33	0.7665	0.7665
Height	H	m	4.5	0.225	0.225
Width	W	m	8	0.4	1
Freeboard	FB	m	1.52	0.076	0.076
Center of gravity	Z_{CG}	m	0.57	0.0285	0.0285
Mass	M_{H}	kg	288000	36	90
Pitch moment of inertia	I_{H}	$\mathrm{kg}\cdot\mathrm{m}^2$	7.712×10^6	2.41	6.025

can be calculated geometrically, and are found to be located at a distance Z_{GC} = 0.0163 m and Z_{CB} = 0.0605 m below the still waterline, respectively (see Fig. 4.6). From Table 4.2, the scaled distance between the center of gravity of the device and waterline is Z_{CG} = 0.0285 m. It can be seen that the CB lies below the CG and GC, satisfying the stability condition for floating bodies. Additionally CG lies below GC because in the real device, more mass is distributed towards the lower half portion.

Similarly, the scaled-down moment of inertia of the hull I_{H} can be argued geometrically. We first estimate the density of the hull from the scaled mass (90 kg) and the area of the sector (0.1225 m^2) to be $\rho_{\mathrm{estimate}} = 734.69\ \mathrm{kg/m}^3$. Then we use ρ_{estimate} to calculate the moment of inertia of the filled sector about its geometric center as I_{GC} = 3.1768 $\mathrm{kg}\cdot\mathrm{m}^2$. In the real device, most of the mass is concentrated along the outer periphery, resembling a ring rather than a filled sector. Since, the moment of inertia of a ring is twice as that of a filled circle, $I_{\mathrm{estimate}} \approx 2I_{\mathrm{GC}} = 6.3536\ \mathrm{kg}\cdot\mathrm{m}^2$, which is close to what we obtain from Table 4.2.

4.4.6 Coupling ISWEC dynamics to the FSI solver

We simplify the treatment of the FSI coupling by only considering immersed bodies with a single unlocked rotational degree of freedom (DOF); a more general approach is described in Bhalla et al. [38]. The Brinkman penalization term is treated implicitly and computed as

(rewriting Eq. (3.9))

$$\mathrm{f}_{\mathrm{c}}^{n+1,k+1} = \frac{\widetilde{\chi}}{\kappa}\left(\mathbf{u}_{\mathrm{b}}^{n+1,k+1} - \mathbf{u}^{n+1,k+1}\right), \tag{4.56}$$

A permeability value of $\kappa \sim \mathscr{O}(10^{-8})$ has been shown to be sufficiently small enough to effectively enforce the rigidity constraint [40, 38, 116]. For the ease of reading, rewriting the solid body velocity Eq. (5.35).

$$\mathbf{u}_{\mathrm{b}}^{n+1,k+1} = \mathbf{U}_{\mathrm{r}}^{n+1,k+1} + \mathbf{W}_{\mathrm{r}}^{n+1,k+1} \times \left(\mathbf{x} - \mathbf{X}_{\mathrm{com}}^{n+1,k+1}\right) \tag{4.57}$$

For the pitching ISWEC device, $\mathbf{U}_{\mathrm{r}} = 0$.

$$\mathbf{u}_{\mathrm{b}}^{n+1,k+1} = \mathbf{W}_{\mathrm{r}}^{n+1,k+1} \times \left(\mathbf{x} - \mathbf{X}_{\mathrm{com}}^{n+1,k+1}\right). \tag{4.58}$$

Moreover, two of the rotational DOFs are locked, i.e. they are constrained to zero. Hence, the expression for $\mathbf{W}_{\mathrm{r}}$ can be simplified even further,

$$\mathbf{W}_{\mathrm{r}}^{n+1,k+1} = \left(\dot{\delta}^{n+1,k+1}, 0, 0\right), \tag{4.59}$$

in which $\dot{\delta}$ is the rotational velocity of the structure about its pitch axis.

The rigid body velocity can be computed by integrating Newton's second law of motion for the pitch axis rotational velocity:

$$I_{\mathrm{H}} \frac{\dot{\delta}^{n+1,k+1} - \dot{\delta}^{n}}{\Delta t} = \mathscr{M}_{\mathrm{hydro}}^{n+1,k} - \mathscr{M}_{\delta}^{n+1,k}, \tag{4.60}$$

in which I_{H} is the moment of inertia of the hull, $\mathscr{M}_{\mathrm{hydro}}$ is the net hydrodynamic torque, and $\mathscr{M}_{\delta}^{n+1,k}$ is the projection of the gyroscopic torque about the x-axis. The net hydrodynamic torque is computed by summing the contributions from pressure and viscous forces acting on the hull

and taking the pitch component

$$\mathscr{M}_{\text{hydro}} = \hat{i} \cdot \left[\sum_{\text{f}} \left(\mathbf{x} - \mathbf{X}_{\text{com}}^{n+1,k} \right) \times \left(-p^{n+1,k} \mathbf{n}_{\text{f}} + \mu_{\text{f}} \left(\nabla_h \mathbf{u}^{n+1,k} + \left(\nabla_h \mathbf{u}^{n+1,k} \right)^T \right) \cdot \mathbf{n}_{\text{f}} \right) \Delta A_{\text{f}} \right]. \tag{4.61}$$

The hydrodynamic traction in the above equation is evaluated on Cartesian grid faces near the hull that define a stair-step representation of the body on the Eulerian mesh [38], with $\mathbf{n}_{\text{f}}$ and ΔA_{f} representing the unit normal vector and the area of a given cell face, respectively. The computation of the gyroscopic action $\mathscr{M}_{\delta}$ is described in the following section.

The ISWEC is allowed to freely rotate about its pitch axis and its motion depends on the hydrodynamic and external torques acting on it. The external torque $\mathscr{M}_{\delta}$ generated by the gyroscopic action is unloaded on the hull and *opposes* the wave induced pitching motion. Therefore, $\mathscr{M}_{\delta}$ appears with negative sign on the right side of Eq. (4.60). The analytical expression for this pitch torque is given by Eq. (4.35), while its discretization is written as

$$\begin{aligned} \mathscr{M}_{\delta}^{n+1,k} = & \left(J \sin^2 \varepsilon^{n+1,k} + I \cos^2 \varepsilon^{n+1,k} \right) \ddot{\delta}^{n+1,k} + J \dot{\phi} \dot{\varepsilon}^{n+1,k} \cos \varepsilon^{n+1,k} \\ & + 2 (J - I) \dot{\delta}^{n+1,k} \dot{\varepsilon}^{n+1,k} \sin \varepsilon^{n+1,k} \cos \varepsilon^{n+1,k} + J \ddot{\phi} \sin \varepsilon^{n+1,k}, \end{aligned} \tag{4.62}$$

in which the pitch acceleration term $\ddot{\delta}^{n+1,k}$ is calculated using a standard finite difference (explicit forward Euler) of the hull's pitch velocity:

$$\ddot{\delta}^{n+1,k} = \begin{cases} \frac{\dot{\delta}^{n+1,k} - \dot{\delta}^{n}}{\Delta t}, & k > 0, \\ \\ \frac{\dot{\delta}^{n} - \dot{\delta}^{n-1}}{\Delta t}, & k = 0. \end{cases} \tag{4.63}$$

We set $\delta^{n+1,0} = \delta^n$, $\varepsilon^{n+1,0} = \varepsilon^n$, $\dot{\delta}^{n+1,0} = \dot{\delta}^n$, and $\dot{\varepsilon}^{n+1,0} = \dot{\varepsilon}^n$ for cycle $k = 0$.

The precession acceleration $\ddot{\varepsilon}$ is given analytically by Eq. (4.37), which in discretized form reads

$$\ddot{\varepsilon}^{n+1,k} = \frac{1}{I}\left[-k\varepsilon^{n+1,k-1} - c\dot{\varepsilon}^{n+1,k-1} - (I-J)\left(\dot{\delta}^{n+1,k}\right)^2 \sin\varepsilon^{n+1,k-1}\cos\varepsilon^{n+1,k-1}\right] + \frac{J}{I}\dot{\phi}\,\dot{\delta}^{n+1,k}\cos\varepsilon^{n+1,k-1}. \tag{4.64}$$

This newest approximation to the precession acceleration $\ddot{\varepsilon}^{n+1,k}$ is explicitly calculated using only the *prior* cycle's values of precession velocity $\dot{\varepsilon}^{n+1,k-1}$ and angle $\varepsilon^{n+1,k-1}$. New approximations to $\dot{\varepsilon}$ and ε at cycle k are computed using the Newmark-β method [117] as follows:

$$\dot{\varepsilon}^{n+1,k} = \dot{\varepsilon}^{n} + \frac{\Delta t}{2}\left(\ddot{\varepsilon}^{n} + \ddot{\varepsilon}^{n+1,k}\right) \tag{4.65}$$

$$\varepsilon^{n+1,k} = \varepsilon^{n} + \Delta t\,\dot{\varepsilon}^{n} + \frac{\Delta t^2}{4}\left(\ddot{\varepsilon}^{n} + \ddot{\varepsilon}^{n+1,k}\right) \tag{4.66}$$

As described in Sec. 4.4, the PTO stiffness k and damping c parameters in the control torque and the gyroscope's angular velocity $\dot{\phi}$, acceleration $\ddot{\phi} = 0$, and moments of inertia I and J are known *a priori* and do not represent additional unknowns in the calculation of $\mathscr{M}_{\delta}^{n+1,k}$. Hence the procedure outlined by Eqs. (4.62) to (4.66) enables the calculation of the external pitch torque shown on the right-hand side of Eq. (4.60), thus coupling the ISWEC dynamics to the FD/BP methodology.

4.5 FSI validation

To validate our implementation of the method described in the Sec. 4.4.6, we simulate the vortex induced vibration of a rectangular plate undergoing galloping motion. This single rotational degree of freedom case has been widely used as a benchmark problem for FSI algorithms in prior literature. It also mimics the ISWEC model well, which primarily oscillates

Table 4.3. Comparison of maximum pitch angle $\vartheta_{\max}$ and galloping frequency f_ϑ with prior numerical studies.

Study	$\vartheta_{\max}$	f_ϑ
Robertson et al. [118]	15°	0.0191
Yang & Stern [119]	15.7°	0.0198
Yang & Stern [120]	16.1°	0.0197
Kolahdouz et al. [121]	15°	0.0198
Present	15.2°	0.0197

in the pitch direction. The governing equation for the spring-mass-damper plate model reads as

$$I_\vartheta \ddot{\vartheta} + C_\vartheta \dot{\vartheta} + K_\vartheta \vartheta = \mathscr{M}_{\text{hydro}}, \tag{4.67}$$

in which ϑ is the pitch angle of the plate measured from the horizontal axis, I_ϑ is the pitch moment of inertia about the center of mass, C_ϑ is the torsional damping constant, K_ϑ is the torsional spring constant, and $\mathscr{M}_{\text{hydro}}$ is the hydrodynamic moment acting on the plate due to the external fluid flow.

To compare of our results with prior simulations, we consider a plate with a width-to-thickness ratio of $\Lambda^* = L_\text{p}/H_\text{p} = 4$, a non-dimensional moment of inertia of $I^*_\vartheta = I_\vartheta/(\rho_\text{s} H_\text{p}^4) = 400$, a non-dimensional damping ratio of $\zeta^*_\vartheta = C_\vartheta/\left(2\sqrt{K_\vartheta I_\vartheta}\right) = 0.25$, and a reduced velocity of $U^* = U_\infty/(f_\vartheta H_\text{p}) = 40$. Here, U_∞ is the free stream velocity and $f_\vartheta = \sqrt{K_\vartheta/I_\vartheta}/2\pi$ is the natural frequency of the spring-mass-damper system. The rectangular plate is centered at the origin with an initial non-zero pitch of $\vartheta = 1°$. The computational domain is taken to be $\Omega = [-32\,\text{cm}, 96\,\text{cm}] \times [-32\,\text{cm}, 32\,\text{cm}]$, a rectangular domain of size $L_x \times L_y$ = 128 cm × 64 cm. Five grid levels are used to discretize the domain, with the structure embedded on the finest grid level. A coarse grid spacing of $h_\text{coarsest} = L_y/32$ is used on the coarsest level. The finest level is refined with a refinement ratio of $n_\text{ref} = 2$, whereas the rest of the finer levels are refined using a refinement ratio of $n_\text{ref} = 4$ from their next coarser level. A uniform inflow velocity $\mathbf{U} = (U_\infty = 1\,\text{cm/s}, 0\,\text{cm/s})$ is imposed on the left boundary (x = -32 cm), whereas zero normal traction and zero tangential velocity boundary conditions are imposed on the right boundary (x =

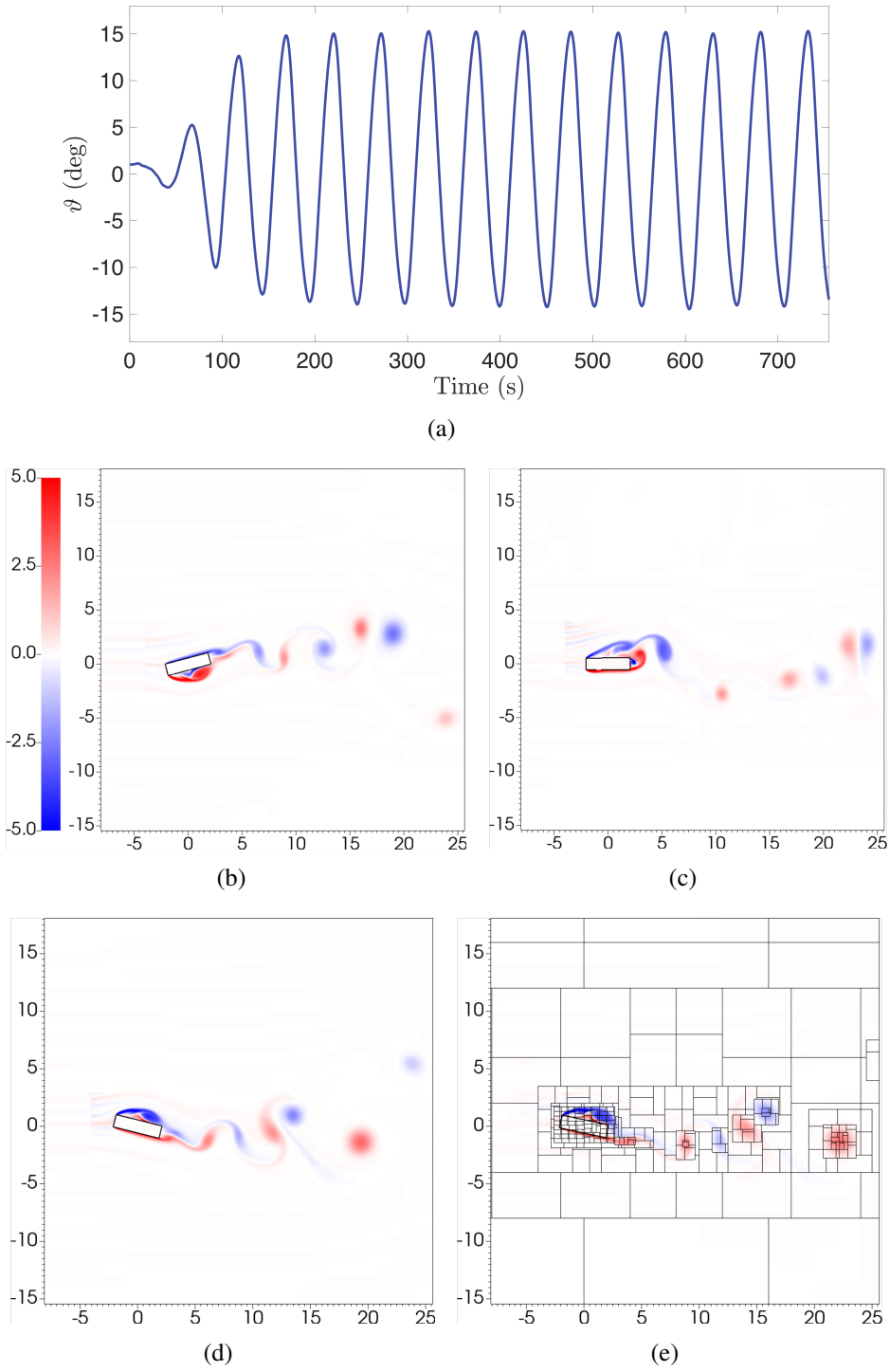

Figure 4.7. Galloping motion of a rectangular plate with $\Lambda^* = 4$, $I^* = 400$, $\zeta^*_\vartheta = 0.25$ and $U^* = 40$.(a) Temporal evolution of pitch angle ϑ; (b)—(d) Vorticity (1/s) plots at three representative time instants t = 221.25 s, t = 309 s, and t = 349.5 s, respectively. (e) Dynamic mesh/patch distribution in the domain at a representative time instant t = 352.5 s.

96 cm). The bottom (y = -32 cm) and top (y = 32 cm) boundaries satisfy zero normal velocity and zero tangential traction boundary conditions. The Reynolds number of the flow based on the inlet velocity is set to Re = $\rho_{\mathrm{f}} U_{\infty} H_{\mathrm{p}} / \mu_{\mathrm{f}} = 250$. A constant time step size of $\Delta t = 0.048\, h_{\mathrm{finest}}$ is used for the simulation. After the initial transients, a vortex shedding state is established, which results in a periodic galloping of the rectangular plate. Fig. 4.7(a) shows the pitch angle of the plate as a function of time. Figs. 4.7(b)-4.7(d) show three representative snapshots of the FSI dynamics and the vortex shedding pattern. Fig. 4.7(e) shows a typical AMR patch distribution in the domain due to the evolving structural and vortical dynamics. Table 4.3 compares the maximum pitch angle ϑ_{max} and galloping frequency of the plate f_{ϑ} with values obtained from previous numerical studies; an excellent agreement with prior studies is obtained for both these rotational quantities.

4.6 Grid convergence study

In this section, we perform a grid convergence study on the 2D ISWEC model in a NWT with regular waves using three different spatial resolutions. We also conduct a temporal resolution study to determine a time step size Δt that is able to adequately resolve the high-frequency wave components of irregular waves. Although our implementation is capable of adaptive mesh refinement, we use *static* grids for all cases presented in this section. As mentioned in Sec. 4.4.6, we lock all the translational degrees of freedom of the hull and only consider its pitching motion.

The size of the computational domain is $\Omega = [0, 10\lambda] \times [0, 2.75d]$ with the origin located at the bottom left corner (see Fig. 5.4). The hull parameters for the 2D model are given in Table 4.2, and the CG of the hull is located at $(5\lambda, d - Z_{\mathrm{CG}})$. The quiescent water depth is $d = 0.65$ m, acceleration due to gravity is $g = 9.81$ m/s (directed in negative z-direction), density of water is $\rho_{\mathrm{w}} = 1025$ kg/m^3, density of air is $\rho_{\mathrm{air}} = 1.2$ kg/m^3, viscosity of water $\mu_{\mathrm{w}} = 10^{-3}$ Pa·s and viscosity of air is $\mu_{\mathrm{air}} = 1.8 \times 10^{-5}$ Pa·s. Surface tension effects are neglected for all cases as they do not affect the wave and converter dynamics at the scale of these problems.

4.6.1 Spatial resolution study

To ensure the wave-structure interaction dynamics are accurately resolved, we conduct a grid convergence study to determine an adequate mesh spacing. The dynamics of the ISWEC hull interacting with regular water waves are simulated on three meshes: coarse, medium, and fine. Each mesh consists of a hierarchy of ℓ grids; the computational domain is discretized by a coarsest grid of size $N_y \times N_z$ and then locally refined $(\ell - 1)$ times by an integer refinement ratio n_{ref} ensuring that the ISWEC device and air-water interface are covered by the finest grid level. The grid spacing on the finest level are calculated using the following expressions: $\Delta y_{\text{min}} = \Delta y_0 / n_{\text{ref}}^{\ell-1}$ and $\Delta z_{\text{min}} = \Delta z_0 / n_{\text{ref}}^{\ell-1}$, where Δy_0 and Δz_0 are the grid spacings on the coarsest level. The time step size Δt is chosen to ensure the maximum Courant-Friedrichs-Levy (CFL) number $= 0.12$ for each grid resolution. The mesh parameters and time step sizes considered here are shown in Table 5.2.

Regular water waves, generated based on the fifth-order wave theory presented in Sec. 4.2.1, enter the left side of the domain and interact with the ISWEC hull. Temporal evolution of the hull's pitch angle δ and the gyroscope's precession angle ε are the primary outputs used to evaluate mesh convergence. The results and the specification of the wave, ISWEC, and gyroscope parameters are shown in Fig. 5.9.

Fig. 4.9(a) shows a close-up of the medium resolution grid and the 2D ISWEC model. A minimum of 8 grid cells vertically span the height of the wave, indicating that the wave elevation is adequately resolved; for the coarse (fine) grid resolution, approximately 4 (15) grid cells span the wave height (results not shown). Additionally, the number of cells covering the ISWEC hull length is approximately 30, 60, and 119 for the coarse, medium, and fine grid resolutions, respectively. Fig. 4.9(b) shows well-resolved vortical structures produced by the interaction of the ISWEC device and air-water interface on the medium resolution grid. From the quantitative and qualitative results shown in Fig. 5.9 and Fig. 4.9, we conclude that the medium grid resolution can capture the WSI dynamics with reasonable accuracy. Therefore for

Table 4.4. Refinement parameters used for the 2D ISWEC dynamics grid convergence study.

Parameters	Coarse	Medium	Fine
n_{ref}	2	2	4
ℓ	2	2	2
N_y	300	600	600
N_z	34	68	68
Δt (s)	2×10^{-3}	1×10^{-3}	5×10^{-4}

the remaining cases studied here, we make use of the medium grid resolution.

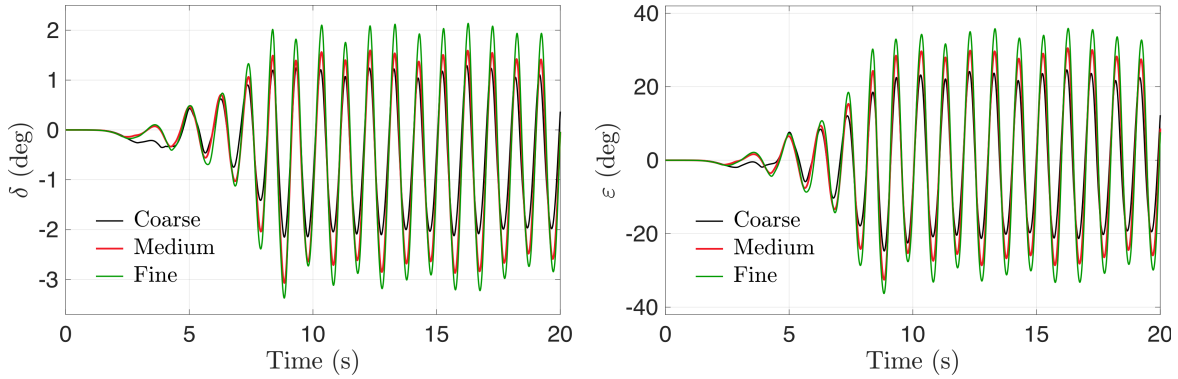

(a) Hull pitch angle (b) Gyroscope precession angle

Figure 4.8. Temporal evolution of (a) hull pitch angle δ and (b) gyroscope precession angle ε, for coarse (——, black), medium (——, red) and fine (——, green) grid resolutions. Fifth-order regular water waves are generated with $\mathscr{H} = 0.1$ m, $\mathscr{T} = 1$ s and $\lambda = 1.5456$ m, satisfying the dispersion relation given by Eq. (4.2). A maximum ISWEC pitch angle $\delta_0 = 5°$ and a maximum gyroscope precession angle of $\varepsilon_0 = 70°$ are used to calculate the rest of the parameters following the procedure described in Sec. 4.4.3: PTO damping coefficient $c = 0.3473$ N·m·s/rad, gyroscope moment of inertia $J = 0.0116$ kg·m^2 and PTO stiffness coefficient $k = 0.4303$ N·m/rad. The speed of the flywheel is $\dot{\phi} = 4000$ RPM, and $I = 0.94 \times J = 0.0109$ kg ·m^2.

4.6.2 Temporal resolution study

Next, we conduct a temporal resolution study to ensure that WSI dynamics of irregular waves and the ISWEC device are adequately resolved. As described in Sec. 4.2.2, irregular water waves are modeled as a superposition of N harmonic wave components. The energy carried by each wave component is related to its frequency ω_i (see Eq. (4.11) and Fig. 4.2(a)). Moreover as shown in Fig. 4.2(a), high frequency waves with ω_i in the range of 10 rad/s to 20

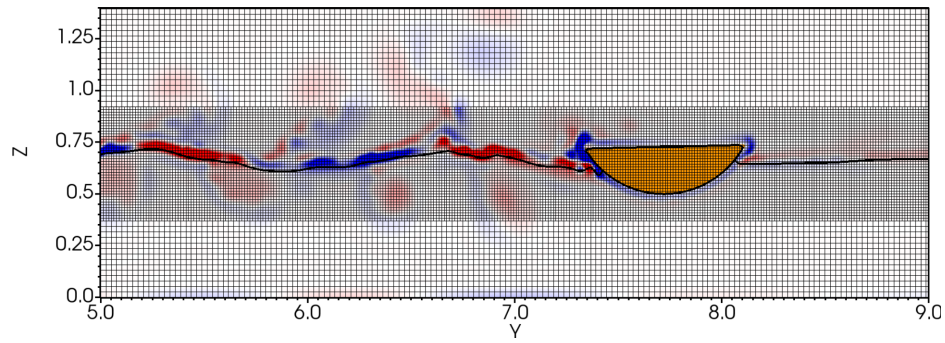

(a) Locally refined Cartesian grid (medium grid resolution)

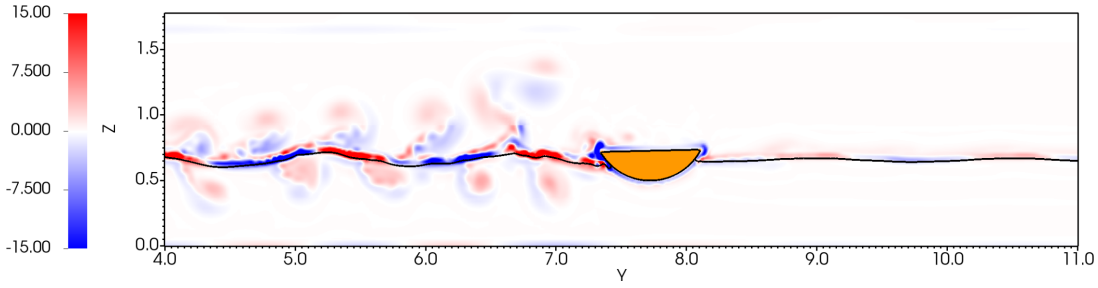

(b) Vorticity (medium grid resolution)

Figure 4.9. Wave-structure interaction of the 2D ISWEC model at $t = 27$ s using the medium grid resolution: (a) locally refined mesh with two levels ($\ell = 2$) and (b) representative vortical and air-water interfacial dynamics resulting from the WSI.

rad/s carry considerable amounts of energy. Hence, the time step Δt should be chosen such that these high frequency (small wave period $\mathscr{T}_i$) components are well-resolved since they contribute significantly to the power absorbed by the device.

The dynamics of the ISWEC hull interacting with irregular water waves are simulated using three different time step sizes: $\Delta t = 10^{-3}$ s, 5×10^{-4} s and 2.5×10^{-4} s. For all three cases, we use a medium resolution grid with refinement parameters given by Table 5.2. Temporal evolution of the hull's pitch angle δ and the power absorbed by the PTO unit P_{PTO} are the primary outputs used to evaluate temporal convergence. The results and the specification of the irregular wave, ISWEC, and gyroscope parameters are shown in Fig. 5.11. It is observed that the hull's pitching motion is relatively insensitive to the chosen time step size Δt. Since its dynamics are governed mainly by those waves carrying the largest energy, we can conclude that the higher frequency wave components are adequately resolved. The difference between the three temporal

resolutions is more apparent in Fig. 4.10(b), in which we calculate the average power absorbed by the PTO unit $\bar{P}_{\text{PTO}}$ over the interval $t = 10$ s and $t = 20$ s. For $\Delta t = 10^{-3}$ s, 5×10^{-4} s and 2.5×10^{-4} s, the power absorbed is $\bar{P}_{\text{PTO}} = 1.7656$ W, 1.8859 W and 1.9484 W, respectively. It is seen that smaller time step sizes allow for the resolution of higher-frequency wave peaks, which directly increases the absorbed power.

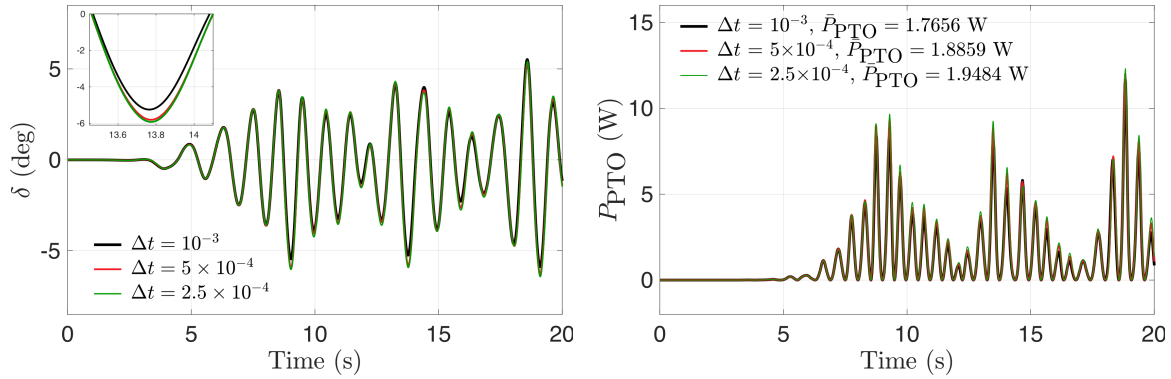

(a) Hull pitch angle

(b) Power absorbed by PTO

Figure 4.10. Temporal evolution of (a) hull pitching dynamics and (b) power absorbed by PTO, for three different time step sizes: $\Delta t = 10^{-3}$ s (——, black), $\Delta t = 5 \times 10^{-4}$ s (——, red) and $\Delta t = 2.5 \times 10^{-4}$ s (——, green). Irregular water waves (satisfying the dispersion relation Eq. (4.2)) are generated with $\mathscr{H}_{\text{s}} = 0.1$ m, $\mathscr{T}_{\text{p}} = 1$ s and $N = 50$ wave components, with frequencies in the range 3.8 rad/s to 20 rad/s distributed at equal $\Delta\omega$ intervals. A maximum ISWEC pitch angle $\delta_0 = 5°$ and a maximum gyroscope precession angle of $\varepsilon_0 = 70°$ are used to calculate the rest of the parameters following the procedure described in Sec. 4.4.3: PTO damping coefficient $c = 0.1724$ N·m·s/rad, gyroscope moment of inertia $J = 0.0057$ kg·m^2 and PTO stiffness coefficient $k = 0.2138$ N·m/rad. The speed of the flywheel is $\dot{\phi} = 4000$ RPM, and $I = 0.94 \times J = 0.0054$ kg·m^2. The mean wave power per unit crest width carried by the irregular waves calculated by Eq. (4.16) is $\bar{P}_{\text{wave}} = 5.0798$ W.

Based on these results, we hereafter use the medium grid spatial resolution, and time step sizes of $\Delta t = 1 \times 10^{-3}$ s and $\Delta t = 5 \times 10^{-4}$ s for regular and irregular wave WSI cases, respectively.

4.7 ISWEC numerical examples

In this section, we investigate several aspects of the dynamics of the inertial sea wave energy converter device:

- First, we compare the PTO power predictions by the 3D and 2D ISWEC models under identical wave conditions. Utilizing the scaling factors presented in Table 4.1, we show that the power predicted by the 3D model can be inferred from the power predicted by the 2D model reasonably well.

- Next, we study the effect of the maximum hull pitch angle parameter δ_0 and make recommendations on how to select it based on the maximum wave steepness δ_s. We consider different "sea states" characterized by regular waves of different heights $\mathscr{H}$, and consequently of different steepnesses.

- Thereafter, a parametric analysis for the 2D ISWEC model is performed using both regular and irregular water waves to study its dynamics. We vary the following parameters to recommend "design" conditions for the device: PTO damping coefficient c, flywheel speed $\dot{\phi}$, moment of inertia J and I, and PTO stiffness coefficient k.

- Afterwards, the effect of varying hull length to wavelength ratios is studied.

- Finally, we simulate a possible device protection strategy during inclement weather conditions and study the resulting dynamics.

All the 2D simulations are conducted in a NWT with computational domain size Ω = $[0,10\lambda] \times [0, 2.75d]$ as shown in Fig. 5.4. For 3D cases the computational domain size is same as in 2D, with the additional dimension having length $5W$; W is the width of 3D model of the hull. The domain sizes are large enough to ensure that the ISWEC dynamics are undisturbed by boundary effects. The origin of the NWT is taken to be the bottom left corner of the domain and shown by the point O in Fig. 5.4. The CG of the ISWEC hull is located at $(2.5W, 5\lambda, d - Z_{\mathrm{CG}})$ for 3D cases and $(5\lambda, d - Z_{\mathrm{CG}})$ for the 2D cases. The rest of the hull parameters are presented in Table 4.2. The water and air material properties are the same as those described in Sec. 4.6.1.

Table 4.5. The PTO and gyroscope parameters for various regular wave heights $\mathscr{H}$ and δ_0 values, as calculated by the procedure described in Sec. 4.4.3. The rated power of the device $\bar{P}_{\mathrm{R}}$ is taken to be the available wave power $\bar{P}_{\mathrm{wave}}$ for these calculations. The prescribed gyroscope parameters are $\varepsilon_0 = 70^\circ$, $\dot{\phi} = 4000$ RPM, and $I = 0.94 \times J$. The parameter units for c are N·m·s/rad, J and I are kg·m^2, and k are N·m/rad.

Regular wave properties	Parameters	Prescribed hull pitch angle δ_0					
		2°	5°	10°	15°	20°	δ_s
$\mathscr{H} = 0.025$ m, $\mathscr{T} = 1$ s	c	0.0217	0.0217	0.0217	0.0217	0.0217	0.0217
	J	0.0018	0.00072	0.00036	0.00024	0.00018	0.0012
	k	0.0673	0.0269	0.0134	0.0089	0.0067	0.0464
$\mathscr{H} = 0.05$ m, $\mathscr{T} = 1$ s	c	0.0868	0.0868	0.0868	0.0868	0.0868	0.0868
	J	0.0072	0.0029	0.0014	0.00090	0.00072	0.0025
	k	0.2692	0.1076	0.0538	0.0358	0.0269	0.0928
$\mathscr{H} = 0.1$ m, $\mathscr{T} = 1$ s	c	0.3473	0.3473	0.3473	0.3473	0.3473	0.3473
	J	0.0290	0.0116	0.0058	0.0039	0.0029	0.0050
	k	1.0777	0.4303	0.2171	0.1421	0.1065	0.1876
$\mathscr{H} = 0.125$ m, $\mathscr{T} = 1$ s	c	0.5427	0.5427	0.5427	0.5427	0.5427	0.5427
	J	0.0453	0.0181	0.0090	0.0060	0.0045	0.0063
	k	1.6827	0.6731	0.3365	0.2243	0.1682	0.2361

4.7.1 3D and 2D ISWEC model simulations

In this section, we investigate the dynamics of the 2D and 3D ISWEC models interacting with regular and irregular water waves. We compare the motion of the hull and the power absorption capabilities of each model. The 2D model is simulated on a medium grid resolution and the 3D model on a coarse grid resolution using the refinement parameters specified in Table 5.2. The third dimension is discretized with $N_x = 38$ grid cells for 3D cases. Fig. 4.11(a) shows the configuration of the locally refined mesh ($\ell = 2$), along with visualizations of regular and irregular waves for the three-dimensional NWT.

First, we consider two different prescribed maximum pitch angles $\delta_0 = 5^\circ$ and 20° for each model. Regular waves are generated with properties $\mathscr{H} = 0.1$ m and $\mathscr{T} = 1$ s. The values for the gyroscope and PTO parameters for this choice of δ_0 are given in Table 4.5. The rated power of the device $\bar{P}_{\mathrm{R}}$ is taken to be the available wave power $\bar{P}_{\mathrm{wave}}$ for calculating the parameters reported in Table 4.5. The hull undergoes pitching motion as the regular waves impact the device,

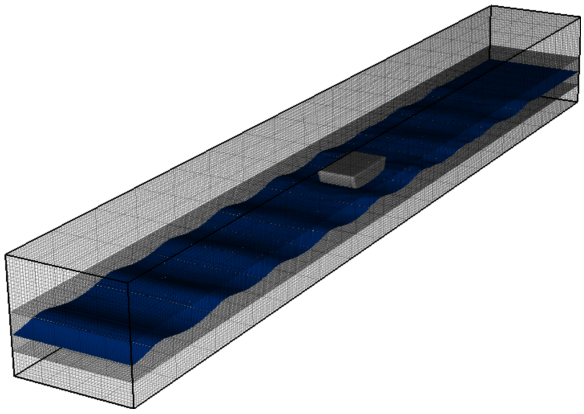

(a) Locally refined Cartesian mesh

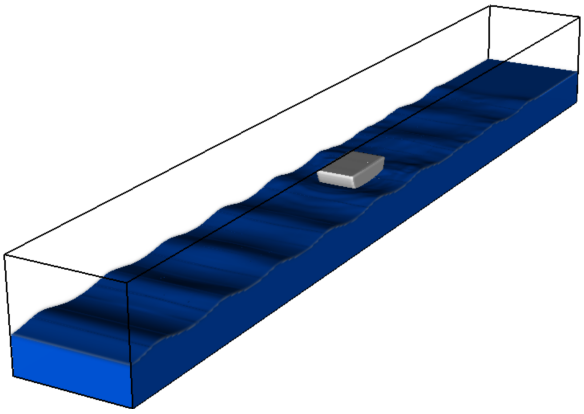

(b) Regular waves

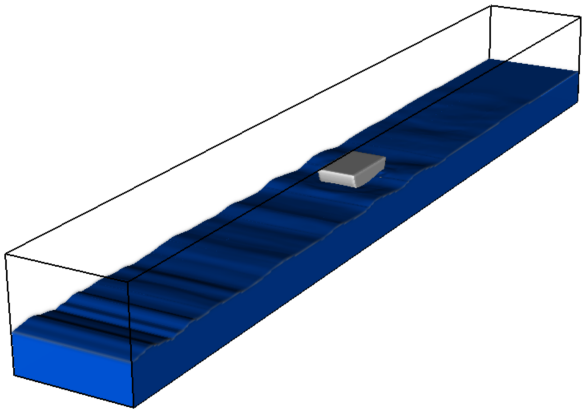

(c) Irregular waves

Figure 4.11. (a) Locally refined Cartesian mesh with two levels of mesh refinement used for the 3D NWT. Representative WSI of the 3D ISWEC model at t = 28.8 s: (b) regular waves, and (c) irregular waves.

as shown in Fig. 4.11(b). The temporal evolution of the hull pitch angle δ for the 2D and the 3D ISWEC models are shown in Figs. 4.12(a) and 4.12(b). From these results, it is observed that the dynamics for the 2D case match well with the 3D case after the initial transients. The power transferred to the hull from the waves P_{hull}, the power generated through the hull-gyroscope interaction P_{gyro}, and the power absorbed by the PTO unit P_{PTO} at $\delta_0 = 5^\circ$ ($\delta_0 = 20^\circ$) for the 2D and 3D models are shown in Figs. 4.12(c) and 4.12(d) (Figs. 4.12(e)and 4.12(f)), respectively. The time-averaged powers $\bar{P}_{\text{PTO}}$, $\bar{P}_{\text{gyro}}$ and $\bar{P}_{\text{hull}}$ over the time interval $t = 10$ s and $t = 20$ s (after the hull's motion achieved a periodic steady state) are also shown in Figs. 4.12(c)-4.12(f). From these results, it is seen that the energy transfer pathway Eq. (4.45) is numerically verified. Furthermore, the power absorbed by the PTO unit for the full-scale device can be calculated by multiplying the power absorbed by the 2D model by the Froude scaling given in Table 4.1

$$\bar{P}_{\text{full-scale}} = \alpha^{\frac{5}{2}} \cdot W \cdot \bar{P}_{\text{2D}}, \qquad \text{(PTO unit)}. \tag{4.68}$$

Similarly for the 3D model,

$$\bar{P}_{\text{full-scale}} = \alpha^{\frac{7}{2}} \cdot \bar{P}_{\text{3D}}, \qquad \text{(PTO unit)}. \tag{4.69}$$

Finally, combining the two expressions above yields

$$\bar{P}_{\text{3D}} = \frac{W_{\text{full-scale}}}{\alpha} \cdot \bar{P}_{\text{2D}} = 0.4 \times \bar{P}_{\text{2D}}, \qquad \text{(PTO unit)}, \tag{4.70}$$

in which $W_{\text{full-scale}} = 8$ m is the width of the full-scale model and $\alpha = 20$ is the length scaling factor. For the 2D cases, the average power absorbed by the PTO unit is $\bar{P}_{\text{2D}} = 1.6972$ W for $\delta_0 = 5^\circ$, and $\bar{P}_{\text{2D}} = 1.1694$ W for $\delta_0 = 20^\circ$. For the 3D cases, the average powers absorbed by the PTO unit are 0.8535 W and 0.5155 W for $\delta_0 = 5^\circ$ and $\delta_0 = 20^\circ$, respectively, which are close to the expected values of 0.6788 W and 0.4677 W predicted by Eq. (4.70). Note that better agreement between the simulated and expected average powers in 3D can be obtained by

increasing the spatial and temporal resolutions. Nevertheless, we are confident that the dynamics are reasonably resolved for the chosen grid spacing and time step size.

Next, we perform a similar scaling analysis for 2D and 3D ISWEC models in irregular wave conditions. Irregular water waves are generated with properties $\mathscr{H}_s = 0.1$ m, $\mathscr{T}_p = 1$ s and 50 wave components with frequencies ω_i in the range 3.8 rad/s to 20 rad/s (see Fig. 4.11(c)). Through empirical testing, fifty wave components were found to be sufficient to represent the energy of the JONSWAP spectrum. We consider a maximum pitch angle of $\delta_0 = 5^\circ$ for the device. The evolution of δ for the two models are compared in Fig. 4.13(a). Similar to the regular wave case presented above, the dynamics of the 2D and 3D models numerically agree and the energy transfer pathway Eq. (4.45) is nearly satisfied. Moreover, the average power absorbed by the PTO unit for the 2D model is $\bar{P}_{2D} = 1.8859$ W, yielding an expected 3D power of 0.7543 W according to Eq. (4.70); this is close to the power value of 0.5810 W obtained by the 3D simulation. Based on these results, we ultimately conclude that the 2D model is sufficient to accurately simulate ISWEC dynamics and to predict the power generation/absorption capability of the converter.

Next, we perform a fast Fourier transform of the power signal obtained at the PTO ($P_{PTO}(t)$) shown in Fig. 4.12(c) and 4.13(b). The transformed signal identifies the main frequency components present in the signal. The transformed signal is seen with spikes when plotted as a function of frequency, see Fig. 4.14. Fig. 4.14(a) is obtained for the 2D ISWEC model in regular waves with condition $\mathscr{H} = 0.1$ m and $\mathscr{T} = 1$ s. The frequency responsible for power generation is observed to be at 2 Hz. A similar analysis is done for the 2D ISWEC model in irregular waves with condition $\mathscr{H}_s = 0.1$ m and $\mathscr{T}_p = 1$ s, see Fig. 4.14(b). The irregular wave is composed of number of wave components with frequencies in the range 0.6 Hz (3.8 rad/s) to 3.18 Hz (20 rad/s). From this the main frequency is found to be at 2 Hz which is responsible for large power generation. These main frequencies obtained from the Fourier analysis corresponds to the frequency of square of the precession velocity of the gyroscope ($\dot{\varepsilon}^2$), as per Eq (4.33). Since the device operates in resonance with the incoming wave, the wave frequency $1/\mathscr{T}$ for regular

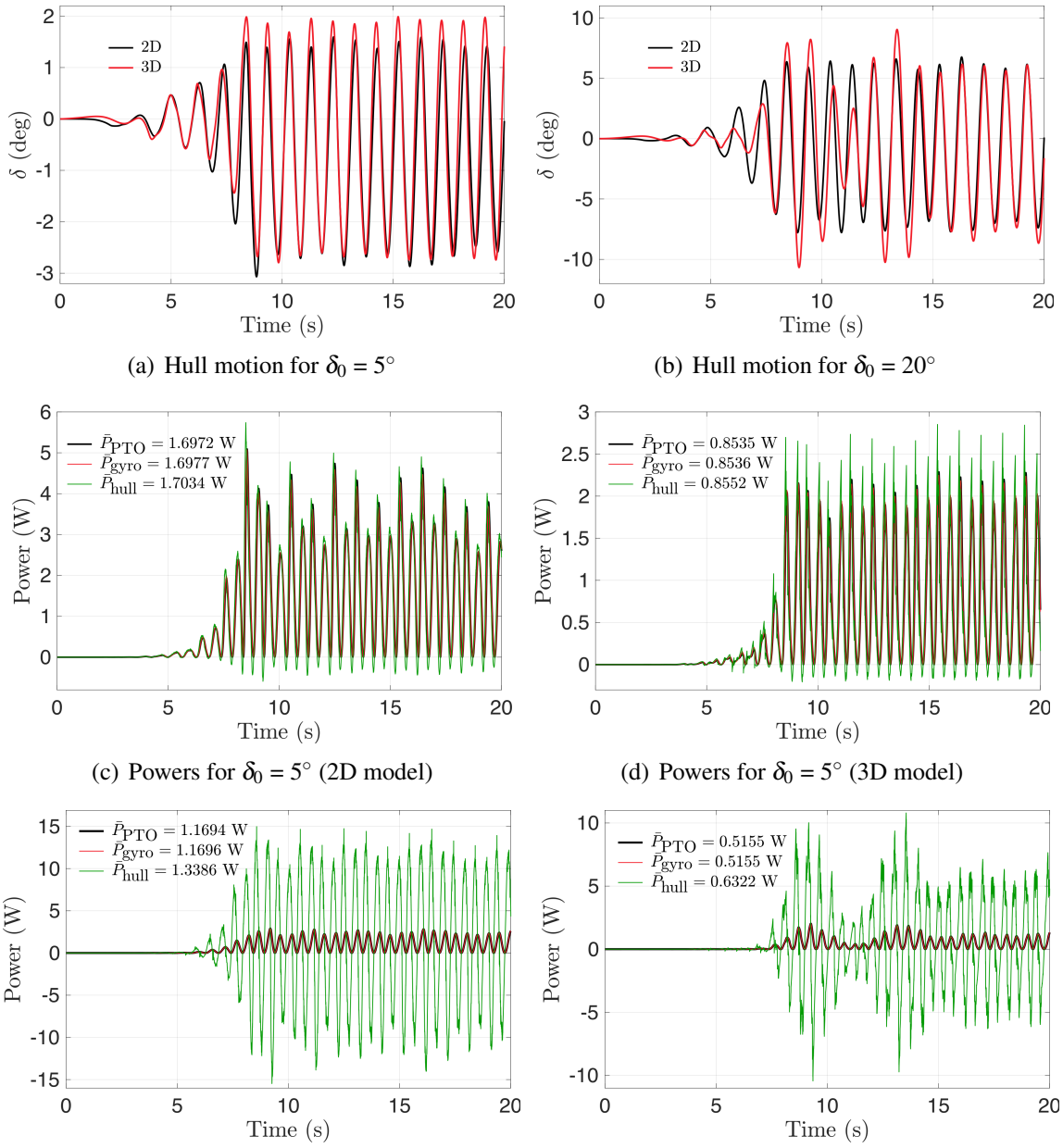

(a) Hull motion for $\delta_0 = 5°$

(b) Hull motion for $\delta_0 = 20°$

(c) Powers for $\delta_0 = 5°$ (2D model)

(d) Powers for $\delta_0 = 5°$ (3D model)

(e) Powers for $\delta_0 = 20°$ (2D model)

(f) Powers for $\delta_0 = 20°$ (3D model)

Figure 4.12. WSI of the 2D and 3D ISWEC models in regular water wave conditions ($\mathscr{H}$ = 0.1 m and $\mathscr{T}$ = 1 s). Temporal evolution of the hull pitch angle (δ) for the 2D and 3D ISWEC models for (a) $\delta_0 = 5°$ and (b) $\delta_0 = 20°$. Power absorbed by the PTO unit P_{PTO} (——, black), power generated through the hull-gyroscope interaction P_{gyro} (——, red) and power transferred to the hull from the regular water waves P_{hull} (——, green) for the (c) 2D model with $\delta_0 = 5°$, (d) 3D model with $\delta_0 = 5°$, (e) 2D model with $\delta_0 = 20°$ and (f) 3D model with $\delta_0 = 20°$. Averaged power over the time period t = 10 s and t = 20 s are shown in the legends.

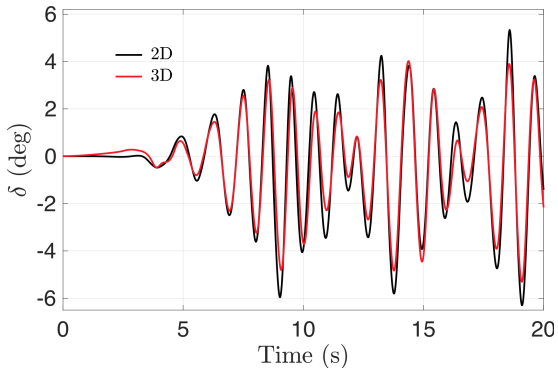

(a) Hull motion for $\delta_0 = 5°$

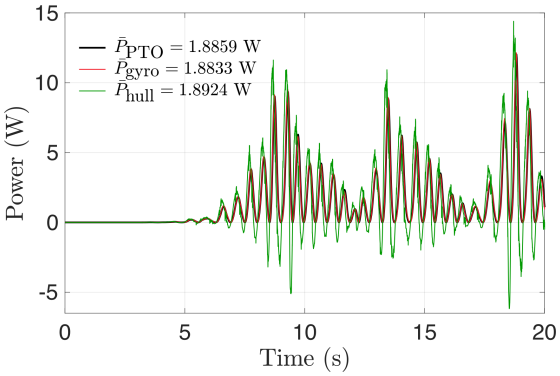

(b) Powers for $\delta_0 = 5°$ (2D model)

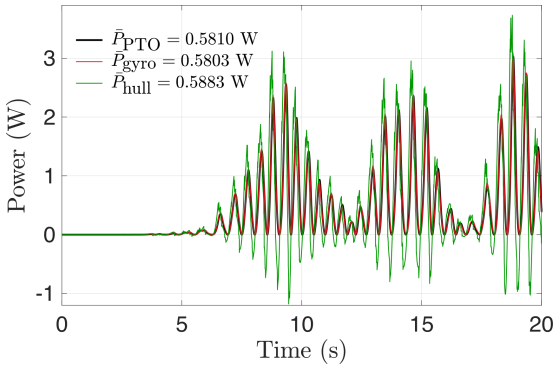

(c) Powers for $\delta_0 = 5°$ (3D model)

Figure 4.13. WSI of the 2D and 3D ISWEC models with $\delta_0 = 5°$ in irregular water wave conditions ($\mathscr{H}_s = 0.1$ m and $\mathscr{T}_p = 1$ s, $N = 50$, and ω_i in the range 3.8 rad/s to 20 rad/s). (a) Temporal evolution of the hull pitch angle (δ) for the 2D and 3D ISWEC models. Power absorbed by the PTO unit P_{PTO} (——, black), power generated through the hull-gyroscope interaction P_{gyro} (——, red) and power transferred to the hull from the irregular water waves P_{hull} (——, green) for the (b) 2D and (c) 3D models.

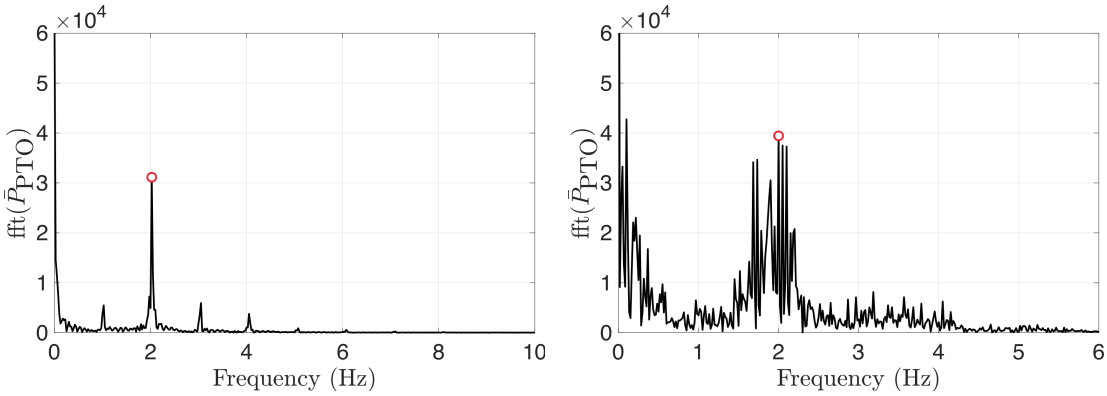

(a) Regular waves (b) Irregular waves

Figure 4.14. Power spectrum as a function of frequency obtained from fast Fourier transform of (a) Fig. 4.12(c), and (b) Fig. 4.13(b).

waves ($1/\mathscr{T}_p$ for irregular waves) and the frequency of $\dot{\varepsilon}$ is same, which is 1 Hz. The frequency of $\dot{\varepsilon}^2$ is twice of $\dot{\varepsilon}$, which is 2 Hz. So, theoretically both the waves have main frequency at 2 Hz. This aligns with the value of main frequency obtained from the Fourier analysis.

In the next section, we focus on further investigating dynamics and parameter choices for the 2D model.

4.7.2 Parametric analyses of hull and gyroscope parameters

In this section, we first investigate the relationship between the prescribed hull pitch angle parameter δ_0, the maximum pitch angle actually attained by the hull $\delta_{\max}$ through WSI, and the maximum wave steepness of the incoming waves δ_{s}.

Next, we conduct a parameter sweep around the energy-maximizing PTO and gyroscope parameters estimated by the theory presented in Sec. 4.4.3. We test the theory's predictive capability and describe the effect of these parameters on the converter's performance and dynamics. In each of the following subsections, only a single parameter is varied at a time.

Simulations are conducted using both regular water waves with $\mathscr{H}$ = 0.1 m and $\mathscr{T}$ = 1 s, and irregular waves with $\mathscr{H}_{\mathrm{s}}$ = 0.1 m, $\mathscr{T}_{\mathrm{p}}$ = 1 s and 50 wave components with frequencies ω_i in the range 3.8 rad/s to 20 rad/s. These wave conditions serve as device "design" conditions at its

installation site. For regular waves, the prescribed pitch angle is taken to be $\delta_0 = 10^\circ$, and the PTO and gyroscope parameters are given in Table 4.5. For irregular waves, the prescribed pitch angle $\delta_0 = 5^\circ$ is used. The PTO and gyroscope parameters remain the same as those used in the temporal resolution study (see Sec.4.6.2). These particular values of δ_0 were found to maximize the RCW of the converter at design conditions; for an example, see Fig. 4.15 for regular waves with $\mathscr{H}$ = 0.1 m and $\mathscr{T}$ = 1 s.

Selection of prescribed hull pitch angle δ_0

The maximum wave steepness is calculated in Sec. 4.2.3 by approximating the fifth-order wave as a linear harmonic wave. We consider the ISWEC dynamics on four regular water waves with same time period $\mathscr{T}$ = 1 s (i.e. λ = 1.5456 m) but varying wave heights: $\mathscr{H} = 0.025$ m, 0.05 m, 0.1 m and 0.125 m, each having maximum wave steepness $\delta_s = 2.9^\circ$, 5.8°, 11.48° and 14.25°, respectively (see Eq (4.21)). The prescribed PTO and gyroscope system parameters for each sea state and six maximum pitch angle values $\delta_0 = 2^\circ$, 5°, 10°, 15°, 20° and δ_s are shown in Table 4.5. Additionally, $\delta_0 = 1^\circ$ and 30° cases are also simulated, but the parameter values are not tabulated for brevity.

The results of this parameter study are shown in Fig. 4.15. It is observed that when $\delta_0 < \delta_s$, δ_{max} increases linearly with δ_0 (Fig. 4.15(a)), illustrating that the hull's maximum oscillation amplitude correlates well with δ_0. When the prescribed δ_0 is greater than δ_s, it is seen that δ_{max} no longer increases; rather it maintains a constant value with respect to δ_0. This indicates that further increasing δ_0 will not lead to larger pitch oscillations, i.e. the δ_{max} attained by the hull is the largest value permitted by the slopes of the wave. In Figs. 4.15(b) and 4.15(c), we show trends in the maximum precession angle attained by the gyroscope ε_{max} and the relative capture width (RCW) η, which measures the device efficiency as a ratio of the average power absorbed by the PTO unit to the average wave power per unit crest width (see Eq. (4.49)). Maximization of both these quantities is achieved when δ_0 is set close to δ_s. As the hull achieves the maximum pitch angle physically permitted by the slopes of the wave, further increasing

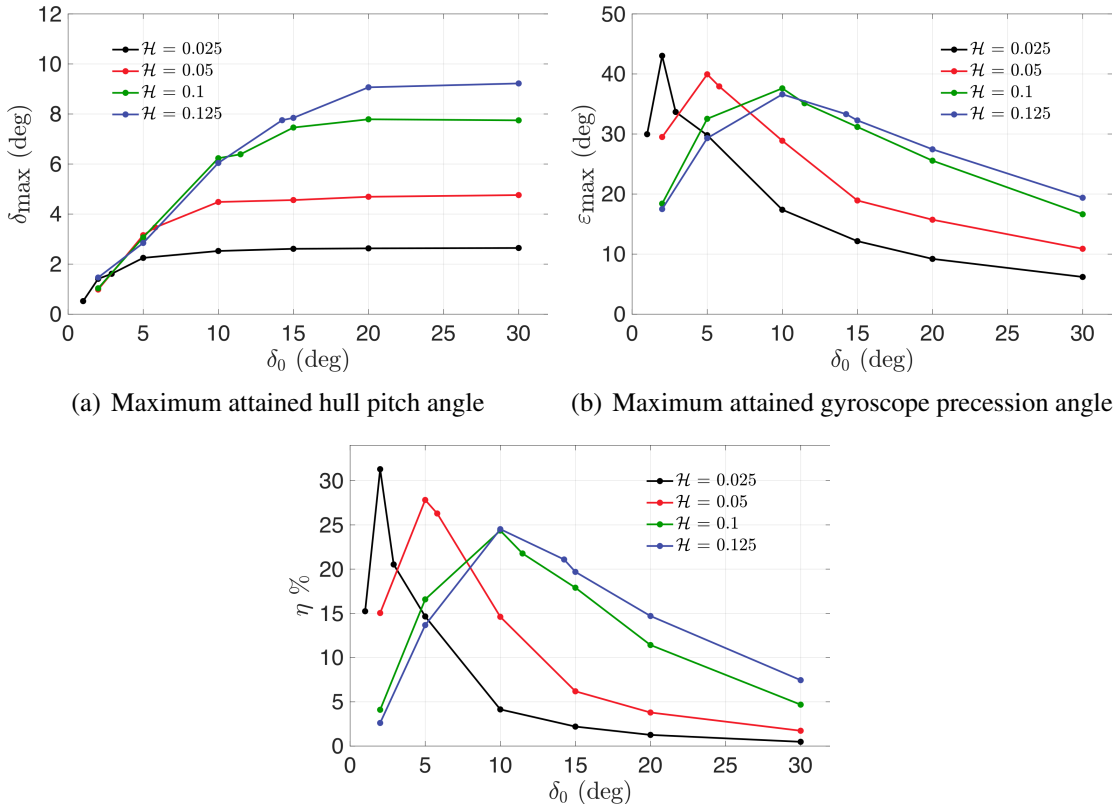

(a) Maximum attained hull pitch angle

(b) Maximum attained gyroscope precession angle

(c) Relative capture width (RCW)

Figure 4.15. (a) Maximum hull pitch angle $\delta_{\max}$, (b) maximum gyroscope precession angle $\varepsilon_{\max}$, and (c) relative capture width η of the ISWEC device for various regular wave sea states and prescribed pitch angles δ_0: $\mathscr{H}$ = 0.025 m (——, black), $\mathscr{H}$ = 0.05 m (——, red), $\mathscr{H}$ = 0.1 m (——, green), and $\mathscr{H}$ = 0.125 m (——, blue). RCW is calculated from time-averaged powers over the interval $t = 10$ s to $t = 20$ s

δ_0 amounts to reducing $J\dot{\phi}$ (Eq. (4.47)) or the hull-gyroscope coupling, which explains the reduction in both maximum precession and device efficiency. Hereafter, we prescribe δ_0 based on the value maximizing η as we conduct further parametric analyses of the 2D ISWEC model.

PTO damping coefficient c

We first consider the PTO unit damping coefficient c, which directly impacts the power absorption capability of the device. We prescribe four different values, $c = 0.05$, 0.3473, 1.0 and 2.0 N·m·s/rad, to evaluate its impact on ISWEC dynamics. The optimal damping coefficient value of $c = 0.3473$ is predicted by the theory. Results for the hull interacting with regular waves are shown in Fig. 4.16. As expected for smaller damping coefficients, the gyroscope is able to attain larger precession angles ε and velocities $\dot{\varepsilon}$, as seen in Fig. 4.16(b). Higher precession velocities yield larger pitch torque $\mathscr{M}_\delta$ values (see Eq. (4.42)), which opposes the motion of the hull and restrict its maximum pitch oscillation; this is consistent with the dynamics shown in Figs. 4.16(a) and 4.16(c). Moreover the hull's pitch velocity $\dot{\delta}$ is reduced with decreasing c, leading to a smaller (in magnitude) precession torque $\mathscr{M}_\varepsilon$ acting on the PTO shaft (see Eq. (4.37)); our simulations show this behavior as observed in Fig. 4.16(d).

In Fig. 4.16(e), we compare the time-averaged powers $\bar{P}_{\text{hull}}$, $\bar{P}_{\text{gyro}}$, and $\bar{P}_{\text{PTO}}$ as a function of varying PTO damping coefficient. It can be seen that these three powers are in reasonable agreement with each other, indicating that the energy transfer pathway Eq. (4.45) is approximately satisfied. In terms of power generation, it is observed that the device achieves peak performance when a PTO damping coefficient $c = 0.3473$ is prescribed, which validates the theoretical procedure. The reason for an optimum value of c is as follows: as the damping coefficient increases, the precession velocity decreases. The power absorbed by the PTO unit is the product of c and $\dot{\varepsilon}^2$ (Eq. (4.33)), and therefore these competing factors must be balanced in order to achieve maximum power generation.

Finally in Fig. 4.16(f), we show the evolution of the the yaw torque $\mathscr{M}_\phi$ acting on the hull for $c = 0.3473$, noting that its magnitude is approximately one-fifth of the pitch torque

$\mathscr{M}_\delta$. Although this is not insignificant, we do not consider the effect of $\mathscr{M}_\phi$ for the 3D ISWEC model (see Sec. 4.4.1) since its contribution will be cancelled out 1) by using an even number of gyroscopic units (if each flywheel pair spins with equal and opposite velocities) [115], and 2) partially by the mooring system. Discounting $\mathscr{M}_\phi$ during the ISWEC design phase would misalign the converter with respect to the main wave direction, which will reduce its performance. It is also interesting to note that the yaw torque in the gyroscopic frame of reference $\mathscr{M}_{z1}$ is at least two orders of magnitude lower than the yaw torque in the inertial reference frame, as evidenced by the inset of Fig. 4.16(f).

Similar dynamics are observed when the ISWEC model is simulated in irregular wave conditions for four different values, c = 0.05, 0.1724, 1.0 and 2.0 N·m·s/rad. The optimal damping coefficient value of $c = 0.1724$ is obtained from the theory. The results are compared in Fig. 4.17 and the theoretically predicted optimum c is verified. The response of the hull and gyroscope to irregular waves can be seen in Figs. 4.17(a) and 4.17(b), respectively. The pitch torque and the precession torque are shown in Figs. 4.17(c) and 4.17(d), respectively. From Fig. 4.17(e), it is verified that the energy transfer pathway given by Eq. (4.45) is satisfied. We note that the device efficiency is higher in irregular wave conditions as compared to regular wave conditions. This can be seen by comparing the maximum value of relative capture width for $\mathscr{H}$ = 0.1 m in Figs. 4.15(c) and 4.17(f): $\eta_{\max} = 24.36\%$ vs. $\eta_{\max} = 37.61\%$, respectively. The power carried by irregular waves is approximately half that of regular waves when they have the same significant height and time period. Therefore for the prescribed device dimensions, the converter is more efficient in less energetic wave conditions.

Flywheel speed $\dot{\phi}$

Next, we conduct a parameter sweep of the flywheel speed $\dot{\phi}$ and investigate its effects on ISWEC dynamics. The speed of the flywheel affects not only the amount of angular momentum $J\dot{\phi}$ generated in the gyroscope, but also the magnitude of the gyroscopic torques produced as seen in Eqs. (4.37) and (4.42). We consider four different flywheel speeds: $\dot{\phi} = 100$ RPM, 1000

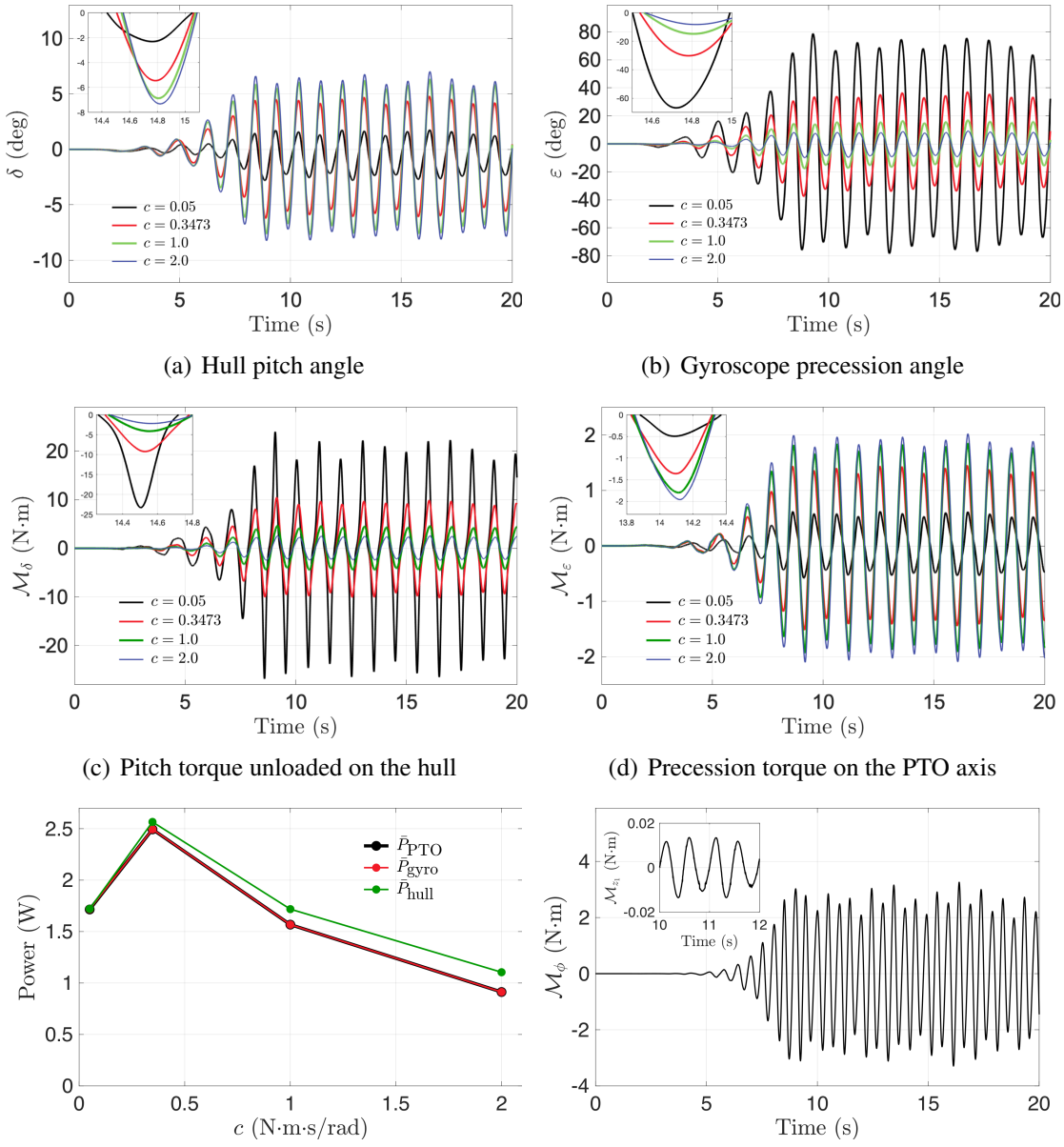

(a) Hull pitch angle

(b) Gyroscope precession angle

(c) Pitch torque unloaded on the hull

(d) Precession torque on the PTO axis

(e) Time-averaged powers in the system

(f) Yaw torque

Figure 4.16. Dynamics of the 2D ISWEC model for four different values of PTO damping coefficient c, with regular wave properties $\mathscr{H}$ = 0.1 m and $\mathscr{T}$ = 1 s. Temporal evolution of (a) hull pitch angle δ, (b) gyroscope precession angle ε, (c) pitch torque $\mathscr{M}_\delta$, and (d) precession torque $\mathscr{M}_\varepsilon$ for c = 0.05 N·m·s/rad (——, black), c = 0.3473 N·m·s/rad (——, red), c = 1.0 N·m·s/rad (——, green), and c = 2.0 N·m·s/rad (——, blue); (e) comparison of time-averaged powers from the interval t = 10 s to t = 20 s for each value of c; (f) yaw torques $\mathscr{M}_\phi$ and $\mathscr{M}_{z_1}$ produced in the inertial reference frame and gyroscope reference frame (inset), respectively.

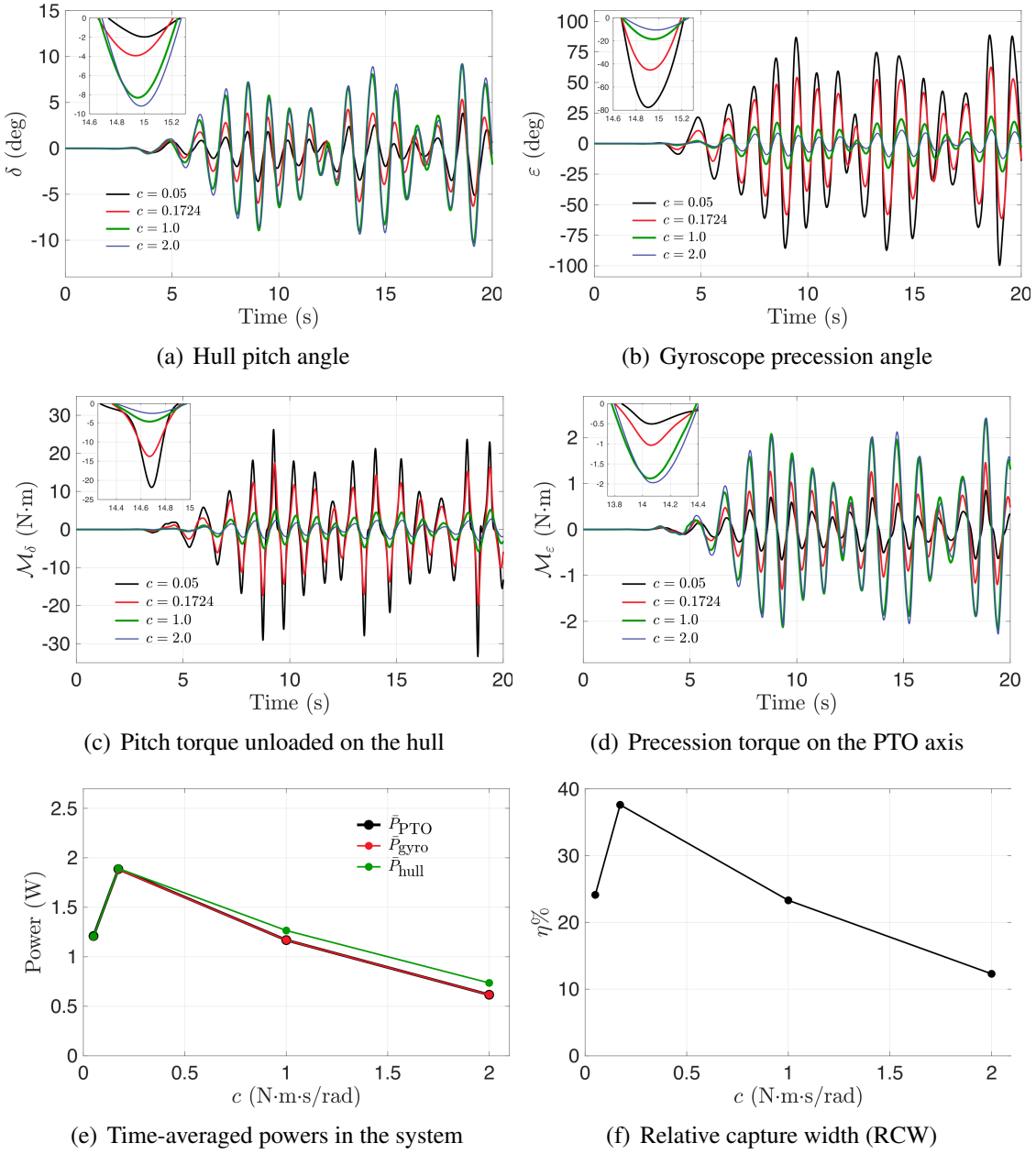

(a) Hull pitch angle

(b) Gyroscope precession angle

(c) Pitch torque unloaded on the hull

(d) Precession torque on the PTO axis

(e) Time-averaged powers in the system

(f) Relative capture width (RCW)

Figure 4.17. Dynamics of the 2D ISWEC model for four different values of PTO damping coefficient c, with irregular wave properties $\mathscr{H}_\text{s}$ = 0.1 m and $\mathscr{T}_\text{p}$ = 1 s and 50 wave components with frequencies ω_i in the range 3.8 rad/s to 20 rad/s. Temporal evolution of (a) hull pitch angle δ, (b) gyroscope precession angle ε, (c) pitch torque $\mathscr{M}_\delta$, and (d) precession torque $\mathscr{M}_\varepsilon$ for c = 0.05 N·m·s/rad (——, black), c = 0.1724 N·m·s/rad (——, red), c = 1.0 N·m·s/rad (——, green), and c = 2.0 N·m·s/rad (——, blue); (e) comparison of time-averaged powers from the interval $t = 10$ s to $t = 20$ s for each value of c; (f) relative capture width η for each value of c.

RPM, 4000 RPM, and 8000 RPM, with $\delta_0 = 10^\circ$ and the remaining gyroscope parameter are prescribed based on Table 4.5. Recall that these values were obtained for $\dot{\phi} = 4000$ RPM in Table 4.5.

The results for a hull interacting with regular waves are shown in Fig. 4.18. It is seen that the maximum pitch angle decreases with increasing $\dot{\phi}$ (Fig. 4.18(a)), while a non-monotonic relationship is seen between the maximum precession angle and $\dot{\phi}$ (Fig. 4.18(b)). Time-averaged powers are shown in Fig. 4.18(c), which again shows that Eq. (4.45) is approximately satisfied. Power absorption is maximized at a flywheel speed of $\dot{\phi} = 4000$ RPM, which can be physically explained as follows. As $J\dot{\phi}$ increases, the gyroscopic system is able to generate significant precession torque which, increases the absorption capacity of the PTO unit. However, this increased angular momentum also increases the pitch torque opposing the hull, thereby limiting its pitching motion and reducing the power absorbed from the waves. These two competing factors leads to an optimum value of $\dot{\phi}$.

Similar dynamics are obtained when the ISWEC interacts with irregular waves for varying values of $\dot{\phi}$. The results are shown in Fig. 4.19. The comparison of pitch angle for various $\dot{\phi}$ values is shown in Fig. 4.19(a) and of precession angle is shown in Fig. 4.19(b). Eq. (4.45) is again satisfied as seen from the time-averaged powers in Fig. 4.19(c). In this case, the power maximizing flywheel speed is $\phi = 3500$ RPM.

Flywheel moment of inertia J and I

The angular momentum $J\dot{\phi}$ generated in the gyroscope can also be modified by varying the flywheel size via its moment of inertia components J and I. First, we consider three different values $J = 0.0005$ kg $\cdot$m^2, 0.0058 kg$\cdot$m^2 and 0.5 kg$\cdot$m^2, which correspond to light, medium, and heavy weight gyroscopes, respectively. The $J = 0.0058$ value is obtained from theoretical estimates based on the prescribed δ_0 and ε_0 values. A value of $I = 0.94 \times J$ is set for each case, and the remaining gyroscope parameters are prescribed based on Table 4.5.

The results for a hull interacting with regular waves are shown in Fig. 4.20. It is seen

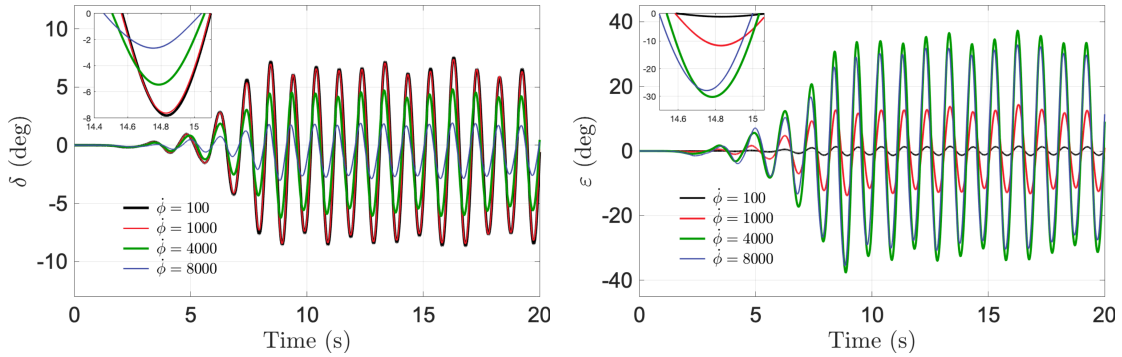

(a) Hull pitch angle

(b) Gyroscope precession angle

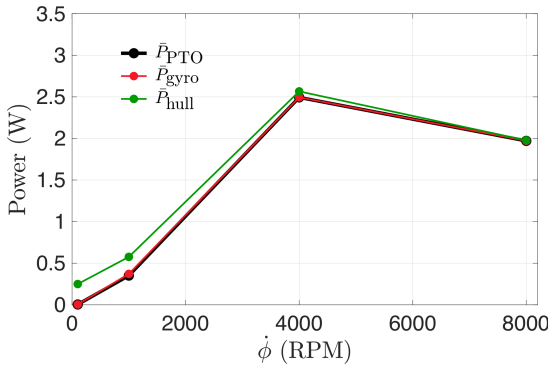

(c) Powers

Figure 4.18. Dynamics of the 2D ISWEC model for four different values of flywheel speed $\dot{\phi}$. The regular wave properties are $\mathscr{H}$ = 0.1 m and $\mathscr{T}$ = 1 s. Temporal evolution of (a) hull pitch angle δ, and (b) gyroscope precession angle ε for $\dot{\phi}$ = 100 RPM (——, black), $\dot{\phi}$ = 1000 RPM (——, red), $\dot{\phi}$ = 4000 RPM (——, green), and $\dot{\phi}$ = 8000 RPM (——, blue); (c) comparison of time-averaged powers from the interval $t = 10$ s to $t = 20$ s for each value of $\dot{\phi}$.

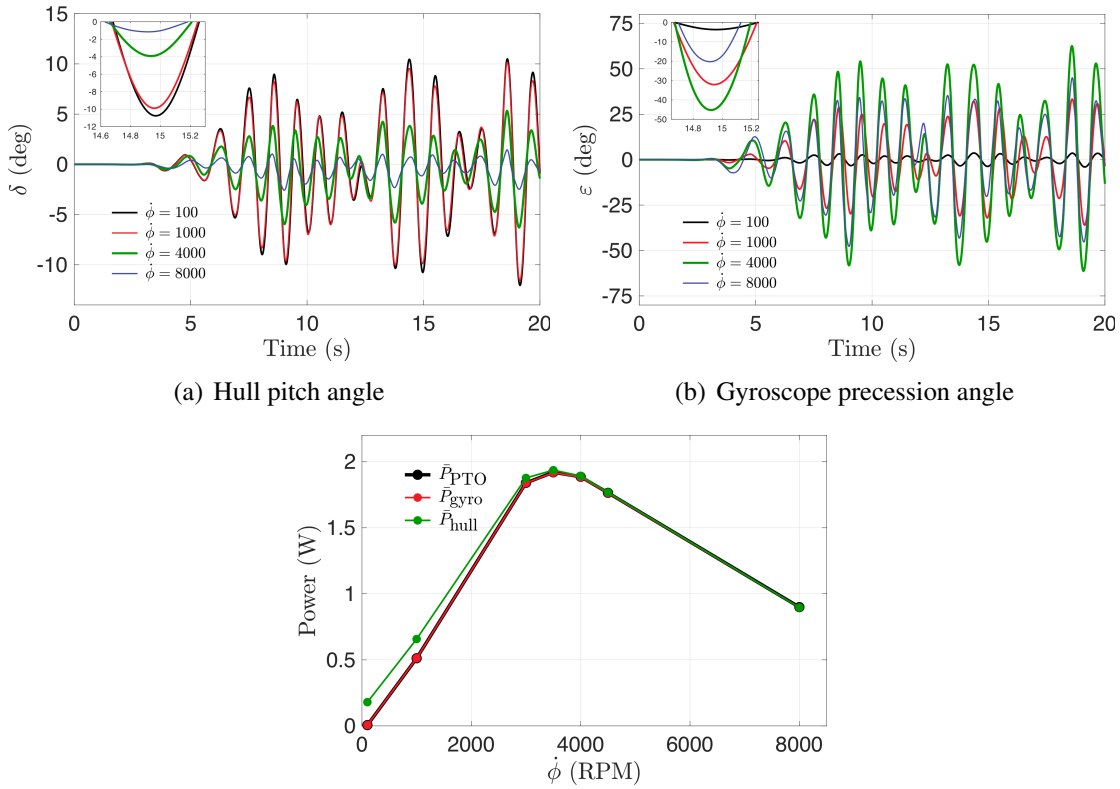

(a) Hull pitch angle

(b) Gyroscope precession angle

(c) Powers

Figure 4.19. Dynamics of the 2D ISWEC model for four different values of flywheel speed $\dot{\phi}$. The irregular wave properties are $\mathscr{H}_{\mathrm{s}}$ = 0.1 m and $\mathscr{T}_{\mathrm{p}}$ = 1 s and 50 wave components with frequencies ω_i in the range 3.8 rad/s to 20 rad/s. Temporal evolution of (a) hull pitch angle δ, and (b) gyroscope precession angle ε for $\dot{\phi}$ = 100 RPM (——, black), $\dot{\phi}$ = 1000 RPM (——, red), $\dot{\phi}$ = 4000 RPM (——, green), and $\dot{\phi}$ = 8000 RPM (——, blue); (c) comparison of time-averaged powers from the interval $t = 10$ s to $t = 20$ s for each value of $\dot{\phi}$.

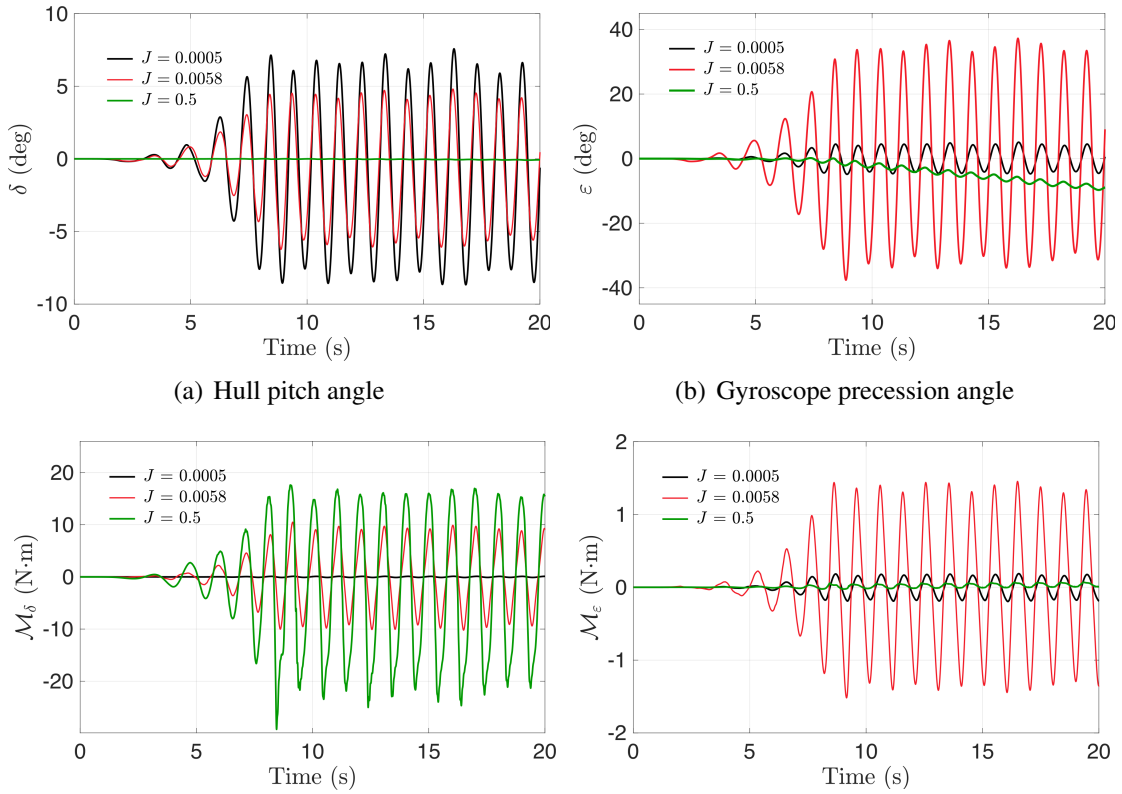

(a) Hull pitch angle

(b) Gyroscope precession angle

(c) Pitch torque unloaded on the hull

(d) Precession torque on the PTO axis

Figure 4.20. Dynamics of 2D ISWEC model for three different values of flywheel moment of inertia J. The regular wave properties are $\mathscr{H} = 0.1$ m and $\mathscr{T} = 1$ s. Temporal evolution of (a) hull pitch angle δ, (b) gyroscope precession angle ε, (c) pitch torque $\mathscr{M}_\delta$, and (d) precession torque $\mathscr{M}_\varepsilon$ for $J = 0.0005$ kg·m^2 (——, black), $J = 0.0058$ kg·m^2 (——, red), and $J = 0.5$ kg·m^2 (——, green). For all cases, $I = 0.94 \times J$.

that the light gyroscope produces insignificant precession angles and torques due to the lack of angular momentum generated by the flywheel. Moreover, the heavy gyroscope produces even smaller $\mathscr{M}_\varepsilon$ torque as it slowly drifts around the PTO axis; the proportional component of the control torque ($k\varepsilon$) is not strong enough to return the gyroscope to its mean position of $\varepsilon = 0°$. Additionally, the light (heavy) weight gyroscope produces small (large) pitch torques $\mathscr{M}_\delta$ opposing the hull, which explains the large (small) pitch amplitudes exhibited by the device. Finally, it is seen that the medium weight gyroscope, with $J = 0.0058$ kg·m^2 calculated from the procedure described in Sec. 4.4.3, produces the largest precession amplitudes ε and velocities $\dot{\varepsilon}$, leading to high power absorption by the PTO unit.

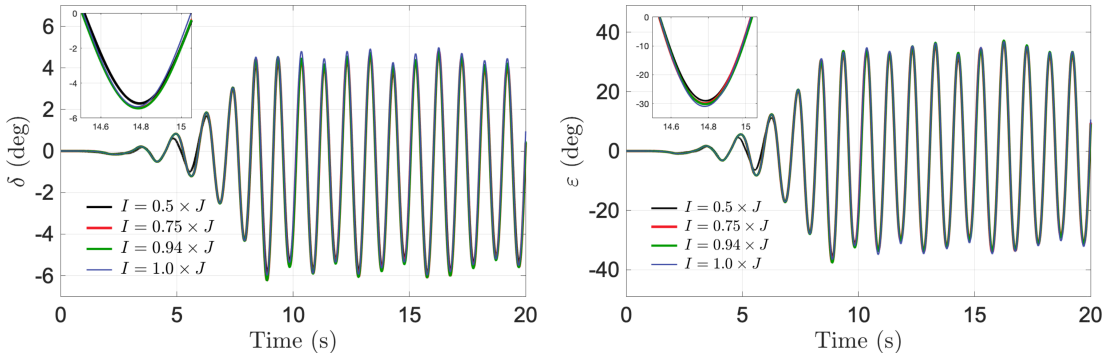

(a) Hull pitch angle

(b) Gyroscope precession angle

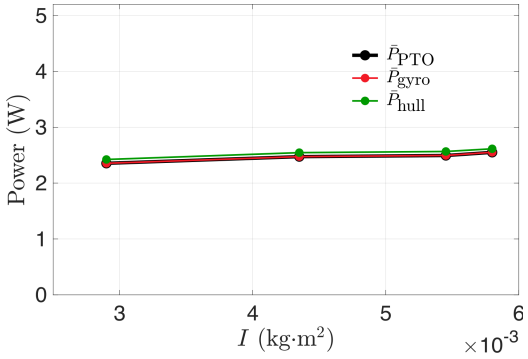

(c) Powers

Figure 4.21. Dynamics of 2D ISWEC model for four different values of I. The regular wave properties are $\mathscr{H}$ = 0.1 m and $\mathscr{T}$ = 1 s. Temporal evolution of (a) hull pitch angle δ, and (b) gyroscope precession angle ε for $I = 0.5 \times J$ (——, black), $I = 0.75 \times J$ (——, red), $I = 0.94 \times J$ (——, green), and $I = 1.0 \times J$ (——, blue). (c) Comparison of time-averaged powers from the interval $t = 10$ s to $t = 20$ s for each value of I. For all cases, J = 0.0058 kg·m^2.

We also study the effect of varying I while keeping $J = 0.0058$ kg·m^2 fixed. We consider four different values $I = 0.5 \times J$, $I = 0.75 \times J$, $I = 0.94 \times J$ and $I = 1.0 \times J$, and the results for a device interacting with regular waves are shown in Fig. 4.21. It is seen that the dynamics of the hull and gyroscope and the system powers are not significantly affected by the choice of I.

Similarly, ISWEC dynamics with irregular waves are studied for three different values of J. Results for varying J values are compared in Fig. 4.22, which are qualitatively similar to the results obtained with regular waves. The effect of varying I with respect to J is also simulated, and the results are shown in Fig. 4.23. It is seen that the hull pitch and the gyroscope precession angles are relatively insensitive to variations in I. It is seen that the powers are relatively constant

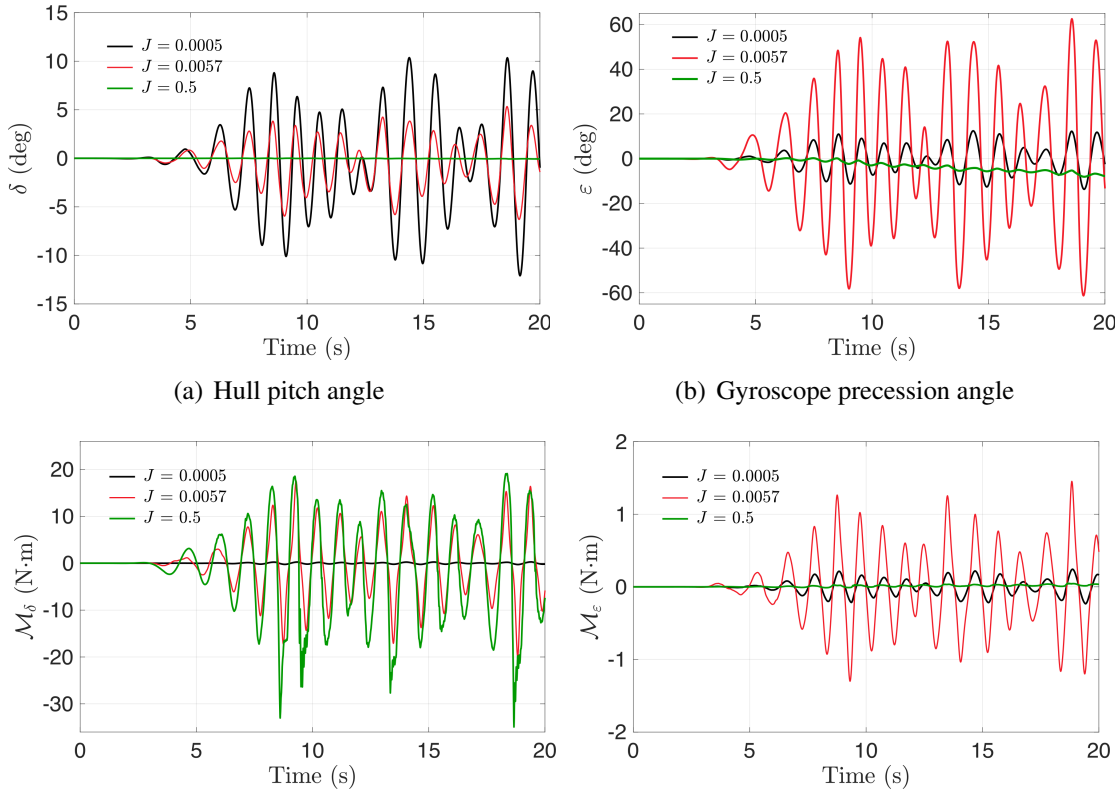

(a) Hull pitch angle

(b) Gyroscope precession angle

(c) Pitch torque unloaded on the hull

(d) Precession torque produced by the gyroscope

Figure 4.22. Dynamics of 2D ISWEC model for three different values of flywheel moment of inertia J. The irregular wave properties are $\mathscr{H}_s = 0.1$ m and $\mathscr{T}_p = 1$ s and 50 wave components with frequencies ω_i in the range 3.8 rad/s to 20 rad/s. Temporal evolution of (a) hull pitch angle δ, (b) gyroscope precession angle ε, (c) pitch torque $\mathscr{M}_\delta$, and (d) precession torque $\mathscr{M}_\varepsilon$ for $J = 0.0005$ kg·m^2 (——, black), $J = 0.0058$ kg·m^2 (——, red), and $J = 0.5$ kg·m^2 (——, green). For all cases, $I = 0.94 \times J$.

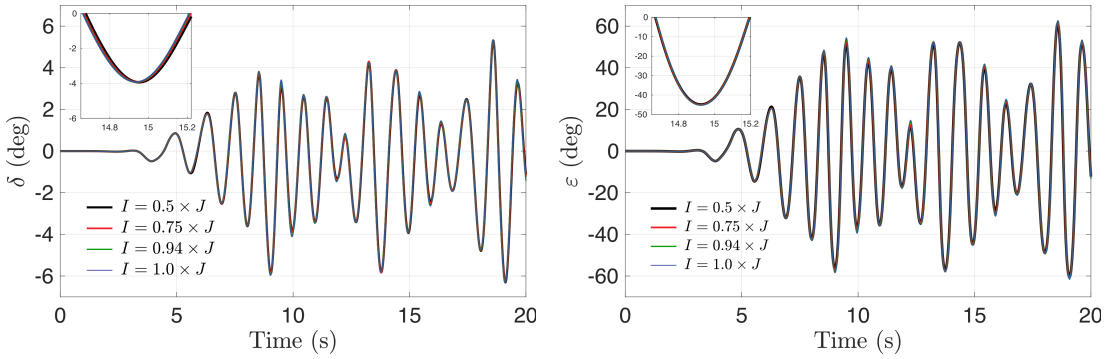

(a) Hull pitch angle

(b) Gyroscope precession angle

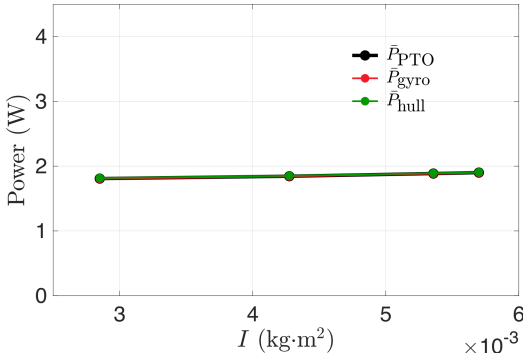

(c) Powers

Figure 4.23. Dynamics of 2D ISWEC model for four different values of I. The irregular wave properties are $\mathscr{H}_s$ = 0.1 m and $\mathscr{T}_p$ = 1 s and 50 wave components with frequencies ω_i in the range 3.8 rad/s to 20 rad/s. Temporal evolution of (a) hull pitch angle δ, and (b) gyroscope precession angle ε for $I = 0.5 \times J$ (——, black), $I = 0.75 \times J$ (——, red), $I = 0.94 \times J$ (——, green), and $I = 1.0 \times J$ (——, blue). (c) Comparison of time-averaged powers from the interval $t = 10$ s to $t = 20$ s for each value of I. For all cases, J = 0.0058 kg·m^2.

across different I values under irregular wave conditions as well.

PTO stiffness coefficient k

Finally, we study the effect of varying the PTO stiffness coefficient k on the dynamics of the ISWEC device. This term appears as a restoring torque $k\varepsilon$ in the precession angle Eq. (4.38) and acts to drive the gyroscope's oscillation about its mean position $\varepsilon = 0^\circ$. The oscillation frequency is directly influenced by k and can be chosen to ensure a resonant condition is attained between the gyroscope and the incoming waves, thus maximizing the power absorbed by the system.

We consider four different values of k = 0.0 N·m/rad, 0.2171 N·m/rad, 1.0 N·m/rad, and 5.0 N·m/rad, with the remaining gyroscope parameter chosen according to Table 4.5. The $k = 0.2171$ value is obtained from theoretical considerations provided in Sec. **??**. The results for a hull interacting with regular waves are shown in Fig. 4.24. As k increases, the maximum precession angle ε and velocity $\dot{\varepsilon}$ decreases leading to decreased power absorption by the device. The increased PTO stiffness value tends to keep the gyroscope close to its zero-mean position, which reduces the hull-gyroscope coupling. This can be observed from the lowered values of $\mathscr{M}_\delta$ torques in Fig. 4.24(c). As a consequence, the hull pitching motion increases, as seen in Fig. 4.24(a).

The $k = 0$ case warrants additional discussion. When the PTO stiffness is zero, the gyroscope attains a larger maximum precession amplitude and generates more power than the $k > 0$ cases over the time period $t = 10$ s and $t = 20$ s. However, Fig. 4.25 shows the long-term dynamics for $k = 0$; it is seen that the gyroscope is unable to sustain its precession oscillation as it eventually falls to one side ($\varepsilon = -90^\circ$) and remains there. At this configuration, the gyroscope yaw axis and the hull pitch axis are aligned, and the precession effect is lost. As these gyroscopic oscillations vanish, the torques tend towards zero, the hull exhibits unrestrained pitch oscillation, and no power is generated.

Next, we simulate ISWEC dynamics with irregular waves using four different values

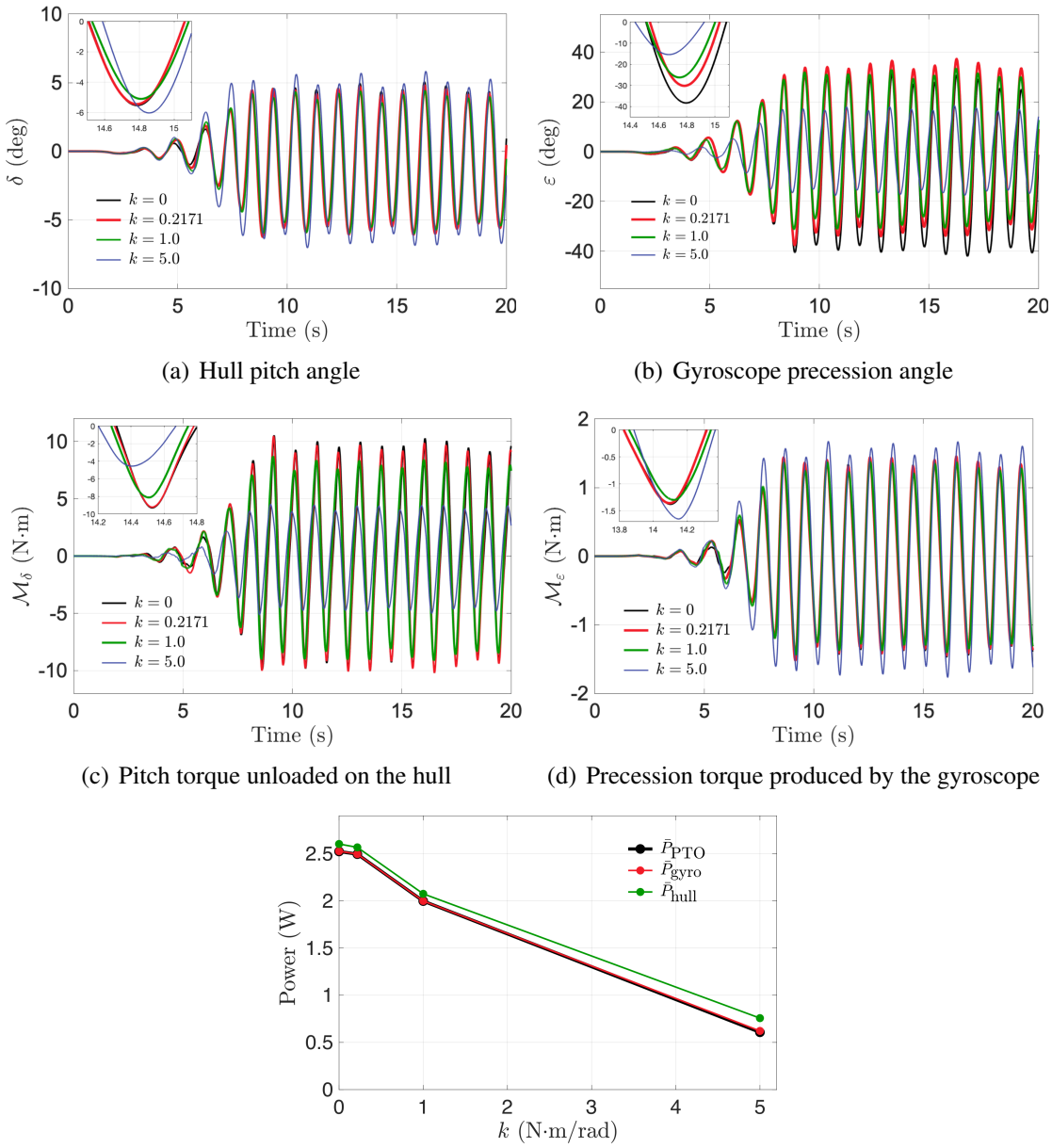

(a) Hull pitch angle

(b) Gyroscope precession angle

(c) Pitch torque unloaded on the hull

(d) Precession torque produced by the gyroscope

(e) Powers

Figure 4.24. Dynamics of 2D ISWEC model for four different values of PTO stiffness k. The regular wave properties are $\mathscr{H}$ = 0.1 m and $\mathscr{T}$ = 1 s. Temporal evolution of (a) hull pitch angle δ, (b) gyroscope precession angle ε, (c) pitch torque $\mathscr{M}_\delta$, and (d) precession torque $\mathscr{M}_\varepsilon$ for k = 0 N·m/rad (——, black), k = 0.2171 N·m/rad (——, red), k = 1.0 N·m/rad (——, green), and k = 5.0 N·m/rad (——, blue); (e) comparison of time-averaged powers from the interval $t = 10$ s to $t = 20$ s for each value of k.

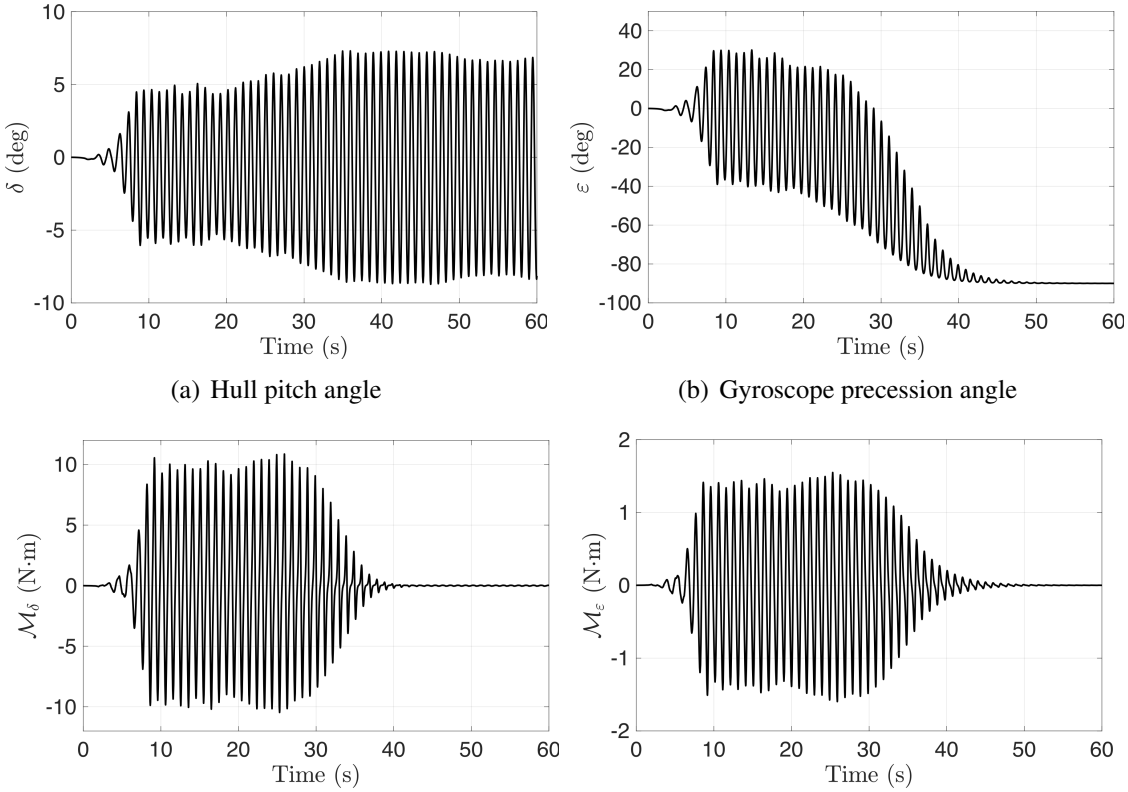

(a) Hull pitch angle

(b) Gyroscope precession angle

(c) Pitch torque unloaded on the hull

(d) Precession torque produced by the gyroscope

Figure 4.25. Long-term dynamics of the 2D ISWEC model for $k = 0$ PTO stiffness: (a) hull pitch angle δ, (b) gyroscope precession angle ε, (c) pitch torque $\mathscr{M}_\delta$, and (d) precession torque $\mathscr{M}_\varepsilon$. The regular wave properties are $\mathscr{H}$ = 0.1 m and $\mathscr{T}$ = 1 s.

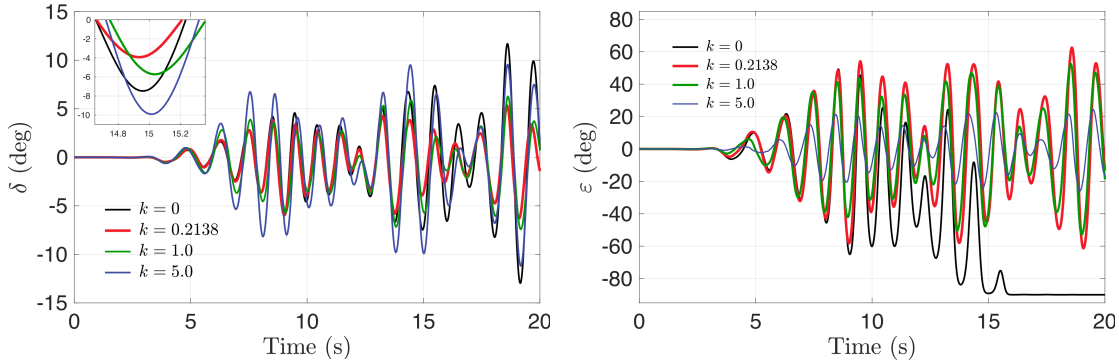

(a) Hull pitch angle

(b) Gyroscope precession angle

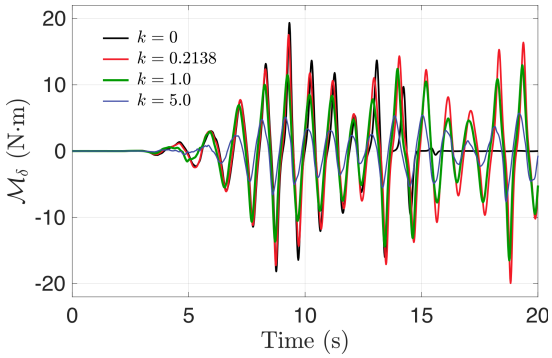

(c) Pitch torque unloaded on the hull

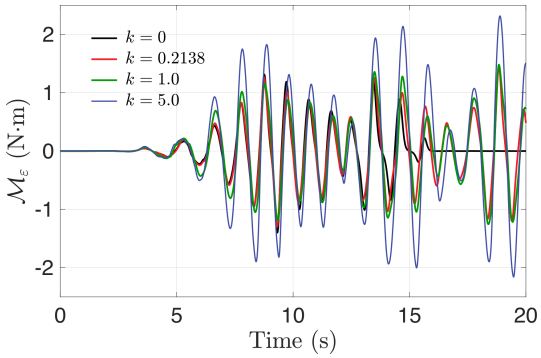

(d) Precession torque produced by the gyroscope

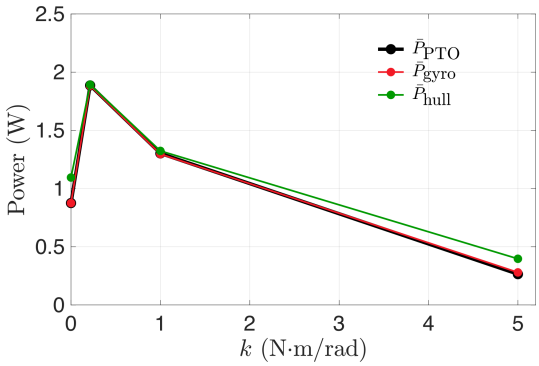

(e) Powers

Figure 4.26. Dynamics of 2D ISWEC model for four different values of PTO stiffness k. The irregular wave properties are $\mathscr{H}_s = 0.1$ m and $\mathscr{T}_p = 1$ s and 50 wave components with frequencies ω_i in the range 3.8 rad/s to 20 rad/s. Temporal evolution of (a) hull pitch angle δ, (b) gyroscope precession angle ε, (c) pitch torque $\mathscr{M}_\delta$, and (d) precession torque $\mathscr{M}_\varepsilon$ for $k = 0$ N·m/rad (——, black), $k = 0.2138$ N·m/rad (——, red), $k = 1.0$ N·m/rad (——, green), and $k = 5.0$ N·m/rad (——, blue); (e) comparison of time-averaged powers from the interval $t = 10$ s to $t = 20$ s for each value of k.

Table 4.6. Calculated values of PTO and gyroscope parameters for different L/λ ratios using L = 0.7665 m, δ_0 = 10°, ε_0 = 70°, and $\dot{\phi}$ = 4000 RPM. $I = 0.94 \times J$ for all cases. Regular water waves with $\mathscr{H}$ = 0.1 m are simulated. The rated power of the device $\bar{P}_{\mathrm{R}}$ is taken to be the available wave power $\bar{P}_{\mathrm{wave}}$ for these calculations. Units: λ is in m, c is in N·m·s/rad, J and I are in kg·m^2 and k is in N·m/rad.

L/λ	λ	PTO and gyroscope parameters		
		c	J	k
0.25	3.0659	1.3491	0.0225	0.3705
0.5	1.5456	0.3473	0.0058	0.2171
0.75	1.0219	0.1773	0.0029	0.1679

of k = 0 N·m/rad, 0.2138 N·m/rad, 1.0 N·m/rad, and 5.0 N·m/rad. The results are compared in Fig. 4.26, and are qualitatively similar to the those obtained with regular waves. Similar behavior of the ISWEC with k = 0 is observed — the gyroscope is unable to oscillate and falls to one side ($\varepsilon = -90°$) and produces vanishing precession effects. However, with irregular waves the precession effects are lost much sooner compared to the regular waves case.

4.7.3 Hull length to wavelength (L/λ) variation

In this section, we study the effect of hull length to wavelength ratio (L/λ) on ISWEC dynamics. We select three ratios L/λ = 0.25, 0.5 and 0.75 for this analysis. The length of the hull is kept constant at L = 0.7665 m, and the wavelength of the regular water waves is varied. The PTO and gyroscope parameters used in the three simulations are presented in Table 4.6. Results consist of temporal evolution of the hull pitch and gyroscope precession angles in Figs. 4.27(a) and 4.27(b), respectively. It is observed that the hull pitch is maximum when $\lambda/3 \leq L \leq \lambda/2$, as discussed in Sec. 4.4.4. As a consequence, the gyroscope precesses more and the conversion efficiency of the device increases (see Fig. 4.27(c)).

4.7.4 Device protection during inclement weather conditions

The ISWEC hull houses costly electro-mechanical components that need to be protected during harsh, stormy weather conditions. During inclement weather, the hull and gyroscope dynamics can be chaotic, which may damage the system components. To protect the housed

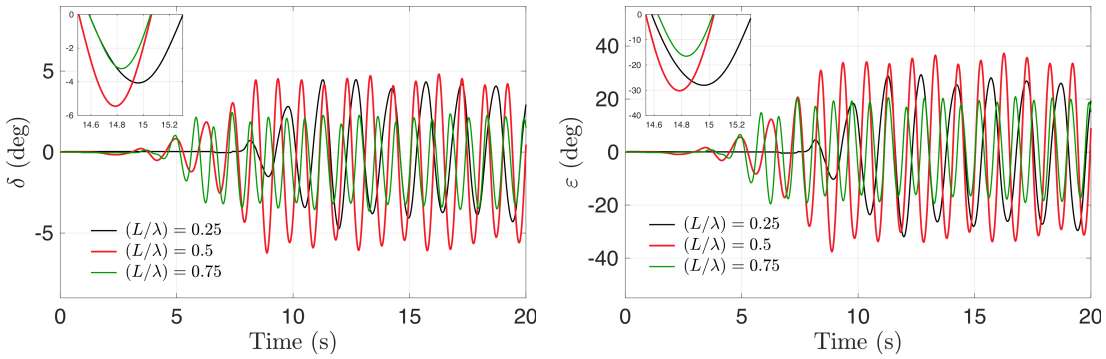

(a) Hull pitch angle

(b) Gyroscope precession angle

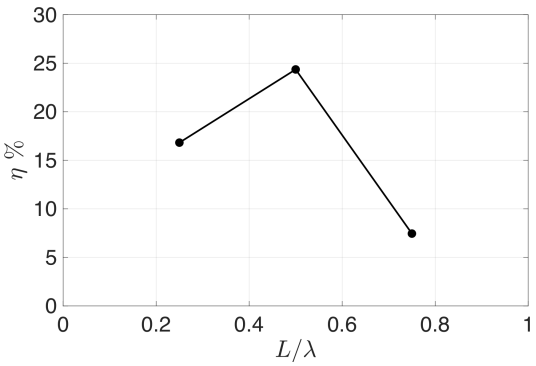

(c) RCW

Figure 4.27. Dynamics of 2D ISWEC model for three different hull length to wavelength ratios L/λ. The regular wave height is $\mathscr{H} = 0.1$ m, while its period $\mathscr{T}$ is calculated based on the dispersion relation given by Eq. (4.3) as wavelength λ is varied. Temporal evolution of (a) hull pitch angle δ and (b) gyroscope precession angle ε for $L/\lambda = 0.25$ (——, black), $L/\lambda = 0.5$ (——, red), and $L/\lambda = 0.75$ (——, green); (c) RCW η computed using time-averaged powers from the interval $t = 10$ s to $t = 20$ s for each value of L/λ.

components, the gyroscope needs to be turned off. This can be done by reducing the flywheel speed to zero using remote human-machine interfaces. The combined hull-gyroscope system then behaves like a single floating entity. In this section, we simulate the dynamics of the ISWEC device as the flywheel speed is reduced to zero amidst steady operation. We simulate this scenario with regular water waves of $\mathscr{H}$ = 0.1 m and $\mathscr{T}$ = 1 s. To reduce the flywheel speed from 4000 RPM to 0 RPM, we use the following relation

$$\dot{\phi}(t) = 4000 \cdot (1 - f(t))/2, \tag{4.71}$$

in which $f(t)$ is a function that smoothly transitions from -1 to 1 in the transition time interval ΔT. The function f is given by

$$f = \tanh\left(\frac{2\pi(t - T_{\text{half}})}{\Delta T}\right), \tag{4.72}$$

in which $T_{\text{half}} = T_{\text{start}} + \Delta T/2$. In our simulation, we set T_{start} = 15 s and ΔT = 5 s. Fig. 4.28(e) shows the smooth transition of the flywheel speed towards zero in 5 s. When the gyroscope is turned off, the precession effects cease and the system attains a mean zero position, thus protecting the device. This is seen in Figs. 4.28(b), 4.28(c), and 4.28(d), which show that ε, $\mathscr{M}_\delta$, and $\mathscr{M}_\varepsilon$ are reduced to zero, respectively. As the gyroscopic effects vanish, the hull is observed to be oscillating with greater pitch amplitude (Fig. 4.28(a)).

4.7.5 Two degrees of freedom ISWEC mode

We compare the hull and gyroscope dynamics obtained using two degrees of freedom (pitch and heave) and one degree of freedom (pitch only) ISWEC models. The same case from Sec. 4.6.1 is simulated using the two models on a medium grid resolution. Figs. 4.29(a) and 4.29(b) show the comparison of hull pitch angle δ and gyroscope precession angle ε, respectively. As can be seen in Fig. 4.29, including an additional heave degree of freedom

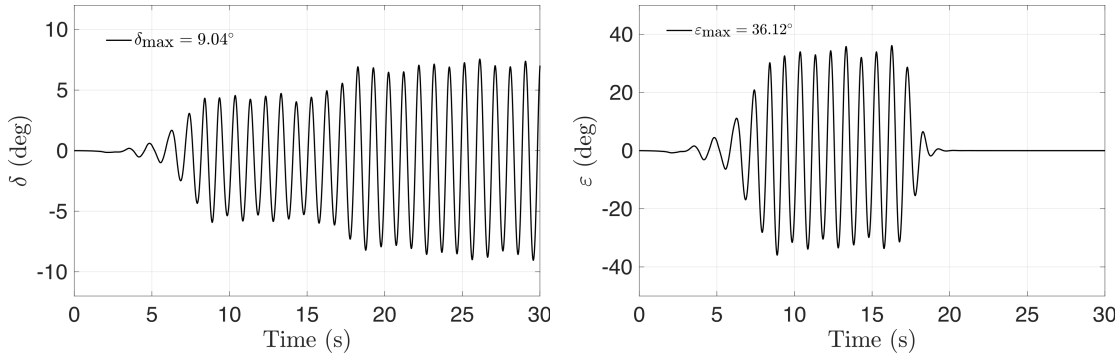

(a) Hull pitch angle

(b) Gyroscope precession angle

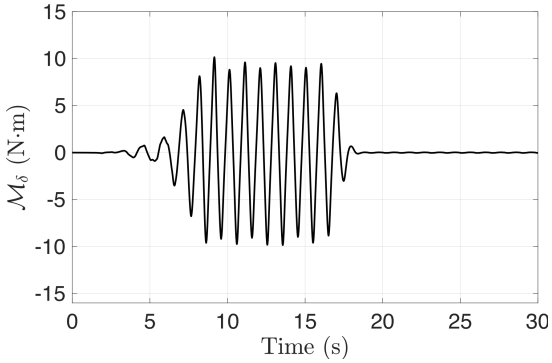

(c) Pitch torque unloaded on the hull

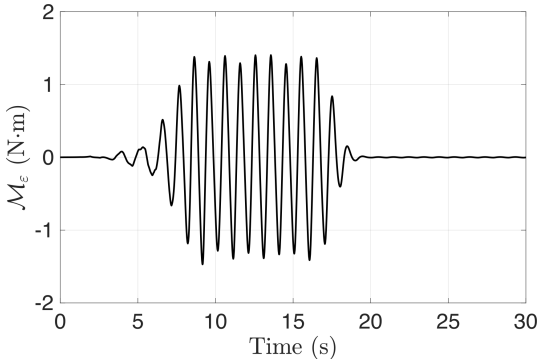

(d) Precession torque on PTO axis

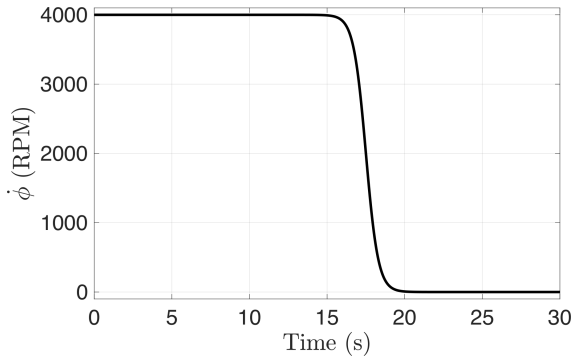

(e) Flywheel speed

Figure 4.28. Dynamics of 2D ISWEC model as the flywheel speed $\dot{\phi}$ is reduced from 4000 RPM to 0 RPM amidst steady operation. The regular wave properties are $\mathscr{H}$ = 0.1 m and $\mathscr{T}$ = 1 s. Temporal evolution of (a) hull pitch angle δ; (b) gyroscope precession angle ε; (c) pitch torque $\mathscr{M}_\delta$; (d) precession torque $\mathscr{M}_\varepsilon$; and (e) temporal variation of flywheel speed.

only marginally affects the rotational motion of the hull and gyroscope, and consequently the power output of the device. Fig. 4.29(c) shows the heave dynamics of the hull about its mean z-location. The heave amplitude is approximately one-tenth of the hull height for the prescribed

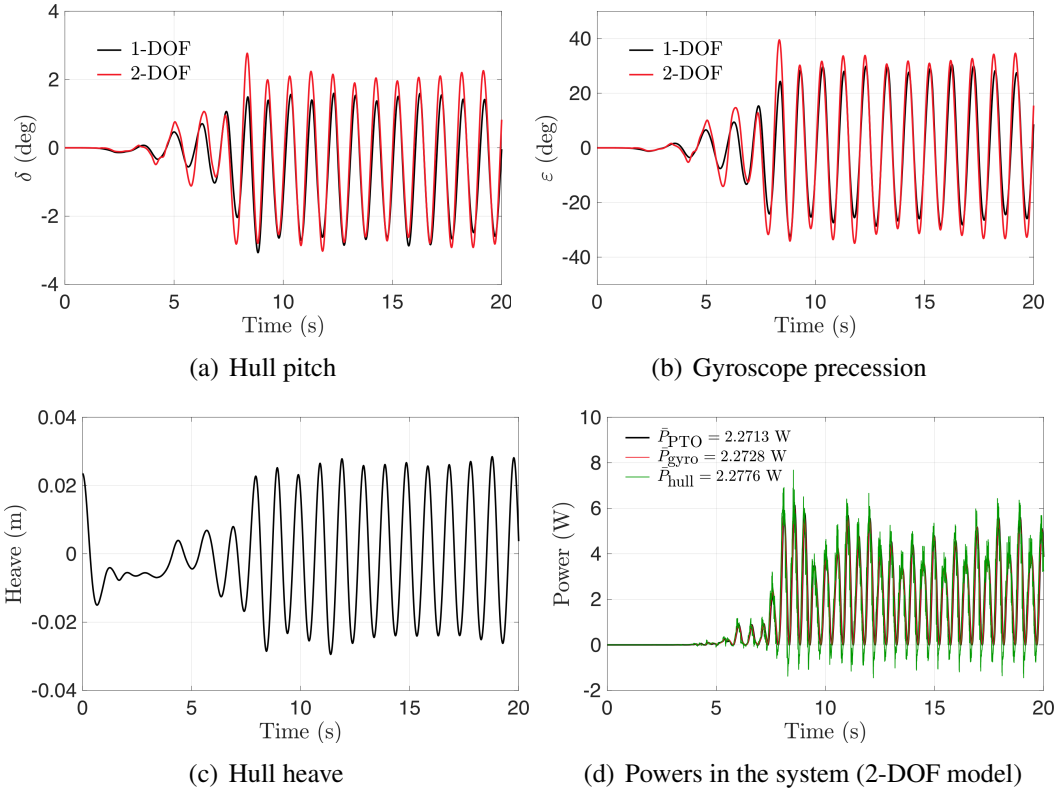

(a) Hull pitch (b) Gyroscope precession

(c) Hull heave (d) Powers in the system (2-DOF model)

Figure 4.29. Comparison of 2-DOF (pitch and heave) and 1-DOF (pitch only) ISWEC models for (a) hull pitch angle δ, and (b) gyroscope precession angle ε. (c) Hull heave displacement, and (d) power at various levels for the 2-DOF ISWEC model. Fifth-order regular water waves are generated with $\mathscr{H} = 0.1$ m, $\mathscr{T} = 1$ s and $\lambda = 1.5456$ m, satisfying the dispersion relation given by Eq. (4.2). A maximum ISWEC pitch angle $\delta_0 = 5^\circ$ and a maximum gyroscope precession angle of $\varepsilon_0 = 70^\circ$ are used. The gyroscope parameters are: damping coefficient $c = 0.3473$ N·m·s/rad, moment of inertia $J = 0.0116$ kg·m^2, and PTO stiffness $k = 0.4303$ N·m/rad. The speed of the flywheel is $\dot{\phi} = 4000$ RPM, and $I = 0.94 \times J = 0.0109$ kg ·m^2.

wave characteristics. Although the heave motion is not negligible in this case, it nonetheless does not significantly affect the rotational dynamics. In contrast to heave, the surge degree of freedom can affect the relative phase between the wave excitation forces and the body motion, which can lead to a different set of optimal parameters of the device than those found without considering the surge motion. However, the surge motion of the ISWEC device is assumed to be negligible, because of the motion constraints imposed by the mooring system. Finally, Fig. 4.29(d) shows that the power transfer equation is satisfied even for the 2-DOF ISWEC model.

4.8 Conclusions

In this study, we systematically investigated the wave-structure interaction dynamics of the inertial sea wave energy converter (ISWEC) device implemented with a reactive control strategy. Our computational model is based on the incompressible Navier-Stokes equations and employs a fictitious domain Brinkman penalization (FD/BP) approach to handle the fluid-structure coupling. The dynamics of the ISWEC hull and gyroscope system were coupled to this CFD solver to enable fully-resolved 1-DOF simulations of the device. To emulate realistic operating conditions of the device, a numerical wave tank was used to generate both regular waves based on fifth-order Stokes theory and irregular waves based on the JONSWAP spectrum. We performed Froude scaling analysis of the full-scale ISWEC model to determine the required parameters for our 1:20 scaled-down two- and three-dimensional simulations.

Our numerical investigation demonstrated that the 2D model was sufficient to accurately simulate the hull's pitching motion, and to predict the power generation/absorption capability of the converter. We showed that setting the prescribed hull pitch angle parameter δ_0 close to the maximum wave steepness will maximize the device's relative capture width (i.e. power generation efficiency). A comprehensive parameter sweep demonstrated that the device achieves peak performance when the gyroscope specifications are chosen based on the reactive control theory described in Sec. 4.4.3. It was also shown that a proportional control of the PTO control torque is required to generate continuous precession effects of the gyroscope, without which the gyroscope tends to align with the hull pitch axis. Under this scenario, the device does not generate any power. We also showed that although the yaw torque in the gyroscope reference frame is small, it is of the same order of magnitude as the pitch torque induced on the hull in an inertial reference frame. Therefore, the yaw torque on the hull should be considered in the design phase of these devices to avoid any misalignment of the converter from the main wave direction. Our simulations also verify that the hull length to wavelength ratio should be between one-half and one-third to achieve high conversion efficiency. Throughout our parameter study,

we numerically verify the theoretical power transfer pathway between the water waves and the hull, the hull and the gyroscope, and the gyroscope to the PTO unit for both regular and irregular wave environments. Although the power transfer is derived for ISWEC devices in this work, an analogous relationship could be derived for heaving or surging point absorbers. Finally, we investigated the dynamics of the ISWEC system as the flywheel speed is reduced to zero to emulate device protection during inclement weather conditions.

By making use of high performance computing, our work demonstrates that it is feasible to use fully-resolved simulations to interrogate the device physics and dynamics of wave energy converters. They can also be used as a design tool to explore the parametric space for further optimization of such devices.

One of the primary drawbacks of the reactive control strategy is its reliance on drawing power from the grid (resulting in negative power), thereby reducing the overall generated power. Additionally, the stiffness of the system must be adjusted to accommodate changes in sea state so that the device resonants with the frequency of the incoming waves. In the subsequent chapter, we introduce an optimal control strategy known as model predictive control (MPC) and implement it for a point absorber WEC device. Our objective is to optimize power absorption and mitigate the need for power flow from the grid to the device eliminating the drawbacks of the reactive control strategy.

Acknowledgement

This chapter, in full, is a reprint of the material as it appears in “The inertial sea wave energy converter (ISWEC) technology: Device-physics, multiphase modeling and simulations”, Kaustubh Khedkar, Nishant Nangia, Ramakrishnan Thirumalaisamy, Amneet Pal Singh Bhalla, Ocean Engineering, Volume 229, 2021. The dissertation author was the primary investigator and author of this paper.

Chapter 5

Model Predictive Control Strategy for Wave Energy Converter Devices

In this chapter, we present a novel MPC-integrated multiphase IB framework that can compute the optimal energy-maximizing control force "on-the-fly" by dynamically interacting with a high-fidelity numerical wave tank (NWT). The computational model closely mimics the working setup of the device at its site of operation. Due to the requirement of solving a constrained optimization problem at each time step of the IB simulation, the MPC algorithm utilizes a low-dimensional dynamical model of the device that is based on the linear potential theory (LPT). The multiphase IB solver, on the other hand, is based on the high-dimensional fictitious domain Brinkman penalization (FD/BP) method presented in Chapter 2 and 3, which fully-resolves the hydrodynamic non-linearities associated with the wave–structure interaction (WSI). A time-series forecasting auto-regressive model is implemented that predicts wave heights (from the past NWT data) to estimate the future wave excitation/Froude–Krylov forces for the MPC algorithm. Moreover, we also experiment with non-linear Froude–Krylov (NLFK) forces for the first time in an MPC formulation. The NLFK forces are computed efficiently using a static Cartesian grid, in which the WEC geometry is implicitly represented by a signed distance function. Under varying sea conditions, the predictions of the MPC-integrated multiphase IB solver are compared to the widely popular LPT-based solvers. In agitated sea conditions and/or under aggressive control, the LPT-based WSI solvers produce too optimistic (and misleading)

power output values. Overall, six WSI/MPC solver combinations are compared for a heaving vertical cylinder to determine the reasons for discrepancies between high- and low-fidelity predictions. We also determine the pathway of energy transfer from the waves to the power take-off (PTO) system and verify the relationships using IB simulations. Additionally, three different sea states are simulated within the IB simulation to test the adaptive capability of MPC for WECs. MPC is demonstrated to adapt to changing sea conditions and find the optimal solution for each sea state.

The interaction between the distributed-memory parallel multiphase IB solver (written in C++) and the serial MPC solver (written in MATLAB) is fully described to facilitate reproducibility. A bespoke communication layer between the two solvers is developed, which can be easily modified by the WEC community to experiment with other optimal controllers and computational fluid dynamics (CFD) solvers. All codes for this work are made open-source for pedagogical and research purposes.

5.1 Introduction

Unlike previous control-integrated CFD studies mentioned in the Sec. 5.1 that used pre-computed controller gains or optimal control force sequences, this work uses the model predictive control (MPC) algorithm to compute the optimal energy-maximizing control force online. Due to its ability to handle many types of device and PTO topologies, model predictive control of WECs has been dubbed the "Tesla" of controllers [122]. In our modeling approach, the MPC interacts with the CFD-based NWT that sends the wave elevation and device dynamics data to the controller, which then solves a constrained optimization problem to find the optimal control force sequence. In the NWT, both regular and irregular sea conditions are modeled. The predictions of the MPC-integrated CFD solver are compared to the MPC-integrated boundary element method (BEM) solvers under varying sea conditions. The current study is the first of its kind and comprehensively examines the reasons for prediction discrepancies between different

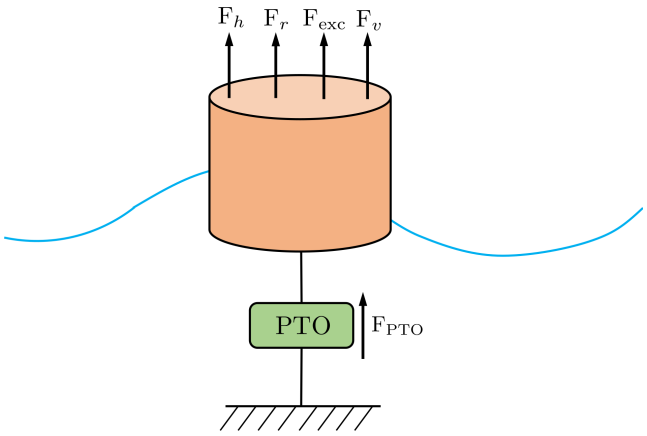

Figure 5.1. Schematic representation of a 1 DOF heaving cylindrical wave energy converter device.

solvers.

5.2 Linear potential theory based WEC dynamical model

The WEC device considered in this study is a one degree of freedom (DOF) cylindrical point absorber[1] that heaves on the air-water interface. A schematic representation of the device is shown in Fig. 5.1. Axisymmetric point absorbers are among the most common WEC-types that mainly absorb wave energy due to their heaving motion. Therefore, for such devices, motion in the other DOFs can be neglected (or is constrained). If the amplitude of the motion of the device is significantly smaller than the wave height, then according to the LPT, the total force acting on the body is a linear sum of the hydrostatic restoring force F_h, radiation force F_r, wave excitation (including wave diffraction) force F_{exc}, and the viscous drag force F_v. The wave-induced motion of the device is retarded by the controller to extract the electrical energy. The WEC controller is typically embedded within a power take-off unit, which exerts the actuator/control force F_{PTO} on the device.

Using the Newton's second law of motion, the dynamics of the device in the heave

[1]Point absorber is a WEC device whose characteristic dimensions are much smaller than the sea/ocean wavelength.

direction (z) can be written as

$$m\ddot{z}(t) = \mathrm{F}_h(t) + \mathrm{F}_r(t) + \mathrm{F}_{\mathrm{exc}}(t) + \mathrm{F}_v(t) + \mathrm{F}_{\mathrm{PTO}}(t), \tag{5.1}$$

in which m is the mass of the cylinder, $z(t), \dot{z}(t)$, and $\ddot{z}(t)$ are the displacement (from the mean equilibrium position), velocity, and acceleration of the device in the heave direction, respectively.

The hydrostatic restoring force due to buoyancy is given by

$$\mathrm{F}_h(t) = -k_{\mathrm{stiff}} \cdot z(t), \tag{5.2}$$

in which k_{stiff} is the hydrostatic stiffness coefficient. For a cylindrical shaped body, the hydrostatic stiffness coefficient is given by $k_{\mathrm{stiff}} = \rho_{\mathrm{w}} g \pi R_{\mathrm{cyl}}^2$, in which ρ_{w} is the density of water, g is the acceleration due to gravity, and R_{cyl} is the radius of the cylinder. The length of the vertical cylinder is L_{cyl}. For a vertical heaving cylinder, k_{stiff} does not change with time because the water plane area of the body does not change. A possible means of modeling nonlinear buoyancy forces for floating bodies whose water plane areas differ is discussed in Sec. 5.4.2. In addition, Giorgi et al. [76, 77] describe an analytical approach to model nonlinear buoyancy forces.

The radiation force $\mathrm{F}_r(t)$ in Eq. (5.1) is written as

$$\mathrm{F}_r(t) = -m_\infty \ddot{z}(t) - \int_0^t \mathrm{K}_r(t-\tau)\dot{z}(\tau)\, \mathrm{d}\tau. \tag{5.3}$$

Here, m_∞ is the added mass [2] at infinite frequency. The radiation force in Eq. (5.3) also includes a convolution integral of the radiation impulse response function (RIRF) $\mathrm{K}_r(t)$ with the velocity of the body. Physically, RIRF explains how kinetic energy is dissipated by the water waves produced by the oscillation of the body, which began its motion at time $t = 0$ and continues to do so until current time t.

Excitation forces due to incident/incoming waves can be computed on either a mean or

[2] The added mass represents the additional inertia of the system due to the motion of the surrounding fluid.

instantaneous wetted surface of the device. In the former case, excitation forces can be expressed as a convolution integral between the wave impulse response function (WIRF) $\mathrm{K}_e(t)$ and the undisturbed wave surface elevation $\eta_{\mathrm{wave}}(t;x_B)$ at the device location x_B:

$$\mathrm{F}_{\mathrm{exc}}(t) = \mathrm{K}_e * \eta_{\mathrm{wave}} = \int_{-\infty}^{\infty} \mathrm{K}_e(\tau)\eta_{\mathrm{wave}}(t-\tau;x_B)\,\mathrm{d}\tau. \tag{5.4}$$

From Eq. (5.4) it can be seen that $\mathrm{F}_{\mathrm{exc}}(t)$ is non-causal because future surface elevations affect the current motion of the body. The non-causality of WIRF has practical implications when it comes to the implementation of MPC of WECs, since the wave elevations at the device location must be forecasted. Discussion of wave prediction is deferred to Sec. 5.4.1. In Sec. 5.4.2, we discuss the evaluation of wave excitation forces using the instantaneous wetted surface.

Lastly, the viscous drag force acting on the body can be written using the non-linear Morison equation [123] as

$$\mathrm{F}_v(t) = -\frac{1}{2}\rho_{\mathrm{w}} C_d \pi R_{\mathrm{cyl}}^2 |\dot{z}(t)|\dot{z}(t), \tag{5.5}$$

in which C_d is the coefficient of drag. Estimating an accurate value of C_d for Eq. (5.5) is a non-trivial task. This work estimates C_d by equating the work done $\left(\int_0^T \mathrm{F}_v \dot{z}\,\mathrm{d}\tau\right)$ by viscous forces on a freely decaying cylinder that heaves on an air-water interface in a NWT with the work done by viscous forces defined according to Eq. ((5.5)). We chose one period of the damped oscillation for the integral.

Putting all terms together, the governing equation for the 1 DOF heaving WEC reads as

$$\ddot{z}(t) + \frac{1}{m+m_\infty}\int_0^t \mathrm{K}_r(t-\tau)\dot{z}(\tau)\mathrm{d}\tau + \frac{1}{m+m_\infty}k_{\mathrm{stiff}}\cdot z(t) = u(t) + v(t) + \frac{\mathrm{F}_v(t)}{m+m_\infty}, \tag{5.6}$$

in which

$$u(t) = \frac{\mathrm{F}_{\mathrm{PTO}}(t)}{m+m_\infty}, \quad v(t) = \frac{\mathrm{F}_{\mathrm{exc}}(t)}{m+m_\infty}.$$

To obtain $\mathrm{K_e}(t)$ and m_∞, we use the boundary element method software ANSYS AQWA [124]. The radiation convolution integral given by Eq. (5.3) is approximated in a state-space form [125] with velocity of the device $\dot{z}(t)$ as input and the approximated convolution integral as output. The state-space representation offers both computational efficiency [126] and representational convenience for matrix-based MPC control. Following Yu and Falnes [125], the state-space representation of the radiation convolution integral reads as

$$\begin{aligned} \dot{\boldsymbol{x}}_{\boldsymbol{r}}(t) &= \mathbf{A}_{\boldsymbol{r}}\boldsymbol{x}_{\boldsymbol{r}}(t) + \mathbf{B}_{\boldsymbol{r}}\dot{z}(t) \\ \int_0^t \mathrm{K}_r(t-\tau)\dot{z}(\tau)\mathrm{d}\tau &\approx \mathbf{C}_{\boldsymbol{r}}\boldsymbol{x}_{\boldsymbol{r}}(t), \end{aligned} \tag{5.7}$$

in which $\boldsymbol{x}_{\boldsymbol{r}} \in \mathbb{R}^{n_r \times 1}$, $\mathbf{A}_{\boldsymbol{r}} \in \mathbb{R}^{n_r \times n_r}$, $\mathbf{B}_{\boldsymbol{r}} \in \mathbb{R}^{n_r \times 1}$, $\mathbf{C}_{\boldsymbol{r}} \in \mathbb{R}^{1 \times n_r}$, and $n_r = 3$ is the approximation order of the radiation force used in this work. The viscous drag force acting on the cylinder is linearized around the current velocity of the cylinder $\dot{z}_0(t)$ and is approximated as

$$\mathrm{F}_v(t) \approx -\beta\,|\dot{z}_0|\,\dot{z}_0 + 2\beta\,|\dot{z}_0|\,\dot{z}, \tag{5.8}$$

in which β[3] $= -\frac{1}{2}\rho_{\mathrm{w}} C_d \pi R_{\mathrm{cyl}}^2$. Using Eqs. ((5.6))-((5.8)), a continuous-time, linear state-space form governing the dynamics of the WEC device is obtained as

$$\dot{\mathbf{X}}_{\boldsymbol{c}}(t) = \mathbf{A}_{\boldsymbol{c}}\mathbf{X}_{\boldsymbol{c}}(t) + \mathbf{B}_{\boldsymbol{c}}\left(u_c(t) + v_c(t) - \beta\,|\dot{z}_0|\,\dot{z}_0\right), \tag{5.9}$$

$$\mathbf{Z}_{\boldsymbol{c}}(t) = \mathbf{C}_{\boldsymbol{c}}\mathbf{X}_{\boldsymbol{c}}(t), \tag{5.10}$$

[3]The definition of β here is different from the one in Chapter 2 and 4

in which the subscript c denotes the continuous-time quantities and

$$\mathbf{A_c} = \begin{bmatrix} 0 & 1 & \mathbf{0} \\ -\frac{k_{\text{stiff}}}{(m+m_\infty)} & \frac{2\beta|\dot{z}_0(t)|}{(m+m_\infty)} & -\frac{\mathbf{C_r}}{(m+m_\infty)} \\ 0 & \mathbf{B_r} & \mathbf{A_r} \end{bmatrix} \in \mathbb{R}^{(n_r+2)\times(n_r+2)}, \quad \mathbf{B_c} = \begin{bmatrix} 0 \\ 1 \\ \mathbf{0} \end{bmatrix} \in \mathbb{R}^{(n_r+2)\times 1},$$

$$\mathbf{C_c} = \begin{bmatrix} 1 & 0 & \mathbf{0} \\ 0 & 1 & \mathbf{0} \end{bmatrix} \in \mathbb{R}^{2\times(n_r+2)}, \quad \mathbf{X_c}(t) = \begin{bmatrix} z(t) \\ \dot{z}(t) \\ \boldsymbol{x_r}(t) \end{bmatrix} \in \mathbb{R}^{(n_r+2)\times 1}, \quad \mathbf{Z_c}(t) = \begin{bmatrix} z(t) \\ \dot{z}(t) \end{bmatrix} \in \mathbb{R}^{2\times 1}.$$

Let us note that except for the linearized drag coefficient, all entries of matrices $\mathbf{A_c}$ and $\mathbf{B_c}$ are time invariant. Therefore, the dynamical system described by Eqs. (5.9) and (5.10) is quasi linear time invariant (QLTI). The dynamical system is reduced to an LTI one if the drag coefficient is linearized around a fixed point, e.g., around the mean equilibrium position of the device.

5.3 Model predictive control of WECs

Having discussed the control-oriented dynamical model of the WEC device, we now focus our attention on model predictive control for WECs. Its basic principles are straightforward. For each control sequence, the controller uses the dynamical model of the plant to predict the plant's future trajectory over a prediction horizon (time period) of $\mathscr{T}_h$. Out of a large set of possible outcomes, MPC selects the control sequence which extremizes (maximizes or minimizes) a predefined objective function. The extremization of the objective function is typically achieved by solving an optimization problem numerically. The first part/signal of the optimal control sequence is used to control the plant, while the rest is discarded. This process is repeated again and again by receding/moving the prediction horizon forward. With WECs, the control objective is to maximize the device's energy output. Thus, to implement MPC for WECs, we require:

1. A discrete-time dynamical model of the device to predict the future dynamics over a finite time horizon $\mathscr{T}_h$. In this work we use the first order hold (FOH) method of Cretel

et al. [127] to obtain the discrete-time model [128] from the continuous-time Eqs. (5.9) and (5.10). More specifically, if Δt denotes the discrete time step size and $k \in \mathbb{N}$ denotes the (discrete) time index, then the current state $\mathbf{X_d}(k)$ is advanced to the next time level $\mathbf{X_d}(k+1)$ as

$$\mathbf{X_d}(k+1) = \mathbf{A_d}\mathbf{X_d}(k) + \mathbf{B_d}\Delta u_d(k+1) + \mathbf{F_d}\Delta v_d(k+1), \tag{5.11}$$

$$\mathbf{Z_d}(k) = \mathbf{C_d}\mathbf{X_d}(k), \tag{5.12}$$

in which the subscript d denotes the discrete-time quantities and

$$\mathbf{A_d} = \begin{bmatrix} \phi(\Delta t) & \Upsilon & \Upsilon \\ 0 & 1 & 0 \\ 0 & 0 & 1 \end{bmatrix} \in \mathbb{R}^{(n_r+4)\times(n_r+4)}, \quad \mathbf{B_d} = \begin{bmatrix} \Lambda \\ 1 \\ 0 \end{bmatrix} \in \mathbb{R}^{(n_r+4)\times 1},$$

$$\mathbf{F_d} = \begin{bmatrix} \Lambda \\ 0 \\ 1 \end{bmatrix} \in \mathbb{R}^{(n_r+4)\times 1}, \quad \mathbf{C_d} = \begin{bmatrix} 1 & 0 & 0 & \dots & 0 & 0 & 0 \\ 0 & 1 & 0 & \dots & 0 & 0 & 0 \\ 0 & 0 & 0 & \dots & 0 & 1 & 0 \end{bmatrix} \in \mathbb{R}^{3\times(n_r+4)},$$

$$\mathbf{X_d}(k) = \begin{bmatrix} \mathbf{X_c}(k\Delta t) \\ u_d(k) \\ v_d(k) \end{bmatrix} \in \mathbb{R}^{(n_r+4)\times 1}, \; \mathbf{Z_d}(k) = \begin{bmatrix} \mathbf{Z_c}(k\Delta t) \\ u_d(k) \end{bmatrix} \in \mathbb{R}^{3\times 1}. \tag{5.13}$$

Here, $\mathbf{X_c}$ and $\mathbf{Z_c}$ denote the possibility of initializing data from a continuous-time solver at the beginning of the time step k. For example, in many cases presented in this work, we use the continuous-time multiphase IB solver that sends the device state $\mathbf{X_c}(k\Delta t)$ to the

MPC algorithm. In the matrices defined above, the following definitions are used:

$$
\begin{aligned}
&\phi(\Delta t) = e^{\Delta t \mathbf{A_c}} \in \mathbb{R}^{(n_r+2)\times(n_r+2)},\\
&\Upsilon = \mathbf{A_c}^{-1}\left(\phi(\Delta t) - \mathbf{I}\right)\mathbf{B_c} \text{ and } \Lambda = \frac{1}{\Delta t}\mathbf{A_c}^{-1}\left(\Upsilon - \Delta t \mathbf{B_c}\right) \in \mathbb{R}^{(n_r+2)\times 1},\\
&u_c(t) = u_d(k) + \left(\frac{t-k\Delta t}{\Delta t}\right)\Delta u_d(k+1),\ \ v_c(t) = v_d(k) + \left(\frac{t-k\Delta t}{\Delta t}\right)\Delta v_d(k+1),\\
&\Delta u_d(k+1) = u_d(k+1) - u_d(k),\ \ \Delta v_d(k+1) = v_d(k+1) - v_d(k).
\end{aligned}
\tag{5.14}
$$

2. A receding strategy in which only the first part/signal of the optimal control sequence is used for actuating the device, and the prediction horizon is moved forward in time to compute the next optimal control sequence (by taking into account the latest device state and wave measurements). We use a prediction horizon of one wave period in this work, unless stated otherwise.

   Assuming that a N_p-step prediction horizon is employed, i.e., $\mathscr{T}_h = N_p \cdot \Delta t_p$, the output vector, $\underline{\mathbf{Z_d}}(k)$, is obtained from the discrete-time model by time marching Eqs. (5.11) and (5.12) through the prediction horizon as [127, 128]

$$
\underline{\mathbf{Z_d}}(k) = \mathscr{P}\mathbf{X_d}(k) + \mathscr{J}_{\boldsymbol{u}}\,\underline{\Delta u_d}(k) + \mathscr{J}_{\boldsymbol{v}}\,\underline{\Delta v_d}(k). \tag{5.15}
$$

In the equation above

$$\underline{\mathbf{Z_d}}(k) = \begin{bmatrix} \mathbf{Z_d}(k+1|k) \\ \mathbf{Z_d}(k+2|k) \\ . \\ . \\ \mathbf{Z_d}(k+N_p|k) \end{bmatrix} \in \mathbb{R}^{(3N_p \times 1)},$$

$$\mathscr{J}_{\boldsymbol{u}} = \begin{bmatrix} \mathbf{C_d}\mathbf{B_d} & 0 & ... & 0 \\ \mathbf{C_d}\mathbf{A_d}\mathbf{B_d} & \mathbf{C_d}\mathbf{B_d} & ... & 0 \\ . & . & . & . \\ . & . & . & . \\ \mathbf{C_d}\mathbf{A_d}^{(N_p-1)}\mathbf{B_d} & \mathbf{C_d}\mathbf{A_d}^{(N_p-2)}\mathbf{B_d} & ... & \mathbf{C_d}\mathbf{B_d} \end{bmatrix} \in \mathbb{R}^{3N_p \times N_p},$$

$$\mathscr{P} = \begin{bmatrix} \mathbf{C_d}\mathbf{A_d} \\ \mathbf{C_d}\mathbf{A_d}^2 \\ . \\ . \\ \mathbf{C_d}\mathbf{A_d}^{N_p} \end{bmatrix} \in \mathbb{R}^{3N_p \times (n_r+4)},$$

$$\mathscr{J}_{\boldsymbol{v}} = \begin{bmatrix} \mathbf{C_d}\mathbf{F_d} & 0 & ... & 0 \\ \mathbf{C_d}\mathbf{A_d}\mathbf{F_d} & \mathbf{C_d}\mathbf{F_d} & ... & 0 \\ . & . & . & . \\ . & . & . & . \\ \mathbf{C_d}\mathbf{A_d}^{(N_p-1)}\mathbf{F_d} & \mathbf{C_d}\mathbf{A_d}^{(N_p-2)}\mathbf{F_d} & ... & \mathbf{C_d}\mathbf{F_d} \end{bmatrix} \in \mathbb{R}^{3N_p \times N_p} \tag{5.16}$$

Sec. 5.4 describes the methods for obtaining the future wave excitation force values stored in the vector $\underline{\Delta v_d}(k)$. Note that the (WSI) solver time step size Δt is generally different from the MPC time step size Δt_p. In many of the examples presented in this work, we employ a continuous-time CFD solver with a much smaller time step of Δt than Δt_p in

order to accommodate the convective Courant-Friedrichs-Levy (CFL) number restriction.

3. An objective function to determine the optimal control sequence over the prediction horizon. Here, the goal is to maximize the amount of energy absorbed by the WEC device, which can be expressed by the relation

$$J_0 = -(m+m_\infty)\int_t^{t+\mathscr{T}_\mathrm{h}} u(\tau)\cdot\dot{z}(\tau)\mathrm{d}\tau. \tag{5.17}$$

The negative sign in the objective function indicates the flow of energy from the device to the power grid. Using the trapezoidal rule to evaluate the definite integral of Eq. (5.17), we obtain

$$J_0 = -(m+m_\infty)\Delta t_p\left(\frac{1}{2}u_d(k)\dot{z}(k) + \sum_{i=k+1}^{k+N_p-1} u_d(i|k)\dot{z}(i|k) + \frac{1}{2}u_d(k+N_p|k)\dot{z}(k+N_p|k)\right) \tag{5.18}$$

For purposes of extremization of J_0, we can remove the constant pre-factor and the known term at time level k ($u_d(k)\dot{z}(k)$) from the discrete summation and redefine the objective function to be

$$J_1(k) = \sum_{i=k+1}^{k+N_p-1} u_d(i|k)\dot{z}(i|k) + \frac{1}{2}u_d(k+N_p|k)\dot{z}(k+N_p|k) \tag{5.19}$$

Since the (constant) negative pre-factor $-(m+m_\infty)\Delta t_p$ has been dropped from J_0 to obtain J_1, the initial maximization problem is now a minimization problem. Moreover, the objective function can be expressed in terms of the output vector as follows:

$$J_1(k) = \frac{1}{2}\underline{\mathbf{Z}_{\boldsymbol{d}}^T}(k)\ \mathrm{Q}\ \underline{\mathbf{Z}_{\boldsymbol{d}}}(k), \tag{5.20}$$

in which

$$\mathrm{Q} = \begin{bmatrix} \mathrm{M} & & & \\ & \ddots & & \\ & & \mathrm{M} & \\ & & & \frac{1}{2}\mathrm{M} \end{bmatrix} \in \mathbb{R}^{3N_p \times 3N_p} \quad \text{and} \quad \mathrm{M} = \begin{bmatrix} 0 & 0 & 0 \\ 0 & 0 & 1 \\ 0 & 1 & 0 \end{bmatrix} \in \mathbb{R}^{3\times 3}$$

By substituting Eq. (5.15) into Eq. (5.20) and expanding the terms, we get

$$\begin{aligned} J_1 = &\frac{1}{2}\underline{\Delta u_d}^T \mathscr{J}_{\boldsymbol{u}}^T \mathrm{Q} \mathscr{J}_{\boldsymbol{u}} \underline{\Delta u_d} + \underline{\Delta u_d}^T \mathscr{J}_{\boldsymbol{u}}^T \mathrm{Q}(\mathscr{P}\mathbf{X}_{\boldsymbol{d}} + \mathscr{J}_{\boldsymbol{v}} \underline{\Delta v_d}) \\ &+ \frac{1}{2}(\mathscr{P}\mathbf{X}_{\boldsymbol{d}} + \mathscr{J}_{\boldsymbol{v}} \underline{\Delta v_d})^T \mathrm{Q}(\mathscr{P}\mathbf{X}_{\boldsymbol{d}} + \mathscr{J}_{\boldsymbol{v}} \underline{\Delta v_d}) \end{aligned} \tag{5.21}$$

The minimization of J_1 with respect to the unknown control sequence $\underline{\Delta u_d}$ yields the optimal control $\underline{\Delta u_d}^\star$ for the entire prediction horizon. Observe that the last term of Eq. (5.21) does not contribute to the evaluation of $\underline{\Delta u_d}^\star$ and can be safely dropped. Therefore, the objective or in this case the cost function to minimize reads as

$$J_1 = \frac{1}{2}\underline{\Delta u_d}^T \mathscr{J}_{\boldsymbol{u}}^T \mathrm{Q} \mathscr{J}_{\boldsymbol{u}} \underline{\Delta u_d} + \underline{\Delta u_d}^T \mathscr{J}_{\boldsymbol{u}}^T \mathrm{Q}(\mathscr{P}\mathbf{X}_{\boldsymbol{d}} + \mathscr{J}_{\boldsymbol{v}} \underline{\Delta v_d}). \tag{5.22}$$

The cost function J_1 is quadratic in $\underline{\Delta u_d}$ and is assumed to be positive semi-definite. We use the quadratic programming (QP) methods available in MATLAB [129] to obtain the optimal control sequence $\underline{\Delta u_d}^\star$. The objective functions J_0 and J_1 assume that the PTO is ideal with no mechanical to electrical conversion losses. Thus, the conversion efficiency ε is taken to be 100%, i.e., $\varepsilon = 1$. Readers are referred to Tona et al. [130], who formulated a MPC problem with $\varepsilon < 1$ and investigated how a non-ideal PTO affects device dynamics and absorbed power [4].

[4] Although we have taken $\varepsilon = 1$ for all the cases in this work, our code (available at https://github.com/IBAMR/cfd-mpc-wecs) can also simulate the controlled dynamics of the WEC device with $\varepsilon < 1$. The non-ideal PTO problem is handled separately because it requires a sequential quadratic programming solver.

5.3.1 Device/Path constraints

In general, if the cost function J_1 is minimized as is, the device displacement, velocity, or actuator force will exceed the physical limits. An unconstrained control force could, for instance, cause the device to overshoot the free surface and slam into water with large impact forces. This can be avoided by using the following path/device constraints in MPC [127, 131, 132]:

$$\begin{aligned} z^{\min} &\leq z(k) \leq z^{\max}, \\ \dot{z}^{\min} &\leq \dot{z}(k) \leq \dot{z}^{\max}, \\ u^{\min} &\leq u(k) \leq u^{\max}. \end{aligned} \tag{5.23}$$

Constraints written in Eq. (5.23) are first expressed in the form $\underline{\mathbf{Z}_{\boldsymbol{d}}^{\min}} \leq \underline{\mathbf{Z}_{\boldsymbol{d}}} \leq \underline{\mathbf{Z}_{\boldsymbol{d}}^{\max}}$, which is then recast as $\underline{\mathbf{Z}_{\boldsymbol{d}}^{\min}} \leq \mathscr{P}\mathbf{X}_{\boldsymbol{d}}(k) + \mathscr{J}_{\boldsymbol{u}}\,\underline{\Delta u_d}(k) + \mathscr{J}_{\boldsymbol{v}}\,\underline{\Delta v_d}(k) \leq \underline{\mathbf{Z}_{\boldsymbol{d}}^{\max}}$ using Eq. (5.15). As both $\mathbf{X}_{\boldsymbol{d}}(k)$ and $\underline{\Delta v_d}(k)$ are known inputs to the quadratic program, the latter form of the inequality allows extraction of the constraint relationship for the variable of interest $\underline{\Delta u_d}$.

5.3.2 Regularizing the MPC objective function

The cost function J_1 of Eq. (5.22) is further modified by adding two additional quadratic penalty terms:

$$J_2(k) = J_1(k) + \lambda_1 \|\underline{\Delta u_d}\|_2^2, \tag{5.24}$$

$$J_3(k) = J_2(k) + \lambda_2 \|\underline{\boldsymbol{u}}\|_2^2. \tag{5.25}$$

Adding the $\lambda_1 \|\underline{\Delta u_d}\|_2^2$ term to J_1 reduces the aggressiveness of the controller, i.e., J_2 results in smoother control force variation over time than the original cost function J_1 [127]. The non-negative parameter λ_1 in Eq. (5.24) has the dimensions of time. It is important to keep λ_1 positive in order to maintain or enhance J_1's convexity. A smaller magnitude of λ_1 ensures that J_1 and J_2 are not too far apart.

J_2 is further modified to J_3 by adding the quadratic penalty term $\lambda_2\|\underline{\boldsymbol{u}}\|_2^2$ (Eq. (5.25)). The objective is to reduce the flow of power from the grid to the device, referred to as reactive power in wave energy literature [132, 133]. Even though reactive power aligns the device velocity with wave excitation forces to provide a higher overall energy output, it can lead to large instantaneous positive and negative powers in the PTO unit [133]. The two-way power flow complicates the design of a PTO system and increases its cost. The goal of J_3 is to enforce the one-way power flow condition in the PTO machinery [127]. As with λ_1, λ_2 should also be positive, smaller in magnitude, and has the dimensions of time.

5.4 Linear potential theory-based wave excitation/Froude-Krylov forces

The wave excitation forces acting on the body according to the LPT are the sum of effects coming from undisturbed incident waves (assuming that the body is removed from the path of the waves) and diffracted waves (which assumes the body is held stationary at its mean position). Wave excitation forces are also known as Froude-Krylov (FK) forces. FK forces can be computed using the undisturbed flow and diffracted wave potentials, ϕ_I and ϕ_D, respectively, as

$$\mathbf{F}_{\mathrm{FK}}(t) = \mathbf{F}_I(t) + \mathbf{F}_D(t) = -\int_{S_b} (p_I(t) + p_D(t))\, \mathbf{n}\, \mathrm{d}S_b, \tag{5.26}$$

in which S_b is the wetted surface area of the body, $\mathbf{n}$ is the unit outward normal to the surface, $p_I = -\rho_{\mathrm{w}} \frac{\partial \phi_I}{\partial t}$ is the pressure due to incident waves, and $p_D = -\rho_{\mathrm{w}} \frac{\partial \phi_D}{\partial t}$ is the pressure due to diffracted waves. It should be noted that the hydrostatic pressure $p_H(t) = -\rho_{\mathrm{w}} g z(t)$ and the radiation pressure $p_R(t) = \rho_{\mathrm{w}} \frac{\partial \phi_R}{\partial t}$ are accounted for in the calculations of $\mathrm{F}_h(t)$ and $\mathrm{F}_r(t)$, respectively in Eq. (5.1). Additionally, in Eq. (5.1), $\mathrm{F}_{\mathrm{exc}}$ is the z-component of $\mathbf{F}_{\mathrm{FK}}$.

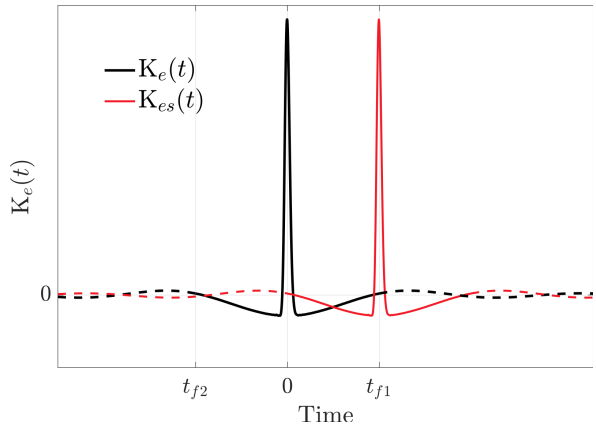

Figure 5.2. Wave impulse response function (WIRF) for a vertical cylindrical in heave motion. The original WIRF $\mathrm{K}_e(t)$ is shown in black and the right shifted WIRF $\mathrm{K}_{es}(t)$ is shown in red. The dashed part of the curves represents the truncated region where the WIRF is close to zero.

5.4.1 Linear Froude-Krylov (LFK) forces: Up-wave measurements and future wave predictions

If the pressure integral of Eq. (5.26) is evaluated while the body is stationary at its mean equilibrium position, the Froude-Krylov forces are linear with respect to free surface elevation and are called linear Froude-Krylov forces (LFK). The LFK forces can be computed more efficiently as a convolution integral between the wave impulse response function (WIRF) and water surface elevation at the device location x_B: $\mathrm{F}_{\mathrm{exc}}(t) = \int_{-\infty}^{\infty} \mathrm{K}_e(\tau)\eta_{\mathrm{wave}}(t-\tau;x_B)\mathrm{d}\tau$ (repeated from Eq. (5.4) for convenience). Assuming that the sea surface is calm prior to the start of the simulation at $t = 0$, i.e., $\eta_{\mathrm{wave}}(t < 0;\forall x) = 0$, the upper limit of the convolution integral $\mathrm{K}_e * \eta_{\mathrm{wave}}$ can be terminated at the current time t.

In Fig. 5.2 we show the non-causal WIRF $\mathrm{K}_{\mathrm{e}}(t)$ as a black line. WIRF is the inverse Fourier transform of the frequency-domain excitation force $\widehat{\mathrm{F}}(\omega) = \widehat{\mathrm{F}}_I(\omega) + \widehat{\mathrm{F}}_D(\omega)$ that we obtain using ANSYS AQWA software:

$$\mathrm{K}_e(t) = \frac{1}{2\pi}\int_{-\infty}^{\infty} \widehat{\mathrm{F}}(\omega)e^{(i\omega t)}\,\mathrm{d}\omega. \tag{5.27}$$

In practice, the incident wave forces $\widehat{\mathrm{F}}_I$ and the diffracted wave forces $\widehat{\mathrm{F}}_D$ can only be computed

for discrete frequencies $\{\omega_i\}$, and a suitable numerical interpolation is required to evaluate the inverse Fourier transform. From Fig. 5.2, it can be seen that when $t > t_{f1}$ or $t < -|t_{f2}|$, $\mathrm{K}_e(t) \to 0$. Truncated $\mathrm{K}_e(t)$ is shown as a dashed line in Fig. 5.2. The finite positive time interval where $\mathrm{K_e}(t) \neq 0$ requires η_{wave} data only until $t - t_{f1}$ in the past to determine the convolution integral. Also, the finite negative time interval where $\mathrm{K_e}(t) \neq 0$ implies that η_{wave} data is only required up to $t + |t_{f2}|$ into the future. The convolution integral of Eq. (5.4) can therefore be performed efficiently as

$$\mathrm{F_{exc}}(t) = \int_{-t_f}^{t_f} \mathrm{K}_e(\tau)\eta_{\text{wave}}(t-\tau;x_B)\,\mathrm{d}\tau, \tag{5.28}$$

in which $t_f = \max\left[t_{f1}, |t_{f2}|\right]$. It follows that (with reasonable accuracy) $\mathrm{F_{exc}}$ at the current time t can be computed if the wave surface elevation data at the device location is available from $t - t_f$ to $t + t_f$.

It is unrealistic to measure the undisturbed wave elevation at the device location since the incident waves cannot pass through the device. Furthermore, the waves near the body are altered by FSI and do not remain undisturbed in reality. Therefore, we need to find another way to estimate η_{wave} at the device location x_B. We can take advantage of the fact that wave propagation is a hyperbolic phenomenon, which means that waves passing an up-wave location x_A will arrive at the device at a later time. In order to locate a convenient up-wave location, we change the variable τ to $\tau' - t_f$ in Eq. (5.28):

$$\begin{aligned}
\mathrm{F_{exc}}(t) &= \int_{-t_f}^{t_f} \mathrm{K}_e(\tau)\eta_{\text{wave}}(t-\tau;x_B)\,\mathrm{d}\tau \\
&= \int_{0}^{2t_f} \mathrm{K}_e(\tau'-t_f)\eta_{\text{wave}}(t+t_f-\tau';x_B)\,\mathrm{d}\tau' \\
&= \int_{0}^{2t_f} \mathrm{K}_{es}(\tau')\eta_{\text{wave}}(t-\tau';x_A)\,\mathrm{d}\tau'.
\end{aligned}$$

Here, K_{es} is the shifted WIRF obtained by shifting the original WIRF to the right side on the time-axis by an amount t_f. Symbolically, the time shift can be expressed by the relation $\mathrm{K}_{es}(t) = \mathrm{K}_e(t - t_f)$. The shifted WIRF is shown as a red line in Fig. 5.2. For the integral

transformation above, we defined the up-wave location x_A so that the waves leaving this location reach the device after an additional time of t_f. Therefore, the water surface elevation at the device location at the present time t is related to the up-wave elevation at the previous time $t-t_f$, i.e., $\eta(t+t_f;x_B)=\eta(t;x_A)$. The distance of the up-wave point from the device is calculated by using the wave velocity (ω/κ_w) as

$$d_f=\frac{\omega}{\kappa_w}\cdot t_f, \tag{5.29}$$

in which ω is the wave frequency and κ_w is the wave number. In our CFD model, x_A is chosen to be a point in the wave generation zone. See Fig. 5.4 for a visual representation. In summary, the convolution integral of Eq. (5.28) is equivalent to

$$\mathrm{F_{exc}}(t)=\int_0^{2t_f}\mathrm{K}_{es}(\tau)\eta_{\mathrm{wave}}(t-\tau;x_A)\,\mathrm{d}\tau. \tag{5.30}$$

It can be seen from Eq. (5.30) that the wave excitation forces acting on the device at the present instant t can be calculated from the η_{wave} data recorded at the up-wave location between the period $[t-2t_f,t]$ for which no prediction or time-series estimation is needed. Wave forecasting is still necessary for MPC even if all the surface elevation data is obtained/measured at a nearby up-wave location. The reason is that for a prediction horizon of $\mathscr{T}_h$, FK forces acting on the device are necessary between the period $[t,t+\mathscr{T}_h]$ (to fill the entries of the vector $\underline{\Delta v_d}$ in Eq. (5.15) or Eq. (5.22)). Accordingly, at the up-wave location x_A, η_{wave} data is required in the interval $[t-2t_f,t+\mathscr{T}_h]$. In this study, we use the auto-regressive (AR) model for time series forecasting, one of the many techniques available to predict the future behavior of a time-series based on its past behavior. Detailed information about the implementation of an AR model for wave forecasting can be found in the thesis by Gieske [134]. A typical AR model is calibrated for a particular sea state and requires (manual) re-tuning to make accurate predictions in a different sea state. Sec. 5.11.4 describes the capability of MPC to adapt to changing sea states in which different AR models are used for different sea states. Considering

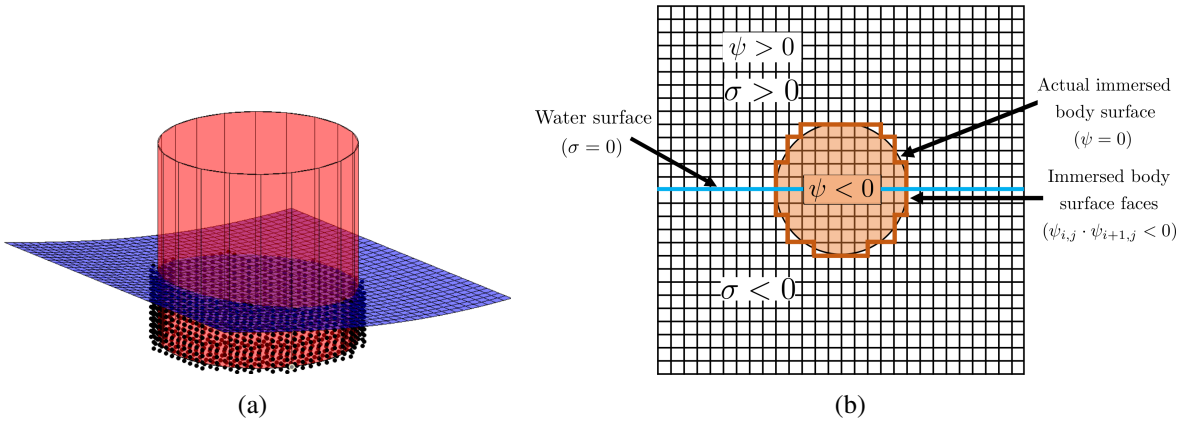

Figure 5.3. NLFK force calculation using implicit signed distance functions σ and ψ. (a) A 3D schematic showing the instantaneous wetted surface area $S_b(t)$ of a vertical heaving cylinder interacting with the undulatory water surface. (b) A 2D schematic showing the stair-step representation of the immersed body on the Cartesian grid and the identification of the grid faces for evaluating the pressure integral using the body SDF ψ.

the importance of wave excitation force prediction, other methods of prediction are also described in the literature, including the recursive least squares filter [135], the Kalman and extended Kalman filters [136, 137, 138, 139, 140], and neural networks [136, 139, 141]. In practice, some of these techniques may be easier to implement than AR.

5.4.2 Non-linear Froude-Krylov (NLFK) forces: A novel static grid approach based on implicit surfaces

A significant amount of modeling accuracy can be achieved by considering the FK forces to be non-linear. The NLFK force is calculated by integrating the incident wave pressure $p_I(t)$ over the instantaneous wetted surface area $S_b(t)$ of the body; see Eq. (5.26) and Fig. 5.3(a). The computation of NLFK forces for practical control of WECs is considered prohibitively expensive in the wave energy literature. It is because such forces are typically computed using dynamic meshes, in which the computational domain is re-meshed to account for the relative motion between the body and the waves. Nevertheless, computationally-efficient approaches have recently been developed for calculating NLFK forces. In [77], Giorgi et al. presented an analytical method for evaluating the pressure integral for axisymmetric WECs. Though the

method described in [77] is computationally attractive, it can only be applied to WEC devices that are geometrically solids of revolution. An alternative approach is presented in this section based upon the level set/signed distance function (SDF) that can effectively model the instantaneous wave-structure interaction of WECs on a static Cartesian grid. Moreover, the proposed technique can be applied to arbitrarily complex-shaped bodies because the SDF can be computed using efficient computational geometry algorithms within a narrow band of grid cells [142]. Further, the level-set methodology is an embarrassingly parallel algorithm that is amenable to both distributed- and shared-memory parallelism.

First, we define a rectangular box region $\mathscr{R} = \mathscr{R}_w(t) \cup \mathscr{R}_a(t)$ around the WEC, which is discretized on a static Cartesian grid with rectangular cells. The grid cells are enumerated using the integer tuple (i, j, k). The static region $\mathscr{R}$ should be a minimal one, covering only the wave amplitude and maximum displacement of the body expected in the simulation for computational efficiency. Next, define two level set functions $\psi(\mathbf{x},t)$ and $\sigma(\mathbf{x},t)$ over the entire box $\mathbf{x} \in \mathscr{R}$ that describe the signed distance to the WEC surface and the undulatory air-water interface, respectively. We take ψ to be negative (positive) inside (outside) the body and σ to be negative (positive) inside the water region $\mathscr{R}_w(t)$ (air region $\mathscr{R}_a(t)$). Zero-contours of ψ and σ implicitly define the WEC-fluid and the air-water interface, respectively. Sec. 2.2 provides more details on level set methodology, where we describe our multiphase CFD solver that is also based on the level set technique. The motion of the waves and the device is captured by redefining SDFs on the static grid [5], which completely eliminates the need to re-mesh the computational domain $\mathscr{R}$. The wave incident pressure p_I is defined on the cell centers $\mathbf{x}_{i,j,k}$ of the static Cartesian grid in

[5] SDF of a vertical cylinder can be prescribed analytically using constructive solid geometry operators, such as min/max acting on SDFs of primitive shapes. SDF of the air-water interface can also be prescribed analytically from the known surface elevation function $\eta_{\text{wave}}(\mathbf{x},t)$.

order to compute the NLFK force as

$$
\begin{aligned}
p_I(\mathbf{x}_{i,j,k},t) &= 0, && \sigma(\mathbf{x},t) > 0, \\
p_I(\mathbf{x}_{i,j,k},t) &= \rho_{\mathrm{w}} g \frac{\mathscr{H}}{2} \frac{\cosh(\kappa_w(d+\sigma)) \cdot \cos(\kappa_w x - \omega t)}{\cosh(\kappa_w d)}, && \sigma(\mathbf{x},t) \leq 0,
\end{aligned} \tag{5.31}
$$

in which $\mathscr{H}$ is the wave height, κ_w is the wavenumber, d is the depth of water above the sea floor, and ω is the wave frequency. The integral of p_I over the wetted surface can be performed numerically as

$$
\mathbf{F}_I(t) = \sum_f -p_I(\mathbf{x}_f,t)\,\mathbf{n}_f\,\Delta A_f. \tag{5.32}
$$

The discrete summation in Eq. (5.32) is carried over the Cartesian grid faces that provide a stair-step representation of the body on the Cartesian grid. This is shown in Fig. 5.3(b). The set of the Cartesian grid faces f can be easily identified by examining the sign change of σ. The $\mathbf{n}_f$ and ΔA_f variables in the equation above represent the unit normal vector and the area of the cell face, respectively. The incident wave pressure $p_I(\mathbf{x}_f,t)$ on the cell face (where σ is taken to be zero) is the weighted average of the neighboring cell center pressures, where the distance to the WEC surface $|\sigma(\mathbf{x}_{i,j,k},t)|$ is used as the weights. In the heave direction, calculating $\mathrm{F}_I(t)$ requires summing only over z-faces.

The diffraction component of NLFK forces remains linear. This is due to the assumption that the body is stationary when computing the diffraction forces. Similarly to LFK forces, the z-component of $\mathbf{F}_D(t)$ can be computed as a convolution integral between the diffraction impulse response function (DIRF) $\mathrm{K}_d(t)$ in the heave direction and the water surface elevation as

$$
\mathrm{F}_D(t) = K_d * \eta_{\mathrm{wave}} = \int_{-\infty}^{\infty} \mathrm{K}_d(\tau)\eta_{\mathrm{wave}}(t-\tau)\,\mathrm{d}\tau = \int_{-t_f}^{t_f} \mathrm{K}_d(\tau)\eta_{\mathrm{wave}}(t-\tau;x_B)\,\mathrm{d}\tau. \tag{5.33}
$$

DIRF is the inverse Fourier transform of frequency-domain diffraction force data $\widehat{F}_D(\omega)$ that we

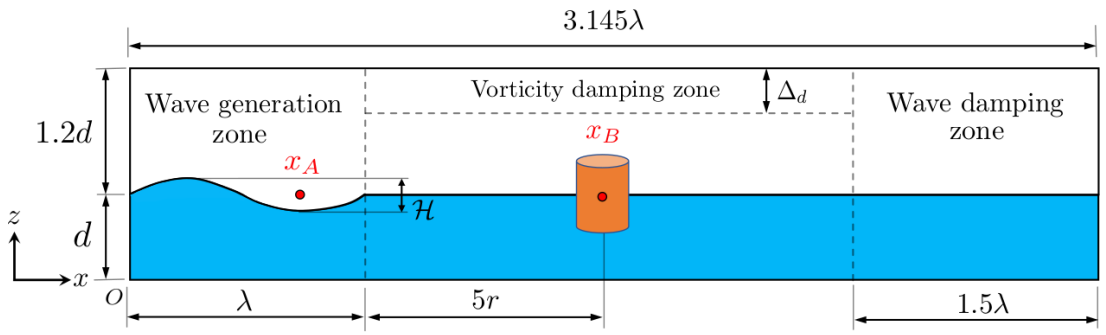

Figure 5.4. Numerical wave tank (NWT) schematic showing wave generation, wave damping, and vorticity damping zones. The WEC device is placed in the working zone of length 3.145λ.

obtain using ANSYS AQWA.

We remark that the technique described in this section can be easily modified to model nonlinear buoyancy forces for varying cross-sectional WEC devices. This is achieved by replacing p_I by $p_H = -\rho_w g z(t)$ in Eq. (5.32).

5.5 NWT and FSI coupling

The fully-resolved and control-informed WSI of the device is simulated using a NWT, depicted in Fig. 5.4. In the tank, the converter is located at position x_B. The wave generation, wave damping, vorticity damping zone, and boundary conditions are implemented as described in Sec. 4.3. The wave generation zone reduces the interaction of the reflected waves (from the device) with the inlet boundary. The wave generation zone being relatively free of reflected waves, the up-wave point x_A is also placed inside this zone, which accurately records the wave elevation data $\eta_{\text{wave}}(t;x_A)$ and sends it to the MPC. Also sent to the controller are the device's displacement and velocity, z and $\dot{z}$, computed from the fully-resolved WSI.

For the ease of reading, we rewrite the Brinkman penalization term f_c given by Eq. (3.9) below. It is treated implicitly in the discretized version of the momentum Eq. (3.7) and computed as

$$\mathrm{f}_c^{n+1,k+1} = \frac{\widetilde{\chi}}{\kappa}\left(\mathbf{u}_b^{n+1,k+1} - \mathbf{u}^{n+1,k+1}\right), \tag{5.34}$$

in which the discretized indicator function is defined using the body Heaviside function (see Eq. (3.4)) as $\widetilde{\chi} = 1 - \widetilde{H}^{\text{body}}$; $\widetilde{\chi} = 1$ inside the solid region. A sufficiently small value of the permeability coefficient $\kappa \sim \mathscr{O}(10^{-8})$ is shown to be effective in enforcing the rigidity constraint [38, 116].

Rewriting the rigid body velocity $\mathbf{u}_b$ given in Eq. (3.9). It can be expressed as the sum of translational $\mathbf{U}_r$ and rotational $\mathbf{W}_r$ velocities:

$$\mathbf{u}_b = \mathbf{U}_r + \mathbf{W}_r \times (\mathbf{x} - \mathbf{X}_{\text{com}}), \tag{5.35}$$

in which $\mathbf{X}_{\text{com}}$ is the position of the center of mass of the body. In this study, the WEC device is allowed to move only in the heave direction. Hence, $\mathbf{U}_r = (0, 0, \dot{z}(t))$ and $\mathbf{W}_r = 0$. The rigid body velocity is simplified to

$$\mathbf{u}_b^{n+1,k+1} = \dot{z}^{n+1,k+1}\,\widehat{\mathrm{z}}. \tag{5.36}$$

The heave velocity $\dot{z}$ resulting from the WSI can be computed using Newton's second law of motion as

$$m\frac{\mathrm{d}\dot{z}}{\mathrm{d}t} = m\frac{\dot{z}^{n+1,k+1} - \dot{z}^{n}}{\Delta t} = \mathscr{F}_{\text{hydro}}^{n+1,k} - mg + \mathrm{F}_{\text{PTO}}^{n+1,k+1}, \tag{5.37}$$

in which $\mathrm{F}_{\text{hydro}}$ is the net hydrodynamic force (pressure and viscous) in the heave direction and m is the mass of the cylinder (same as the one used in Eq. (5.1)). The method that was previously described in Sec. 5.4.2 to compute NLFK forces using the SDF ψ (see Eq. (5.32) can be easily extended to include both pressure and viscous force contributions. Following the SDF approach, the net hydrodynamic force acting on the body is computed as

$$\mathscr{F}_{\text{hydro}}^{n+1,k} = \sum_f \left(-p^{n+1,k}\mathbf{n}_f + \mu_{\text{f}} \left(\nabla_h \mathbf{u}^{n+1,k} + \left(\nabla_h \mathbf{u}^{n+1,k} \right)^T \right) \cdot \mathbf{n}_f \right) \Delta A_f. \tag{5.38}$$

We remark that whereas Eq. (5.32) is evaluated using a simple and a minimal box region $\mathscr{R}$

surrounding the device and the waves near it, Eq. (5.38) is evaluated using the actual CFD grid that is distributed across multiple processors. Lastly, the F_{PTO} term of Eq. (5.37) is computed by the MPC algorithm as discussed in Sec. 5.3.

5.6 Power transfer from waves to the PTO

Here, we mathematically describe the pathway of power transfer from the sea waves to the PTO system. The relationships derived in this section can also be used to quickly verify the accuracy of the CFD simulations. To begin, multiply the dynamical Eq. (5.37) by the heave velocity $\dot{z}$ and rearrange the terms to obtain:

$$m\frac{\mathrm{d}}{\mathrm{d}t}\left(\frac{\dot{z}(t)^2}{2}\right) = \mathscr{F}_{\text{hydro}}(t)\dot{z}(t) - mg\dot{z}(t) + \mathrm{F}_{\text{PTO}}(t)\dot{z}(t). \tag{5.39}$$

Taking the time average of the above equation over one wave period $\mathscr{T}$ and rearranging terms, we get

$$\langle \mathscr{F}_{\text{hydro}}(t)\dot{z}(t)\rangle = \langle m\frac{\dot{z}(t)^2}{2}\rangle + \langle mg\dot{z}(t)\rangle - \langle \mathrm{F}_{\text{PTO}}(t)\dot{z}(t)\rangle, \tag{5.40}$$

in which $\langle(\cdot)\rangle = \int_t^{t+\mathscr{T}}(\cdot)\,\mathrm{d}\tau$ represents the time-averaging operator. For regular waves, contributions from the inertial and the gravity terms are zero due to the time periodicity of the heave velocity. Hence, we have:

$$\langle \mathscr{F}_{\text{hydro}}(t)\dot{z}(t)\rangle = -\langle \mathrm{F}_{\text{PTO}}(t)\dot{z}(t)\rangle. \tag{5.41}$$

The term $\langle \mathscr{F}_{\text{hydro}}(t)\dot{z}(t)\rangle$ describes the mechanical work done by the waves to oscillate the converter and the term -$\langle \mathrm{F}_{\text{PTO}}(t)\dot{z}(t)\rangle$ describes the power absorbed by the device. For irregular waves, the inertial and gravity terms may not equal zero when averaged over an exact wave period. Nevertheless, Eq. (5.40) remains valid. The power transfer relationships are verified in Sec. 5.11.3.

Table 5.1. Various WSI/MPC solver combinations considered in this work.

	Solver	MPC
1	BEM-LFK	LFK
2	BEM-LFK	NLFK
3	BEM-NLFK	LFK
4	BEM-NLFK	NLFK
5	CFD	LFK
6	CFD	NLFK

5.7 WSI and MPC solvers

Secs. 5.2 describe methods naturally suited to different types of WSI and MPC solvers. There are two types of WSI solvers that can be derived from Sec. 5.2: (**1**) BEM-LFK and (**2**) BEM-NLFK. Here, BEM implies a WSI solver that solves Eq. (5.6), LFK implies the excitation force is calculated using Eq. (5.28) (or Eq. (5.30)), and NLFK implies the excitation force is calculated using Eqs. (5.32) and (5.33). MPC solvers can also be divided into two types: (**1**) MPC-LFK and (**2**) MPC-NLFK., where the excitation force vector $\underline{\Delta v_d}$ is computed linearly and non-linearly, respectively. Lastly, based upon Chapter 2 and Sec 5.5, we have a multiphase IB/CFD solver that solves Eqs. (2.1)-(2.2). Table 5.1 shows six possible WSI/MPC combinations. Note that it is computationally unfeasible (if not impossible) to implement MPC using a CFD-based solver. Moreover, results of Sec. 5.11.1 suggest that a higher fidelity hydrodynamical model within MPC does not necessarily improve accuracy.

5.8 Communication layer between the CFD and MPC solvers

In this section, we present the custom communication layer between the CFD and MPC solvers. The "glue code" is written using PETSc [48], which provides a high-level communication channel between IBAMR [43] and MATLAB [129]. As discussed in Sec. 5.3, MPC requires quadratic programming (QP) and autoregressive models (AR). Although there are several compiled language implementations of QP (e.g., QuadProg++ [143]) and AR (e.g.,

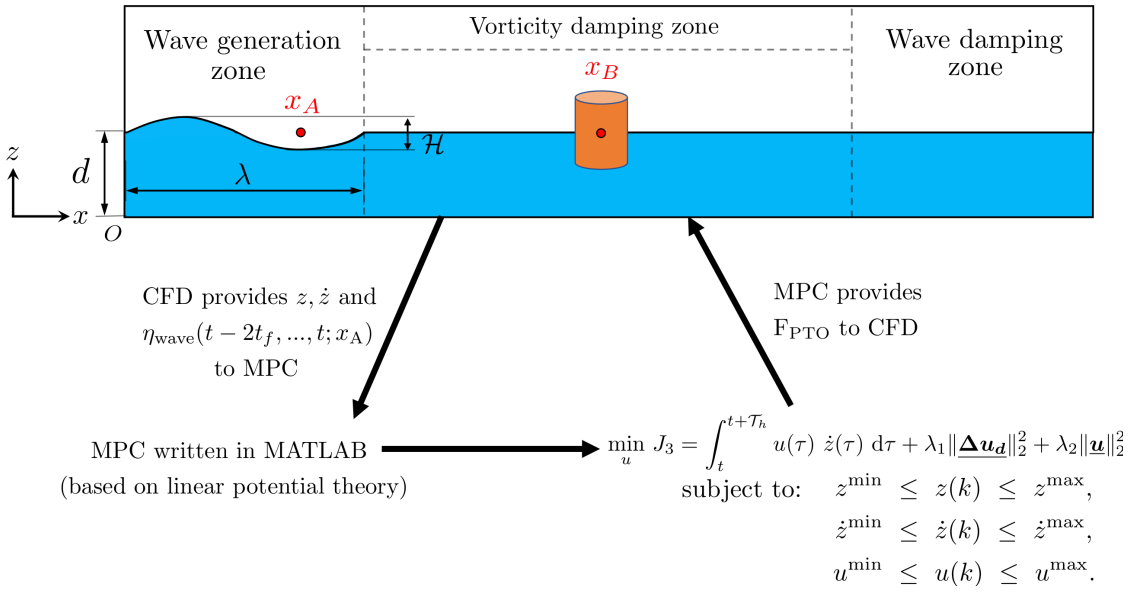

Figure 5.5. Schematic representation of the dynamic interaction between the MPC algorithm and multiphase IB solver.

Cronos [144]) techniques, we implement the MPC algorithm in MATLAB, which has built-in support for QP and AR techniques. MATLAB is probably the most widely used programming environment for dynamical systems modeling and control in academia and industry, so our current implementation can easily be adapted to integrate other optimal control strategies for WECs into a different CFD code of choice, e.g., OpenFOAM.

In the following, we describe the interaction between the CFD and MPC solver codes as a three-part algorithm. Fig. 5.5 shows this interaction pictorially. Communication between the CFD and MPC codes is handled by the PETScMatlabEngine object provided by the PETSc library. Details on the PETSc functions and objects can be found in its user manual [47].

1. **Accessing the MATLAB workspace**: Algorithm 1 is called towards the beginning of the driver code to create the PETScMatlabEngine object 'mengine' on MPI (Message Passing Interface) rank 0. Next, line 2 of the algorithm calls the PETSc function `PetscMatlabEngineCreate()`, in which 'PETSC_COMM_SELF' is the MPI communicator containing the single MPI rank 0. Next, the MATLAB workspace is cleared for any data already present and the path to the 'MPC_matlab_code' directory is added

to MATLAB's standard search path. The directory 'MPC_matlab_code' contains all the MPC code scripts and related functions. The PETSc function to achieve this is called on line 3 of Algorithm 1. Then, various wave ($\mathscr{H}$, $\mathscr{T}_p$, ω, κ_w, d) and device parameters (m, R_{cyl}, L_{cyl}) are loaded into the workspace by calling the PETSc function `PetscMatlabEngineEvaluate()` on line 4, wherein a MATLAB variable 'var' is created with the numerical value of var_value. Next, the BEM data is read and loaded into the workspace by executing the MATLAB script 'load_mpc_parameters.m'. This includes the added mass of the cylinder m_∞ and the impulse response functions $\text{K}_e(t)$ and $\text{K}_d(t)$. The script also sets various MPC parameters (Δt_p, $\mathscr{T}_h$, N_p, n_r, t_f), device constraints ($z_{\text{min/max}}$, $\dot{z}_{\text{min/max}}$, $u_{\text{min/max}}$), wave type (regular or irregular), and the method of wave excitation force calculation (LFK or NLFK). The coefficients of the quadratic penalty terms λ_1 and λ_2 and the MPC solver options (maximum iterations, solver tolerance, etc.) are also set by the same script 'load_mpc_parameters.m'. Since the CFD solver sends the device and wave elevation data to the MPC code, it needs to know the MPC time step size Δt_p and the next time to synchronize data with the controller $t_{\text{next-sync}}$. The values from the MATLAB workspace are obtained by calling the function `PetscMatlabEngineGetArray()`. Finally, the remaining CFD parameters and variable values (Δt, X_{com}, x_{B}, and x_{A}) that could not be added to the workspace earlier (on line 4) are loaded to the workspace on line 8.

2. **The main time loop**: Algorithm 2 describes the time-loop interaction between the CFD and MPC solvers. First, the MPI rank 0 updates the MATLAB workspace with the CFD solver time $t_{\text{CFD}} = t^{n+1}$ and the device displacement and velocity data, as shown on line 4 of the algorithm. Next, the algorithm checks if the CFD solver time is greater than or equal to the controller synchronization time $t_{\text{next-sync}}$. If the statement evaluates to true, then a new set of MPC matrices $\mathscr{P}$, $\mathscr{J}_{\boldsymbol{u}}$, and $\mathscr{J}_{\boldsymbol{v}}$ are calculated and the radiation damping vector $\boldsymbol{x_r}$ is advanced in time using the MATLAB scripts 'calculate_mpc_matrices.m'

Algorithm 1: Creating and initializing the MATLAB workspace.

```
1 if (MPI_rank == 0) then
2     PetscMatlabEngineCreate(PETSC_COMM_SELF, NULL, &(mengine));
        // Create a MATLAB engine on MPI rank 0.
3     PetscMatlabEngineEvaluate(mengine, "clc; clear all; close all;
        addpath('./MPC_matlab_code')"); // Execute MATLAB commands and add the
        MPC code directory path to the standard search path.
4     PetscMatlabEngineEvaluate(mengine,"var = %f", var_value); // Load the
        wave and device parameters into the MATLAB workspace.
5     PetscMatlabEngineEvaluate(mengine, "load_mpc_parameters"); // Execute
        the script to read and load the BEM data and MPC parameters into the
        MATLAB workspace.
6     PetscMatlabEngineGetArray(mengine, ...); // Load the values of the
        MATLAB variables into the CFD code.
7     ..... // Code to do CFD related setup and calculations.
8     PetscMatlabEngineEvaluate(mengine, ...); // Load the remaining CFD
        variables into the workspace that were not available/calculated
        earlier.
9 end
```

and 'calculate_radiation_damping_xr.m', respectively. To enable the calculation of wave excitation forces over a prediction horizon of $\mathscr{T}_h$, the CFD solver sends the past up-wave surface elevation data (from the NWT) to the MATLAB workspace. Using the updated matrices, vectors, and FK forces, the MPC solver predicts the optimal control sequence for the entire prediction horizon on line 9. The first signal of the optimal control sequence is sent to the CFD solver, which is then interpolated to time t_{CFD} using Eq. (5.14). Note that since the CFD solver time step size Δt is typically smaller than the MPC solver time step size Δ_p, line 13 of Algorithm 2 ensures that F_{PTO} is computed at the correct time level in the case the if block is not executed. Lastly, both $t_{\text{next-sync}}$ and t_{CFD} are updated and the time level is moved to $n+2$.

3. **The MPC routine**: Algorithm 3 describes the AR predictions and the LFK and NLFK force calculations required by the MPC to compute an optimal control force sequence. This algorithm is executed by the MATLAB script 'calculate_control_force.m'. First, line

Algorithm 2: Time-loop interaction between the CFD and MPC solvers.

Initialize the MATLAB workspace and load the BEM data and MPC parameters.
// See Algorithm 1.
while $(t_{CFD} \leq t_{end})$ **do**
  if *(MPI_rank == 0)* **then**
    PetscMatlabEngineEvaluate (mengine, "$t_{\text{CFD}} = \%f$; $\Delta t = \%f$; $z = \%f$; $\dot{z} = \%f$;" , t_{CFD}, Δt, z, $\dot{z}$); // Send the latest CFD and device data to MATLAB workspace.
    if $(t_{CFD} \geq t_{next\text{-}sync})$ **then**
      PetscMatlabEngineEvaluate(mengine, "calculate_mpc_matrices; calculate_radiation_damping_xr;"); // Execute the MATLAB scripts to update the discrete-time dynamical matrices.

      // Send the past up-wave surface elevation data to the MATLAB workspace.
      PetscMatlabEnginePutArray(mengine, t_{past}.size(), 1, &(t_{past}[0]),"t_{past}");
      PetscMatlabEnginePutArray(mengine, η_{A}.size(), 1, &(η_{A}[0]),"$\eta_{\text{A}_{\text{past}}}$");

      PetscMatlabEngineEvaluate(mengine, "calculate_control_force;");
        // Compute the optimal control sequence using Algorithm 3.
      PetscMatlabEngineGetArray(mengine, 1, 1, &(u),"u"); // Get the first signal of the optimal control sequence from MPC for the CFD solver.
      $t_{\text{next-sync}} \leftarrow t_{\text{next-sync}} + \Delta t_p$ // Update the synchronization time.
    end
    Interpolate $F_{\text{PTO}} \leftarrow (m + m_\infty)u$ to t_{CFD} using Eq. (5.14).
  end
  MPI_Bcast(F_{PTO}); // Broadcast the value of the PTO force to all processors.
  Solve the FSI problem using the multiphase IB solver.
  $t_{\text{CFD}} \leftarrow t_{\text{CFD}} + \Delta t$
end

1 calculates the discrete time instants over the prediction horizon at a uniform interval Δt_p. Next, the algorithm checks if AR predictions are to be used or not. If the value of the variable *AR_start_time* is set to a large number (larger than the simulation end time), then the if condition on line 2 always evaluates to true. In this case, the algorithm computes the LFK or the NLFK force based on the analytical expression of the wave elevation. In the case *AR_start_time* is set to the controller/MPC start time, the if condition on line 2 evaluates to false when t_{CFD} becomes equal or larger than the MPC start time. In that case, the wave elevation data over the prediction horizon is calculated using AR predictions; see line 16. The wave excitation force is computed using the convolution integral given by Eq. (5.30) based on the AR predictions of wave elevation. Next, other necessary terms like the viscous force, the state vector $\mathbf{X_d}$, etc., are calculated on lines 19-21. Finally, the QP functionality of MATLAB is used to compute the optimal control force sequence $\underline{\Delta u_d}$ considering the necessary device constraints and penalty terms.

5.9 Validation of the BEM and MPC solvers and motivation behind this work

While MPC has been used in the process industries (chemical plants and oil refineries) since the 1980s, its formulation for the wave energy conversion application was first suggested by Gieske [134] in 2007. The study involved optimizing the control of the Archimedes wave swing (AWS) device modeled as a second-order linear system. In 2010, Cretel et al. [63] implemented a zero-order hold (ZOH) method based MPC for a half-submerged heaving vertical cylinder A later study published by Cretel et al. [127] suggested using the first-order hold (FOH) method, which yielded better results than ZOH-based MPC. The BEM-LFK solver was used in all the aforementioned studies.

In order to validate our (FOH-based) BEM-LFK solver and MPC implementations, we consider the same half-submerged vertical cylinder case as Cretel et al. [127]. The cylinder has a

Algorithm 3: MATLAB-based MPC routine.

time_horizon = t_{CFD} + (0:N_p) $\times \Delta t_p$; // Calculate the discrete time horizon.
if *($t_{CFD} \leq AR\_start\_time$)* **then**
  if *(strcmp($F_{exc\text{-}type}$, 'LINEAR_FK'))* **then**
    $\text{F}_{\text{exc}} \leftarrow$ calculate_excitation_force(time_horizon); // Calculate F_{exc} using Eq. (5.28). η_{wave} is calculated using Eq. (4.1) for regular and Eq. (4.9) for irregular waves.
  else
    $z_{\text{predicted}} \leftarrow$ AR_prediction(z_{past}, t_{past}, N_p, AR_order, Δt_p); // Predict the device displacement using the AR model based on past data.
    $\text{F}_D \leftarrow$ calculate_diffraction_force(time_horizon); // Calculate the wave diffraction force using Eq. (5.33). η_{wave} is calculated using Eq. (4.1) for regular and Eq. (4.9) for irregular waves.
    for $(m = 1$ **to** $(N_p + 1))$ **do**
      $\psi \leftarrow$ calculate_level_set_for_cylinder($z_{\text{predicted}}(m)$, R_{cyl}, L_{cyl}); // Compute the level set for the cylinder on a static grid region $\mathscr{R}$.
      $\sigma \leftarrow$ calculate_level_set_for_wave(time_horizon(m)); // Compute the level set for the undulatory air-wave interface.
      $\text{F}_I(\text{m}) \leftarrow$ calculate_NLFK_force(ψ, σ, time_horizon(m)); // Calculate the incident wave force using Eq. (5.32).
    end
    $\text{F}_{\text{exc}} \leftarrow \text{F}_D + \text{F}_I$ // Compute F_{exc} for $\forall t \in$ time_horizon.
  end
else
  $\eta_{\text{A}_{\text{predicted}}} \leftarrow$ AR_prediction($\eta_{\text{A}_{\text{past}}}$, t_{past}, N_p, AR_order, Δt_p);
  Calculate the future N_p values of F_{exc} for $\forall t \in$ time_horizon using Eq (5.30).
end
Calculate the first term in the linearized form of the viscous force F_v given in Eq. (5.8).
Calculate the vectors $\text{X}_{\mathbf{d}}$ and $\underline{\Delta v_d}$.
Calculate $\mathscr{J}_{\boldsymbol{u}}^T Q \mathscr{J}_{\boldsymbol{u}}$ and $\mathscr{J}_{\boldsymbol{u}}^T Q(\mathscr{P}\mathbf{X}_{\boldsymbol{d}} + \mathscr{J}_{\boldsymbol{v}}\underline{\Delta v_d})$ terms of Eq. (5.21).
Minimize the cost function J_3 (with constraints) using the QP functionality of MATLAB to obtain the optimal control sequence $\underline{\Delta u_d}$.

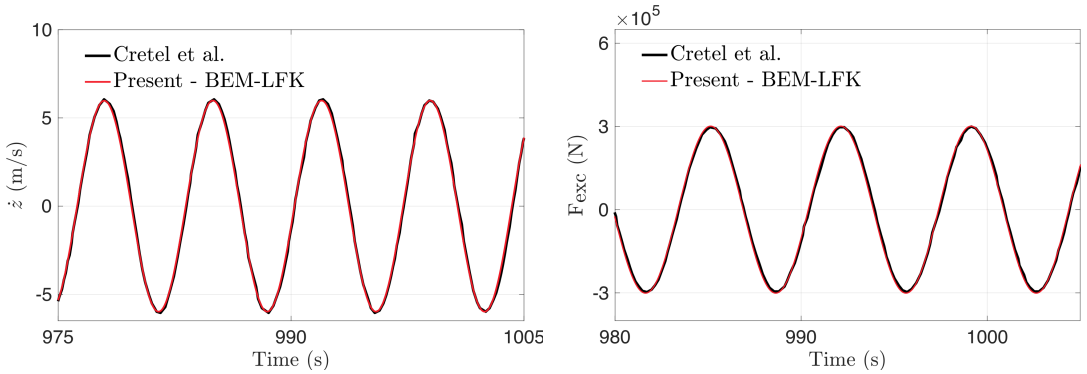

(a) Heave velocity (b) Wave excitation force

Figure 5.6. Temporal evolution of (a) the heave velocity and (b) wave excitation forces acting on the heaving vertical cylinder. Results are compared against Cretel et al. [127] for first-order regular waves of height $\mathscr{H} = 2$ m and time period $\mathscr{T} = 7$ s. The MPC parameters are $\Delta t_p = 0.1$ s, $\mathscr{T}_h = 6$ s, $\lambda_1 = 2$ s, and $\lambda_2 = 0$ s.

radius of $R_{\text{cyl}} = 5$ m and an upright length of $L_{\text{cyl}} = 16$ m. Regular waves of height $\mathscr{H} = 2$ m and time period $\mathscr{T} = 7$ s are used. This corresponds to a small have height case and the BEM solvers are expected to be accurate in this wave regime. The BEM parameters m_∞ and $\mathrm{K}_e(t)$ are obtained using ANSYS AQWA by performing frequency domain WSI simulations. The MPC parameters are taken to be $\Delta t_p = 0.1$ s, $N_p = 60$ (and consequently a prediction horizon of $\mathscr{T}_h = 6$ s), $\lambda_1 = 2$ s, and $\lambda_2 = 0$ s. There are no device constraints included, and J_2 cost function is used in the MPC to match Cretel et al.'s setup. Fig. 5.6 shows the temporal evolution of the heave velocity and excitation forces and compares it against the steady-state results of Cretel et al. [127]. Both studies agree very well. The steady-state time-averaged power $\overline{P}_{\text{PTO}}$ absorbed by the device is 353.5301 kW, which is also close to the value of 395.08 kW reported in [127]. We conclude from these results that our BEM-LFK solver and MPC implementations are correct.

Next, we compare the predictions of the BEM and CFD solvers for a 1:20 scaled-down version of the device (using Froude scaling). We do this to reduce the computational cost of CFD simulations, as the full-scale WEC device requires a larger computational domain and a higher mesh resolution to resolve the high Reynolds number flow. For further details on the Froude scaling of the device and wave characteristics ($\mathscr{H}$ and $\mathscr{T}$), the readers are referred to

Khedkar et al. [59]. The size of the domain, grid resolution, and time step size of the CFD simulation are determined by the spatial-temporal simulation performed in the next Sec. **??**. Both solvers use regular waves of height $\mathscr{H} = 0.1$ m and time period $\mathscr{T} = 1.5652$ s and the MPC parameters are $N_p = 60$, $\Delta t_p = 0.0223$ s, $\mathscr{T}_h = 1.3415$ s, $\lambda_1 = 2$ s, and $\lambda_2 = 0$ s. Fig. 5.7 compares the predictions of the two solvers. Fig. 5.7(a) clearly shows that the wave excitation force of the CFD simulation is much larger than that of the BEM-LFK simulation. A similar discrepancy is observed using the BEM-NLFK solver whose results are closer to the BEM-LFK solver. Since this is a low wave amplitude case, we attribute the discrepancy between the CFD and BEM solvers to the non-linear WSI caused by the controller. To confirm this hypothesis an additional CFD simulation is conducted, in which hydrodynamic loads are calculated on a vertical cylinder that has the same dimensions, but is fixed at equilibrium. The case is represented by the green curve in Fig. 5.7(a). It is clear that both solvers (CFD and BEM-LFK) estimate the same hydrodynamic force on the stationary cylinder. Furthermore, an uncontrolled dynamics case is simulated in the next Sec. **??**, where the BEM and CFD solvers' predictions match for the same wave conditions of this section. These additional tests confirm our hypothesis that even in calm sea conditions, the controller can cause a mismatch between the solvers' predictions.

Figs. 5.7(b) and 5.7(c) compare the MPC control force and the instantaneous power absorbed by the heaving device (respectively) using the BEM-LFK and CFD solvers. The comparison shows that, while the BEM-LFK solver estimates the power produced by the device at 10.6 W [6] during its steady-state operation, the CFD solver predicts a large withdrawal of power from the grid (-43.8 W). The power results of the BEM-NLFK solver are close to those of the BEM-LFK solver. There was only a small effect of changing the penalty term λ_1 on the power results of the two solvers. The results presented in this section, therefore, suggest that the BEM solvers may not always provide a reliable estimate of the power production capability of the WEC device under certain operating/controlled conditions. Furthermore, it can also be

[6] Using Froude scaling, this value corresponds to $10.6 \times (20)^{\frac{7}{2}} = 379.2$ kW for the full-scale device, which is close what is predicted earlier in this section.

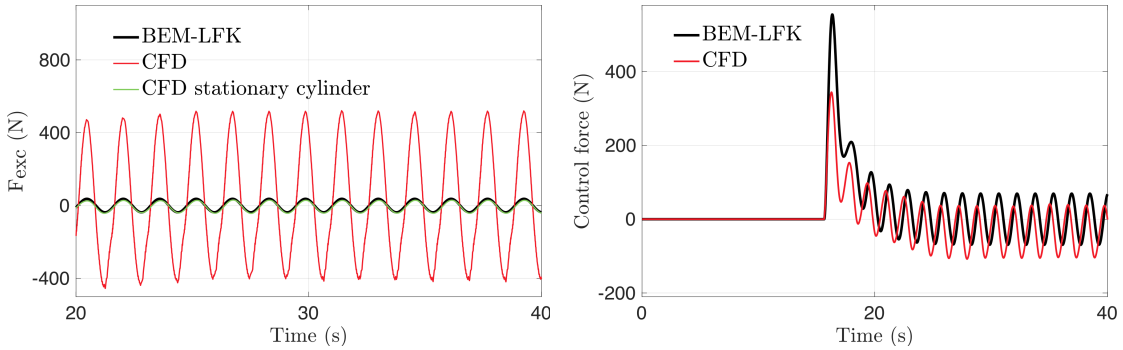

(a) Wave excitation force (b) Control force

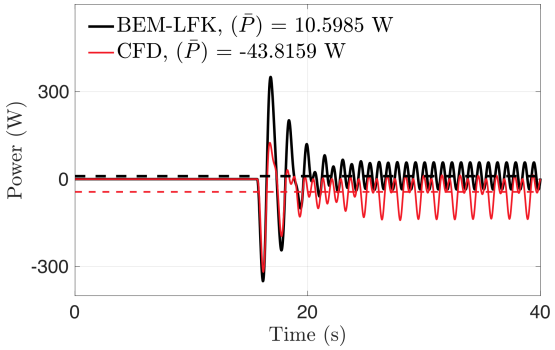

(c) Instantaneous and steady-state powers

Figure 5.7. Temporal evolution of (a) wave excitation force, (b) control force, and (c) instantaneous power absorbed for vertical cylinder WEC device heaving on the sea surface for first order regular wave of $\mathscr{H} = 0.1$ m and $\mathscr{T} = 1.5652$ s. The MPC parameters are $N_p = 60$, $\Delta t_p = 0.0223$ s, $\mathscr{T}_h = 1.3415$ s, $\lambda_1 = 2$ s, and $\lambda_2 = 0$ s.

appreciated that it is necessary to include the λ_2 term in the objective function to eliminate or mitigate the large negative powers. This section summarizes the motivation for the work conducted in this chapter, which is to investigate why the performance of various types of solvers differs and to compare them under different operating conditions. Due to the reasons noted above, we compare the performance of various solvers using J_3 instead of J_2 in the results and discussion Sec. 5.11. The case of this section is also repeated (Case 2 of Table 5.3) using the J_3 cost function because it is more suitable for the model predictive control of WECs.

Before proceeding to the main results Sec. 5.11, we first perform a grid convergence study for the CFD solver in the next section.

5.10 Grid convergence study

In this section, we perform a grid convergence study on the heaving WEC device using the CFD solver. Convergence tests are performed without the MPC. In WSI simulations, both regular and irregular waves are considered. The spatial resolution study is based on three spatial resolutions listed in Table 5.2, while the temporal resolution study is based on three values of the time step size Δt for irregular waves. In all tests, the maximum Courant-Friedrichs-Levy (CFL) number is less than or equal to 0.5. Simulations are performed on locally refined grids in order to reduce computational costs.

The computational domain for regular waves is $\Omega = [0,\ 3.145\lambda] \times [0,\ 12R_{\text{cyl}}] \times [0,\ 2.2d]$, whereas for irregular waves it is $\Omega = [0,\ 3.176\lambda] \times [0,\ 12R_{\text{cyl}}] \times [0,\ 2.2d]$. The domain size is large enough to eliminate boundary effects. This is based on our previous experience modeling WSI of WEC devices [55, 59]. The origin of the domain is located at the bottom left corner; see Fig. 5.4. The initial center of mass of the device is located at $\mathbf{X}_{\text{com}} = (\lambda + 5R_{\text{cyl}},\ 6R_{\text{cyl}},\ d)$. $R_{\text{cyl}} = 0.25$ m and $L_{\text{cyl}} = 0.8$ m, which is a 1:20 scaled-down version of the one presented in [127]. The cylinder is half-submerged in its equilibrium position.The quiescent water depth is d = 2 m, acceleration due to gravity is g = 9.81 m/s^2 (directed in the negative z-direction), density of water is ρ_{w} = 1025 kg/m^3, density of air is $\rho_{\text{a}} = 1.225$ kg/m^3, viscosity of water is $\mu_{\text{w}} = 10^{-3}$ Pa·s, and viscosity of air is $\mu_{\text{a}} = 1.8 \times 10^{-5}$ Pa·s. At this scale, surface tension at the air-water interface has no effect on WEC dynamics and is therefore ignored. All of the CFD simulations in this work, including those of the previous Sec. 5.9 use the same material properties and computational domain setup. Fig. 5.8 shows the grid layout and typical wave-structure interactions of the device in the NWT.

5.10.1 Spatial resolution study

Here, a grid convergence study is performed to determine the optimal mesh spacing for the CFD simulations. Three grid sizes are used to conduct the grid convergence test: coarse,

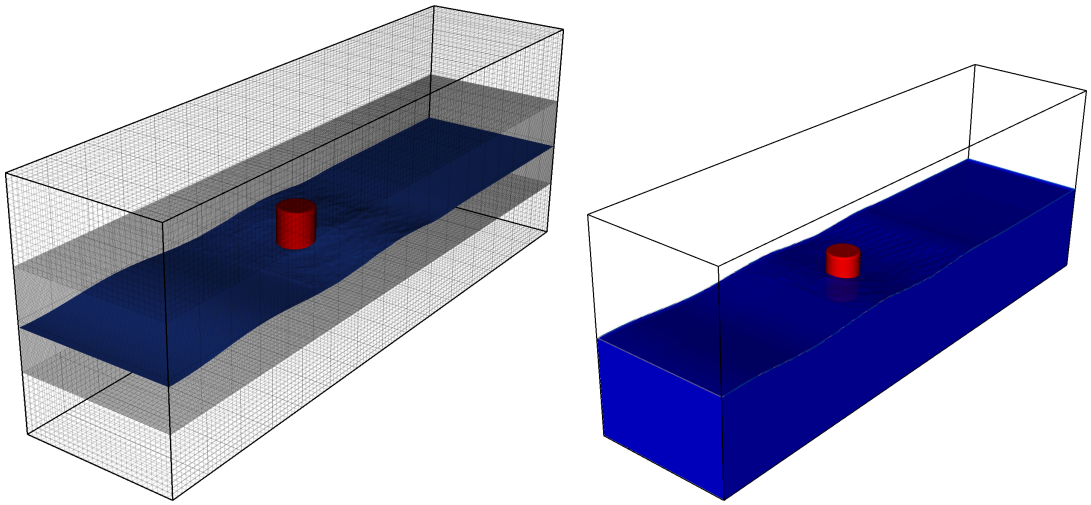

(a) Locally refined Cartesian mesh

(b) Regular waves

(c) Irregular waves

Figure 5.8. (a) Locally refined Cartesian mesh with two levels of mesh refinement for the 3D NWT. Representative WSI of the 3D WEC model at t = 37.5 s: (b) for regular waves and (c) for irregular waves.

medium, and fine (see also Table 5.2). The coarse mesh size corresponds to 5 cells per radius of the cylinder (CPR), the medium mesh size is 10 CPR, and the fine mesh size is 15 CPR. The computational mesh consists of a hierarchy of ℓ grid levels. The coarsest grid level is discretized into $N_x \times N_y \times N_z$ grid cells and covers the entire computational domain Ω. A sub-region of the coarsest level is then locally refined $(\ell - 1)$ times by an integer refinement ratio of n_{ref}. The local refining is done in such a way that the device and the air-water interface remains embedded on the finest grid level throughout the simulation. The grid spacing on the finest grid level is calculated as: $\Delta x = \Delta x_0 / n_{\text{ref}}^{\ell-1}$, $\Delta y = \Delta y_0 / n_{\text{ref}}^{\ell-1}$, and $\Delta z = \Delta z_0 / n_{\text{ref}}^{\ell-1}$, in which Δx_0, Δy_0, and Δz_0 are the grid spacings on the coarsest grid level.

First-order regular waves of height $\mathscr{H}$ = 0.1 m and time period $\mathscr{T}$ = 1.5652 s enter from the left side of the domain and interact with the 3D vertical cylinder. The temporal evolution of the device displacement and velocity using three mesh resolutions are shown in Figs. 5.9(a) and 5.9(b), respectively. The average percentage change in the peak values of the heave displacement between two consecutive grid resolutions is calculated from t = 20 s to 30 s. The average percentage change between the coarse and medium grids is 6 %, and between the medium and fine grids is 2.7 %. For heave velocity these values are 3.6 % and 2.5 %, respectively. Fig. 5.10 shows the air-water interface and the vortical structures arising from the WSI using the medium grid (CPR10) resolution. It can be observed that both these fluid dynamical quantities are adequately resolved by the CPR10 grid. From Figs. 5.9 and 5.10, it can be concluded that the medium grid resolution is able to capture the WSI dynamics with good accuracy and hence is used for the rest of the CFD simulations.

The device dynamics are also simulated using the BEM-LFK solver, which solves Eqs. (5.9)-(5.10) of Sec. 5.2. Since the present test simulates the WSI without MPC, the device undergoes a small motion from its mean equilibrium position under the action of first-order Stokes waves. Therefore, the CFD results are expected to match the BEM results in this situation. Indeed, this can be confirmed from the results of Figs. 5.9(a) and 5.9(b).

Table 5.2. Grid refinement parameters used for the grid convergence study.

Parameters	Coarse	Medium	Fine
n_{ref}	4	4	4
ℓ	2	2	2
N_x	60	120	180
N_y	15	30	45
N_z	22	44	66
$\Delta x_0 = \Delta y_0 = \Delta z_0$ (m)	0.2	0.1	0.0667
$\Delta x = \Delta y = \Delta z$ (m)	0.05	0.025	0.0166
Δt (s)	5×10^{-3}	2.5×10^{-3}	1.5×10^{-3}

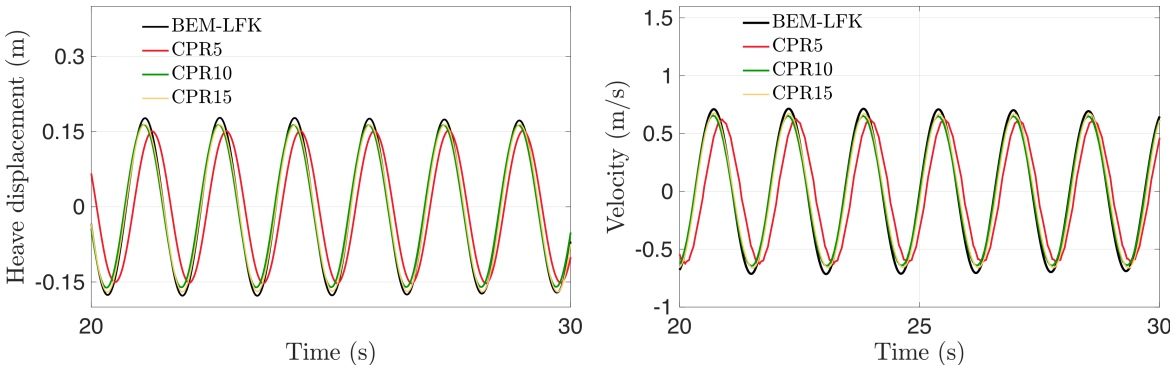

(a) Heave displacement (b) Heave velocity

Figure 5.9. Temporal evolution of the heave (a) displacement and (b) velocity of the uncontrolled WEC device using BEM-LFK (——, black) and CFD solvers. Three grid resolutions of CPR5 (——, red), CPR10 (——, green), and CPR15 (——, yellow) are used for the CFD solver. The first-order regular wave characteristics are: $\mathscr{H}$ = 0.1 m, $\mathscr{T}$ = 1.5652 s, and λ = 3.8144 m.

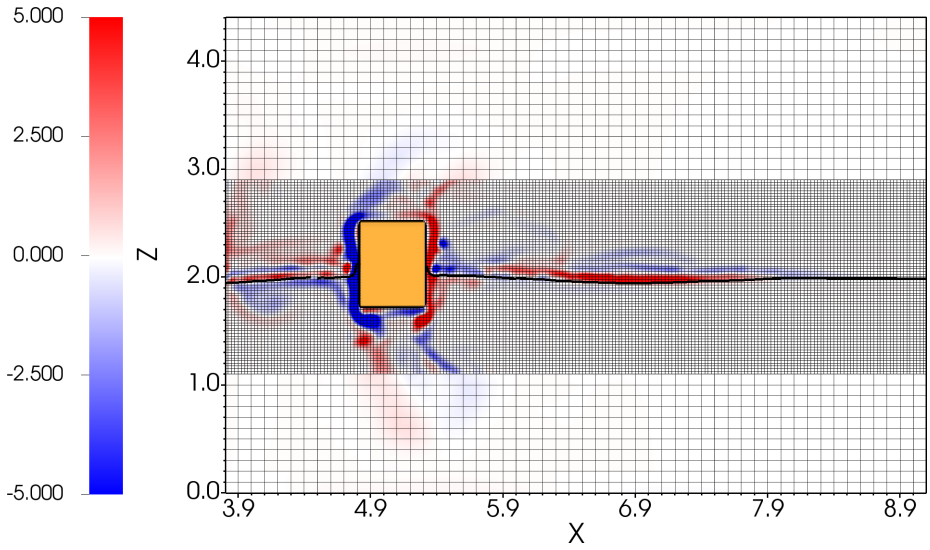

Figure 5.10. Wave-structure interaction of the 3D vertical cylinder WEC device (here shown in the $x-z$ plane) at $t = 22$ s using the medium grid resolution (CPR10). A locally refined mesh with $\ell = 2$ and $n_{\text{ref}} = 4$ is used. The air-water interface and the vortical structures resulting from the WSI are plotted.

5.10.2 Temporal resolution study

In this section, we conduct a time step size study to find the step size Δt that adequately resolves the energy content of irregular waves. Specifically, Δt should be such that the high-frequency wave components that carry a considerable amount of energy are adequately represented in the simulation. Irregular waves of height $\mathscr{H} = 0.15$ m, peak time period $\mathscr{T}_p = 1.7475$ s, and $N = 50$ wave components are generated at the left end of the NWT. We use three different time step sizes for the temporal convergence study: $\Delta t = 2.5 \times 10^{-3}$ s, 1.25×10^{-3} s, and 7×10^{-4} s. The medium grid resolution (CPR10) of the previous section is used here. The temporal evolution of the heave displacement and velocity of the device are compared in Fig. 5.11. With smaller Δt values, we are able to resolve the amplitudes of the heave displacement and velocity more accurately, as seen in Fig. 5.11(a) and Fig. 5.11(b), respectively. The average percentage change in the peak values of the heave displacement and velocity between two consecutive time step sizes is calculated from $t = 20$ s to 40 s. The average percentage change for the heave displacement between $\Delta t = 2.5 \times 10^{-3}$ s and $\Delta t = 1.25 \times 10^{-3}$ s is 15.06

% and betwen $\Delta t = 1.25 \times 10^{-3}$ s and $\Delta t = 7 \times 10^{-4}$ s is 9.89 %. For velocity, the percentage changes are 14.68 % and 5.45 %, respectively. According to these results, $\Delta t = 1.25 \times 10^{-3}$ s is sufficient to model WSI with irregular waves.

Based on the tests of this section, we hereafter use the medium grid spatial resolution with $\Delta t = 2.5 \times 10^{-3}$ s for regular waves and $\Delta t = 1.25 \times 10^{-3}$ s for irregular waves.

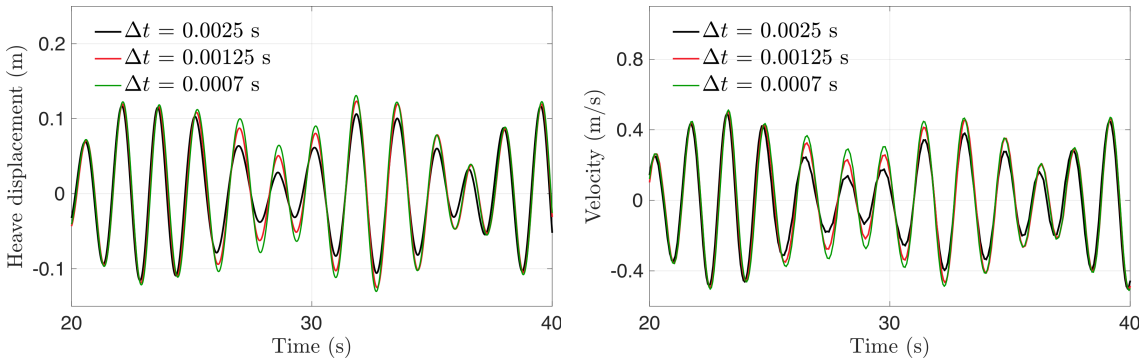

(a) Heave displacement

(b) Heave velocity

Figure 5.11. Temporal evolution of (a) the heave displacement and (b) heave velocity for three different time step sizes: $\Delta t = 2.5 \times 10^{-3}$ s (——, black), $\Delta t = 1.25 \times 10^{-3}$ s (——, red), and $\Delta t = 7 \times 10^{-4}$ s (——, green). Irregular water waves are generated with $\mathscr{H}_s$ = 0.15 m, $\mathscr{T}_p$ = 1.7475 s, and N = 50 wave components, with wave component frequencies in the range 1.6 rad/s to 20 rad/s distributed uniformly.

5.11 Point absorber WEC with MPC numerical examples

Sec. 5.9 motivates us to investigate the following questions:

1. At various sea states, how do the predictions of different WSI and MPC solvers compare?
2. In the case of the predictions of the solvers differing widely, what is the main reason for this?
3. How do AR predictions affect MPC performance?
4. By using CFD simulations, can the wave-to-PTO power transfer relationships be adequately captured?

5. How well does the MPC adapt to changing sea states?

We perform MPC-integrated WSI simulations of the cylindrical WEC device operating in different sea states to answer these questions. CFD simulations are conducted in a computational domain described in Sec. 5.10. The following MPC parameters are used in all simulations, unless stated otherwise: $\Delta t_p = 0.05$ s, $\mathscr{T}_h = \mathscr{T}$ (or $\mathscr{T}_p$), $N_p = \lceil \frac{\mathscr{T}_h}{\Delta t_p} \rceil$, $\lambda_1 = 2$ s, and $\lambda_2 = 0.2$ s. Here, $\lceil \cdot \rceil$ is the nearest-integer/ceil function. The controller is activated at $t = 10\ \mathscr{T}$ (or $10\ \mathscr{T}_p$), i.e., when the device starts oscillating steadily. We do this to avoid the possibility of creating a large PTO force at the start of the simulation, which could destabilize it.

5.11.1 Comparing the predictions of different solvers

This section compares the predictions of various WSI and MPC solvers listed in Table 5.1. The results presented here are not based on the AR model, but on analytical expressions to predict the wave elevation data. We discuss the effect of AR predictions on MPC performance separately in Sec. 5.11.2. Table 5.3 lists the sea states and the PTO force limits. In order to simplify the discussion, constraints on the device displacement and velocity are not included in the MPC. Furthermore, preliminary testing showed that adding the displacement and velocity constraints (along with the PTO force constraint) did not significantly alter the results of this section.

Table 5.3. Cases considered for comparing results for various solvers and MPC methodologies.

Case	Wave type	Wave height (m)	Control force (F_{PTO}) constraint (N)
1	First-order regular	0.1	$\pm$ 25
2	First-order regular	0.1	$\pm$ 100
3	First-order regular	0.5	$\pm$ 25
4	First-order regular	0.5	$\pm$ 100
5	First-order regular	0.5	$\pm$ 300
6	Irregular	0.15	$\pm$ 25
7	Irregular	0.15	$\pm$ 100
8	Irregular	0.3	$\pm$ 25
9	Irregular	0.3	$\pm$ 100

Table 5.4. Time-averaged power output using different WSI and MPC solvers for Cases 2, 5, 7, and 9 of Table 5.3.

	Solver	MPC	Time-averaged power (W)			
			Case 2	Case 5	Case 7	Case 9
1	BEM-LFK	LFK	5.4458	138.9282	3.9463	12.6718
2	BEM-LFK	NLFK	5.674	142.7581	3.8786	12.1793
3	BEM-NLFK	LFK	5.4766	40.9436	3.726	13.0561
4	BEM-NLFK	NLFK	5.5401	36.9532	3.7235	12.8456
5	CFD	LFK	3.7216	34.2936	2.4871	7.9284
6	CFD	NLFK	3.7407	34.4263	2.7513	9.0553

Comparing the predictions with regular waves

Here, the controlled heave dynamics of the WEC device operating in regular sea conditions are compared. As listed in Table 5.3, Cases 1 and 2 consider regular waves of small height $\mathscr{H} = 0.1$ m and time period $\mathscr{T} = 1.5652$ s, with control force limits of ± 25 N and ± 100 N, respectively. Cases 3, 4, and 5 consider regular waves of large height $\mathscr{H} = 0.5$ m and (the same) time period $\mathscr{T} = 1.5652$ s, with control force limits of ± 25 N, ± 100 N, and ± 300 N, respectively. Allowing a larger control force in MPC leads to a higher heave amplitude of the device. However, this puts more strain on the actuator system, which can damage the hardware or negatively impact the actuator efficiency (actuator efficiency is not considered in this work).

Figs. 5.12(a) and 5.12(b) compare the heave displacement, 5.12(c) and 5.12(d) compare the optimal control force, and 5.12(e) and 5.12(f) compare the instantaneous power absorbed by the device using different WSI and MPC solvers for Case 2 and 5, respectively. The time-averaged power of the device for Cases 2 and 5 is listed in Table 5.4. The time-averaged power is calculated between $t = 30$ s to 40 s when the device dynamics become steady. Other simulations produce similar trends, which for brevity are not shown. Instead, the time-averaged powers are shown in Fig. 5.14(a).

From the results presented in Fig. 5.12 and Table 5.4, it is observed that for the small wave height Case 2, the BEM-LFK solver results are close to those of BEM-NLFK and CFD solvers. In contrast, for the large wave height Case 5, the dynamics and the power absorbed by the WEC

device are largely over-predicted. Another important observation from Table 5.4 and Fig. 5.14(a) is that the MPC-LFK and MPC-NLFK solvers produce almost the same time-averaged powers, when used either with the BEM or the CFD solver. It can also be observed that the BEM-NLFK and CFD solver results are in good agreement.

The results of this section provide two meaningful insights: (**1**) the main cause of discrepancy between the BEM-LFK and the CFD (or the BEM-NLFK) solver is the manner in which wave excitation forces are computed; and (**2**) there is a little advantage to increasing the complexity of the hydrodynamical model within MPC. The latter also implies that the simpler and computationally faster LFK model is sufficiently acurate for the model predictive control of WECs. .

One can also note that by using $\lambda_2 = 0.2$ s, the negative part of the power cycle is largely eliminated for all WSI solvers. This can be verified from the instantaneous power curves of Figs. 5.12(e) and 5.12(f).

Comparing the predictions with irregular waves

Next, the controlled heave dynamics of the WEC device operating in irregular sea conditions are compared. Cases 6 and 7 in Table 5.3 are of irregular waves of small significant wave height $\mathscr{H}_s = 0.15$ m and peak time period $\mathscr{T}_p = 1.7475$ s, with control force limits of ± 25 N, and ± 100 N, respectively. Cases 8 and 9 concern irregular waves of moderate significant wave height $\mathscr{H}_s = 0.3$ m and (the same) peak time period $\mathscr{T}_p = 1.7475$ s, with control force limits of ± 25 N and ± 100 N, respectively.

Fig. 5.13 presents the WEC dynamics for Cases 7 and 9. Results for Cases 6 and 8 are not presented for brevity, as they show similar trends. Figs. 5.13(a) and 5.13(b) compare the heave dynamics, 5.13(c) and 5.13(d) compare the optimal control force, and 5.13(e) and 5.13(f) compare the instantaneous power absorbed by the device using different WSI and MPC solvers for Case 7 and 9, respectively. The time-averaged power of the device is listed in Table 5.4 and is calculated between t = 30 s to 40 s when the device dynamics become steady. Simulations of

the other cases produce similar trends and are not shown for brevity. Instead, the time-averaged powers are plotted in Fig. 5.14(b).

As shown in Fig. 5.13 and Table 5.4, all WSI and MPC solvers perform almost the same, though the CFD solver predicts slightly lower power for Case 9 than the BEM-LFK and BEM-NLFK solvers. This is not surprising since the wave heights considered in this section are relatively low. At larger (significant) wave heights, we expect the differences between BEM-LFK and CFD (or BEM-NLFK) solvers to increase; this is confirmed in the next section. Waves with large significant wave heights are not considered here, since the CFD solver requires very small time steps to maintain the numerical stability. As a result, the 3D simulation will take very long to run, which is something we cannot afford at the moment.

The results of Secs. 5.11.1 and 5.11.1 suggest that the BEM-LFK solver may give too optimistic results, especially when the hydrodynamic nonlinearities increase. Conversely, the CFD solver can resolve hydrodynamical non-linearities with high-fidelity, albeit at an increased computational cost, and provides more realistic results. Between these two extremes is the BEM-NLFK solver, which yields somewhat optimistic power values, but not quite as large as the BEM-LFK solver. In addition, either MPC-LFK or MPC-NLFK is equally effective for a specific WSI solver since they give very close results. Since the MPC-LFK technique is computationally faster than MPC-NLFK, it is better suited for practical control of WEC devices.

Comparing the predictions with varying wave periods

This section compares the predictions of the BEM-LFK and BEM-NLFK solvers for varying wave periods. Regular and irregular sea conditions are considered. For the two WSI solvers, MPC-LFK is used. Due to the high computational cost associated with simulating waves of longer durations and wavelengths, CFD simulations are not performed here.

Results compare the time-averaged power absorbed by the WEC device for regular waves in Fig. 5.15(a) and for irregular waves in Fig. 5.15(b). The regular waves have wave heights of $\mathscr{H}$ = 0.1 m, 0.3 m, and 0.5 m, with time periods varying from 1.2 s to 4.6 s. The irregular waves

considered here have significant wave heights of $\mathscr{H}_s$ = 0.1 m, 0.3 m, 0.5 m, and 1 m, with peak time periods varying from 1.2 s to 3.4 s.

The results show that the BEM-LFK solver over-predicts the time-averaged power absorbed by the device for large waves; for regular waves, $\mathscr{H}$ = 0.5 m and for irregular waves, $\mathscr{H}_s$ = 1 m. Further, for both regular and irregular waves, the difference between the two solvers' predictions is greater at smaller time periods than at larger time periods. This is because the natural period of oscillation of the device is 1.54 s, which falls in the small time period region, where the device oscillates with large amplitude due to the waves and actuator induced resonance. The BEM-LFK solver inherently violates the small motion assumption used in its formulation near or at resonance, and therefore provides inaccurate power estimates.

5.11.2 CFD simulations with AR-enabled wave predictions

In this section, we examine the effect of AR predictions on MPC performance. In this test, we use the MPC-LFK and CFD solvers with regular waves of height $\mathscr{H}$ = 0.5 m and time period $\mathscr{T}$ = 1.5652 s, and with irregular waves of significant wave height $\mathscr{H}_s$ = 0.3 and peak time period $\mathscr{T}_p$ = 1.7475 s. We set *AR_start_time* equal to MPC start time: $t = 10\,\mathscr{T}$ (or $10\,\mathscr{T}_p$). Therefore, the controller and the AR predictions will begin once the device exhibits steady-state oscillations under the influence of incoming waves. MPC and NWT interaction is schematically represented in Fig. 5.5. In particular, wave elevation data at an up-wave probe point A (η_A) for the past two wave periods is collected and sent to the AR model to allow for wave elevation prediction over one wave period into the future (at the same location A). For predicting regular and irregular waves, we use AR models of order 3 and 5, respectively. Figs. 5.16(a) and 5.16(b) illustrate that the chosen AR models are sufficiently accurate for predicting regular and irregular waves, respectively. Based on the past and predicted wave data, the wave excitation force $\mathrm{F_{exc}}$ acting on the device is calculated using Eq. (5.30).

As a test of the accuracy of the AR-integrated MPC solver, the results are compared with those obtained using analytical forcing, which was also used in Sec. 5.11.1. As for regular

waves, Figs. 5.17(a), 5.17(c), and 5.17(e) compare the heave displacement, control force, and the instantaneous power absorbed by the device, respectively. Figs. 5.17(b), 5.17(d), and 5.17(f) compare these quantities for irregular waves. The results show that the device dynamics are very close with or without the AR predictions. The time-averaged power absorbed by the WEC device subject to regular waves is 40.5546 W when the AR model is enabled. The value of 41.0097 W obtained by analytical forcing agrees well with this result. In the case of irregular waves, these values are 9.9799 W and 7.9284 W, which also match fairly well. Further improvements can be obtained for the irregular wave case by using a better method of time-series forecasting or by fine-tuning the AR model.

We conclude from the results of this section that our technique of collecting wave elevation data from an up-wave location in the NWT and predicting future waves based on it (through an AR model) works well with the CFD/MPC-LFK solver combination.

5.11.3 Power transfer from waves to the PTO system: Verifying the relationships with CFD simulations

We re-analyze the AR-enabled CFD simulations of the previous section to verify the power transfer relations in Sec. 5.6. In the case of regular waves of height $\mathscr{H}$ = 0.5 m and time period $\mathscr{T}$ = 1.5652 s, the power transferred by the waves to the device (or the work done by the hydrodynamic forces) is $\overline{P}_{\text{waves} \rightarrow \text{cyl}}$ = 38 W and that absorbed by the PTO unit is $\overline{P}_{\text{PTO}}$ = 39 W. A time average is taken from t = 30 s to 31.5652 s, i.e., for one wave period. Based on these power values, we conclude that the power transfer Eq. (5.41) is verified in the case of regular waves. In the case of irregular waves, we calculate the left and right sides of Eq. (5.40) separately. t = 30 s to 40 s is chosen as the time interval for time-averaging the terms of the equation. Accordingly, the two sides of the equation evaluate to 72.06 W and 71.47 W, respectively, which also match reasonably well.

Based on the results of this section, we conclude that our CFD simulations satisfy the power transfer relationships of Sec. 5.6.

5.11.4 MPC adaptivity

To test the adaptive capability of MPC for WEC devices, we simulate the dynamics of the 3D vertical cylinder subject to changing sea states. Specifically, three consecutive sea states are considered within a single CFD simulation: sea state 1 consisting of first-order regular waves of height $\mathscr{H}$ = 0.1 m and time period $\mathscr{T}$ = 1.5652 s between $t_1 = 0$ s to $t_2 = 40$ s, sea state 2 consisting of first-order regular waves of height $\mathscr{H}$ = 0.2 m and time period $\mathscr{T}$ = 2 s between $t_2 = 40$ s to $t_3 = 60$ s, and sea state 3 consisting of first-order regular waves of height $\mathscr{H}$ = 0.15 m and time period $\mathscr{T}$ = 1.7475 s between $t_3 = 60$ s to $t_4 = 120$ s. The wave elevation is smoothly varied from one sea state to the other using the following expression:

$$\eta_{i,i+1}(t) = \eta_i(t) + (\eta_{i+1}(t) - \eta_i(t)) \cdot (1 + \tanh(t - (t_{i+1} - t_{\text{half-interval}}))/2, \tag{5.42}$$

in which $\eta_i(t) = (\mathscr{H}_i/2)\cos(\kappa_{wi}x - \omega_i t)$ and $t_{\text{half-interval}} = 5$ s is the transition time between sea state i to $i+1$. AR predictions are also enabled for the CFD simulation. For MPC, each sea state uses a pre-configured AR model that is optimized offline. While this is inconvenient, it is necessary to allow accurate predictions of wave excitation forces.

Fig. 5.18 shows the temporal evolution of the heave displacement and velocity. We compare the CFD results with three separate BEM-LFK simulations for different sea states. Because all three sea states have small amplitude waves, the BEM-LFK solver is expected to be accurate. Indeed, it is observed that the adaptive CFD simulation agrees well with the BEM-LFK solver results, which indicates that the MPC algorithm is able to adapt according to the current sea state and produces an optimal solution in each case.

5.12 Conclusions

In this study, we simulated the controlled dynamics of a heaving 3D vertical cylinder WEC device using BEM and multiphase IB solvers. A MPC strategy was used to maximize the

energy absorption capacity of the WEC device under regular and irregular sea conditions.

We validated our BEM-LFK and MPC-LFK implementations by simulating a benchmarking case from Cretel et al. [127] in Sec. 5.9. The scaled-down version of the same device was then simulated using the multiphase IB solver, and its wave excitation forces were significantly greater than those predicted by the BEM solvers. A more surprising result was that the WEC device drew a large amount of power from the grid instead of producing energy, as predicted by the BEM solvers. Moreover, it was observed that J_3 is a better choice for the model predictive control of WECs compared to J_2, as the latter can provide misleading power output. To understand the main cause of the discrepancy, we examined six different combinations of the WSI and MPC solvers using J_3 as the cost function. It is found that when the sea state is calm and the wave height is small, the BEM solvers' predictions match well with the CFD solver's. However, in agitated sea conditions, the BEM solvers over-predict the device performance, which can be misleading to the device designer. On the other hand, the CFD solver provides realistic results both in calm and agitated sea conditions. It is evident that resolving the hydrodynamic non-linearities associated with the WSI is essential to obtaining realistic estimates of the device's power. It is further confirmed by the results of the BEM-NLFK solver, which are closer to those of the multiphase IB solver. Therefore, we recommend using the BEM-NLFK solver to study the controlled dynamics of WECs when computational resources are limited to employing a CFD solver. In addition, it is straightforward to switch to the BEM-NLFK solver by using the static grid technique described in Sec. 5.4.2. Additionally, we found that the choice between MPC-LFK or MPC-NLFK is irrelevant, as both algorithms give very similar results. Nevertheless, MPC-LFK solver is computationally-efficient and is proposed as a practical model-based control for WECs.

We also compared the performance of MPC-LFK with and without AR predictions in Sec. 5.11.1. We found that the AR prediction strategy worked well in both regular and irregular waves. The AR model can be tuned further or a different time-series forecasting algorithm can be used for further improvements. The pathway of energy transfer from waves to the PTO unit for the heaving WEC device was also derived and confirmed. By simulating three different sea

states consecutively within a single CFD simulation, we tested the adaptive capabilities of MPC of WECs. The MPC is shown to adapt to different sea states and find the optimal solution for each situation, thus living up to its reputation as the "Tesla" of control approaches.

One significant challenge inherent in model-based control strategies arises from the necessity to adjust the dynamical model to accommodate shifting system dynamics which happen over a period of time, such as those influenced by marine growth and sub-system failures. Also, modeling errors can negatively affect the performance of the device, particularly in highly energetic waves where the non-linear effects are significant. Failure to update the model accordingly results in the adoption of sub-optimal control strategies. This motivates us to explore model-free control strategies, particularly those grounded in reinforcement learning. By continuously adapting to evolving system dynamics, these approaches circumvent the limitations associated with model-based controllers.

Acknowledgement

This chapter, in full, is a reprint of the material as it appears in "A model predictive control (MPC)-integrated multiphase immersed boundary (IB) framework for simulating wave energy converters (WECs)", Kaustubh Khedkar, Amneet Pal Singh Bhalla, Ocean Engineering, Volume 260, 2022. The dissertation author was the primary investigator and author of this paper.

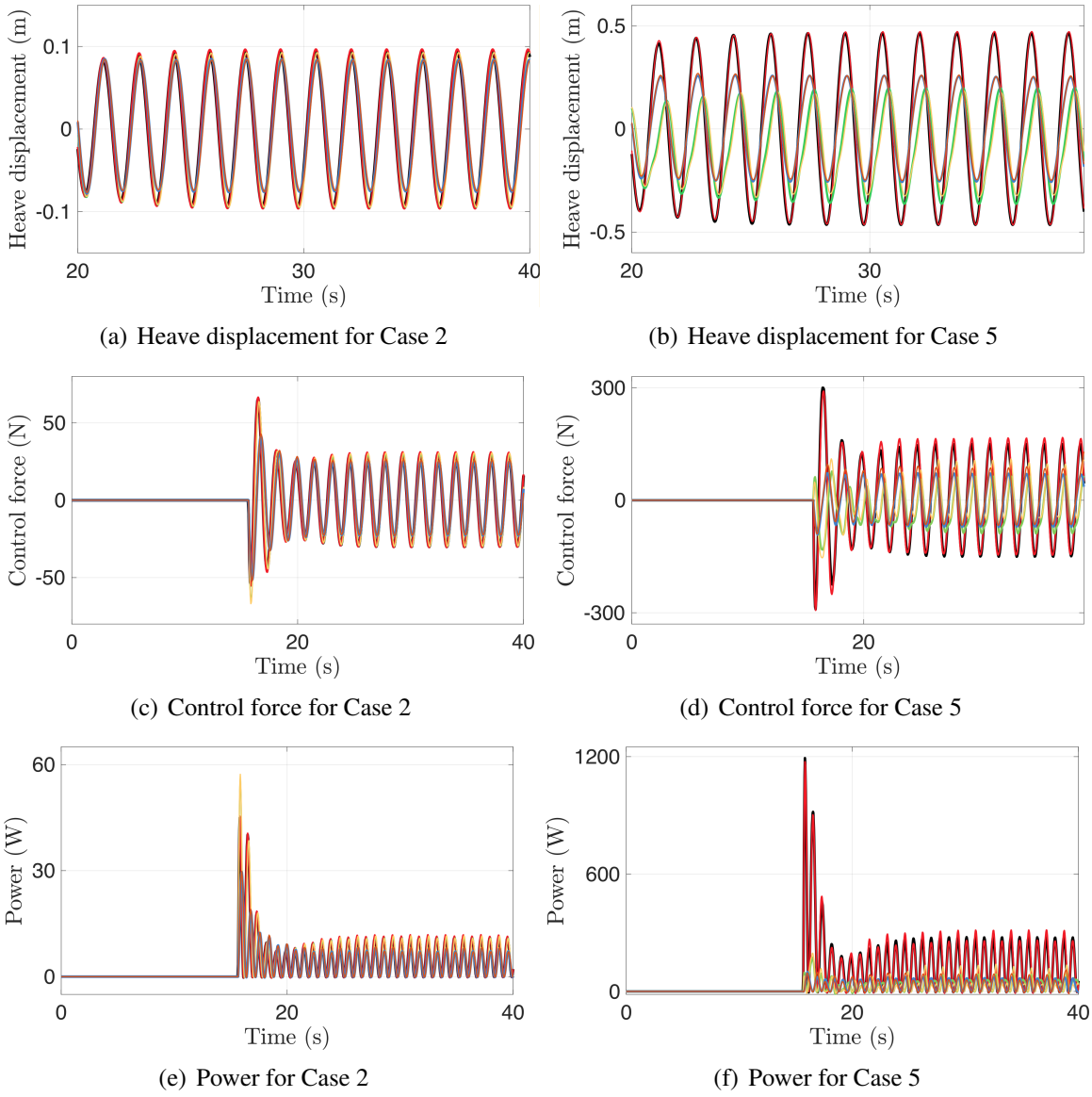

(a) Heave displacement for Case 2

(b) Heave displacement for Case 5

(c) Control force for Case 2

(d) Control force for Case 5

(e) Power for Case 2

(f) Power for Case 5

Figure 5.12. Comparison of the controlled heave dynamics of the 3D vertical cylinder WEC device with regular waves. Case 2 and Case 5 of Table 5.3 are considered here. The WSI and MPC solver combinations are: BEM-LFK and MPC-LFK (——, black); BEM-LFK and MPC-NLFK (——, red), BEM-NLFK and MPC-LFK (——, green), BEM-NLFK and MPC-NLFK (——, mustard), CFD and MPC-LFK (——, blue), and CFD and MPC-NLFK (——, orange).

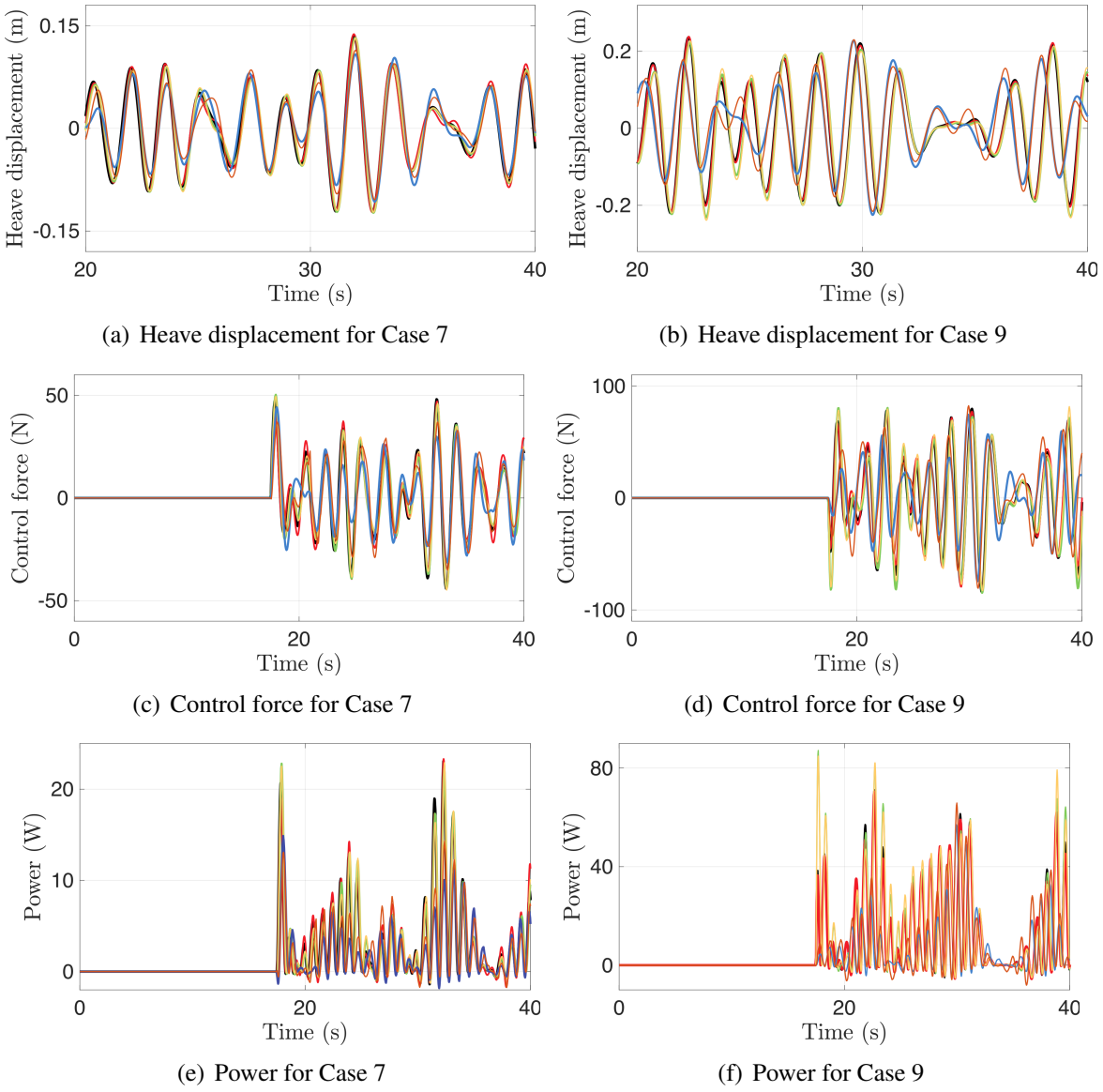

(a) Heave displacement for Case 7

(b) Heave displacement for Case 9

(c) Control force for Case 7

(d) Control force for Case 9

(e) Power for Case 7

(f) Power for Case 9

Figure 5.13. Comparison of the controlled heave dynamics of the 3D vertical cylinder WEC device with irregular waves. Case 7 and Case 9 of Table 5.3 are considered here. The WSI and MPC solver combinations are: BEM-LFK and MPC-LFK (——, black), BEM-LFK and MPC-NLFK (——, red), BEM-NLFK and MPC-LFK (——, green), BEM-NLFK and MPC-NLFK (——, mustard), CFD and MPC-LFK (——, blue), and CFD and MPC-NLFK (——, orange).

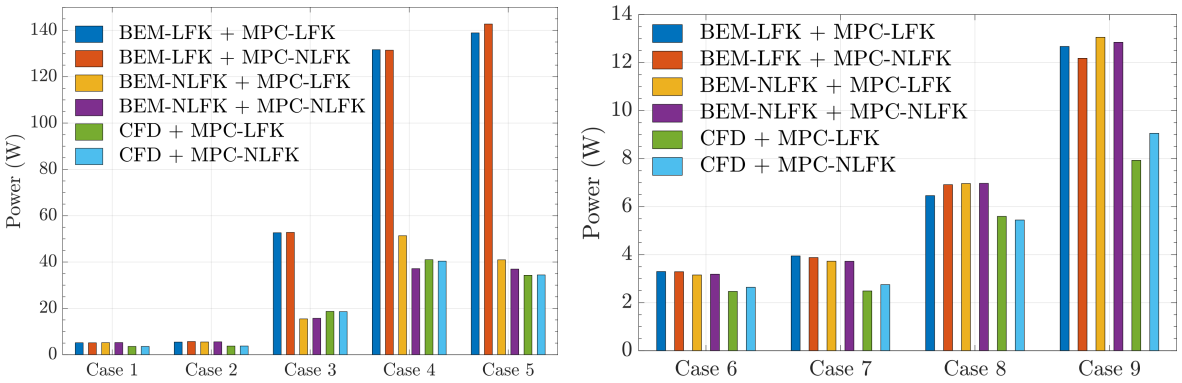

(a) Regular waves (b) Irregular waves

Figure 5.14. Comparison of time-averaged powers for cases given in Table 5.3

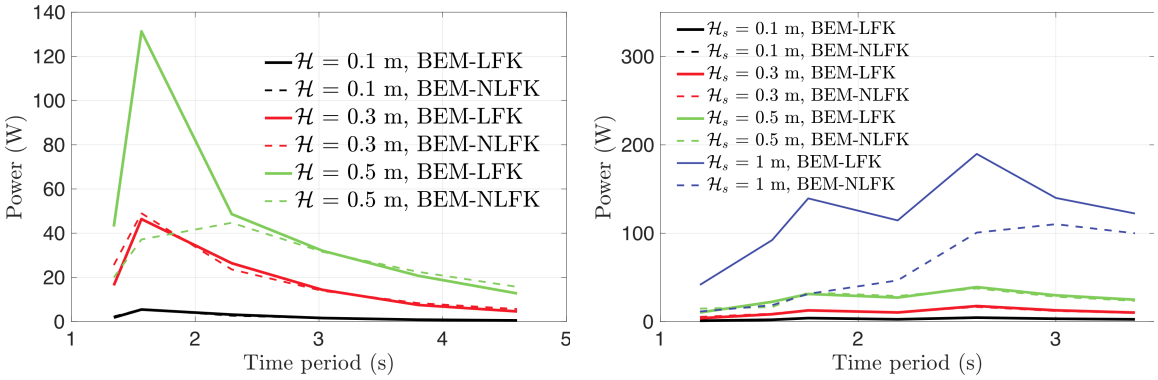

(a) Regular waves (b) Irregular waves

Figure 5.15. Comparison of time-averaged power absorbed by the WEC device operating in (a) regular and (b) irregular sea conditions with varying wave periods and heights. The BEM-LFK (BEM-NLFK) solver results are shown with solid (dashed) lines.

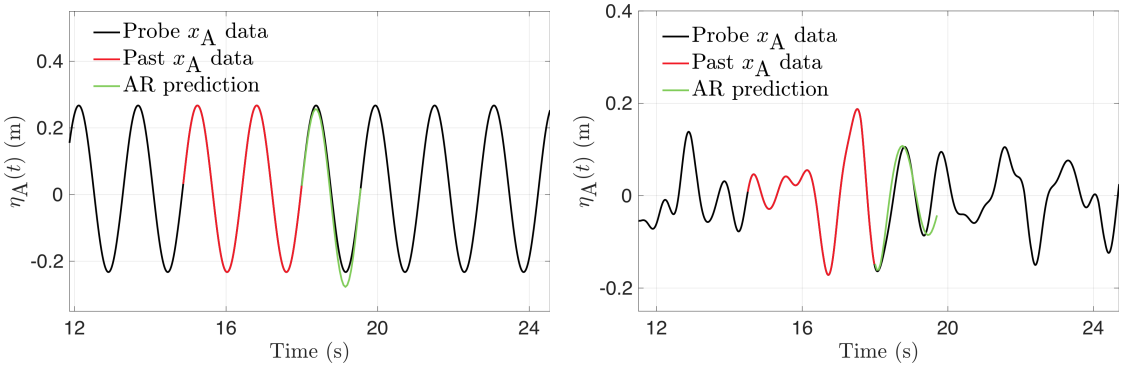

(a) AR model prediction for regular waves (b) AR model prediction for irregular waves

Figure 5.16. AR model predictions (——, green) of (a) regular and (b) irregular waves for one wave period into the future using the past two wave period elevation data (——, red).

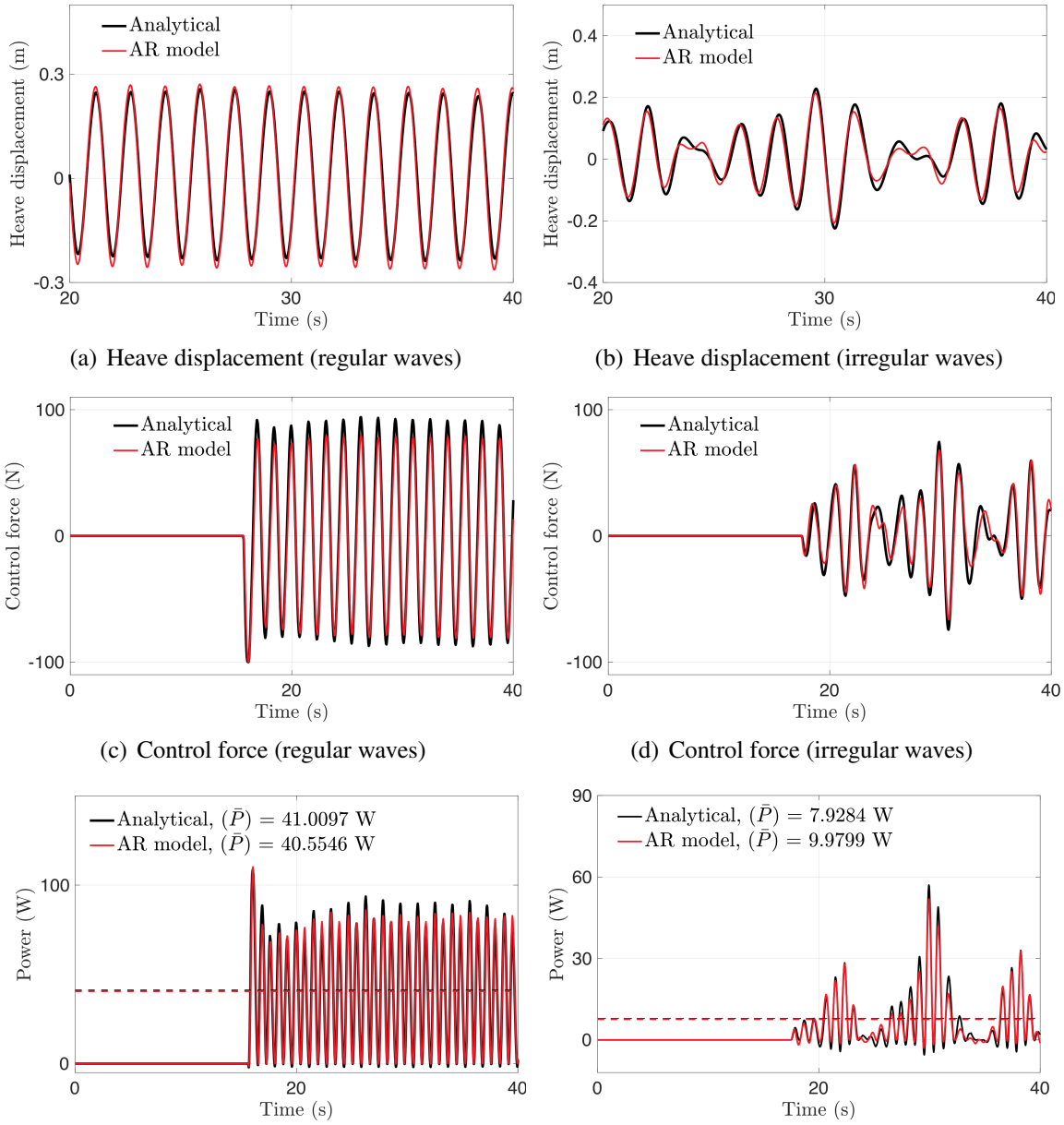

(a) Heave displacement (regular waves)

(b) Heave displacement (irregular waves)

(c) Control force (regular waves)

(d) Control force (irregular waves)

(e) Power (regular waves)

(f) Power (irregular waves)

Figure 5.17. Comparison of the controlled heave dynamics of the 3D vertical cylinder with and without AR predictions. The WEC dynamics are simulated using the CFD and MPC-LFK solver. For regular water waves of height $\mathscr{H}$ = 0.5 m and time period $\mathscr{T}$ = 1.5652 s results are compared for (a) heave displacement, (c) control force, and (e) instantaneous power. For irregular water waves of significant wave height $\mathscr{H}_s$ = 0.3 m and peak time period $\mathscr{T}_p$ = 1.7475 s results are compared for (b) heave displacement, (d) control force, and (f) instantaneous power. In all cases the control force limits are set to $\pm$ 100 N.

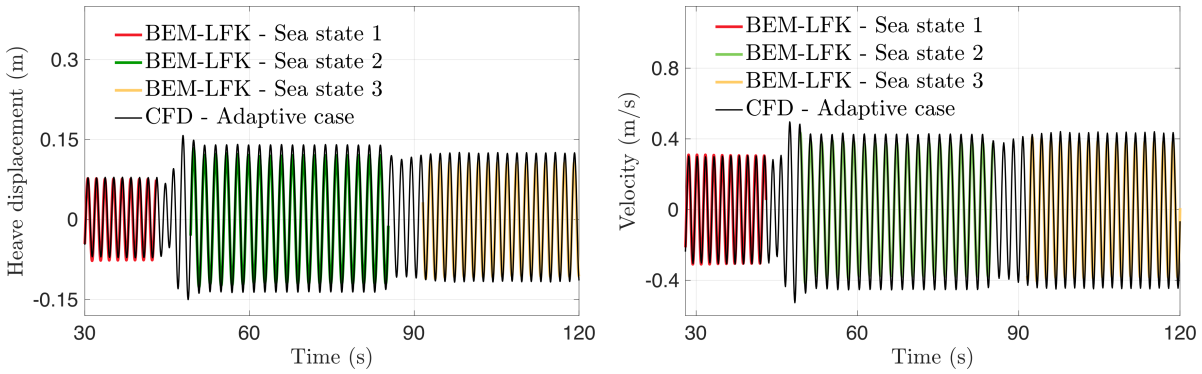

(a) Heave displacement

(b) Heave velocity

Figure 5.18. Comparison of the (a) heave displacement and (b) velocity of the device subject to changing sea states using CFD and BEM-LFK solvers. The BEM-LFK solver solves the three sea states separately, whereas the CFD solver considers them consecutively.

Chapter 6

Reinforcement Learning Based Control Strategy for Wave Energy Converter Devices

Several critical challenges in ocean wave energy harvesting can be addressed by designing a robust controller to optimize the wave energy converter (WEC) performance under changing sea states and WEC dynamics in its lifespan. In contrast to the renowned model-based controllers, this can be done using model-free reinforcement learning (RL) techniques. In this chapter, we employ deep Q-network (DQN) and double DQN (DDQN) RL algorithms to obtain the optimal damping and stiffness PTO coefficients for a vertical cylindrical shaped point absorber WEC device as described in Chapter 5. These RL algorithms train an agent (a deep neural network) to output optimal actions taking the current sea state as an input. Basically, the trained agent serves as a function approximator, generating optimal actions to maximize the reward function .i.e. to absorb maximum wave power. Initially, we implement this framework on our LPT based WEC model described in Chapter 5 and demonstrate the trained agent drives the device towards optimal performance. Subsequently, we deploy the trained agent within our CFD based WEC simulation environment, showcasing its efficacy in driving the device towards optimal performance in a more realistic setting.

6.1 Introduction

In the past decade the field of reinforcement learning (RL) has demonstrated exceptional performance across various domains: from predicting the traffic flow [145], forecasting the inside air temperature of a pillar cooler [146], marine hydrodynamic prediction [147] of scour of breakwaters using the genetic programming and artificial neural networks, control of reservoir flooding [148] using bang-bang control, and playing Atari games attaining human level performance [149, 150, 151].

Recent works have explored model-free adaptive algorithms rooted in RL techniques [152]. These algorithms are capable of dynamically tuning the control parameters as a function of the sea state and system functioning conditions for WEC devices [153, 154]. Li et al. [141] applied artificial neural network to optimize the latching control of a heaving buoy by collecting real-time wave elevation data and predicting wave forces. Anderlini et al. [154] implemented RL to obtain optimal control of a two-body point absorber device. The controller's damping and stiffness coefficients are varied in steps according to varying sea states and the associated reward is observed. Furthermore, Bruzzone et al. [155] implemented the Q-learning method to dynamically adjust the generator speed-torque ratio as a function of the sea state to optimize the power absorption of an onshore oscillating arm WEC device. In all these RL based methods, the idea is to implement an artificial neural network as a function approximator to calculate the optimal control force to simulate the dynamics of the device thus eliminating the use of explicit dynamic models.

6.2 Background on reinforcement learning

In RL, a controller (also referred as an agent or decision maker) interacts with a dynamic process (the environment), through three signals: a state signal describing the current state of the process, an action signal allowing the controller to influence the process, and a scalar reward signal offering immediate performance feedback to the controller. At each discrete

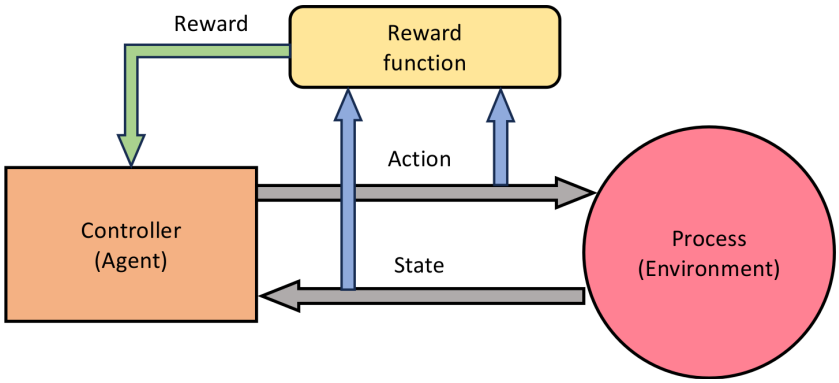

Figure 6.1. Schematic representation of the RL elements and their flow of interaction.

time step, the controller observes the current state, selects and executes an action, causing the process to transition to a new state. A reward is then computed, evaluating the efficacy of this transition. Subsequently, the controller receives feedback on the new state, initiating the cycle again. This interactive flow is illustrated in Figure 6.1. For further insights into RL, refer the books: [152, 156, 157].

6.2.1 RL as a Markov decision process

Consider, a transition function responsible to move an environment from one state to another. In RL, transition functions are formulated as a Markov decision process (MDP) which provides a mathematical framework that models sequential decision making. The theory of this section is taken from [157]. Consider, a general formulation shown by

$$s_{t+1} \sim P(s_{t+1}|(s_0,a_0),(s_1,a_1),.....,(s_t,a_t)), \tag{6.1}$$

where, P is the probability distribution. Eq. (6.1) means the next state s_{t+1} at time step t is sampled from the probability distribution P conditioned on the entire history of states and actions. This means the probability of transitioning from state s_t to s_{t+1} depends on all of the preceding states s and actions a that have occurred so far. Modeling such transition function becomes challenging as it needs to account for vast combination of effects that have occurred in the

past. To make the environment transition more practical, we turn it into a MDP by adding the assumption that transition to the next state s_{t+1} only depends on the previous state s_t and the action a_t. This is known as the Markov property. The new transition function becomes

$$s_{t+1} \sim P(s_{t+1}|s_t, a_t). \tag{6.2}$$

The Markov property implies that the current state s and action a at time step t provide sufficient information to fully determine the transition probability for the next state s_{t+1}.

A MDP is defined by a tuple $\mathscr{S}, \mathscr{A}, P(\cdot), \mathscr{R}(\cdot)$, where $\mathscr{S}$ is the set of states, $\mathscr{A}$ is the set of actions, $P(s_{t+1}|s_t, a_t)$ is the state transition function of the environment, and $\mathscr{R}(s_t, a_t, s_{t+1})$ is the reward function of the environment. The objective of the agent is to maximize the cumulative reward. The return $R(\tau)$ using a trajectory from an episode, $\tau = (s_0, a_0, r_0), ..., (s_T, a_T, r_T)$ is defined as

$$R(\tau) = r_0 + \gamma r_1 + \gamma^2 r_2 + ... + \gamma^T r_T = \sum_{t=0}^{T} \gamma^t r_t, \tag{6.3}$$

where, $\gamma \in [0, 1]$ is the discount factor and the return is a discounted sum of the rewards in a trajectory. The objective $J(\tau)$ is simply the expectation of the returns over many trajectories

$$J(\tau) = E_{\tau \sim \pi}[R(\tau)] = E_{\tau}[\sum_{t=0}^{T} \gamma^t r_t] \tag{6.4}$$

The return $R(\tau)$ is the sum of discounted rewards $\gamma^t r_t$ over all time steps $t = 0, ..., T$. The objective $J(\tau)$ averages the return over many episodes. The expectation accounts for the stochasticity in actions and the environment. Maximizing the objective is the same as maximizing the return. The discount factor is an important variable which changes the way future rewards are valued. A smaller value of γ means less weight is given to rewards in future time steps, making it "short sighted". For $\gamma = 0$, the objective considers the initial reward r_0 only. Large value of γ means more weight is given to rewards in future time steps and the objective becomes more "farsighted". For $\gamma = 1$, all rewards are weighted equally.

We have established the reinforcement learning as a MDP and the objective function, we now express the reinforcement learning control loop from Fig. 6.1 as an MDP control loop in Algorithm 4

Algorithm 4: MDP control loop.

```
1  Given an environment env and an agent.
2  for episode = 0, ....., episode_max do
3      state = env.reset()
4      agent.reset()
5      for t = 0, ....., T do
6          action = agent.act(state)
7          state, reward = env.step(action)
8          agent.update(action, state, reward)
9          flag = env.done()
10         if flag then
11             break
12         end
13     end
14 end
```

Algorithm 4 outlines the interaction between an agent and an environment over multiple episodes and time steps. At the start of each episode, the environment and the agent are reset (line 3-4). This produces produces an initial state for the environment. Next, the agent produces an action given the state (line 6). This action transitions the environment to the next state and a reward (line 7) by stepping into the next time step. The agent is then updated (trained) based on the generated experience `(action, state, reward)`. This iterative process continues till time step T is reached or when the environment terminates. Over multiple time steps and episodes this algorithm generates experiences and trains the agent to maximize the objective. Here, the command `agent.update()` calls the agent's learning algorithm which is discussed in Sec. 6.2.2.

6.2.2 Learnable functions in RL

Fundamental question that arises is how the agent should learn? The agent can learn an action producing function known as policy. However, there are other properties of an environment

that can be helpful for the agent in the learning process. In particular, there are three primary functions to learn in RL.

1. a policy π, which maps state to action, $a \sim \pi(s)$,
2. a value function, $V^{\pi}(s)$ or $Q^{\pi}(s,a)$, to estimate the expected return $E_{\tau}[R(\tau)]$,
3. the environment model, $P(s'|s,a)$[1].

We consider the value function $Q^{\pi}(s,a)$. The value function gives information about the objective and helps the agent understand how good states and available actions are in terms of expected future return. The Q-value function Q^{π} measures the expected return from taking action a in state s assuming that the agent continues to act according to its current policy, π. It serves as a forward looking measure, disregarding all rewards received before state s.

$$Q^{\pi}(s,a) = E_{s_0=s,a_0=a,\tau\sim\pi}\left[\sum_{t=0}^{T}\gamma^t r_t\right] \tag{6.5}$$

6.2.3 Exploration strategy

When the agent solely prioritizes maximizing the reward function, it is called as exploitation. This makes the agent stick with usual states and potentially missing out on higher rewards available in unexplored regions on the environment. This issue is known as exploration versus exploitation. Hence, it is beneficial to adopt an approach that ensures some exploration at the expense of exploitation to avoid the suboptimal actions and get stuck in a local minima, particularly in the initial episodes. Once the simulation has progressed, the balance may be shifted towards exploitation.

The most famous techniques are the ε-greedy, and Boltzmann exploration. Given the

[1]To make the notations more compact, the next state s_{t+1} will now be written as s'.

current state s, an ε-greedy policy selects the action at the start of each step of the algorithm

$$a = \begin{cases} \underset{a' \in \mathscr{A}(s)}{\arg\max}\ Q(s,a') & \text{with probability } (1-\varepsilon), \\ \text{random action} & \text{with probability } \varepsilon, \end{cases} \tag{6.6}$$

where ε is the exploration rate. This means the greedy action is selected with probability $(1-\varepsilon)$, i.e. the exploitative action that maximizes the value function and thus the expected total future reward; otherwise an exploitative action is chosen instead. In order to ensure greater exploration at the start of reinforcement learning control, the focus is on explorative actions as learning progresses.

The ε-greedy policy strikes a balance between exploration and exploitation by gradually reducing the probability ε of taking random actions as training progresses which makes the exploration strategy naive. The agents explore randomly and do not use any learned knowledge about the environment. A good policy should strike a balance between exploring the state-action space and exploiting the knowledge learned by an agent. The Boltzmann policy in an improvement over random exploration by selecting actions using their relative Q-values. The Q-value maximizing action a in state s will be selected most often, but other actions with relatively high Q-values will also have a high probbability of being chosen. This focusses the exploration on more promising actions off the Q-value maximizing path instead of selecting all actions with equal probability. To produce a Boltzmann policy, a probability distribution over the Q-values for all actions a in state s is derived by applying the softmax function. The softmax function is further parameterised by a temperature parameter $\tau \in (0,\infty)$, which controls how uniform or concentrated the resulting probability distribution is. High values of τ push the distribution to become more uniform, low values of τ push the distribution to become more concentrated.

Actions are then sampled according to this distribution.

$$p_{softmax}(a|s) = \frac{e^{Q(s,a)}}{\sum_{a'} e^{Q(s,a')}} \tag{6.7}$$

$$p_{Boltzmann}(a|s) = \frac{e^{Q(s,a)/\tau}}{\sum_{a'} e^{Q(s,a')/\tau}} \tag{6.8}$$

The advantage of such policy is that it explores the environment less randomly.

6.2.4 Experience replay

To train the agent, we need the experiences which is the set (s, a, s', r), i.e. state, action, new-state and the reward. These experiences are generated over many time steps and episodes. An experience replay memory stores the k most recent experiences an agent has generated interacting with the environment. If the memory is full, the oldest experience is discarded to make space for the latest one. Each time an agent trains, one or more batches of data are sampled randomly with uniform probability from the experience replay memory. Each of these batches are used in turn to update the parameters of the Q-function network. The value of k is large, between 10^4 to 10^6, where as the number of elements in a training batch is much smaller between 32 to 2048. The size of the memory should be large enough to contain the experiences generated from many episodes. Each batch will contain experiences from different episodes and different policies which de-correlate the experiences used to train an agent. The memory should be small enough so that each experience is likely to be sampled more than once before being discarded from the experience replay, which makes the learning more efficient.

6.2.5 Deep Q-Network (DQN) algorithm

The pseudocode for DQN is given in Algorithm 5. First we initialize various parameters (line 1 to 7): learning rate α, temperature parameter τ to be used for Boltzmann policy, number of batches per training step B, number of updates per batch U, batch size N, size of experience replay memory K, and the randomly initialized neural network parameters θ. Next, we gather

experiences (s_i, a_i, r_i, s_i') generated using the Boltzmann policy with Q-values generated from current $Q^{\pi\theta}$ and store in the experience replay memory (line 9). The experiences can also be generated using the ε-greedy policy. The agent is now trained by sampling B batches of experiences from the experience replay memory (line 9 to 10). For each of these batch of data, we complete U parameter updates by first calculating the target Q-values for each element in the batch (line 14). Then we calculate the loss (line 16) using the mean squared error (MSE). Finally, we update the network parameters θ by calculating the gradient of the loss (line 17). When the trainig step is completed, we update the parameter τ (line 20).

Algorithm 5: DQN.

1 Initialize learning rate, α.
2 Initialize τ.
3 Initialize number of batches per training step, B.
4 Initialize number of updates per batch, U.
5 Initialize batch size, N.
6 Initialize experience replay memory with max size K.
7 Randomly initialize the network parameters θ.
8 **for** $m = 1, ..., MAX_{STEPS}$ **do**
9 Gather and store m experiences (s_i, a_i, r_i, s_i') using the current policy.
10 **for** $b = 1, ..., B$ **do**
11 Sample a batch b of experiences from the experience replay memory.
12 **for** $u = 1, ..., U$ **do**
13 **for** $i = 1, ..., N$ **do**
14 $y_i = r_i + \delta_{s_i'} \gamma \max_{a_i'} Q^{\pi_\theta}(s_i', a_i')$; // Calculate target Q-values. Here, $\delta_{s_i'} = 0$ if s_i' is terminal, 1 otherwise.
15 **end**
16 $L(\theta) = \frac{1}{N} \sum_i (y_i - Q^{\pi_\theta}(s_i, a_i))^2$; // Calculate the loss using MSE.
17 $\theta = \theta - \alpha \nabla_\theta L(\theta)$; // Update the network's parameters.
18 **end**
19 **end**
20 Decay τ.
21 **end**

The time taken for training the DQN given by Algorithm 5 can be improved significantly by using one more network called the target network Q^{π_ϕ} [157, 158]. In the original DQN Algorithm 5, the target Q-values given by y_i are constantly changing ("moving target") as they

depend on $Q^{\pi_\theta}(s,a)$. Hence, it is difficult to minimize the difference between y_i and $Q^{\pi_\theta}(s_i,a_i)$ due to the continuously updating Q-network parameters θ. To reduce the changes in y_i between training steps, we use a target network $Q^{\pi_\phi}(s,a)$ which is a second network with parameters ϕ. This network is a lagged copy of the Q-network $Q^{\pi_\theta}(s,a)$. The target network Q^{π_ϕ} is used to calculate the y_i values as shown in Algorithm 6 (line 16) which stops the target from moving. The target network parameters ϕ are periodically updated with update frequency F. This is called the replacement update (line 24). Another way to update the target network parameters ϕ is using a weighted average of ϕ and θ known as the Polyak update. Here, ϕ is changed each time step , but more slowly than the training network θ.

$$\phi \leftarrow \beta\phi + (1-\beta)\theta \tag{6.9}$$

where, β is a hyper-parameter that control the speed at which ϕ changes. A large value of *beta* means more slowly the ϕ network will change. The hyper-parameter needs to be tuned to find a good balance between stability and training speed.

6.2.6 Double deep Q-Network (DDQN) based control strategy

The original DQN Algorithm 5 overestimates the Q-values [159]. In DQN, we calculate the target value $Q_t^{\pi}ar(s,a)$ by selecting the maximum Q-value in state s'.

$$\begin{aligned} Q_{tar}^{\pi_\theta}(s,a) &= r + \gamma \max_{a_i'} Q^{\pi_\theta}(s',a') \\ &= r + \max\left(Q^{\pi_\theta}(s',a_1'), Q^{\pi_\theta}(s',a_2'), ..., Q^{\pi_\theta}(s',a_n')\right) \end{aligned} \tag{6.10}$$

If $Q^{\pi_\theta}(s',a')$ contains any errors, then $\max_{a_i'} Q^{\pi_\theta}(s',a')$ will be positively biased and the resulting Q-values are overestimated. Function approximation using neural networks is not perfect as an agent may not fully explore the environment and the environment can itself be noisy. The double DQN algorithm reduces the overestimation problem of Q-values by learning two Q-function

Algorithm 6: DQN with target network.

Initialize learning rate, α.
Initialize τ.
Initialize number of batches per training step, B.
Initialize number of updates per batch, U.
Initialize batch size, N.
Initialize experience replay memory with max size K.
Initialize target network update frequency F.
Randomly initialize the network parameters θ.
Initialize the target network parameters $\phi = \theta$.
for $m = 1, ..., MAX_{STEPS}$ **do**
    Gather and store m experiences (s_i, a_i, r_i, s_i') using the current policy.
    for $b = 1, ..., B$ **do**
        Sample a batch b of experiences from the experience replay memory.
        for $u = 1, ..., U$ **do**
            for $i = 1, ..., N$ **do**
                $y_i = r_i + \delta_{s_i'} \gamma \max_{a_i'} Q^{\pi_\phi}(s_i', a_i')$; // Calculate target Q-values. Here, $\delta_{s_i'} = 0$ if s_i' is terminal, 1 otherwise.
            end
            $L(\theta) = \frac{1}{N} \sum_i (y_i - Q^{\pi_\theta}(s_i, a_i))^2$; // Calculate the loss using MSE.
            $\theta = \theta - \alpha \nabla_\theta L(\theta)$; // Update the network's parameters.
        end
    end
    Decay τ.
    if $m \; mod \; F == 0$ **then**
        $\phi = \theta$; // Update the target network.
    end
end

estimates using different experiences. The first estimate selects the Q-maximizing action a' and the Q-value that is used to calculate the target value $Q_t^{\pi}ar(s,a)$ is generated by the second estimate using the action a selected by the first estimate. The second estimate of the Q-function which is trained using different experiences removes the positive bias in the estimation. The expression to calculate the target value using the DDQN algorithm is

$$Q_{tar}^{\pi}(s,a) = r + \gamma Q^{\pi_\phi}\left(s', \max_{a'} Q^{\pi_\theta}(s',a')\right) \tag{6.11}$$

The DDQN algorithm with target network is given by Algorithm 7. The training network θ is used to select the action (line 16) and the target network ϕ is used to evaluate that action. If $\phi = \theta$ then DDQN becomes the DQN algorithm.

6.3 RL applied to reactive control of WEC

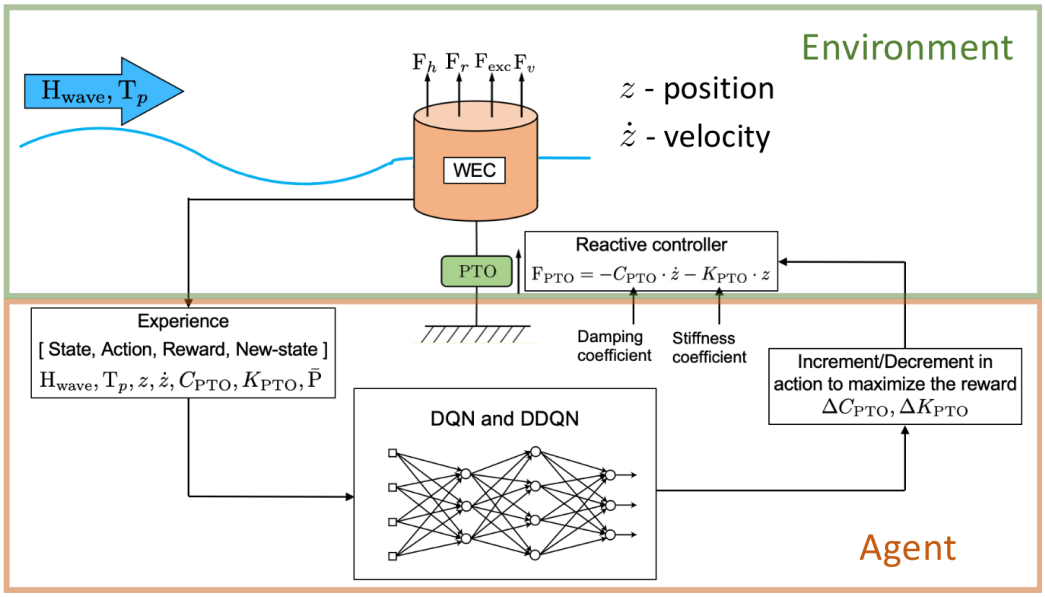

Figure 6.2. Schematic representation of the RL applied to optimal control of WEC using reactive control strategy.

The schematic illustrating the application of RL algorithms described in Sec. 6.2.5 and 6.2.6, to optimize the performance of a point absorber WEC device described in Chapter 5 is

Algorithm 7: DDQN with target network.

Initialize learning rate, α.
Initialize τ.
Initialize number of batches per training step, B.
Initialize number of updates per batch, U.
Initialize batch size, N.
Initialize experience replay memory with max size K.
Initialize target network update frequency F.
Randomly initialize the network parameters θ.
Initialize the target network parameters $\phi = \theta$.
for $m = 1, ..., MAX_{STEPS}$ **do**
    Gather and store m experiences (s_i, a_i, r_i, s_i') using the current policy.
    for $b = 1, ..., B$ **do**
        Sample a batch b of experiences from the experience replay memory.
        for $u = 1, ..., U$ **do**
            for $i = 1, ..., N$ **do**
                $y_i = r_i + \delta_{s_i'} \gamma Q^{\pi_\phi} \left(s_i', \max_{a_i'} Q^{\pi_\theta}(s_i', a_i') \right)$; // Calculate target Q-values. Here, $\delta_{s_i'} = 0$ if s_i' is terminal, 1 otherwise.
            end
            $L(\theta) = \frac{1}{N} \sum_i (y_i - Q^{\pi_\theta}(s_i, a_i))^2$; // Calculate the loss using MSE.
            $\theta = \theta - \alpha \nabla_\theta L(\theta)$; // Update the network's parameters.
        end
    end
    Decay τ.
    if $m \; mod \; F == 0$ **then**
        $\phi = \theta$; // Update the target network.
    end
end

shown in Fig. 6.2. The dynamical model of WEC is based on the LPT described in Sec. 5.2 serves as the environment which the agent interacts with. The agent is implemented as a deep neural network (DNN) trained using DQN/DDQN algorithms to output the step changes in the PTO damping coefficient (ΔC_{PTO}) and the spring stiffness coefficient (ΔK_{PTO}) for a reactive control strategy. The input to the agent is the sea state ($\mathscr{H}_{\text{wave}}, \mathscr{T}_p$), current PTO coefficients C_{PTO} and K_{PTO} and the reward which is the average power absorbed $\overline{P}$ by the device over a specified time interval. The PTO coefficients are used to calculate the control force F_{PTO} as

$$F_{\text{PTO}} = -C_{\text{PTO}} \cdot \dot{z} - K_{\text{PTO}} \cdot z \tag{6.12}$$

The average power absorbed by the device is calculated using

$$\overline{P} = \frac{1}{(t_f - t_i)} \int_{t_i}^{t_f} C_{\text{PTO}} \cdot \dot{z}^2 \mathrm{d}t \tag{6.13}$$

where, t_i and t_f are the initial and final times used for averaging the instantaneous power. The state-space $\mathscr{S}$, action-space $\mathscr{A}$, reward function r are given by

$$\mathscr{S} = \left\{ \begin{array}{rr} & i = 1:I \\ s|s_{i,j,m,n} = \left[\mathscr{H}_i,\ \mathscr{T}_j,\ C_{\text{PTO,m}},\ K_{\text{PTO,n}}\right], & j = 1:J \\ & m = 1:M \\ & n = 1:N \end{array} \right\}, \tag{6.14}$$

$$\mathscr{A} = \{a = [(-\Delta C_{\text{PTO}}, 0),\ (0, -\Delta K_{\text{PTO}}),\ (0,0),\ (\Delta C_{\text{PTO}}, 0),\ (0, \Delta K_{\text{PTO}})]\}, \tag{6.15}$$

$$r = \frac{\overline{P}}{\mathscr{H}_i^2} = \frac{1}{\mathscr{H}_i^2} \frac{1}{(t_f - t_i)} \int_{t_i}^{t_f} C_{\text{PTO},m} \cdot \dot{z}^2 \mathrm{d}t. \tag{6.16}$$

where, $\mathscr{H}$ is the wave height, $\mathscr{T}_p$ is the time period of the wave, C_{PTO} is the PTO damping coefficient, and K_{PTO} is the spring stiffness coefficient. Here, I is the total number of wave heights simulated, J is the total number of time periods of waves simulated, M is the possible

number of damping coefficient values, and N is the possible number of spring stiffness coefficient values. The action space consists of a combination to either increase, decrease or not change the PTO coefficient values. We prefer to vary only one coefficient at a time in order to limit the action-space and hence the state-action value function. This improves the learning rate. Also, states corresponding to the minimum or maximum coefficient values, i.e. $C_{\mathrm{PTO},1}$, $K_{\mathrm{PTO},1}$, $C_{\mathrm{PTO},M}$, and$K_{\mathrm{PTO},N}$ cannot take some of the actions from the action-space as the new coefficient values can exceed the defined state-space boundary. For example, for $C_{\mathrm{PTO},1}$, the action $(-\Delta C_{\mathrm{PTO}}, 0)$ is invalid. The average power is calculated from t_i and onwards till t_f time is reached. Here, t_i is chosen such that device's oscillations (dynamics) have stabilized from application of the new control force F_{PTO}. Additionally, the average power is also normalized by $\mathscr{H}_i^2$ to make the magnitude of rewards for different wave heights comparable, as the absorbed power is proportional to wave height. To avoid the device enter unstable regions like complete submergence or emergence the C_{PTO}. and K_{PTO} values that generate such experiences are given a penalty. The displacement of the device in such cases is large and a limit of $z_{\max}$ is set which if exceeded sets a penalty value or a negative value to the reward r.

6.3.1 Software implementation

The WEC model based on LPT, the DQN and DDQN algorithms, are implemented using the Python programming language by making use of the `PyTorch` module for reinforcement learning and deep neural network generation, management, and training. Training the agent requires substantial number of experiences. To expedite this process, we employ parallel computing using `mpi4py` module available in `Python`. In this setup, a master or host processor initiates multiple independent WEC simulations each with actions which are generated using the current policy and are uncorrelated. The WEC simulations are initiated on worker processors. See Fig. 6.4. Once the simulations are completed, the master processor collects the generated experiences and proceeds to train the neural network.

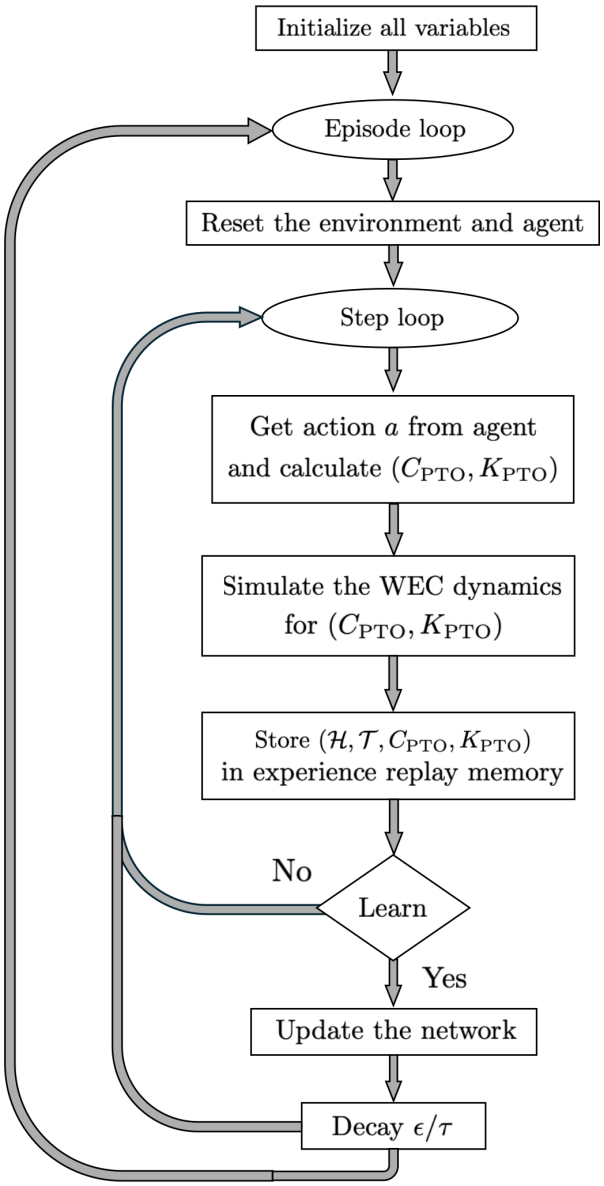

Figure 6.3. Flowchart of the RL algorithm for reactive control of a WEC device.

6.4 WEC numerical examples

In this section, first we train the agent to maximize the power absorption from regular sea waves for a reactive controlled vertical cylinder shaped point absorber device. Next, we train the agent to maximize the power absorption from irregular sea waves. Following this, we deploy the trained agent on our CFD based WEC simulation environment demonstrating its efficacy in driving the device to optimal performance in a more realistic setting. This required

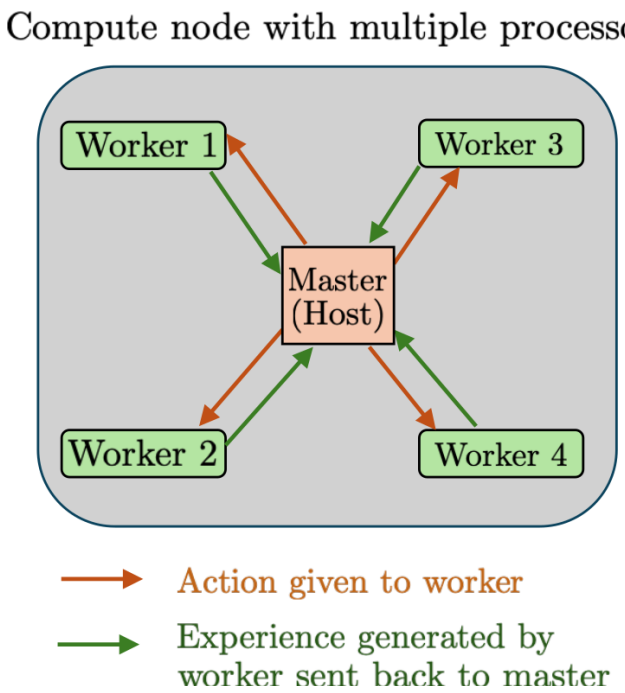

Figure 6.4. Schematic showing the generation of experiences in parallel making use of multiple WEC simulation environments.

the development of a novel communication algorithm for Python-C++ codes.

The agent trains a neural network (NN) of size $4 \times 24 \times 24 \times 5$. The first layer of the NN comprises 4 nodes representing 4 inputs of the state-space s defined in Eq. (6.14). The final layer (fourth layer) of the NN corresponds to Q-values each associated with an action a taken from $\mathscr{A}$ in Eq. (6.15). The experience replay memory, used to store experiences, has a capacity of 10^5 and a training batch size of 64 is employed for regular wave case and 128 for irregular waves case. Each training step involves 3 batches with each batch going through 3 updates. The maximum number of episodes are set to 1000 and each episode simulates 100 steps, i.e. 100 states s. For average power calculations, $t_i = 5 \times \mathscr{T}_p$ and $t_f = 20 \times \mathscr{T}_p$ is used. A penalty of -100 is imposed if the displacement constraint of $z_{max} = 0.9 \times (L_{cyl}/2)$ is violated. The learning rate is set to $\alpha = 0.001$ and the discount factor $\gamma = 0.9$. The initial value for the temperature parameter for the Boltzmann policy is $\tau = 20$ with a decay rate of 0.05 and minimum value of 1. A solver time step of $\Delta t = 0.001$ s is used in all simulations. Experiences are generated with 4

worker processors.

The wave energy absorption of a WEC device is maximum when the device oscillates in resonance with the incoming sea waves. According to reactive control theory, this can be made possible by adjusting the damping and spring stiffness coefficients of the PTO system [55, 160]. For a wave with wave frequency of ω, the optimal damping coefficient is given by

$$C_{\mathrm{OPT}} = B(\omega) \tag{6.17}$$

and the optimal spring stiffness coefficient is given by

$$K_{\mathrm{OPT}} = \omega^2(m + m(\omega)) \tag{6.18}$$

The details on obtaining the values for $B(\omega)$ and $m(\omega)$ using ANSYS AQWA [124] simulations is given in Sec. 5.2. The optimal power in each case is calculated by simulating the dynamics of the WEC device for optimal PTO coefficients. All the geometric dimensions and material properties of the device are same as used in Chapter 5.

6.4.1 Training agent for WEC device on regular waves

Here, we train the agent to optimize the performance of a WEC device simulated on regular waves of wave height $\mathscr{H} = 0.1$ m and time period of $\mathscr{T}_p = 1.3757$ s. DQN algorithm is used to train the agent with an objective to maximize the energy absorption from waves by driving the set of coefficients $(C_{\mathrm{PTO}}, K_{\mathrm{PTO}})$ towards optimal values: $C_{\mathrm{OPT}} = 15.592$ Ns/m and $K_{\mathrm{OPT}} = 297.83$ N/m. Initially, as a starting point, the coefficient values are randomly selected in the range C_{PTO} = 8 Ns/m to 36 Ns/m with $\Delta C_{\mathrm{PTO}} = 4$ Ns/m and K_{PTO} = 240 N/m to 360 N/m with ΔK_{PTO} = 20 N/m. The training progress is illustrated in Fig. 6.5(a). The episode reward is the cumulative sum of the r obtained in each step in that episode. The average reward is calculated based on the rewards of the past 10 episodes. We consider the agent is adequately trained once the

average reward stabilizes close to the maximum value (episode = 25). In Fig. 6.5(b), at episode = 1 (—, black curves), the agent explores the state-action space. As the training progresses and the agent is said to be trained, see episode = 25 (—,green curves), it drives the coefficients to optimal values, maximizing the reward.

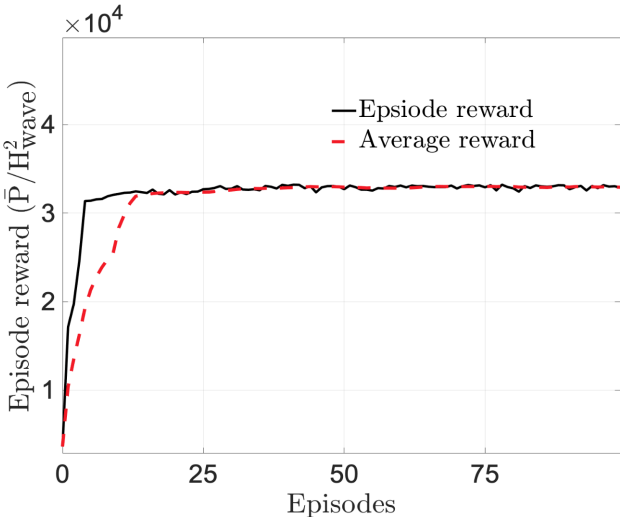

(a) Reward vs episodes

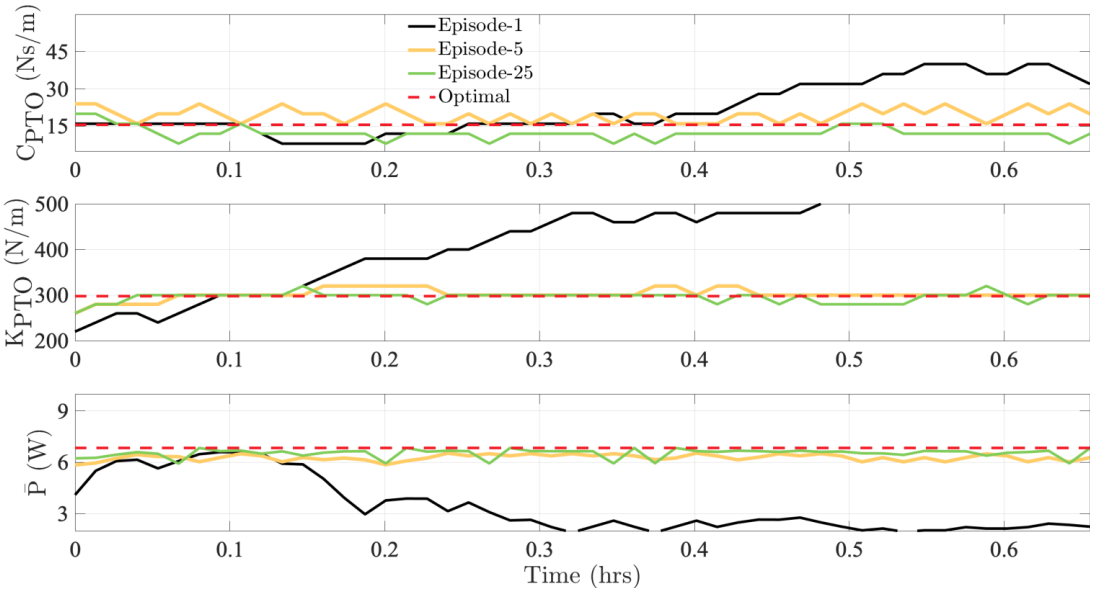

(b) PTO coefficients approaching optimal values as training progresses

Figure 6.5. DQN algorithm used to train DNN of size $4 \times 24 \times 24 \times 5$ for a WEC device on regular waves of $\mathscr{H} = 0.1$ m and $\mathscr{T}_p = 1.3657$ s implemented with a reactive control strategy.

6.4.2 Training agent for WEC device on irregular waves

In this section, we train the agent to optimize the performance of a WEC device on irregular waves with significant wave height $\mathscr{H} = 0.15$ m and time period of $\mathscr{T}_p = 1.7475$ s. DDQN algorithm is used to train the agent to drive the set of coefficients $(C_{\text{PTO}}, K_{\text{PTO}})$ to optimal values of $C_{\text{OPT}} = 14$ Ns/m and $K_{\text{OPT}} = -830$ N/m. To start as an initial point the coefficient values are randomly selected in the range C_{PTO} = 6 Ns/m to 30 Ns/m with $\Delta C_{\text{PTO}} = 4$ Ns/m and K_{PTO} = -900 N/m to -400 N/m with ΔK_{PTO} = 20 N/m. Fig. 6.6(a) shows the training progression. The agent is said to be adequately trained at episode = 126. In Fig. 6.6(b), at episode = 1 (—, black curves), the agent explores the state-action space. At a later stage when the agent is said to be trained, see episode = 126 (—,green curves), the agent drives the coefficients to optimal values where the reward is maximum.

6.4.3 Deploying trained agent on CFD solver

In this section, we deploy the trained agent from Sec. 6.4.1 in our CFD based 3D WEC simulation environment. We simulate the device dynamics under the influence of regular waves described in Sec. 6.4.1. The 3D WEC device setup is described in Sec. 5.10. Fig. 6.7 shows the agent driving the PTO damping and spring stiffness coefficients to optimal values. It is observed that the coefficient values remain in close proximity to the optimal values through the simulation. However, it is observed that the power absorbed in this simulation is much smaller than that obtained in the LPT based simulations. This significant discrepancy arises from several key factors. Firstly, the wave excitation force in CFD simulations is much larger than that in the LPT based simulations, see Sec. 5.9. Additionally, the CFD simulations accurately capture the non-linear WSI effects caused by the controller, which is not reflected in the LPT based simulations. Consequently, to accurately evaluate and refine the RL-based controllers in a more realistic setting, training the agent within CFD based WEC environments is essential. This requires an extensive amount of computational resources.

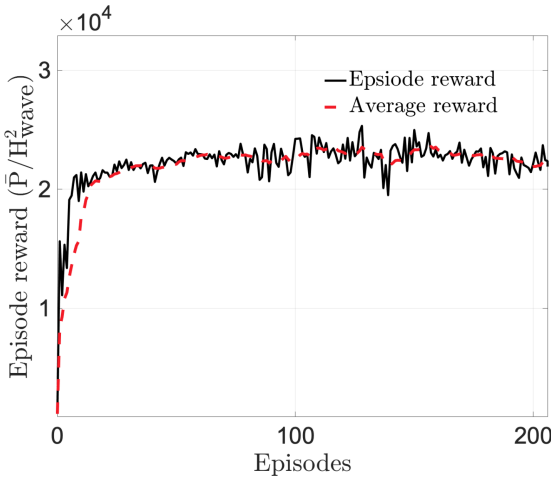

(a) Reward vs episodes

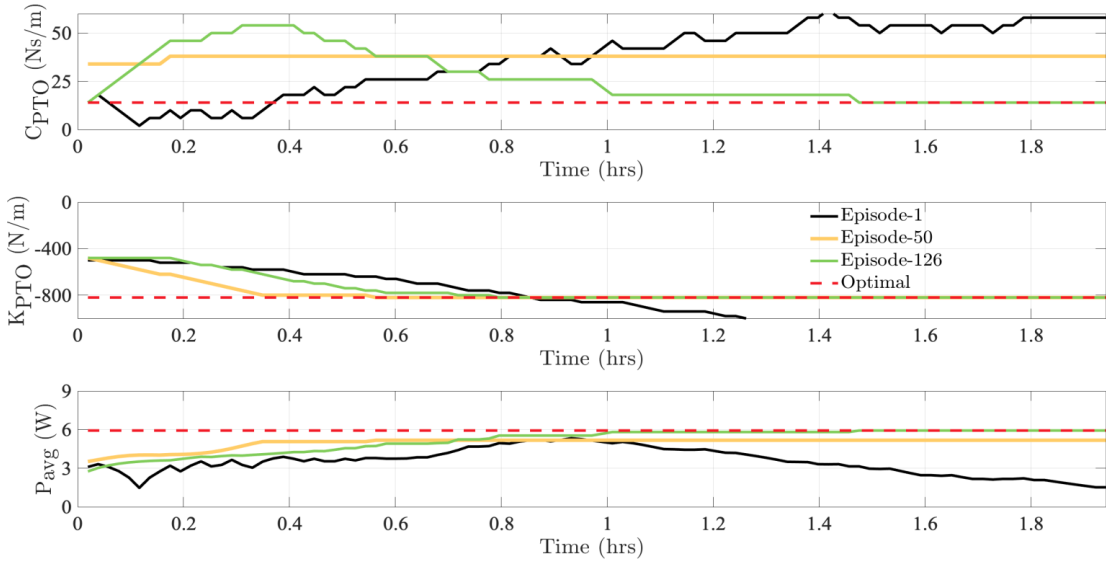

(b) PTO coefficients approaching optimal values as training progresses

Figure 6.6. DDQN algorithm used to train DNN of size $4 \times 24 \times 24 \times 5$ for a WEC device on irregular waves of $\mathscr{H}_s = 0.15$ m and $\mathscr{T}_p = 1.7475$ s implemented with a reactive control strategy.

6.5 Conclusions

In this chapter, we introduced the theory behind RL and its application to optimizing the WEC device performance with reactive control strategy. We discussed the DQN and the DDQN algorithms with discrete states and actions, and outlined their implementation to optimize the performance of a reactive controlled vertical cylinder shaped point absorber device. Next, we

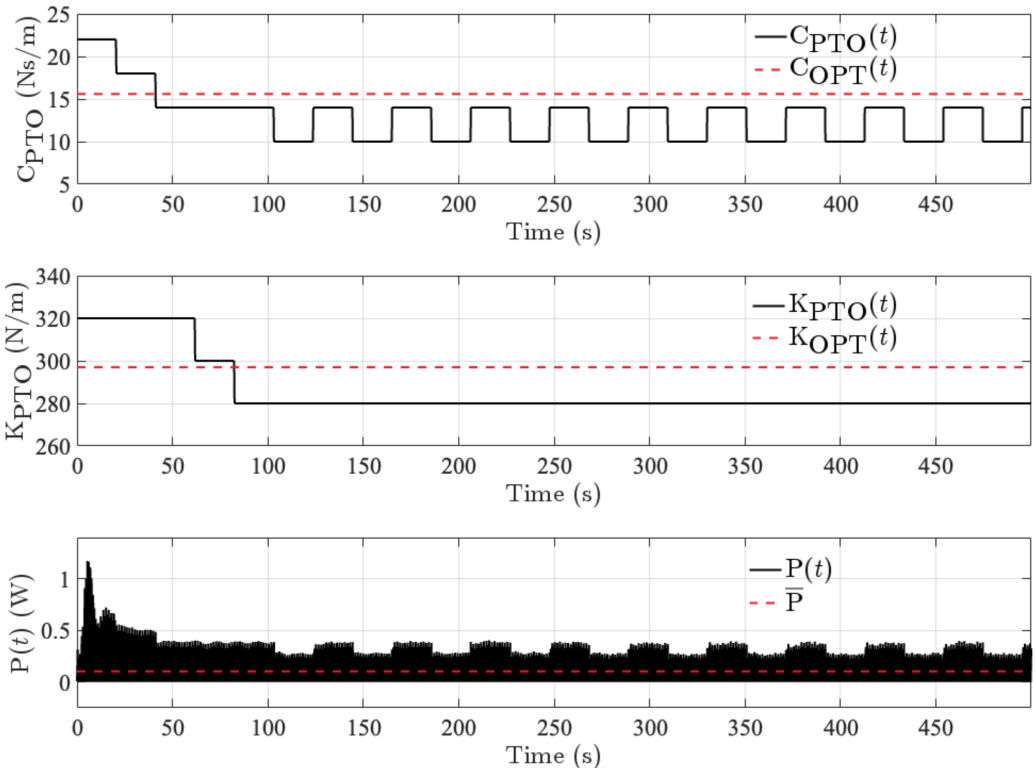

Figure 6.7. PTO coefficients approaching optimal values in a CFD based 3D WEC simulation environment.

trained the agent (controller) to maximize the power absorption of a WEC device under regular and irregular sea waves conditions. The trained agent successfully adjusted the PTO coefficients to optimal values, thereby maximizing the power absorption from sea waves.

Finally, we deployed the trained agent within a CFD based 3D WEC simulation environment and observed its capability to drives the PTO coefficients to optimal values. However, despite successful coefficient adjustment, the power absorbed by the device was notably lower compared to the LPT based simulation. We attribute this discrepancy to the differing capabilities of the CFD and the LPT based solvers in capturing the non-linear WSI effects. To further investigate this phenomenon, it is important to train the agent using CFD based WEC environments rather than replying on LPT based models. Such an approach will provide a more accurate representation of real-world dynamics, facilitating better insights for analysis and improving the RL-based controllers for WEC applications.

Acknowledgement

This chapter, in full, is not published. Investigators of the study were Kaustubh Khedkar, and Amneet Pal Singh Bhalla. The dissertation author was the primary investigator and author of this work.

Chapter 7

Future direction

Some future directions to continue the research on WEC technology:

1. It has been observed that BEM-based models tend to over-predict WEC device dynamics and power absorption capabilities, especially when the device resonates with incoming sea waves or operates under highly energetic sea states. Consequently, relying solely on BEM-based solvers for simulating WEC dynamics may not be entirely reliable. However, they can still be useful for testing various control strategies on WEC devices under calm sea conditions. To gain a better understanding of WEC dynamics, it is advised to utilize CFD-based solvers, which offer more realistic performance.

2. For Model-based control strategies such as the model predictive controller presented in this work, a more effective and fast approach is needed to predict wave excitation forces. Various methods, ranging from estimators to neural networks, can be explored, and the most efficient and rapid method can be adopted.

3. To train the model-free RL-based agents on high quality experiences, it is advisable to train them on CFD-based WEC environments rather than relying solely on LPT-based models. This approach provides a more accurate representation of real-world dynamics, facilitating better insights for analysis and improving RL-based controllers, albeit at a higher computational cost. Constraints on damping and stiffness coefficients can be imposed to prevent the device from entering unstable regions, such as complete submergence

or emergence from the water surface. An MPC-based controller can also be employed to predict unstable regions in advance and prevent the RL agent from taking such actions.

4. Fully resolved CFD simulations can be conducted for an array of WEC devices in a NWT to determine the optimal spacing between them. RL techniques can also be applied to optimize the spacing between WEC devices.

5. Implementing a latching or bang-bang controller, whose optimal latching time is determined using RL techniques, can be beneficial.

Appendix A

Analytical calculations

A.1 Analytical calculations for rise in water level for half submerged rectangle block

Consider a rectangular block of dimensions $W \times H = 2H \times H$ released from a small height above the air-water interface as depicted in Fig. 3.17. In equilibrium (hydrostatic conditions) the block settles as shown in Fig. A.1. The water level rises by an amount of Δ from its initial level. The amount of displaced water is shown by hashed lines in the figure. Its volume ($2V_2$) is equal to the volume of the submerged part of the block (V_1) below the initial water level, which is shown by the dashed line in Fig. A.1.

Equating these volumes gives a relation

$$\begin{aligned} V_1 &= 2 \times V_2 \\ W \times \alpha H &= 2 \times \Delta \times W_0, \\ \Delta &= \frac{\alpha H \times W}{2W_0}. \end{aligned} \tag{A.1}$$

At equilibrium the weight of the rectangle is balanced by the buoyancy force, which yields the

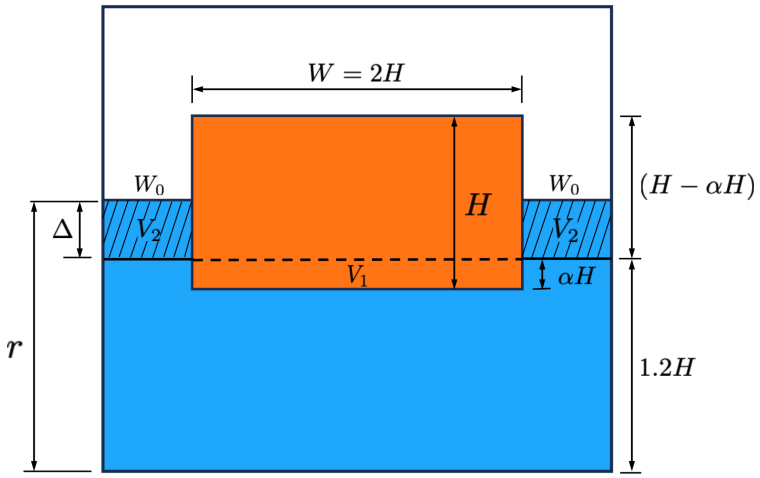

Figure A.1. Equilibrium conditions for the floating rectangular block problem.

condition

$$\rho_s \times W \times H \times g = \rho_w \times (\Delta + \alpha H) \times W \times g,$$
$$\alpha = \frac{\rho_s \times H - \rho_w \times \Delta}{\rho_w \times H}. \tag{A.2}$$

Substituting Eq. (A.1) into Eq. (A.2) and rearranging the terms, we get

$$\alpha = \frac{\rho_s}{\rho_w \left(1 + \frac{W}{2W_0}\right)}. \tag{A.3}$$

For a very wide domain, i.e., when $W_0 \to \infty$, we get the well-known result $\alpha_\infty = \frac{\rho_s}{\rho_w}$.

Substituting problem specific parameters of Sec. **??**, we get $\alpha = 0.1428$ and $\Delta = 0.02678$ m. The position of the new water level from the bottom of the container is $r = \Delta + 1.2H = 0.1167$ m.

A.2 Analytical calculations for the floating cylinder problem

Consider a cylinder of radius R released from a small height above the air-water interface as depicted in Fig. 3.25. In equilibrium (hydrostatic conditions) the cylinder settles as shown

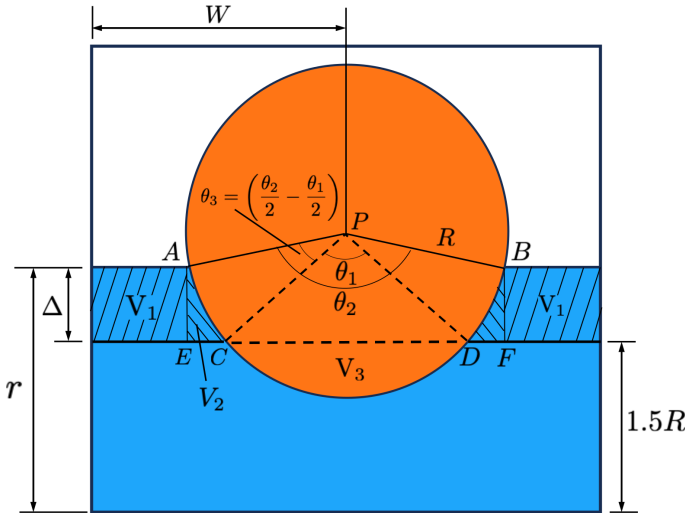

Figure A.2. Equilibrium conditions for the floating cylinder problem.

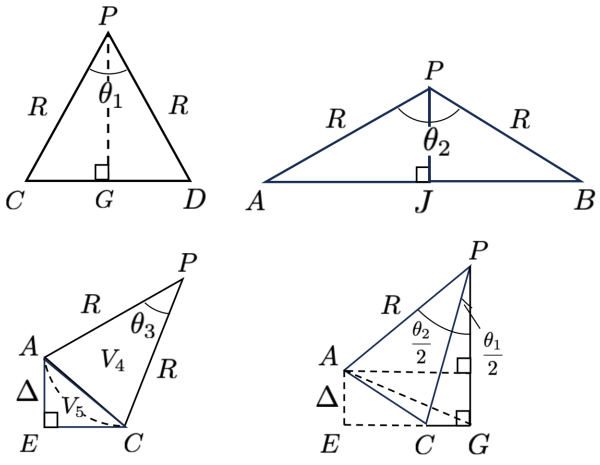

Figure A.3. Sub-geometries derived from Fig. A.2 for the analytical calculation of rise in the water level for the floating cylinder problem.

in Fig. A.2. To compute the amount of water level rise δ we first use the volume conservation principle to equate

$$V_3 = 2(V_1 + V_2), \tag{A.4}$$

in which, V_3 is the volume of the submerged part of the cylinder below the initial water level (horizontal dotted line) as illustrated in Fig. A.2. At equilibrium, the weight of the cylinder is balanced by the buoyancy force, which gives the condition

$$\begin{aligned} \rho_{\mathrm{s}} \times \pi R^2 \times g &= \left[\left(\frac{\theta_2}{2\pi} \right) \times \pi R^2 - \frac{R^2}{2} \times \sin\theta_2 \right] \times \rho_{\mathrm{w}} g \\ \theta_2 - \sin\theta_2 &= \frac{2\pi\rho_{\mathrm{s}}}{\rho_{\mathrm{w}}}. \end{aligned} \tag{A.5}$$

The following geometric relations are derived using Fig. A.3, which are used to calculate volume V_3,

$$\begin{aligned} CG &= R \times \sin\left(\frac{\theta_1}{2} \right), \\ PG &= R \times \cos\left(\frac{\theta_1}{2} \right), \\ V_3 &= \frac{\theta_1}{2\pi} \times \pi R^2 - \frac{1}{2} \times (2 \times CG) \times PG \\ &= \frac{R^2}{2} \left(\theta_1 - \sin\theta_1 \right), \end{aligned} \tag{A.6}$$

volume V_1

$$\begin{aligned} AJ &= R\sin\left(\frac{\theta_2}{2} \right), \\ V_1 &= \left(W - R\sin\left(\frac{\theta_2}{2} \right) \right) \delta, \end{aligned} \tag{A.7}$$

and volume V_2

$$V_4 = \frac{R^2}{2} \times \sin\theta_3, \tag{A.8}$$

$$V_5 = \frac{1}{2} \times \Delta \times EC, \tag{A.9}$$

$$\begin{aligned} EC &= \left(W - R\sin\left(\frac{\theta_1}{2}\right)\right) - \left(W - R\sin\left(\frac{\theta_2}{2}\right)\right) \\ &= R\left(\sin\left(\frac{\theta_2}{2}\right) - \sin\left(\frac{\theta_1}{2}\right)\right), \end{aligned} \tag{A.10}$$

$$\theta_3 = \frac{1}{2}(\theta_2 - \theta_1), \tag{A.11}$$

$$\begin{aligned} V_2 &= V_4 + V_5 - \left(\frac{\theta_3}{2\pi}\right) \times \pi R^2 \\ &= \frac{R^2}{2} \times \sin\theta_3 + \frac{1}{2} \times \Delta \times EC - \frac{\theta_3 R^2}{2}. \end{aligned} \tag{A.12}$$

The rise in the water level can be expressed in terms of the angles θ_1 and θ_2 as

$$\Delta = R\cos\left(\frac{\theta_1}{2}\right) - R\cos\left(\frac{\theta_2}{2}\right). \tag{A.13}$$

Finally, Eq. (A.4) simplifies to yield

$$\begin{aligned} V_3 &= 2(\mathrm{V}_1 + \mathrm{V}_2) \\ \frac{R^2}{2}(\theta_1 - \sin\theta_1) &= 2\left[\left(W - R\sin\left(\frac{\theta_2}{2}\right)\right)\Delta + \frac{R^2}{2}\sin\theta_3 + \frac{\Delta \times EC}{2} - \frac{\theta_3 R^2}{2}\right]. \end{aligned} \tag{A.14}$$

Substituting (A.5), (A.10), (A.11) and (A.13) into Eq. (A.14) along with the problem specific parameters of Sec. 3.5.3, we get $\theta_1 = 126.66^\circ$, Δ = 0.02692 m and $r = 0.1169$ m.

Appendix B

ISWEC dynamics

B.1 Effect of domain width in 3D simulations

Here we simulate the ISWEC dynamics by taking three different tank widths to select a sufficiently wide tank that reduces the interference caused by the lateral walls on the device dynamics. The 3D regular wave case with a prescribed pitch angle of $\delta_0 = 5^\circ$, as discussed in Sec. 4.7.1 is considered. The selected widths for the wave tank are $3W$, $5W$, and $7W$, in which W is the hull width of the 3D ISWEC model. Among the considered widths, the $7W$ tank width case has the ISWEC device located farthest away from the lateral walls, and is therefore expected to be least affected from the wall interference effects. The temporal evolution of hull pitch angle is compared for three wave tank widths, and the results are shown in Fig. B.1. From the plots, it is observed that there is not much difference in the pitch dynamics of the device. However, taking a closer look at the inset plot reveals that the results obtained using a tank width of $5W$ is closer to those obtained using a width of $7W$. Hence, we take the tank width to be $5W$ in our 3D simulations, which has a lower computational cost compared to the $7W$ case.

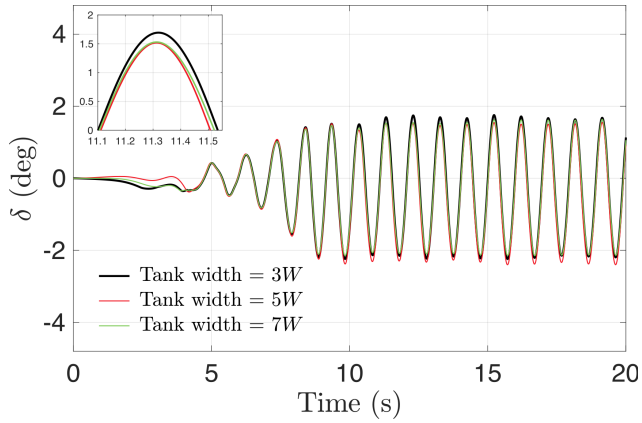

Figure B.1. Comparison of ISWEC pitch dynamics for three different computational domain widths $3W$, $5W$, and $7W$. Fifth-order regular water waves are generated with $\mathscr{H}$ = 0.1 m, $\mathscr{T}$ = 1 s and λ = 1.5456 m. A maximum ISWEC pitch angle δ_0 = 5° and a maximum gyroscope precession angle of ε_0 = 70° are used. The gyroscope parameters are: damping coefficient c = 0.1389 N·m·s/rad, moment of inertia $J = 0.0046$ kg·m^2, and PTO stiffness k = 0.1697 N·m/rad. The speed of the flywheel is $\dot{\phi} = 4000$ RPM, and $I = 0.94 \times J = 0.0043$ kg ·m^2.

Bibliography

[1] D. Gueyffier, J. Li, A. Nadim, R. Scardovelli, S. Zaleski, Volume-of-fluid interface tracking with smoothed surface stress methods for three-dimensional flows, Journal of Computational Physics 152 (2) (1999) 423–456.

[2] D. Lorstad, L. Fuchs, High-order surface tension VOF-model for 3D bubble flows with high density ratio, Journal of Computational Physics 200 (1) (2004) 153–176.

[3] S. Osher, J. A. Sethian, Fronts propagating with curvature-dependent speed: Algorithms based on hamilton-jacobi formulations, Journal of Computational Physics 79 (1) (1988) 12–49.

[4] M. Sussman, P. Smereka, S. Osher, A level set approach for computing solutions to incompressible two-phase flow, Journal of Computational physics 114 (1) (1994) 146–159.

[5] H. Ding, P. D. Spelt, C. Shu, Diffuse interface model for incompressible two-phase flows with large density ratios, Journal of Computational Physics 226 (2) (2007) 2078–2095.

[6] K. Erik Teigen, P. Song, J. Lowengrub, A. Voigt, A diffuse-interface method for two-phase flows with soluble surfactants, Journal of Computational Physics 230 (2) (2011) 375–393.

[7] M. Sohaib, A. Shah, Fully decoupled pressure projection scheme for the numerical solution of diffuse interface model of two-phase flow, Communications in Nonlinear Science and Numerical Simulation 112 (2022) 106547.

[8] S. Aland, A. Voigt, Benchmark computations of diffuse interface models for two-dimensional bubble dynamics, Int. J. Numer. Meth. Fluids 69 (3) (2012) 747–761.

[9] M. Muradoglu, G. Tryggvason, A front-tracking method for computation of interfacial flows with soluble surfactants, Journal of Computational Physics 227 (4) (2008) 2238–2262.

[10] G. Tryggvason, B. Bunner, A. Esmaeeli, D. Juric, N. Al-Rawahi, W. Tauber, J. Han, S. Nas, Y.-J. Jan, A front-tracking method for the computations of multiphase flow, Journal of Computational Physics 169 (2) (2001) 708–759.

[11] S. Ganesan, L. Tobiska, A coupled arbitrary lagrangian–eulerian and lagrangian method for computation of free surface flows with insoluble surfactants, Journal of Computational Physics 228 (8) (2009) 2859–2873.

[12] M. Souli, J. Zolesio, Arbitrary lagrangian–eulerian and free surface methods in fluid mechanics, Computer Methods in Applied Mechanics and Engineering 191 (3) (2001) 451–466.

[13] J. J. Xu, Z. Li, J. Lowengrub, H. Zhao, A level-set method for interfacial flows with surfactant, Journal of Computational Physics 212 (2) (2006) 590–616.

[14] J. J. Xu, W. Ren, A level-set method for two-phase flows with moving contact line and insoluble surfactant, Journal of Computational Physics 263 (2014) 71–90.

[15] Z. Solomenko, P. D. Spelt, L. Ó Náraigh, P. Alix, Mass conservation and reduction of parasitic interfacial waves in level-set methods for the numerical simulation of two-phase flows: A comparative study, International Journal of Multiphase Flow 95 (2017) 235–256.

[16] M. Sussman, E. G. Puckett, A coupled level set and volume-of-fluid method for computing 3D and axisymmetric incompressible two-phase flows, Journal of Computational Physics 162 (2) (2000) 301–337.

[17] D. Enright, R. Fedkiw, J. Ferziger, I. Mitchell, A hybrid particle level set method for improved interface capturing, Journal of Computational Physics 183 (1) (2002) 83–116.

[18] A. Asuri Mukundan, T. Ménard, J. C. Brändle de Motta, A. Berlemont, A hybrid moment of fluid–level set framework for simulating primary atomization, Journal of Computational Physics 451 (2022) 110864.

[19] V. Dyadechko, M. Shashkov, Reconstruction of multi-material interfaces from moment data, Journal of Computational Physics 227 (11) (2008) 5361–5384.

[20] H. T. Ahn, M. Shashkov, Adaptive moment-of-fluid method, Journal of Computational Physics 228 (8) (2009) 2792–2821.

[21] H. T. Ahn, M. Shashkov, M. A. Christon, The moment-of-fluid method in action, Communications in Numerical Methods in Engineering 25 (10) (2009) 1009–1018.

[22] H. L. Wen, C. H. Yu, T. W. H. Sheu, S. W. Chau, A mass-preserving level set method for simulating 2D/3D fluid flows with deformed interface, Ocean Engineering 283 (2023) 115063.

[23] C. Kees, I. Akkerman, M. Farthing, Y. Bazilevs, A conservative level set method suitable for variable-order approximations and unstructured meshes, Journal of Computational Physics 230 (12) (2011) 4536–4558.

[24] S. Osher, R. Fedkiw, The Level Set Methods and Dynamic Implicit Surfaces, Vol. 57, Springer, 2004.

[25] P. Angot, C.-H. Bruneau, P. Fabrie, A penalization method to take into account obstacles in incompressible viscous flows, Numerische Mathematik 81 (4) (1999) 497–520.

[26] G. Carbou, P. Fabrie, Boundary layer for a penalization method for viscous incompressible flow, Advances in Differential Equations 8 (12) (2003) 1453 – 1480.

[27] Y. Bhosale, T. Parthasarathy, M. Gazzola, A remeshed vortex method for mixed rigid/soft body fluid–structure interaction, Journal of Computational Physics 444 (2021) 110577.

[28] M. Sussman, E. Fatemi, P. Smereka, S. Osher, An improved level set method for incompressible two-phase flows, Computers & Fluids 27 (5-6) (1998) 663–680.

[29] E. Olsson, G. Kreiss, A conservative level set method for two phase flow, Journal of computational physics 210 (1) (2005) 225–246.

[30] S. Parameswaran, J. Mandal, A stable interface-preserving reinitialization equation for conservative level set method, European Journal of Mechanics-B/Fluids 98 (2023) 40–63.

[31] A. P. S. Bhalla, N. Nangia, P. Dafnakis, G. Bracco, G. Mattiazzo, Simulating water-entry/exit problems using eulerian–lagrangian and fully-eulerian fictitious domain methods within the open-source ibamr library, Applied Ocean Research 94 (2020) 101932.

[32] E. Jettestuen, J. O. Helland, M. Prodanović, A level set method for simulating capillary-controlled displacements at the pore scale with nonzero contact angles, Water Resources Research 49 (8) (2013) 4645–4661.

[33] N. Nangia, B. E. Griffith, N. A. Patankar, A. P. S. Bhalla, A robust incompressible Navier-Stokes solver for high density ratio multiphase flows, Journal of Computational Physics 390 (2019) 548–594.

[34] M. Cai, A. Nonaka, J. B. Bell, B. E. Griffith, A. Donev, Efficient variable-coefficient finite-volume stokes solvers, Communications in Computational Physics 16 (5) (2014) 1263–1297.

[35] B. E. Griffith, An accurate and efficient method for the incompressible Navier-Stokes equations using the projection method as a preconditioner, Journal of Computational Physics 228 (20) (2009) 7565–7595.

[36] A. P. S. Bhalla, R. Bale, B. E. Griffith, N. A. Patankar, A unified mathematical framework and an adaptive numerical method for fluid–structure interaction with rigid, deforming, and elastic bodies, Journal of Computational Physics 250 (2013) 446–476.

[37] C.-W. Shu, Essentially non-oscillatory and weighted essentially non-oscillatory schemes for hyperbolic conservation laws, Advanced Numerical Approximation of Nonlinear Hyperbolic Equations (1998) 325–432.

[38] A. P. S. Bhalla, N. Nangia, P. Dafnakis, G. Bracco, G. Mattiazzo, Simulating water-entry/exit problems using Eulerian-Lagrangian and fully-Eulerian fictitious domain methods within the open-source IBAMR library, Applied Ocean Research 94 (2020) 101932.

[39] N. Nangia, N. A. Patankar, A. P. S. Bhalla, A DLM immersed boundary method based wave-structure interaction solver for high density ratio multiphase flows, Journal of Computational Physics 398 (2019) 108804.

[40] R. Thirumalaisamy, K. Khedkar, P. Ghysels, A. P. S. Bhalla, An effective preconditioning strategy for volume penalized incompressible/low mach multiphase flow solvers, Journal of Computational Physics 490 (2023) 112325.

[41] M. Bergmann, A. Iollo, Modeling and simulation of fish-like swimming, Journal of Computational Physics 230 (2) (2011) 329–348.

[42] E. L. Sharaborin, O. A. Rogozin, A. R. Kasimov, The coupled volume of fluid and Brinkman penalization methods for simulation of incompressible multiphase flows, Fluids 6 (9) (2021) 334.

[43] IBAMR: An adaptive and distributed-memory parallel implementation of the immersed boundary method.
URL https://github.com/IBAMR/IBAMR

[44] R. D. Hornung, S. R. Kohn, Managing application complexity in the SAMRAI object-oriented framework, Concurrency Comput Pract Ex 14 (5) (2002) 347–368.

[45] SAMRAI: Structured Adaptive Mesh Refinement Application Infrastructure.
URL http://www.llnl.gov/CASC/SAMRAI

[46] S. Balay, W. D. Gropp, L. C. McInnes, B. F. Smith, Efficient management of parallelism in object oriented numerical software libraries, in: E. Arge, A. M. Bruaset, H. P. Langtangen (Eds.), Modern Software Tools in Scientific Computing, Birkhäuser Press, 1997, pp. 163–202.

[47] S. Balay, S. Abhyankar, M. F. Adams, J. Brown, P. Brune, K. Buschelman, L. Dalcin, V. Eijkhout, W. D. Gropp, D. Kaushik, M. G. Knepley, L. C. McInnes, K. Rupp, B. F. Smith, S. Zampini, H. Zhang, PETSc users manual, Tech. Rep. ANL-95/11 - Revision 3.6, Argonne National Laboratory (2015).
URL http://www.mcs.anl.gov/petsc

[48] S. Balay, S. Abhyankar, M. F. Adams, J. Brown, P. Brune, K. Buschelman, L. Dalcin, A. Dener, V. Eijkhout, W. D. Gropp, D. Karpeyev, D. Kaushik, M. G. Knepley, D. A. May, L. C. McInnes, R. T. Mills, T. Munson, K. Rupp, P. Sanan, B. F. Smith, S. Zampini, H. Zhang, H. Zhang, PETSc Web page (2021).
URL https://www.mcs.anl.gov/petsc

[49] W. Rider, D. Kothe, Stretching and tearing interface tracking methods, AIAA Paper 95-17171 (06 1995).

[50] Z. Wang, J. Yang, F. Stern, A new volume-of-fluid method with a constructed distance function on general structured grids, Journal of Computational Physics 231 (9) (2012) 3703–3722.

[51] J. Brackbill, D. B. Kothe, C. Zemach, A continuum method for modeling surface tension, Journal of Computational Physics 100 (2) (1992) 335–354.

[52] C. S. Peskin, The immersed boundary method, Acta Numerica 11 (2002) 479–517.

[53] S. Hysing, S. Turek, D. Kuzmin, N. Parolini, E. Burman, S. Ganesan, L. Tobiska, Quantitative benchmark computations of two-dimensional bubble dynamics, Int. J. Numer. Meth. Fluids 60 (11) (2009) 1259–1288.

[54] A. Calderer, S. Kang, F. Sotiropoulos, Level set immersed boundary method for coupled simulation of air/water interaction with complex floating structures, Journal of Computational Physics 277 (2014) 201–227.

[55] P. Dafnakis, A. P. S. Bhalla, S. A. Sirigu, M. Bonfanti, G. Bracco, G. Mattiazzo, Comparison of wave-structure interaction dynamics of a submerged cylindrical point absorber with three degrees of freedom using potential flow and computational fluid dynamics models, Physics of Fluids 32 (9) (2020).

[56] K. J. Richards, P. K. Senecal, E. Pomraning, CONVERGE 3.1, Convergent Science, Madison, WI, 2023.

[57] ANSYS FLUENT, 2021 R2. User's and theory guide. Canonsburg, Pennsylvania, USA: ANSYS, Inc.

[58] A. Crespo, J. Domínguez, B. Rogers, M. Gómez-Gesteira, S. Longshaw, R. Canelas, R. Vacondio, A. Barreiro, O. García-Feal, DualSPHysics: open-source parallel CFD solver based on smoothed particle hydrodynamics (SPH), Computer Physics Communications 187 (2015) 204–216.

[59] K. Khedkar, N. Nangia, R. Thirumalaisamy, A. P. S. Bhalla, The inertial sea wave energy converter (ISWEC) technology: Device-physics, multiphase modeling and simulations, Ocean Engineering 229 (2021) 108879.

[60] K. Khedkar, A. P. S. Bhalla, A model predictive control (MPC)-integrated multiphase immersed boundary (IB) framework for simulating wave energy converters (WECs), Ocean Engineering 260 (2022) 111908.

[61] A. Pathak, M. Raessi, A 3D, fully Eulerian, VOF-based solver to study the interaction between two fluids and moving rigid bodies using the fictitious domain method, Journal of Computational Physics 311 (2016) 87–113.

[62] E.-M. Yettou, A. Desrochers, Y. Champoux, Experimental study on the water impact of a symmetrical wedge, Fluid Dynamics Research 38 (1) (2006) 47–66.

[63] J. Cretel, A. Lewis, G. Lightbody, G. Thomas, An application of model predictive control to a wave energy point absorber, IFAC Proceedings Volumes 43 (1) (2010) 267–272, 1st IFAC Conference on Control Methodologies and Technology for Energy Efficiency.

[64] K. Gunn, C. Stock-Williams, Quantifying the global wave power resource, Renewable Energy 44 (2012) 296–304.

[65] J.M.J. Journée and W.W. Massie, Offshore Hydromechanics, Delft University of Technology, 2001.

[66] L. H. Holthuijsen, Waves in Oceanic and Coastal Waters, Cambridge University Press, 2007.

[67] N. G. Jacobsen, D. R. Fuhrman, J. Fredsøe, A wave generation toolbox for the open-source cfd library: Openfoam®, International Journal for Numerical Methods in Fluids 70 (9) (2012) 1073–1088.

[68] C. Huh, L. E. Scriven, Hydrodynamic model of steady movement of a solid/liquid/fluid contact line, Journal of colloid and interface science 35 (1) (1971) 85–101.

[69] U. A. Korde, J. Ringwood, Hydrodynamic control of wave energy devices, Cambridge University Press, 2016.

[70] K. Gunn, C. Stock-Williams, Quantifying the global wave power resource, Renewable Energy 44 (2012) 296–304.

[71] W. Cummins, The impulse response function and ship motions, Tech. rep., DTIC Document (1962).

[72] J. Davidson, R. Costello, Efficient nonlinear hydrodynamic models for wave energy converter design—a scoping study, Journal of Marine Science and Engineering 8 (1) (2020).

[73] M. Penalba, G. Giorgi, J. V. Ringwood, Mathematical modelling of wave energy converters: A review of nonlinear approaches, Renewable and Sustainable Energy Reviews 78 (2017) 1188–1207.

[74] A. Merigaud, J. C. Gilloteaux, J. Ringwood, A nonlinear extension for linear boundary element methods in wave energy device modelling, Vol. 4, 2012.

[75] M. P. Retes, G. Giorgi, J. Ringwood, A review of non-linear approaches for wave energy converter modelling, Proceedings of the 11th European Wave and Tidal Energy Conference (2015).

[76] G. Giorgi, M. Penalba, J. Ringwood, Nonlinear hydrodynamic models for heaving buoy wave energy converters, 2016.

[77] G. Giorgi, J. Ringwood, Nonlinear Froude-Krylov and viscous drag representation for wave energy converters in the computation/fidelity continuum, Ocean Engineering 141 (2017) 164–175.

[78] E. B. Agamloh, A. K. Wallace, A. von Jouanne, Application of fluid–structure interaction simulation of an ocean wave energy extraction device, Renewable Energy 33 (4) (2008) 748–757.

[79] A. Ghasemi, M. Anbarsooz, A. Malvandi, A. Ghasemi, F. Hedayati, A nonlinear computational modeling of wave energy converters: A tethered point absorber and a bottom-hinged flap device, Renewable Energy 103 (2017) 774–785.

[80] M. Anbarsooz, M. Passandideh-Fard, M. Moghiman, Numerical simulation of a submerged cylindrical wave energy converter, Renewable Energy 64 (2014) 132–143.

[81] M. Penalba, J. Davidson, C. Windt, J. V. Ringwood, A high-fidelity wave-to-wire simulation platform for wave energy converters: Coupled numerical wave tank and power take-off models, Applied energy 226 (2018) 655–669.

[82] G. Giorgi, J. V. Ringwood, Implementation of latching control in a numerical wave tank with regular waves, Journal of Ocean Engineering and Marine Energy 2 (2016) 211–226.

[83] C. Windt, N. Faedo, M. Penalba, F. Dias, J. V. Ringwood, Reactive control of wave energy devices – the modelling paradox, Applied Ocean Research 109 (2021) 102574.

[84] N. Faedo, G. Scarciotti, A. Astolfi, J. Ringwood, Energy-maximising control of wave energy converters using a moment-domain representation, Control Engineering Practice 81 (2018) 85–96.

[85] G. Bracco, E. Giorcelli, G. Mattiazzo, ISWEC: A gyroscopic mechanism for wave power exploitation, Mechanism and machine theory 46 (10) (2011) 1411–1424.

[86] A. Cagninei, M. Raffero, G. Bracco, E. Giorcelli, G. Mattiazzo, D. Poggi, Productivity analysis of the full scale inertial sea wave energy converter prototype: A test case in Pantelleria Island, Journal of Renewable and Sustainable Energy 7 (2015) 061703.

[87] G. Vissio, ISWEC toward the sea - Development, Optimization and Testing of the Device Control Architecture, Ph.D. thesis, Politecnico di Torino (2017).

[88] M. Bergmann, G. Bracco, F. Gallizio, A. Giorcelli, E. Iollo, G. Mattiazzo, M. Ponzetta, A two-way coupling CFD method to simulate the dynamics of a wave energy converter., in: OCEANS 2015 - Genova, Italy, IEEE, pp. 1–6.

[89] J. D. Fenton, The numerical solution of steady water wave problems, Computers & Geosciences 14 (3) (1988) 357–368.

[90] J. D. Fenton, A fifth-order stokes theory for steady waves, Journal of waterway, port, coastal, and ocean engineering 111 (2) (1985) 216–234.

[91] A. M. Miquel, A. Kamath, M. Alagan Chella, R. Archetti, H. Bihs, Analysis of different methods for wave generation and absorption in a CFD-based numerical wave tank, Journal of Marine Science and Engineering 6 (2) (2018) 73.

[92] C. Windt, J. Davidson, J. V. Ringwood, High-fidelity numerical modelling of ocean wave energy systems: A review of computational fluid dynamics-based numerical wave tanks, Renewable and Sustainable Energy Reviews 93 (2018) 610–630.

[93] C. Windt, J. Davidson, P. Schmitt, J. V. Ringwood, On the assessment of numerical wave makers in CFD simulations, Journal of Marine Science and Engineering 7 (2) (2019) 47.

[94] P. Higuera, J. L. Lara, I. J. Losada, Realistic wave generation and active wave absorption for Navier–Stokes models: Application to OpenFOAM® , Coastal Engineering 71 (2013) 102–118.

[95] P. Frigaard, M. Brorsen, A time-domain method for separating incident and reflected irregular waves, Coastal Engineering 24 (3-4) (1995) 205–215.

[96] H. A. Schäffer, G. Klopman, Review of multidirectional active wave absorption methods, Journal of waterway, port, coastal, and ocean engineering 126 (2) (2000) 88–97.

[97] J. Choi, S. B. Yoon, Numerical simulations using momentum source wave-maker applied to RANS equation model, Coastal Engineering 56 (10) (2009) 1043–1060.

[98] T. Ha, P. Lin, Y.-S. Cho, Generation of 3D regular and irregular waves using Navier–Stokes equations model with an internal wave maker, Coastal Engineering 76 (2013) 55–67.

[99] A. Ghasemi, A. Pathak, M. Raessi, Computational simulation of the interactions between moving rigid bodies and incompressible two-fluid flows, Computers & Fluids 94 (2014) 1–13.

[100] Z. Dong, J. Zhan, Comparison of existing methods for wave generating and absorbing in VOF-based numerical tank, Journal of Hydrodynamics, Ser. A 24 (1) (2009) 15–21.

[101] N. G. Jacobsen, M. R. van Gent, G. Wolters, Numerical analysis of the interaction of irregular waves with two dimensional permeable coastal structures, Coastal Engineering 102 (2015) 13–29.

[102] Z. Hu, W. Y. Tang, H. X. Xue, X. Y. Zhang, Numerical wave tank based on a conserved wave-absorbing method, China Ocean Engineering 30 (1) (2016) 137–148.

[103] N. Nangia, N. A. Patankar, A. P. S. Bhalla, A DLM immersed boundary method based wave-structure interaction solver for high density ratio multiphase flows, Journal of Computational Physics 398 (2019) 108804.

[104] G. Bracco, E. Giorcelli, G. Mattiazzo, M. Pastorelli, J. Taylor, ISWEC: Design of a prototype model with gyroscope, IEEE, 2009, pp. 57–63.

[105] G. Bracco, E. Giorcelli, G. Mattiazzo, D. Poggi, J. Taylor, ISWEC: experimental tests on a small scale prototype model, 2010.

[106] G. Bracco, E. Giorcelli, G. Mattiazzo, ISWEC: Design of a prototype model for wave tank test, American Society of Mechanical Engineers, 2010.

[107] G. Bracco, E. Giorcelli, G. Mattiazzo, M. Pastorelli, M. Raffero, Testing of a gyroscopic wave energy system, IEEE, 2012.

[108] J. Medeiros, S. Brizzolara, Mathematical framework for hydromechanical time-domain simulation of wave energy converters, Mathematical Problems in Engineering 2018 (2018).

[109] G. Bracco, E. Giorcelli, G. Giorgi, G. Mattiazzo, B. Passione, M. Raffero, G. Vissio, Performance assessment of the full scale ISWEC system, in: 2015 IEEE International Conference on Industrial Technology (ICIT), IEEE, 2015, pp. 2499–2505.

[110] G. Bracco, M. Canale, V. Cerone, Energy harvesting optimization of an inertial sea wave energy converter through model predictive control, IEEE, 2019, pp. 85–90.

[111] M. Raffero, M. Martini, B. Passione, G. Mattiazzo, E. Giorcelli, G. Bracco, Stochastic Control of Inertial Sea Wave Energy Convertor, The Scientific World Journal (2015).

[112] G. Bracco, A. Cagninei, E. Giorcelli, G. Mattiazzo, D. Poggi, M. Raffero, Stochastic Control of Inertial Sea Wave Energy Convertor, Ocean Engineering 120 (2016) 40–51.

[113] K. Ruehl, C. Michelen, S. Kanner, M. Lawson, Y.-H. Yu, Preliminary verification and validation of WEC-Sim, an open-source wave energy converter design tool, in: ASME 2014 33rd International Conference on Ocean, Offshore and Arctic Engineering, American Society of Mechanical Engineers Digital Collection.

[114] Y.-H. Yu, Y. Li, Reynolds-Averaged Navier–Stokes simulation of the heave performance of a two-body floating-point absorber wave energy system, Computers & Fluids 73 (2013) 104–114.

[115] M. Raffero, Design of a Wave Energy Converter-A case of application: ISWEC, Ph.D. thesis, Politecnico di Torino (2014).

[116] M. Gazzola, O. V. Vasilyev, P. Koumoutsakos, Shape optimization for drag reduction in linked bodies using evolution strategies, Computers & Structures 89 (11-12) (2011) 1224–1231.

[117] N. M. Newmark, A method of computation for structural dynamics, Journal of the engineering mechanics division 85 (3) (1959) 67–94.

[118] I. Robertson, L. Li, S. Sherwin, P. Bearman, A numerical study of rotational and transverse galloping rectangular bodies, Journal of fluids and structures 17 (5) (2003) 681–699.

[119] J. Yang, F. Stern, A simple and efficient direct forcing immersed boundary framework for fluid–structure interactions, Journal of Computational Physics 231 (15) (2012) 5029–5061.

[120] J. Yang, F. Stern, A non-iterative direct forcing immersed boundary method for strongly-coupled fluid–solid interactions, Journal of Computational Physics 295 (2015) 779–804.

[121] E. M. Kolahdouz, A. P. Bhalla, B. A. Craven, B. E. Griffith, An Immersed Lagrangian-Eulerian Method for Fluid-Structure Interaction, arXiv preprint arXiv:2003.12046 (2020).

[122] M. Previsic, A. Karthikeyan, J. Scruggs, WEC CONTROLS – Approaches and Lessons Learned (2020).
URL https://tethys-engineering.pnnl.gov/sites/default/files/publications/previsicetal.pdf

[123] T. Sarpkaya, Force on a circular cylinder in viscous oscillatory flow at low Keulegan—Carpenter numbers, Journal of Fluid Mechanics 165 (1986) 61–71.

[124] ANSYS AQWA theory manual (2014).

[125] Z. Yu, J. Falnes, State-space modelling of a vertical cylinder in heave, Applied Ocean Research 17 (5) (1995) 265–275.

[126] R. Taghipour, T. Perez, T. Moan, Hybrid frequency–time domain models for dynamic response analysis of marine structures, Ocean Engineering 35 (7) (2008) 685–705.

[127] J. Cretel, G. Lightbody, G. Thomas, A. Lewis, Maximisation of Energy Capture by a Wave-Energy Point Absorber using Model Predictive Control, IFAC Proceedings Volumes 44 (1) (2011) 3714–3721, 18th IFAC World Congress.

[128] G. F. Franklin, J. D. Powell, M. L. Workman, Digital Control of Dynamic Systems, Vol. 3, Menlo Park: Addison-Wesley, 1998.

[129] MATLAB, 9.7.0.1586710 (R2019b), The MathWorks Inc., Natick, Massachusetts, 2019.

[130] P. Tona, H. N. Nguyen, G. Sabiron, Y. Creff, An Efficiency-Aware Model Predictive Control Strategy for a Heaving Buoy Wave Energy Converter, 11th European Wave and Tidal Energy Conference - EWTEC 2015, Sept 2015, Nantes, France.

[131] L. Wang, Model Predictive Control System Design and Implementation Using MATLAB®, Springer-Verlag London, 2009.

[132] N. Faedo, S. Olaya, J. V. Ringwood, Optimal control, MPC and MPC-like algorithms for wave energy systems: An overview, IFAC Journal of Systems and Control 1 (2017) 37–56.

[133] U. A. Korde, J. Ringwood, Hydrodynamic control of wave energy devices, Cambridge University Press, 2016.

[134] P. Gieske, Model Predictive Control of a Wave Energy Converter: Archimedes Wave Swing, Master's thesis, Delft University of Technology (2007).

[135] B. A. Ling, B. A. Batten, Real time estimation and prediction of wave excitation forces on a heaving body, in: International Conference on Offshore Mechanics and Arctic Engineering, Vol. 56574, American Society of Mechanical Engineers, 2015, p. V009T09A017.

[136] M. Bonfanti, A. Hillis, S. A. Sirigu, P. Dafnakis, G. Bracco, Mattiazzo, Real-time wave excitation forces estimation: An application on the iswec device, Journal of Marine Science and Engineering 8 (2020).

[137] S. Zou, O. Abdelkhalik, Time-varying linear quadratic gaussian optimal control for three-degree-of-freedom wave energy converters, Renewable Energy 149 (2020) 217–225.

[138] M. G. Abril, F. Paparella, J. Ringwood, Excitation force estimation and forecasting for wave energy applications, IFAC-PapersOnLine 50 (1) (2017) 14692–14697, 20th IFAC World Congress.

[139] F. Fusco, J. V. Ringwood, Short-Term Wave Forecasting for Real-Time Control of Wave Energy Converters, IEEE Transactions on Sustainable Energy 1 (2) (2010) 99–106.

[140] J. Hals, J. Falnes, T. Moan, Constrained Optimal Control of a Heaving Buoy Wave-Energy Converter, Journal of Offshore Mechanics and Arctic Engineering 133 (1) (11 2010).

[141] L. Li, Z. Gao, Z. M. Yuan, On the sensitivity and uncertainty of wave energy conversion with an artificial neural-network-based controller, Ocean Engineering 183 (2019) 282–293.

[142] J. A. Bærentzen, H. Aanaes, Signed distance computation using the angle weighted pseudonormal, IEEE Transactions on Visualization and Computer Graphics 11 (3) (2005) 243–253.

[143] QuadProg++: A C++ library for Quadratic Programming which implements the Goldfarb-Idnani active-set dual method.
URL https://github.com/liuq/QuadProgpp

[144] Cronos: An Open Source Time Series Analysis Package.
URL https://github.com/codemedic/cronos

[145] Y. Lv, Y. Duan, W. Kang, Z. Li, F.-Y. Wang, Traffic flow prediction with big data: A deep learning approach, IEEE Transactions on Intelligent Transportation Systems 16 (2) (2015) 865 – 873.

[146] M. Islam, T. Morimoto, Non-linear autoregressive neural network approach for inside air temperature prediction of a pillar cooler, International Journal of Green Energy 14 (2) (2017) 141–149.

[147] A. Pourzangbar, M. A. Losada, A. Saber, L. R. Ahari, P. Larroudé, M. Vaezi, M. Brocchini, Prediction of non-breaking wave induced scour depth at the trunk section of breakwaters using genetic programming and artificial neural networks, Coastal Engineering 121 (2017) 107–118.

[148] M. Zandvliet, O. Bosgra, J. Jansen, P. Van den Hof, J. Kraaijevanger, Bang-bang control and singular arcs in reservoir flooding, Journal of Petroleum Science and Engineering 58 (1) (2007) 186–200.

[149] V. Mnih, K. Kavukcuoglu, D. Silver, A. Graves, I. Antonoglou, D. Wierstra, M. Riedmiller, Playing atari with deep reinforcement learning, arXiv preprint arXiv:1312.5602 (2013).

[150] D. Silver, A. Huang, C. J. Maddison, A. Guez, L. Sifre, G. van den Driessche, J. Schrittwieser, I. Antonoglou, V. Panneershelvam, M. Lanctot, S. Dieleman, D. Grewe, J. Nham, N. Kalchbrenner, I. Sutskever, T. Lillicrap, M. Leach, K. Kavukcuoglu, T. Graepel, D. Hassabis, Mastering the game of go with deep neural networks and tree search, Nature 529 (7587) (2016) 484–489.

[151] T. Schaul, J. Quan, I. Antonoglou, D. Silver, Prioritized experience replay (2016). arXiv:1511.05952.

[152] R. S. Sutton, A. G. Barto, et al., Reinforcement learning, Vol. 11, 1999.

[153] E. Anderlini, D. I. M. Forehand, P. Stansell, Q. Xiao, M. Abusara, Control of a point absorber using reinforcement learning, IEEE Transactions on Sustainable Energy 7 (4) (2016) 1681 – 1690.

[154] E. Anderlini, D. Forehand, E. Bannon, Q. Xiao, M. Abusara, Reactive control of a two-body point absorber using reinforcement learning, Ocean Engineering 148 (2018) 650–658.

[155] L. Bruzzone, P. Fanghella, G. Berselli, Reinforcement learning control of an onshore oscillating arm wave energy converter, Ocean Engineering 206 (2020) 107346.

[156] L. Busoniu, R. Babuska, B. De Schutter, D. Ernst, Reinforcement learning and dynamic programming using function approximators, CRC press, 2017.

[157] L. Graesser, W. L. Keng, Foundations of deep reinforcement learning: theory and practice in Python, Addison-Wesley Professional, 2019.

[158] V. Mnih, K. Kavukcuoglu, D. Silver, A. A. Rusu, J. Veness, M. G. Bellemare, A. Graves, M. Riedmiller, A. K. Fidjeland, G. Ostrovski, et al., Human-level control through deep reinforcement learning, nature 518 (7540) (2015) 529–533.

[159] H. Van Hasselt, A. Guez, D. Silver, Deep reinforcement learning with double q-learning, in: Proceedings of the AAAI conference on artificial intelligence, Vol. 30, 2016.

[160] J. Falnes, Ocean Waves and Oscillating Systems: Linear Interactions Including Wave-Energy Extraction, Cambridge University Press, 2002.